Methods for the system calibration of the DSSC detector for the European XFEL

Dissertation
zur Erlangung des Doktorgrades

an der Fakultät für Mathematik, Informatik und Naturwissenschaften
Fachbereich Physik
der Universität Hamburg

vorgelegt von

Stephan A. Schlee
aus München

Hamburg
2018

Abstract

The DSSC (DEPFET Sensor with Signal Compression) is a silicon based, 2d imaging detector for the European X-ray Free Electron Laser facility (European XFEL) in Hamburg and Schenefeld, Germany. The megapixel camera is foreseen for soft X-radiation from 0.5 keV up to 6 keV. Driven by the scientific requirements of the planned experiments, the design goals of the detector system are single photon detection, high dynamic range and a high frame rate of up to 4.5 MHz. Signal compression and amplification will be performed at the analog signal stage either in the silicon sensor pixels or in the read-out ASIC, yielding a low signal noise. Utilizing an in-pixel active filtering stage and an 8/9-bit ADC, the detector will provide parallel read-out of all pixels. Due to inhomogeneities in the chip production and in the biasing of the large format detector chips, each of the one million pixels will have to be calibrated individually.

This work presents an overview over the building blocks of the detector system and an introduction to the proposed calibration strategy. It proposes and compares several methods for the detector gain and offset calibration and the characterization of the system noise and evaluates their performance on datasets comparable to data expected from the full-format camera, that will be available in autumn 2018. The experimental part focusses on the adaption of the proposed methods on data measured with DSSC prototypes. A successful cross check of the calibration strategy using different calibration energies is presented.

Zusammenfassung

Der DSSC (DEPFET Sensor mit Signalkompression) ist ein auf Silizium basierender, bildgebender 2d-Detektor für den Europäischen Freie-Elektronen-Röntgenlaser (European XFEL). Die Megapixel-Kamera soll im Bereich weicher Röntgenstrahlung von 0.5 keV bis 6 keV eingesetzt werden. Die wissenschaftlichen Anforderungen der geplanten Experimente bedingen folgende Design-Ziele: Einzelphotonenauflösung, ein hoher dynamischer Bereich und eine hohe Bildwiederholrate von 4.5 MHz. Signalkompression und -verstärkung werden entweder innerhalb des Sensors selbst oder des Auslese-ASICs realisiert, was ein niedriges Signalrauschen ermöglicht. Der Detektor ist in jedem Pixel mit einem aktiven Signalfilter sowie einem 8/9-bit ADC ausgestattet und bietet die Möglichkeit, alle Pixel parallel auszulesen. Aufgrund von Ungleichmäßigkeiten bei der Chipfertigung und der Stromversorgung der großformatigen Detektorchips muss jedes einzelne der 1 Mio Pixel individuell kalibriert werden.

Diese Arbeit gibt eine Übersicht über die einzelnen Bausteine des Detektorsystems und eine Einführung in die vorgeschlagene Kalibrationsstrategie. Verschiedene Methoden für die Kalibration der Verstärkung und des Offsets sowie die Charakterisierung des Systemrauschens werden vorgeschlagen und ihre Leistung anhand von Datensätzen analysiert, die vergleichbar mit denen sind, die von der ab Herbst 2018 verfügbaren Vollformat-Kamera erwartet werden. Der experimentelle Teil der Arbeit legt den Fokus auf die Anwendung der vorgeschlagenen Methoden auf Datensätze, die mit DSSC Prototypen gemessen wurden. Ein erfolgreicher Cross-Check der Kalibrationsstrategie mittels verschiedener Kalibrationsenergien wird präsentiert.

Contents

1. Introduction

Figure 1.1: Stonehenge in Wiltshire, England. From de.wikipedia.org.

The prehistoric monument "Stonehenge" was built approximately 2000 B.C. and is located 3 km west of today's city of Amesbury, England. As of today, the exact purpose remains unknown to scientific research, as the culture that constructed the impressive assembly of stone blocks and earthworks left no written notes. However, it is quite evident that the alignment of the individual stones has been carefully adjusted to match specific astronomical events such as the winter and summer solstice [1]. It is not certain if "Stonehenge" was used as an instrument to measure the beginning of summer and winter, but it is safe to say that it was somehow "calibrated" before being set into service.

The calibration of the measuring apparatus has been a fundamental part of every measurement in the history of science. "Calibration" means that the measured quantity is put into relation with a measurement standard, such as for example a distance that is measured by comparison with a "yardstick" of a defined length. In the past the employed standards were instances of physical objects such as the "international prototype metre" established in Paris. Today's efforts have accomplished to link most of the fundamental units of the so-called "base quantities" (e.g. elapsed time, distance, mass, etc.) to standards given by natural constants, such as the speed of light. With the development of digital instruments, the assignment of the output of a measuring device in arbitrary digital units (ADU) to the respective physically measured signal level has become a common task attributed to the domain of system calibration.

The DSSC is a digital, ultra-fast megapixel detector that will be used for X-ray diffraction imaging at the European XFEL. This thesis presents methods for the system calibration of the DSSC instrument.

This work is organized into five main chapters: Chapter two introduces the science case of the European XFEL light source that is currently set into operation in Hamburg. The European XFEL, currently being the most powerful man-made light source of the world, will allow progress in many fields of research such as structural biology and chemistry, material sciences and the

study of matter under extreme conditions. The scientific requirements of the planned experiments motivate the development of new detector concepts such as the DSSC.

In chapter three, the working principle of the DSSC detector system is explained and an overview of the calibration methods is given. The central challenges of the system calibration are presented here: The intrinsic low resolution and built-in signal compression of the DSSC necessitate the development of a custom calibration approach. Also, the experimental setups used for the preparation of this thesis are introduced here.

Chapter four illustrates how the characteristical, non-linear system response of the DSSC detector pixels can be simulated and will introduce the DSSC detector simulation software package that is used to generate test data for the verification of the calibration algorithms. The methods used to characterize and calibrate the detector offset, noise and gain are presented in chapter five, which represents the core of this work. The achievable accuracy of the algorithms is evaluated by a comparison of the results with the settings of the simulated test data.

The calibration approach for the DSSC has been continuously tested with detector prototypes. In chapter six, measurement data are analyzed with the proposed methods and a verfication of the system calibration is given by comparison with an independent reference signal source: In a first step, the multi-step approach based on measurements with an X-ray tube, electronic signal generation and an infrared laser diode is used to calibrate the non-linear system response of the DSSC. In a second step, this calibration is cross-checked by irradiating the detector with protons providing signal energy in the MeV range.

2. The European XFEL
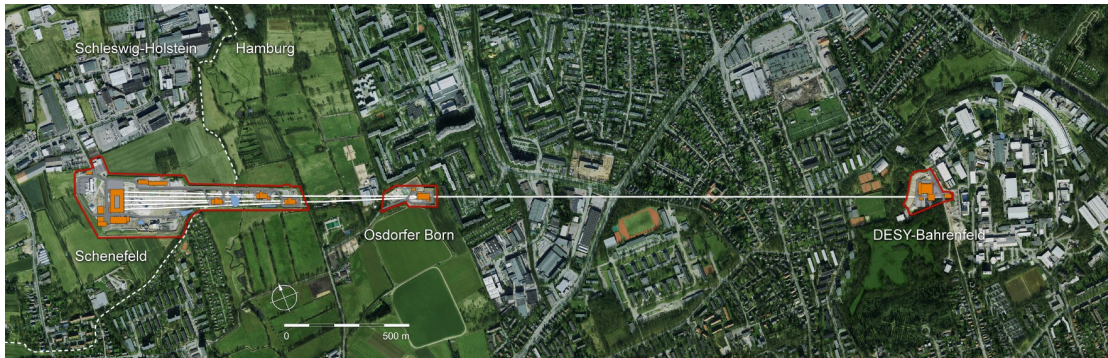
Figure 2.1: Aerial view of the three main XFEL sites in Bahrenfeld (DESY), Osdorfer Born and in Schenefeld. The underground linear accelerator starts in Bahrenfeld. The accelerated electron bunches are distributed into fanned out tunnels at Osdorfer Born. Between there and the experimental stations in Schenefeld, the X-ray light is generated [2].

The European X-ray free electron laser (XFEL) is a 4th generation light source currently being set into full operation in Hamburg and Schenefeld in Northern Germany [2]. Fig. 2.1 gives an aerial view of the experiment site. The European XFEL will provide the scientific community with a photon beam with unprecedented properties. The ultra-short (below 100 fs), ultra high-intensity X-ray flashes in the energy range from 0.26 keV up to 25 keV (corresponding to wavelengths from 4.7 nm down to 0.05 nm) will open up a fundamentally new physical domain in the field of photon science.

The central motivation for the development of this new light source was the improvement of one specific figure of merit, the so-called "brilliance" (B). It comprises the measures of the flux of photons of a given energy bandwidth, the beam spot size and its directional collimation, i.e the phase-space density of the beam [3]. For the European XFEL, once fully operational, the magnitude of this measure during a photon pulse is expected to be

$$B_{\text{peak}} = 5 \times 10^{33} \frac{\gamma}{\text{s mm}^2 \text{ mrad}^2 \, 0.1\% \, \text{bandwidth}}$$

which is nine orders of magnitude higher than that of the best conventional (synchrotron) X-ray sources [2], as is illustrated in fig. 2.2. Also, the average brilliance of the European XFEL will be very high due its superconducting linear electron accelerator that can be operated at a very high duty cycle [3].

2.1 Working principle of free electron lasers

While the beam amplification in conventional lasers is based upon the transitions of excited electrons in bound atomic or molecular states of either a solid, a liquid or a gas, the gain medium
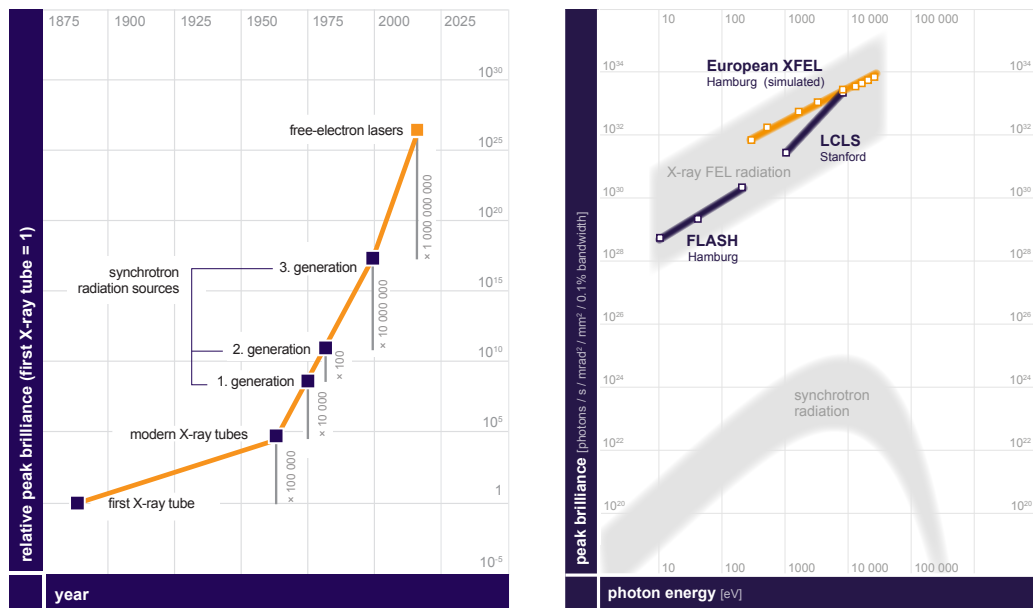
Figure 2.2: Evolution and comparison of the peak brillance of X-ray light sources over time [2].

in a FEL (free electron laser) is a beam of relativistic "free" (unbound) electrons [4]. These electrons propagate with a velocity near the speed of light along a sinusoidal path due to the magnetic field of a so-called undulator, a linear sequence of dipole magnets with alternating north-south orientation. Thereby, they emit synchrotron radiation in a narrow cone in the forward direction and, in a simplified view, interact with this radiation, which causes an exponential increase of the radiation amplitude along the undulator.

The European XFEL employs the SASE (self-amplified spontaneous emission) principle. With this technique, that is illustrated in fig. 2.3, the exponential light amplification is started spontaneously during *one pass* of the electrons through the undulator. This allows operation in the ultraviolet and X-ray regime for two reasons [5]:

- The start-up of the FEL process by so-called "seed radiation" in the ultraviolet and X-ray regime is complicated due to the lack of suitable lasers. A SASE FEL is operated without the need for a seed laser.

- Due to lack of mirrors in the vacuum-ultraviolet ($\lambda < 200\,nm$) and X-ray regime, an optical resonator cannot be constructed and the light amplification must be achieved in one single pass through the undulator.

In contrast to synchrotron-type light sources, where the electrons pass the undulator many times, a SASE FEL undulator also has the essential advantage of a much higher intensity due to the larger amount of electrons radiating coherently [5]: For the emission to be coherent, it must originate from electrons located at a distance smaller than the wavelength of the emitted radiation [4]. For the typical amount of accelerated electrons (order of 10^9) and the aspired wavelengths (UV and X-ray regime), this can only be achieved by the so-called "microbunching",

4
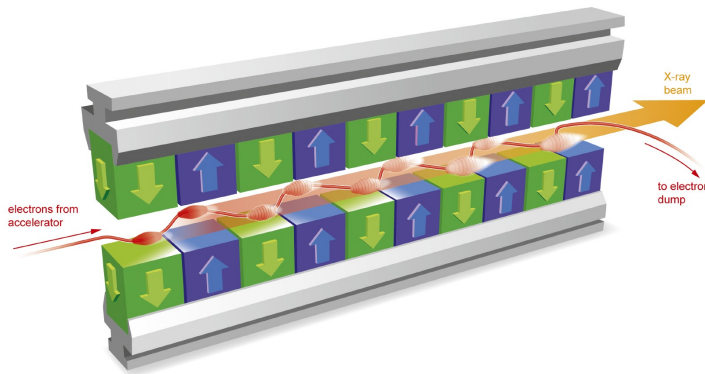
Figure 2.3: Illustration of the SASE (self-amplification spontaneous emission) principle in a magnetic undulator. A bunch of electrons is accelerated to near c by a linear accelerator and enters the undulator from the left. Due to the alternating magnetic field, the electrons are forced onto a sinusoidal path, causing the emission of synchrotron radiation. So-called electron microbunches are formed due to the energy exchange of the electrons with the generated radiation. At the end of the process the electrons are dumped and the photon beam goes to the experiment [2].

the slicing of the electron bunch inside the undulator due to the energy exchange of the electrons with the generated radiation. In a storage ring the electrons pass the same undulator and acceleration cavities many times (even millions of time per second). The random perturbations by the magnetic and electromagnetic fields imply a lower limit of the phase-space volume of the accelerated electrons [3], making the regime of microbunching inaccessible.

The FEL process is essentially a phenomenon that can be described as radiation-induced collective instability [3]. A complete mathematic description of a high-gain (= "single-pass") SASE FEL would exceed the scope of this thesis, but the basic working principle can be explained by the two following considerations [5]:

- **Overlap:** A relativistic electron in a magnetic field emits radiation tangentially in a narrow cone with the approximate opening angle

$$\phi = \frac{1}{\gamma} = \frac{1}{\sqrt{1 - \left(\frac{v}{c}\right)^2}} = \frac{m_e c^2}{E_e} \qquad (2.1)$$

  expressed either by the relativistic Lorentz factor γ or the mass m_e of the electron, the speed of the electron v, the speed of light c and the total energy E_e of the electron. Assuming that the magnetic field B of the undulator only has a component perpendicular to the trajectory of the electrons propagating in direction x, it can be written as

$$B = -B_0 \sin(k_u x) \qquad (2.2)$$

  with $k_u = \frac{2\pi}{\lambda_u}$ being the angular repetency of the undulator, as λ_u is the undulator period. Solving the equation of motion of the relativistic electron under influence of the Lorentz force leads to a sinusoidal deflection y of the electron which is perpendicular to both the

initial trajectory of the electron and the magnetic field (assuming that $v \approx c$):

$$y(x) \approx \frac{K}{\gamma k_u} \sin(k_u x) \tag{2.3}$$

using the dimensionless, so-called "undulator parameter" K:

$$K = \frac{eB_0}{m_e c k_u} = \frac{eB_0 \lambda_u}{2\pi m_e c} = 0.934 \cdot B_0[T] \cdot \lambda_u[cm] \tag{2.4}$$

with e being the elementary charge. The maximum angle of the undulation $\theta_{\max}$ with respect to the direction x can now be estimated with

$$\theta_{\max} \approx \left[\frac{dy(x)}{dx} \right]_{max} = \frac{K}{\gamma} \tag{2.5}$$

Comparing 2.5 with 2.1 one can conclude, that for $K < 1$ the electron beam always overlaps with the generated synchrotron radiation during its propagation through the undulator, enabling a constant interaction (i.e. energy exchange) of the electron beam with the radiation field. For $K \gg 1$, this condition is not given anymore and the machine is called a "magnetic wiggler".

- **Dispersion and microbunching:** The energy exchange between the electrons and the radiation field caused by the undulation is given by:

$$\frac{dE_e}{dt} = -e\,\boldsymbol{v} \cdot \boldsymbol{F} = -ev_y F_y \tag{2.6}$$

with $\boldsymbol{v}$ being the electron velocity vector and $\boldsymbol{F}$ being the electric field vector. The transverse electric field F_y and the electron exchange energy in the following way: If the transverse electron velocity v_y and the electric field are parallel, then $\frac{dE_e}{dt} < 0$. That means, that energy is transferred into the electric field, and the electron is decelerated. For anti-parallel electron velocity v_y and electric field, the electron is accelerated. This is illustrated in fig. 2.4 a).

The magnetic field of the undulator now acts as a dispersive medium: Electrons with a higher energy propagate on shorter trajectories and vice versa, as is illustrated in fig. 2.4 b). This dispersion leads to regions of increased density in the electron bunch, separated by regions of decreased density. These regions form at the periodicity of the (optical) wavelength of the radiation field λ_{FEL}. This process is called "microbunching".

As the electron bunch – massive particles moving on a wiggly line – moves slower than the radiation field, a steady energy transfer (and thereby the desired self-amplification) is only given, if the light wave advances exactly by one optical wavelength λ_{FEL} in one full period (or an odd multiple) of the electron trajectory. This condition is expressed by

$$\lambda_{\text{FEL}} = \frac{\lambda_u}{2\gamma^2} \left(1 + \frac{K^2}{2} \right) \tag{2.7}$$
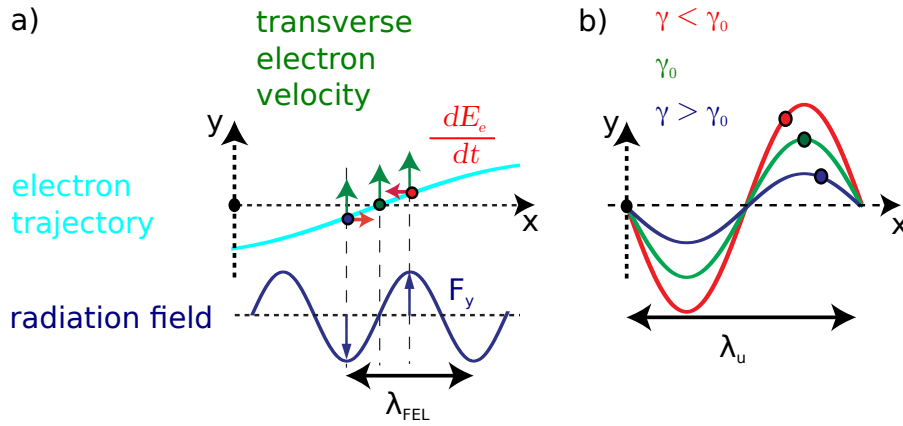
Figure 2.4: a) The energy exchange between the undulated electron beam and the radiation field causes electrons with a transverse electron velocity that is in phase with the electric field to decelerate and vice versa. b) The resulting spread in energy leads to a dispersion, as faster electrons propagate on shorter trajectories than slower electrons. Illustration after [4].

with Lorentz factor γ, undulator period λ_u and undulator parameter K. Only if this so-called "interference condition" is met, the microbunches form and the electrons interact with the radiation field close to the point of the maximum possible energy exchange. They emit coherent radiation – as the longitudinal dimension of the microbunches is close to λ_{FEL} – and always in phase with the already present radiation field.

The intensity of the emitted radiation scales quadratically with the number of particles that act coherently. Over the length of the undulator, the increasingly stronger radiation intensifies the microbunching – a self-amplifying process, that leads to an exponential increase of the radiation power.

2.2 Experiments at the European XFEL

The unprecedented properties of the high intensity X-ray beam at the European XFEL will open up the stage for novel explorations in fields such as material physics, plasma physics, planetary science and astrophysics, chemistry, structural biology and biochemistry [3]. Significant impact is expected also on biomedical and pharmaceutical studies.

The layout of the experimental stations and beam lines at the European XFEL is as diverse as its portfolio of research applications. Several instruments have been specifically designed for the individual scientific needs of the respective experiments in order to provide the suitable beam energy, probe handling and manipulation techniques and detector orchestration.

As of September 2017, the first user experiments at the European XFEL have started. They are located at the SASE 1 (sec. 2.1) beamline that provides an energy range of 3 keV to over 25 keV (corresponding to a wavelength of 0.4 nm to below 0.05 nm): The FXE (Femtosecond X-Ray Experiments) instrument will enable the research of extremely fast (timescale < 100 fs) processes, focused at so-called pump-probe experiments. The SPB/SFX (Single Particles, Clusters, and Biomolecules / Serial Femtosecond Crystallography) instrument will be used to achieve a better
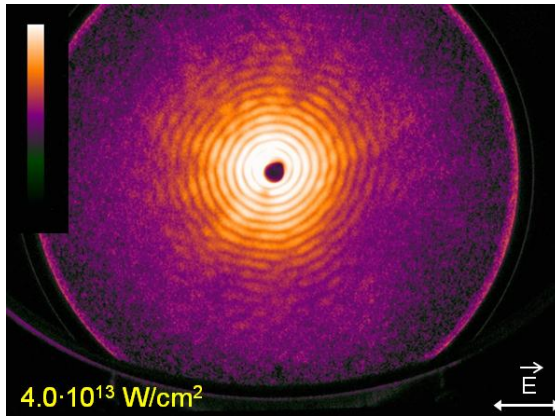
Figure 2.5: Single-shot diffraction pattern of single-cluster Xe^{4+} recorded at FLASH [6].

understanding of the shape and function of biomolecules, such as proteins, that are otherwise difficult to study.

The DSSC detector is one of three large-scale, fast 2d-imaging detectors that are being developed for the European XFEL. It is foreseen for usage at the low end of the European XFEL energy range. It will be operated predominantly at the SCS (spectroscopy and coherent scattering) and the SQS (small quantum systems) instruments at the SASE 3 beamline, where the beam energy is in the range of 0.26 keV to 3 keV (corresponding to a wavelength of 4.7 nm to 0.4 nm).

One of the scientific goals at the SQS (small quantum systems) instrument is the investigation of ultrafast electronic processes of highly excited states of matter [7] that exist e.g. in the interior of stars [8]. In [6], the results of a study based on the irradiation of single-clusters of xenon with intense X-ray laser pulses at the FLASH facility ([9], [10]), a predecessor of the European XFEL at the DESY in Hamburg, are presented:

- Atomic clusters of Xenon are brought into the focus of the X-ray laser beam and are thereby converted into highly excited plasma.

- Studying the electronic configuration of the excited state with conventional time-of-flight spectroscopy is ineffective due the fast electronic recombination occurring in the samples.

- In order to investigate the ionization dynamics of the nanometer-sized objects, diffraction patterns are recorded with the help of a 2d-imaging detector. An example of such a pattern can be found in fig. 2.5. Due to the small wavelength of the free electron laser (~ 14 nm in the example), the atomic clusters (size ~ 140 nm, $\sim 2 \cdot 10^8$ atoms) can be resolved.

- The scattered X-ray signal is affected by the change in the electronic configuration of the sample. The signal at large scattering angles increases more than linearly for higher incoming power densities of the X-ray beam.

- In order to describe the diffraction properties for large angles and high intensities, the study relies on the Mie-scattering model. For large angles and high intensities, the imaginary
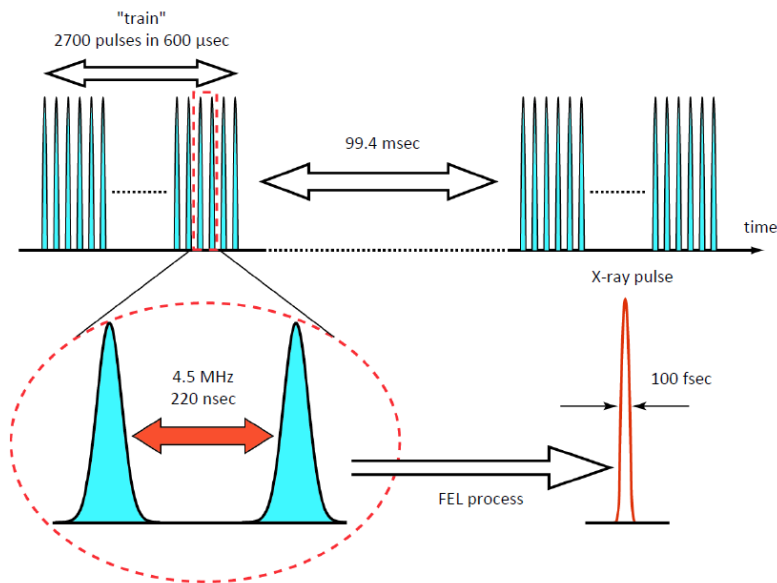
Figure 2.6: XFEL pulse structure. In the 4.5 MHz operation mode of the XFEL, the sensor itself has to take image data every 220 ns. In the time slot of about 0.1 s between the individual pulse trains, the data from the sensor can be read out and transmitted to a storage system. From [2].

part of the refraction index of the irradiated clusters increases strongly, which describes an unexpectedly strong increase in the scattering cross section.

- A theoretical description of the underlying effects could not be verified experimentally due to the lack of measurement techniques.

- However, the imaging was performed with a so-called micro-channel plate detector, in case of the study a combination of a pixelated photomultiplier, a scintillator screen and a CDD camera. In comparison to modern semiconductor imaging detectors these instruments show several disadvantages, primarily regarding their speed, background noise and dynamic range [11]. The study notices for example, that the first diffraction maxima in the patterns recorded with higher intensity (fig. 2.5) already suffer from detector saturation.

The study [6] summarizes that ultrafast processes in highly excited states of matter, non-equilibrium plasmas and dense exotic systems can be studied with intense, ultrashort X-ray pulses and 2d diffraction imaging. Its conclusion points towards the already mentioned new research opportunities in that area and the associated need for new detector concepts.

Due to the shorter wavelength, higher intensity and higher repetition rates available at the European XFEL, the expected scientific yield of experiments of this type can only be achieved if the employed detectors meet the experimental requirements.

2.3 Detector requirements and detectors

The scientific demands for the 2d-imaging detectors at the European XFEL are dictated by the properties of the X-ray beam and the individual needs of the planned experiments. The two central requirements that drive the development of the DSSC detector are:

- **Readout speed:** Fig. 2.6 shows the XFEL pulse structure that forms due to the microbunching in the SASE undulators that were presented in the previous section. The high repetition rate of the ultra-short pulses on the one hand enables time-resolved studies of ultra-fast processes on the femtosecond scale and on the other hand allows to record high amounts of data of samples that are difficult to produce and are therefore available only in sparse amounts or for a short period of time.

  In certain experiments, each sample being hit by the intense X-ray beam is destructed due to the high photon density. As the time scale of the destruction process is much longer than the laser pulse duration (~ 100 fs), the particle geometry remains the same on the time scale of the interaction with the laser pulse and a diffraction pattern can be recorded – a technique referred to as "diffraction before destruction" [12]. Due to the destruction of the sample, every shot must be treated as a separate experiment.

  The imaging detectors at the European XFEL are therefore required to record full 2d diffraction patterns with the frame rate of the X-ray flashes (4.5 MHz).

- **High dynamic range and single photon sensitivity:** To allow the later reconstruction of the atomic and electronic structure of the samples in the experiments at the European XFEL, mainly two properties of the recorded diffraction patterns impose critical requirements for the detectors:

  On the one hand, it is expected that up to 10^4 photons per pulse per pixel will be generated in the most intense parts of the scattering images. On the other hand, "photon-counting-statistics" resolution at the Poisson limit is needed due to the low intensity regions in the image, where the difference between zero and one photon can be crucial for the successful interpretation of the data [3].

  A high sensitivity for low photon count numbers in the pixels will not only allow the resolution of higher scattering orders and thereby improve the precision of the reconstruction algorithms, but will also help to characterize the X-ray background resulting from scattering on residual gases in the vacuum or on the carrier medium of the experiment sample [13].

Three different fast 2d-imaging detectors, all based on silicon semiconductor sensors, are being developed for operation at the European XFEL. They are designed to fulfill the scientific requirements at the European XFEL each in a conceptually different manner [14]:

- The **AGIPD** (Adaptive Gain Integrating Pixel Detector) is developed by a collaboration between DESY, the University of Hamburg, the University of Bonn (all in Germany) and the Paul Scherrer Institute (PSI) in Switzerland [15]. It will provide a high dynamic range due to a gain switching amplifier in each pixel. This will allow counting more than 10^4 photons with an energy of 12.4 keV in the lowest gain and single photon sensitivity in the highest

gain. It is equipped with an analog memory capable of storing 352 images and is able to operate at up to 4.5 MHz speed. The pixel size is about 200 microns.

- The **LPD** (Large Pixel Detector) [14] has been developed by a UK group led by the Rutherford Appleton Laboratory/STFC (Science and Technology Facilities Council) with contributions from Glasgow University. LPD is using three parallel amplifiers with low, medium and high gain per pixel as well as three corresponding analog signal pipelines. The three-fold layout requires relatively large pixels with a pitch of about 500 microns.

- The **DSSC** ([16],[17],[18]) is the only detector currently being developed that is able to provide single photon resolution at the low energies (from 0.26 keV up to 3 keV) of the SASE 3 beam-line combined with a high dynamic range, capable of counting up to 10^4 photons at an energy of 1 keV. Its pixels have a pitch of about 200 microns.
  In order to enable a full parallel readout that is needed for the required high frame rate of 4.5 MHz, each individual DSSC pixel is equipped with its own analog read-out electronics that provide signal filtering, digitization and digital storage space.

3. Technical overview

The DSSC detector will have to be calibrated before its usage in experiments at the European XFEL. Sec. 3.3 will explain why the calibration cannot be done at a later point, i.e. retroactively on already recorded, scientific data. The individual steps of the calibration are closely connected to the working principle of the DSSC detector system. The technical features most relevant for the calibration will be presented in sec. 3.1. Experimental prototypes that have been used for the measurements performed in the scope of this thesis are introduced in sec 3.4.

3.1 Working principle of the DSSC detector

Fig. 3.1 shows a CAD drawing of the complete detector system. The camera will be equipped with 1024 x 1024 hexagonal pixels, covering a sensitive area of about 0.24 x 0.25 m^2. Each sub-matrix of 64 x 64 sensor pixels is connected to a specifically designed read-out ASIC (application-specific integrated circuit). The DSSC read-out ASICs [20] provide each individual pixel with its own read-out pipeline[1] that comprises signal filtering and digitization. Each ASIC pixel also houses digital storage so that the measurement result of 800 X-ray flashes[2] can be temporally stored before they are processed by the data acquisition (DAQ) electronics.

Fig. 3.2 is a schematic side-view of the focal plain of the DSSC. It is connected to cooling blocks providing sub-zero degrees Celsius temperature regulation via a ceramic heat spreader. Due to the short electrical connection lengths and resulting small parasitic capacities in the analog signal path, the DSSC will excel regarding its noise performance. Other relevant features of the detector system are:

- As the sensor is irradiated through its homogeneous (back-)side, a high and homogeneous quantum efficiency can be achieved.

- During the XFEL pulse train, the recording of individual frames can be arbitrarily prohibited by an external veto-signal. By overwriting frames that do not contain useful information, a higher number of frames of a pulse train that are of scientific interest can be recorded.

- The sensor system is divided into four individual quadrants that can be moved perpendicular to the X-ray beam in order to record signal in scattering directions that are of interest to the experiment.

3.1.1 Interaction of radiation with matter

For the DSSC detector system, two different sensor concepts are being developed. Both are silicon semiconductor structures. In those, the detection of ionizing radiation is based upon the

---

[1]Later also referred to as "signal chain".
[2]Individual images recorded with the detector are often referred to as "frames". It is also common to call the respective individual output value of a single pixel a "frame".
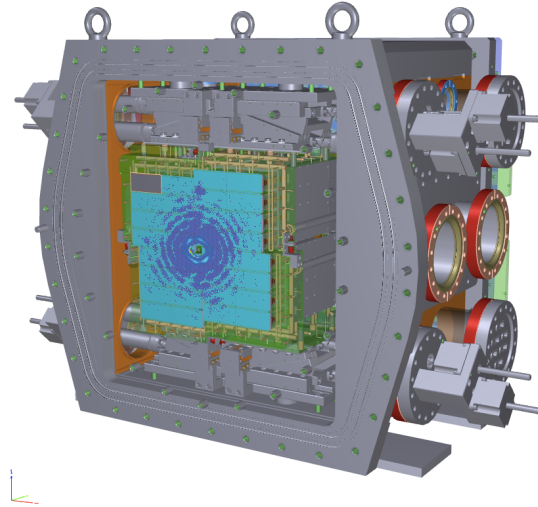
Figure 3.1: CAD drawing of the DSSC detector system, together with its custom vacuum chamber and quadrant movement stages. The sensor area is drawn in cyan. Four quadrants with 8 sensors each are arranged around a central beam hole for the unscattered X-ray beam. Each individual sensor chip matrix has a size of 128 x 256 pixels. The most upper left sensor matrix is marked in a different color. The active sensor surface of the detector is about 0.24 x 0.25 m^2 (CAD drawing by the DSSC Mechanics/Thermal work package, group lead C.Wunderer, DESY).

For illustration, a diffraction pattern of a T4 virus, plotted after measurements at the LCLS (Linac Coherent Light Source, Stanford Linear Accelerator Center), is projected upon the detector surface (from [19]).
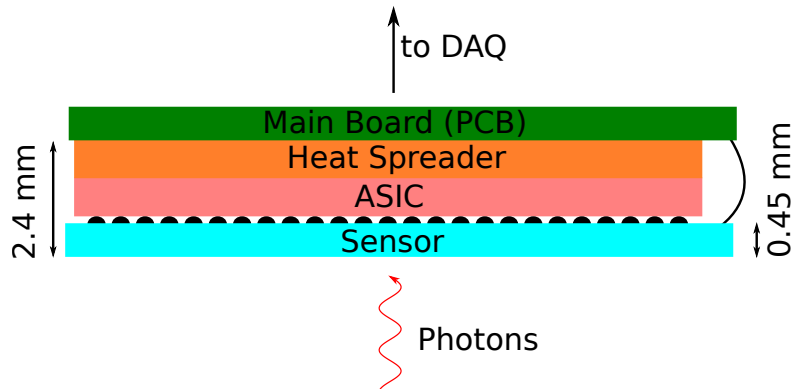
Figure 3.2: Schematic drawing of the "sandwich" design of the focal plane of the DSSC detector. Photons arrive from the backside of the silicon sensor modules. Each sensor pixel is connected via bump bonds (small black dots) to the read-out ASIC. There, the analog signal is filtered, digitized and temporally stored. The sensor module also serves as an interlink for the data transfer to the main board. It is connected to the printed circuit board (PCB) via wire bonds (curved line), that also provide biasing for sensor and ASIC.
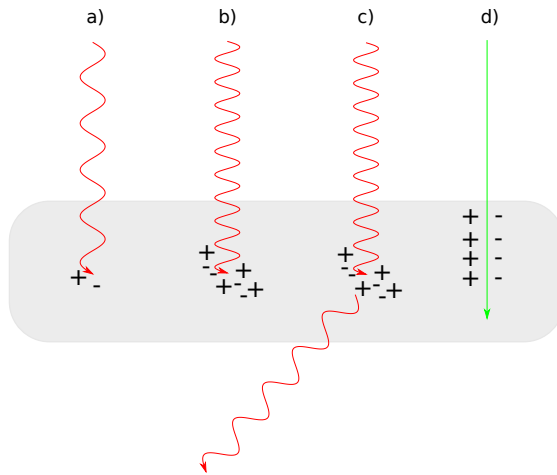
Figure 3.3: Different forms of radiation interacting with matter: a) Photoelectric effect with optical photon, b) X-ray photoelectric effect, c) inelastic Compton scattering, d) particle radiation, e.g. protons

generation of electron-hole pairs in the valence respectively conductance band that then propagate in the semiconductor. The process that generates these signal carriers depends on the energy level and the type of the incident radiation.

Electromagnetic radiation:

- **Fig. 3.3, a):** Photons with an energy above, but in the order of the band gap of the semiconductor can generate an electron-hole pair by ionizing the outer shell electrons of the material. Silicon has a band gap of 1.12 eV and is therefore sensitive to optical light, with a corresponding maximal wavelength of 1107 nm. Due to the band gap in silicon being indirect, oscillations of the crystal lattice, so-called phonons, are involved in every charge carrier generation. Therefore, the average energy $\epsilon_{e/h}$ to create an electron-hole pair in silicon is about 3.63 eV [21].

- **Fig. 3.3, b):** Photons with a higher energy such as X-rays also excite electrons from the inner shells of the atoms. The electrons filling up these vacancies result in the emission of either so-called Auger electrons or fluorescence photons. Both the primary excited electron and Auger electrons can excite further electrons into the conduction band [22]. A single photon can therefore generate more than one electron-hole pair. For a photon with an energy of 1 keV this yields about 275 electron-hole pairs due to $\epsilon_{e/h} = 3.63\,\text{eV}$.

  Both a) and b) are referred to as photoelectric effect or photo effect. The whole energy of the photon is transferred into either signal charge generation or lattice oscillation. This effect dominates the interaction of photonic radiation with silicon up to about $5 \cdot 10^4$ eV.

- **Fig. 3.3, c):** Photons with higher energies are scattered and will deposit only a part of their energy in the first interaction with the material. This process is called Compton scattering or "incoherent" scattering. This effect is dominating from $\sim 5 \cdot 10^4$ eV up to

~ 10 MeV) The scattered photon has a longer wavelength due to the energy loss and can either be involved in another interaction process or leave the detector material. The photo electron from the scattering process will loose its energy by exciting further electrons as in b), leading to the generation of electron-hole pairs.

- Photons with energies higher than at least twice the rest mass of an electron (511 keV) can also convert directly into electron-positron pairs in accordance to Einstein's formula $E = mc^2$. This effect is called "pair production". The right panel of fig. 3.4 shows that pair production will dominate the interaction for energies higher than about 10 MeV. Additional photon energy will lead to further ionization and the generation of electron-hole pairs. Both pair production and Compton scattering are of no interest for the scope of this thesis.
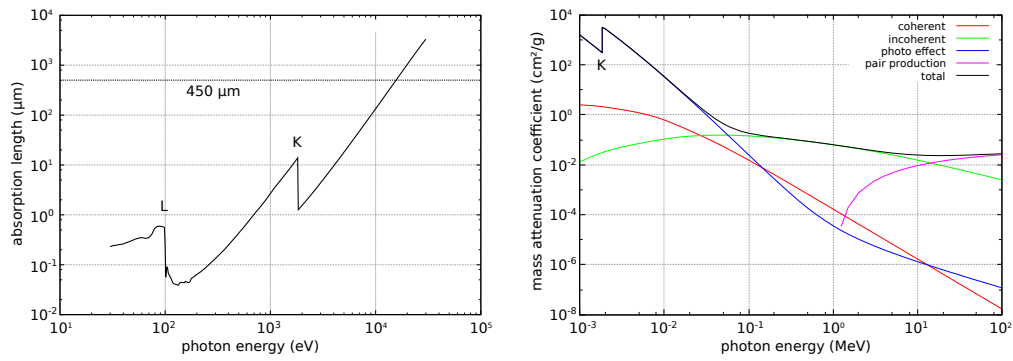

Figure 3.4: Left (from [23]): Absorption length of UV and X-ray photons in silicon. The two edges reflect the excitation of electrons from the L respectively the K shell. The thickness of the DSSC sensor modules is $450\,\mu m$. Right (from [24]): Mass attenuation coefficient for electromagnetic radiation in silicon for higher energies.

The attenuation of electromagnetic radiation in matter is described by the Beer-Lambert law:

$$I(x) = I_0 \cdot e^{-\frac{x}{\mu}} = I_0 e^{-\alpha x} \tag{3.1}$$

where $I(x)$ denotes the intensity after a certain depth x in relation to the intensity at the start of the interaction $I_0 = I(0)$. μ is the attenuation (or "absorption") length, defined as distance in the detector material after which $1/e \approx 63\%$ of the photons have been absorbed. α is the attenuation factor ($\mu = \frac{1}{\alpha}$). This quantity is a material constant that depends on the energy of the incident radiation.

The left panel of fig. 3.4 shows the absorption length in silicon for a variable photon energy in the range dominated by the photo effect. The steps in the curve correspond to photon energies high enough to excite electrons from the next shell. Above around 100 eV, electrons from the L shell can be excited. Above around 2 keV (1839 eV), electrons from the K-shell of the silicon atoms are excited, resulting in the K-absorption edge. The thickness of the sensor structures used in this thesis is $450\,\mu m$, yielding a detection probability (i.e. quantum efficiency) of 99% for energies up to of 8 keV [23]. Another approach to describe the interaction of electromagnetic radiation with matter is depicted in the right panel of fig. 3.4: It shows the mass attenuation

coefficient, a variant of the "absorption cross section", for higher photon energies in the range from 1 keV up to 100 MeV in silicon. The plot illustrates the composition of the individual effects described above.

Statistical fluctuations of the charge generation process in the semiconductor material are commonly described by Fano statistics [21]. The Fano factor reflects the fact, that the individual charge carrier generation processes of a certain interaction are not independent from each other, resulting in a lower net variance than pure Poissonian statistics. The variance σ_{Fano} is given by

$$\sigma_{\text{Fano}} = \sqrt{\frac{F\,E}{w}} \tag{3.2}$$

with F being the Fano factor, E being the energy of the incident radiation and w being the pair generation energy of the respective material. For silicon, the Fano factor has been determined to be $F_{Si} = 0.115$.

Particle radiation:
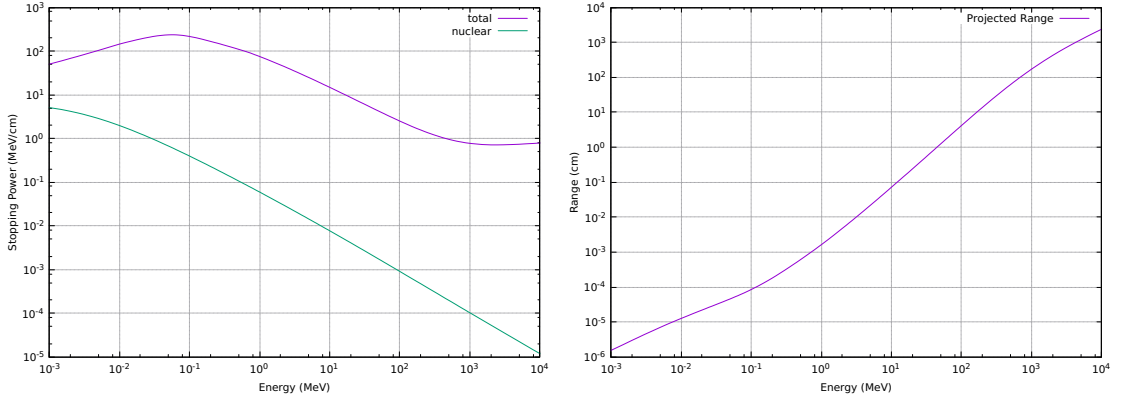
Figure 3.5: Stopping power (left) and projected range (right) of accelerated protons in silicon. Data from [24].

Signal charges in the detector material can also be generated by incident particles. Focusing on charged particles such as protons or electrons, the interaction with the material is dominated by inelastic Coulomb collisions with the orbital electrons of the material [11]. This is illustrated in the left panel of fig. 3.5, where the so-called stopping power for protons in silicon is plotted with initial energies between 1 keV and 10^4 MeV. The total stopping power comprises electronic stopping and stopping due to elastic collisions with the nuclei of the target.

At any given time, the particle interacts with many electrons at once. The maximum energy transfer for each of these interactions is $4\,E\frac{m_e}{m}$, with E being the kinetic energy of the particle, m being its mass and m_e being the mass of an electron. E.g. for protons with an energy of 1 MeV this corresponds to an energy loss of about 0.4% per collision.

Stopping processes of fast, charged, heavy particles are described best by the Bethe-Bloch formula that can be used to calculate the energy loss $-\frac{\mathrm{d}E}{\mathrm{d}x}$ for the distance x traveled in the

Figure 3.6: Cut through a circular DEPFET-pixel. On the right side, an equivalent circuit for the two FET-transistors is given. Their functional principle is given in the text. Figure by P. Lechner.
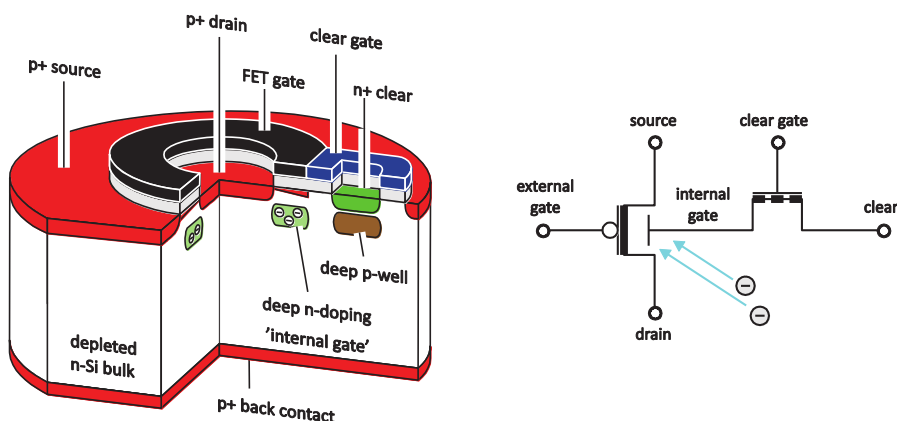
stopping medium, depending on the speed and charge of the incident particle and the electron density of the medium. The so-called projected range (fig. 3.5, right panel) of a particle refers to the distance between the entrance point into the stopping medium and the point were the particle is stopped completely – projected onto the initial direction of the particle.

3.1.2 Detection with depleted semiconductor sensors

Charge carrier depletion is essential to the function of any semiconductor radiation detector, as the depleted regions provide the electric field that is needed to separate the generated electrons and holes which would otherwise recombine and therefore not amount to any detectable signal. A completely depleted detector is desirable, as then the volume sensitive to incident radiation is maximized. It has been shown [25] that it is possible to deplete the full volume of a semiconductor device by applying the readout contact as a local n^+-implantation to the bulk – a concept also known as "sidewards depletion". One of the main advantages of this concept is the avoidance of parasitic capacities caused by large contact anodes that would imped the noise performance of the sensor. The silicon sensors employed in the DSSC detector system use "sidewards depletion" to fully deplete the detector volume.

Two individual sensor concepts have been developed for usage with the read-out electronics of the DSSC:

- The **DEPFET** (Depleted p-channel field effect transistor, [16], fig. 3.6) is an active-pixel sensor that provides intrinsic signal compression due to the unique design of its internal electronic potential structure. By supplying a high negative voltage to the p^+ back contact, the device is fully depleted. Signal electrons are collected in a so-called "internal gate" underneath the p-channel of a field effect transistor and steer its conductivity by inducing mirror charges. As the internal gate, that serves as a potential well for the signal electrons, expands further into the device (not shown in fig. 3.6), the influence of the accumulated charge carriers on the p-channel is diminished for higher signal levels. The resulting signal compression and the direct amplification of the signal allows for a high dynamic range
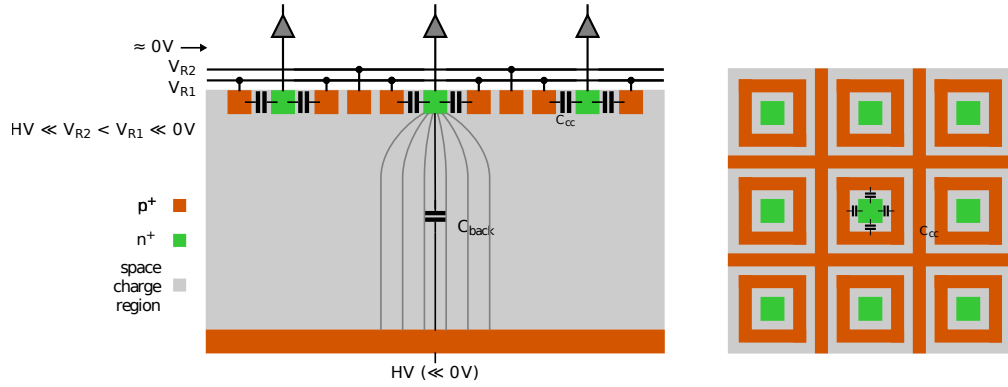
17

Figure 3.7: Cut trough (left) and top-view (right) of a MiniSDD pixel matrix with square pixels. In the DSSC, hexagonal pixels are used. For illustration, the (parasitic) capacities are given. Figure from [26].

combined with low noise figures. An additional field effect transistor is used to "clear" i.e. reset the DEPFET. Thereby the accumulated charge is removed from the internal gate by applying a positive potential to the DEPFET gate and clear contact. A detailed study on the development and test of DEPFET sensors for their application in the DSSC detector is given in [13].

- In comparison to the DEPFET, the **MiniSDD** (Miniature Silicon Drift Detector, based on the functional principle of the silicon drift detector described in [25]) is a simpler sensor concept. The manufacturing process of DEPFET matrices is complicated due to the many implantation and deposition steps needed to produce the internal gate and the two field effect transistors. The MiniSDD detector was introduced to equip the full megapixel camera with sensors at its first day of operation. Fig. 3.7 is a schematic illustration of a pixelated MiniSDD matrix, depicting square pixels. The MiniSDDs produced for the DSSC have the identical, hexagonal pixel geometry as the DEPFET sensor matrices. Equally to the DEPFET, the backside is supplied with a high negative voltage (HV) and generated signal charges are separated by the electric field. The signal electrons are then collected in the readout anode (n^+). The black lines in the left figure visualize the electrical field that draws the signal electrons towards the n^+-read-out anodes (green squares). As in the DEPFET sensors (not illustrated there), two so-called ring structures (p^+) arranged around the read-out anodes are also supplied with negative voltages (V_{R1}, V_{R2}) and shape the internal electrical potential well. In contrast to the DEPFET sensor, the MiniSDD does neither provide intrinsic signal compression nor signal amplification.

Fig. 3.8 shows the equivalent circuit diagram for the two different sensor concepts. The electrical front end of the read-out ASIC is designed to process a signal current I_{sig} that depends on the amount of accumulated signal electrons. In the DEPFET, this current (I_{sig}) is steered by signal charges collected in the internal gate (Q_{in}) of the field effect transistor. The equivalent circuit of the MiniSDD is a diode.

The signal charge collected on the input capacitance (C_{in}) of the pixel read-out chain directly
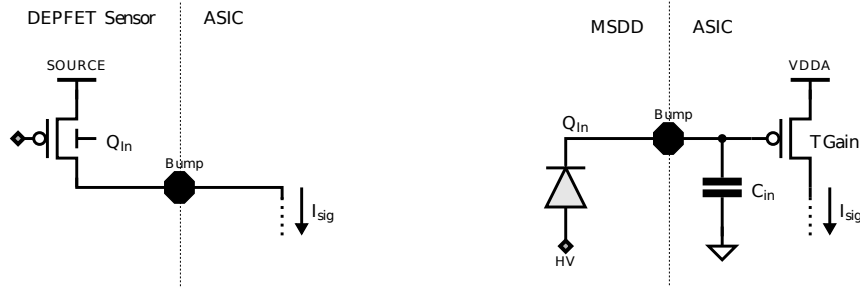
Figure 3.8: Read-out circuit diagram for DEPFET (left) and MiniSDD (right) DSSC sensors. Figure from [26].

changes the gate voltage of a transistor inside the read-out ASIC (TGain), that is supplied with a fixed source voltage (VDDA). By that, a signal current is generated that can be processed in the downstream read-out electronics identically to the DEPFET current signal.

3.1.3 Analog signal compression and filtering
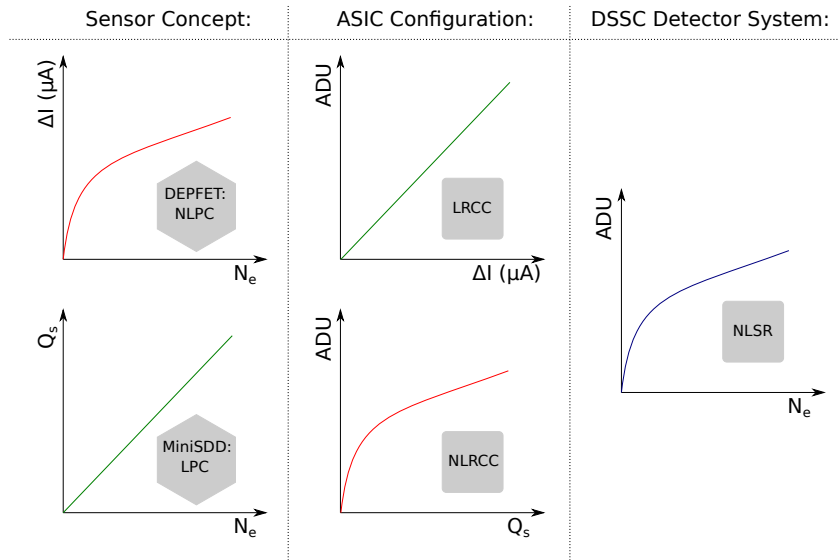
Figure 3.9: Illustration of the composition of the non-linear system response (NLSR) for the two different DSSC sensor concepts (sec. 3.1.2).

The DSSC detector is designed to provide high-speed photon sensitivity via single-shot integration. The number of incident photons can be inferred from the collected signal charge since the photon energy at the XFEL beam line is known. Besides the requirement for a fast rast-out speed, a high dynamic range of the detector system is needed to interpret the scientific data of the experiments at the European XFEL (sec. 2.3). Due to size constraints – every individual

pixel is equipped with own signal read-out chain, digitization stage and digital storage – an 8 bit ADC was used in the design of the DSSC ASIC. This causes a system-inherent problem: With a resolution of 8 bit only 256 analog signal values at maximum can be discerned. If one would assign each ADC step[3] to a signal increment corresponding to 1 photon, the highest signal value that could be digitized would correspond to 256 photons. A high dynamic range e.g. from $0, 1, 2, \ldots, \mathcal{O} \, 10^4$ photons can therefore only be realized, if the number of photons attributed to one ADC bin increases as a function of the collected signal [17]. This system property is referred to as "non-linear system response" (NLSR). For the NLSR, the analog signal needs to be compressed before entering the ADC, that is designed to convert analog signal levels to arbitrary digital units (ADU) with a linear transfer characteristic. As the DSSC detector is designed with two different sensor concepts, two different strategies are applied (fig. 3.9):

- The signal current increment ΔI of the DEPFET sensor decreases for higher signals (i.e. number of signal electrons N_e) due to the structure of the internal gate. This sensor-intrinsic compression is referred to as "non-linear pixel characteristic" (NLPC). In case DEPFET sensors are used, the DSSC ASIC is configured with a linear read-out channel characteristic (LRCC).

- The MiniSDD sensor does not provide internal signal compression. The signal charge Q_s at the input node of the read-out ASIC is directly proportional to the number of signal electrons N_e. This is referred to as "linear pixel characteristic" (LPC). In the first DSSC prototypes equipped with MiniSDD sensors that were used in this thesis, the analog signal compression is realized by the specific circuiting and biasing of the first amplifying transistor (fig. 3.8, TGain) [27]. One major drawback of this technique is its high sensitivity with respect to its optimum operating (biasing) point [26]. This configuration of the DSSC ASIC is referred to as non-linear read-out characteristic (NLRCC).

The function[4] of the signal processing in the DSSC read-out ASIC can be explained with the help of a simplified block circuit diagram (fig. 3.10):

1. The current signal coming either directly from the DEPFET sensor or the MiniSDD front-end transistor is initially stabilized by a so-called "cascode" (a circuit that improves the input-output isolation based on two amplifying transistors put in series, [28]) and the majority of the signal baseline current ($\sim 100 \, \mu A$) is drained off ("subtracted") with a self-calibrating circuit.

2. The central element of the analog signal read-out front end is the so-called "flip-capacitor filter" [29] that provides correlated double-sampling of the analog current signal: The sensor baseline current before the arrival of the photon signal is integrated by storing it on the capacitor C_f. By switching the polarity of this capacitor, it is then subtracted from the value of the subsequent signal integration. This technique is used in order to reduce flicker

---

[3]The individual steps of an analog to digital converter are also often referred to as "bins".

[4]A much more detailed presentation of the design and study of all DSSC ASIC building blocks and their properties can be found in [26].

noise (also known as $1/f$ noise). The resulting signal weighting function can be found in fig. 3.10.

3. The signal voltage V_{signal} is then sampled on one of the two sample-and-hold capacities and then digitized, which is described in the next section.

In addition, each ASIC is equipped with several electronic circuits that can be used as internal sources of reference. One of them is a 14-bit internal digital-to-analog converter (DAC) that provides voltage levels derived from the global reference voltage V_{ref}.
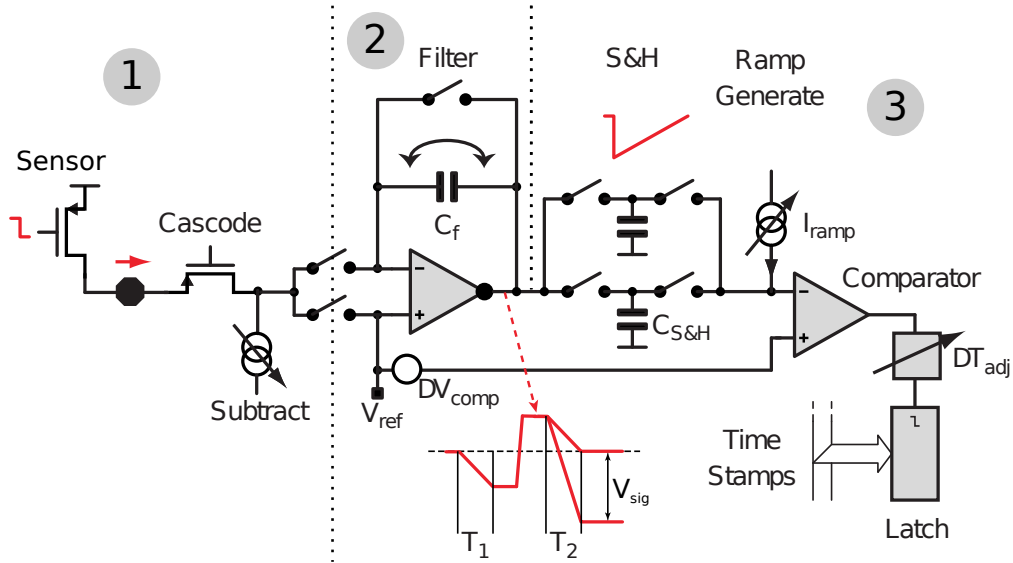

Figure 3.10: Simplified block circuit diagram of the DSSC ASIC. The current signal is filtered via so-called "double integration" in the flip capacitor filter (see small diagram): If no signal is present, the output of the filter does not change. If the signal current changes after the first integration (T_1), a voltage V_{signal} proportional to the signal current change ΔI is stored on the next block. Figure provided by Prof. P. Fischer, ZITI.

3.1.4 Digitization

The signal voltage V_{signal} output of the flip capacitor filter is first stored on the sample-and-hold capacitors and then digitized with an 8 bit ADC that has been designed by DESY ([30]). The type of the ADC is a single slope comparator, which can be implemented in a compact space as it does not need its own digital to analog (DAC) stage like a successive-approximation type ADC [28].

The ADC converts[5] the signal information into the time domain by discharging the sample-and-hold capacitors with a defined ramp current I_{ramp}. An in-pixel counter is started at the beginning of the ramping process. As soon as the voltage reaches the level of a defined threshold reference voltage V_{ref}, a voltage comparator fires and the counter value is saved to the digital

---

[5]The following description presents the operation of the ADC in a simplified fashion, sparing detail on the propagation and source of electronic system noise that is not necessary for the understanding of the studies presented in this work.
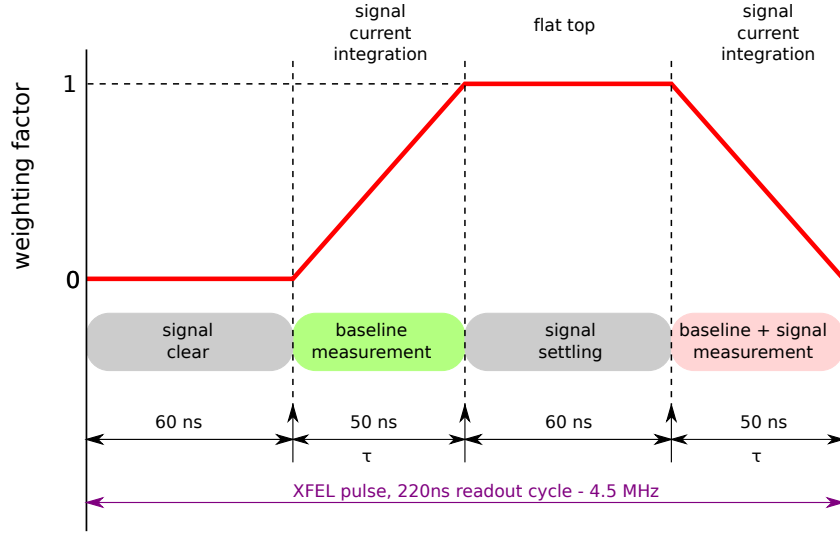
Figure 3.11: Standard timing diagram and weighting function (red line) of the flip capacitor filter for 4.5 MHz operation mode. The DSSC operation is synchronized to the XFEL timing, signal charges therefore arrive at the beginning of the flat top (110 to 170 ns). Signal arriving during the integration is only partially measured, signal arriving completely outside the trapezoid is weighted with "zero" and will therefore not be measured.

storage. Since the I_{ramp} is constant, the ramp slope is constant and therefore the required time is proportional to the input signal voltage V_{signal}. The duration t_{ramp} of the digital sampling can be described with the following relation:

$$t_{ramp} = \frac{C_{SH}}{I_{ramp}} \cdot (V_{ref} - V_{signal}) \tag{3.3}$$

With C_{SH} being the capacity of the sample-and-hold capacitor. In order to change the gain of the ADC, the value of I_{ramp} can be adjusted with help of a 6 bit DAC in 5% steps around its nominal value of $5\mu A$.

A programmable delay (DT_{adj} in fig. 3.10) between the start of the discharge of the sample-and-hold capacitor and the start of the in-pixel counter is implemented in order to change the offset of the ADC. The comparator therefore triggers at a time t_{trig} given by

$$t_{trig} = t_{ramp} + \Delta t_{pixdel} \tag{3.4}$$

The quantity of the pixel delay Δt_{pixdel} can be derived from the equation

$$\Delta t_{pixdel} = (t_{pixdel0} + k \cdot t_{pixdeladj}), \text{ with } k \in \{0, \dots, 15\}. \tag{3.5}$$

The pixel delay base value $t_{pixdel0}$ and the pixel delay adjust increment $t_{pixdeladj}$ are pixel-by-pixel specific, hardware dependent constants. k is the so-called "pixel-delay" setting. It allows an adjustment of the offset in 16 delay steps 10% of the "bin width":

For any analog to digital converter (ADC), the least significant bit (LSB) corresponds to an

analog signal interval, the center of which is assigned to the digital output value (in units of ADU). In an ideal ADC, the width of this signal interval, also called "bin width", is identical over its whole dynamic range. The sequence of bin boundaries S_{bb} of an ideal n bit ADC (2^n bins) can be defined as

$$s_{bb,i} = (i - \frac{1}{2}) \cdot \text{LSB}, \text{ for } i = 0, \ldots, 2^n \tag{3.6}$$

These bin boundaries correspond to the analog signal values that give the edges of the ADC bins. The lower boundary of the first bin, and the upper boundary of the last bin, are given by $s_{bb,0}$ and $s_{bb,2^n}$. In comparison to an ideal ADC that gives a linear dependence between the input signal and its output and also equal step size of the bins, ADC's implemented in reality are afflicted with imperfection:

- The **differential non-linearity** (DNL) measures the deviation of the actual from the ideal bin-width. When the bin boundaries of a real ADC steps are denoted with $s'_{bb,i}$, then the DNL of bin i calculates to [31]:

$$\text{DNL}_i = \frac{s'_{bb,i} - s'_{bb,i-1}}{\text{LSB}} - 1 \tag{3.7}$$

  A positive DNL means that the actual bin width is larger than the ideal bin width.

- The **integral non-linearity** (INL) describes the overall deviation of the real ADC transfer function of the ideal one. That means, that the real analog signal values $s'_{bb,i}$ corresponding to the ADC bin boundaries are in fact different from the saltus values of the ideal ADC transfer function, $s_{bb,i}$. The INL therefore calculates to:

$$\text{INL}_i = \frac{s'_{bb,i} - s_{bb,i}}{\text{LSB}} \tag{3.8}$$

  The INL describes a deviation from the linear transfer characteristic of the ideal ADC. Positive values describe the situation of an ADC switching "to late", resulting in an assigned real signal value of the ADC step that is "to low" in comparison to the real signal level.

Figure 3.12 shows a comparison of an ideal and a real 3-bit ADC. The real ADC depicted in blue shows both differential and integral non-linearities. Differential non-linearity does not necessarily cause a shift of the ADC transfer characteristic: The centers of the first two bins still are located on the ideal, linear (green line) characteristic. After the first two bins, the integral non-linearities of this exemplary ADC "add up" to a distinct shift, that decreases again for the last step. The figure illustrates: The DNL of an ADC can in theory "correct" itself, that means overly wide and small bins can compensate each other. In that case, the correct analog signal value could still be assigned to the output of the ADC. If multiple overly wide or small bins add up, the assignment of the analog signal value to the ADC output is erroneous.

In practice, it is often possible to determine the ADC transfer characteristic, i.e. the DNL and INL, by gradually altering the input signal of the ADC. Fig. 3.13 shows an example of such
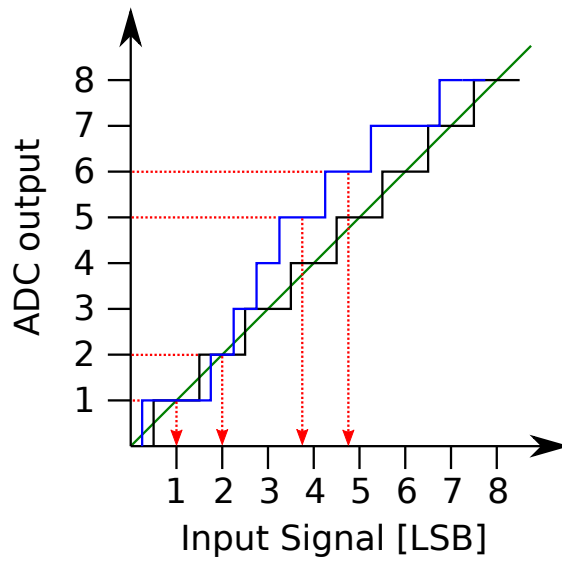
Figure 3.12: A real ADC (blue) is compared to an ideal ADC (black). ADC bins 1 and 2 show a DNL that "corrects" itself – the assigned signal value corresponds to the value of the ideal ADC. ADC bins 5 and 6 show no DNL, but are shifted from the assumed linear characteristic due to (negative) INL. The red dashed lines show the analog signal values assigned to the ADC output.
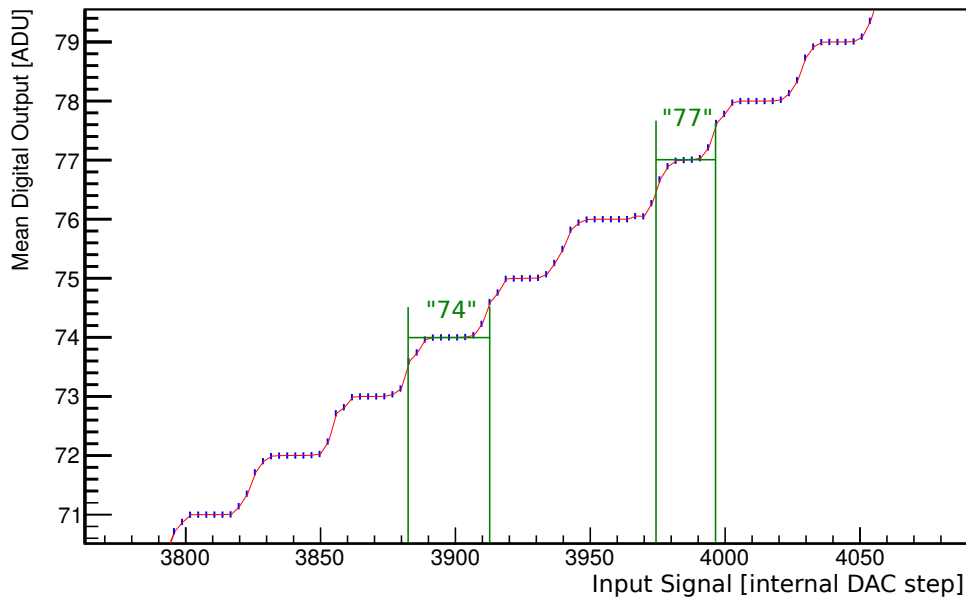
Figure 3.13: Measurement of the ADC non-linearity performed with the internal, 14-bit DAC of the DSSC ASIC. The blue tick marks show the granularity the internal DAC was swept with. At each point, 2400 individual measurements (ADC conversions) have been performed – the ordinate value of the blue marks is the mean of these measurements. The averaging is the reason for the smooth transition between the individual steps. A linear interpolation is given in red. Examples for an overly broad (74) and an overly small (77) bin are given in green.

a measurement that has been performed with a DSSC prototype. An algorithm determining the individual bin-widths of the ADC using this data has been presented in [31] and will be studied in more detail in [32]. It is based upon the following idea: The gradual change of the input signal causes a shift of the distribution of digitized values relative to the binning. Each ADC bin boundary $s'_{bb,i}$ can be seen as a threshold that divides this distribution into two sub-classes, left and right of the boundary. When the relative frequency of entries in these sub-classes changes its algebraic sign, the position of the bin boundary relative to the input signal stepping can be determined by linear interpolation. Using the determined bin boundaries, the DNL and INL can then be taken into account when the ADC output values are mapped back to the analog signal values for further usage.

Ch. 5 will present a study on the influence of the transfer characteristic of the DSSC ADC on calibration methods and what influence errors in the measurement of this characteristic will have on the calibration accuracy. It will show that the more coarse the ADC binning or resolution is in relation to the analog signal levels of a measurement, the more important the knowledge about the DNL and INL becomes.

For a counter based converter such as the single-slope ADC of the DSSC, the bin width corresponds to the time t_{LSB} it takes to measure one ADC step. The bin boundaries $s_{bb,i}$ correspond then to certain points in time. The ASIC-global digital time information is distributed to all 64 x 64 pixels via 8 individual bit-lines from a central so-called "Gray Code Counter" (GCC). Its advantage is, that for every of its (in the case of the DSSC) $2^8 = 256$ different output values only one single bit flips to get to the next higher value. In other words the so-called "Hamming distance" [33] of two consecutive counter values is always 1. This reduces the possibility for data read errors e.g. due to run-time differences in the bit-lines and the switching of the in-pixel flip-flops to a quantum of only one ADC step. However, the individual bit-lines are subject to physical mismatch in the wires, transmitters and receivers which causes skewing of the signal. This "jitter" results in the described DNL and INL effects. Due to the cyclicity of the Gray code, the DNL of the DSSC ADC exhibits periodic patterns of larger and smaller bins (see sec. 5.2.5 for simulated examples).

3.2 Measurement types

This section gives an overview over different measurement routines that can be performed with the DSSC detector system in order to characterize certain system properties used for the calibration algorithms. In general, a series of individual, repetitive measurements that is performed while changing a specific detector parameter is called a "(single) parameter sweep". "Grids" or "grid measurements" are understood as combinations of individual sweeps of detector parameters, leading to a multidimensional set of measurements. The measured parameter settings can also be a sub-set of the full available parameter setting space, which is then called a "sub-grid".

3.2.1 Internal and external calibration sources

The DSSC detector system includes several electronic circuits that can be used for self-checks and system calibration. The most important options are listed in the following:

- A method for internal charge or current injection has been presented in [34]. The high accuracy injection circuit for pixel-level calibration of readout electronics can be used for self-checks and trimming of the analog front-end.

- In the final version of the DSSC ASIC, the 14 bit high-accuracy internal DAC can be either connected directly to the ADC to serve as a sweepable voltage reference for characterization of the ADC DNL and INL (sec. 3.1.4), or serve as a tunable current source for the characterization of the analog front-end.

- A DEPFET-specific charge injection method using the inner substrate contact of the sensor has been proposed and studied in [13]. This method can be used to scan the NLPC of the DEPFET sensor and was used in the studies presented in [35].

- A method that can be used to generate signal charge in the sensor by pulsing the backside depletion voltage, which is explained in more detail in sec. 6.2.3.

Whereas measurements with internal calibration sources are based on the electronic generation of signal, all methods that rely on signal charge generation by means of incident radiation (e.g. laser light, X-ray calibration lines, high-energetic protons) are referred to as "external" calibration sources.

3.2.2 The "I_{ramp}– pixel delay" grid

A grid sweep of the two detector setting parameters "I_{ramp}" and "pixel delay" (sec. 3.1) can be utilized for multiple analysis and calibration methods. The DSSC ASIC provides 16 individual pixel delay settings that lead to an offset shift of the digital output due to an additional time delay during the digitization in the ADC. The I_{ramp} parameter has 64 different settings, each of them changing the ADC gain and, as a side effect, the ADC offset. In summary, the properties of an "I_{ramp}– pixel delay" grid are in theory (i.e. by design):

- Identical noise (in units of LSB, in this chapter simply referred to as "noise") and gain for all pixel delay settings of a given setting of I_{ramp}.

- The offset increases with an increasing setting of both I_{ramp} and "pixel delay".

- Offset shift of approximately 8% of the ADC bin width per each of the 15 pixel delay steps, leading to a total dynamic range of about 1.25 LSB.

- The individual pixel delay step sizes have a variation of about 20% by design (sec. 3.1). The accuracy is limited by electronic design constraints.

- A higher I_{ramp} setting results in higher ADC gain and, by design, an (undesired) offset shift, again limited by electronic design constraints.

- The gain changes from approx. -38% up to $+35\%$ in increments of 1% to 2% from its nominal value in the I_{ramp} dimension.

- By design, the pixel delay offset shift does not depend on the I_{ramp} setting.

The parameter of the I_{ramp} setting of the DSSC is indexed with the letter j, the pixel delay setting is denoted with index k. Therefore, an "$I_{ramp}-$ pixel delay" grid is abbreviated as "jk-grid".

3.3 Overview of the DSSC calibration

The central motivation for the DSSC system calibration is to provide the user of the instrument with the ability to interpret the digital output data in such a way, that the incident photon intensity in each individual pixel can be determined. Due to the non-linear system response (NLSR), inferring the number of incident photons from the digital output is not trivial.

As the foreseen photon energy range for the DSSC is low[6] enough, the number of signal electrons N_e is assumed to be directly proportional to the number of incident photons N_γ due to the high quantum efficiency. The central scope of the calibration is therefore the determination of the relation of the digital output value in ADU that corresponds to a certain number of signal electrons respectively photons:

$$ADU \cong f_{NLSR}(N_e) = k \cdot f_{NLSR}(N_\gamma) + K \tag{3.9}$$

Thereby, k is equal to $\epsilon_{e/h}$ (sec. 3.1.1), if the quantum efficiency is 100% and no charge sharing[7] between the pixels occurs. The constant K is assumed to be zero, as noise and leakage current in the detector should by design never amount to more than one signal electron. Two design features that help realize this property are the cold operation temperature and the short signal integration time of the DSSC. Ultimately, the user of the DSSC instrument will be working with the reverse of f_{NLSR}, which is the "mapping" of the digital output value to the incident number of photons:

$$f^{-1}_{NLSR}(N_\gamma) : ADU \mapsto N_\gamma \tag{3.10}$$

Based on the presumption that the photon energy is known, e.g. from the settings of the accelerator, the mapping of the digital output of the DSSC to the number of incident photons N_γ can be applied via eq. 3.9.

Due to the intrinsically low number of totally available ADC bins, it is necessary to achieve single photon detection with as few bins as possible. The lowest possible number of bins to safely discern between zero and one incident photons is two. Thereby the bin-width, i.e. the analog signal difference assigned to the ADC step size, must be small enough to resolve the sensor output related to the input of one single photon. In addition, the electronic detector noise must be small

---

[6]photons of an energy up to 3 keV have an absorption length lower than $100\,\mu m$ in silicon, the DSSC sensors have a thickness of $450\,\mu m$ (sec. 3.1.1, fig. 3.4).

[7]an illustrative explanation of charge sharing and the resulting signal is given in sec. 5.3.2.
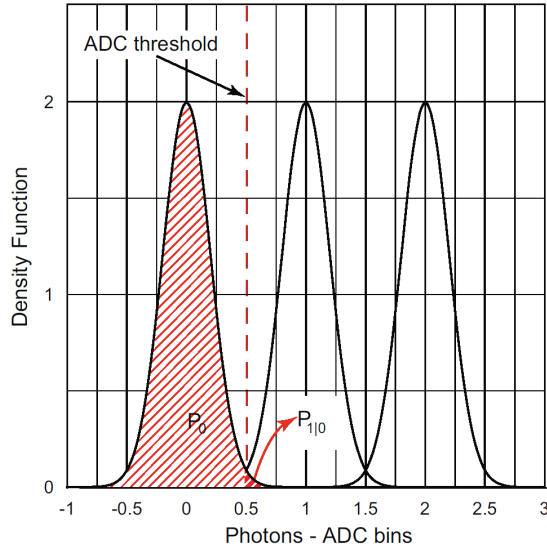
Figure 3.14: In order to achieve the highest detection accuracy for single photons with as few bins as possible, exactly one ADC bin is assigned to the signal of one photon. The electronic detector noise is assumed to be Gaussian distributed. The probability $P_{1|0}$ to falsely detect one instead of zero photons depends on the noise level, and on the accuracy of the determination of the ADC binning and the position of the noise peak relative to the ADC binning. From [17].

enough to not cause a false detection, as illustrated in fig. 3.14. From this approach follows that two detector system properties must be set correctly before scientific data can be recorded:

- The gain of the system must be set in a way, that the digitized signal of one photon of a given energy exactly corresponds to the ADC bin width.

- In order to keep the probability of false detections (e.g. detection of zero instead of one, $P_{0|1}$, or detection of one instead of zero photons, $P_{1|0}$) as low as possible, the base line signal or noise peak must be as narrow as possible and centered in the middle of an ADC bin.

The presented DSSC detector system provides, dependent on the employed sensor chip, various setting options. By changing e.g. the voltage setting of the backside and the drift rings of the sensors, the charge collection characteristics can be altered. The biasing of the on-chip FET amplifier of the DEPFET can be used to modify its non-linear pixel characteristic (NLPC), which is closely investigated in [13]. The signal response of the MiniSDD front-end can be tuned as well as the properties of the flip-capacitor filter (sec. 3.1.2) by changing the biasing voltages and the sequencing. However, it is momentarily not foreseen to use these "tuning" options for the sensor calibration, mainly for two reasons:

- Not every combination of the available settings has the same performance regarding the overall system noise. Also the voltage swing of the individual system components (sensor to filter to ADC) must be matched. The ideal operation window for the combination of

sensor biasing and front-end settings is therefore determined by the design values that have been tested thoroughly on various DSSC prototype setups, as can be found in [36].

- Certain trimming options of the analog ASIC front-end are reserved for the homogenization of the detector matrix properties. For example, the DSSC shows gradient behavior in direction of the pixel columns due to voltage drops along the pixel supply lines. These trimming techniques are thoroughly investigated in [37].

The calibration of the NLSR is therefore understood as the correct setting of the gain and offset of the read-out ADC in order to achieve the system properties mentioned above. This thesis will present and study methods that can be used to characterize and calibrate offset, noise and gain of the DSSC detector system.

3.3.1 Calibration goals

The goals of the system calibration of the DSSC detector can be summarized as follows:

- Provide sufficient resolution and the correct offset and gain setting for detecting a low number of photons depending on the experimental requirements. Currently, 12 individual operation modes are foreseen for the DSSC detector: In addition to single photon resolution, gain settings of 2, 5, and 10 γ/bin need to be calibrated for three different XFEL photon energies: 0.7, 1, and 1.5 keV.

- Calibrate the NLSR that provides the high dynamic range of the DSSC for the requirements of the scientific experiments.

- Characterize the system baseline noise and measure the DNL and INL of the pixel-wise ADCs in order to determine the probability of misinterpreting the measurement data (fig. 3.14).

3.3.2 Calibration of the NLSR: A two-step strategy

For the calibration of the NLSR of the DSSC, a procedure comprising two consecutive steps has been proposed [19]. In the first step, gain and offset are calibrated, in the second step, the NLSR is determined. Fig. 3.15 gives an illustration of the procedure:

- In the **first step**, the ADC offset is calibrated by sweeping the full range of the ADC I_{ramp} and Δt_{pixdel}-settings. This is necessary, as the offset depends on both of these settings. Sec. 5.2 will present three individual methods for this sub-step of the calibration and compare their stability and accuracy. In addition, the noise in digital units of LSB can be determined.
  For certain operation modes, the ADC gain must be set in a way that assures that the digital output is proportional to the number of incident photons on a one-to-one scale. The most conservative approach to finding the desired gain setting is to scan all 64 individual I_{ramp}-settings and record a calibration line spectrum for each setting. If a parameterization
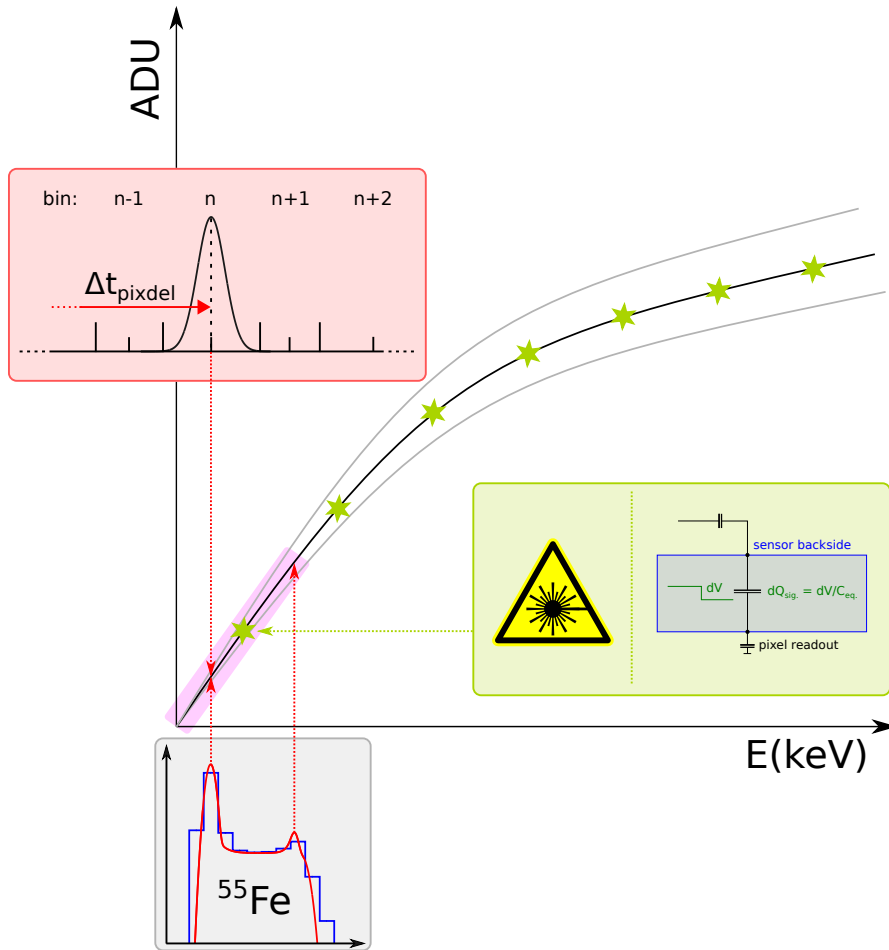
Figure 3.15: Two-step strategy for calibrating the non-linear system response: In the **first step**, the system offset and noise are characterized by measuring dark frames. The offset calibration is performed by adjusting the pixel delay (Δt_{pixdel}, red box) in such a way, that the noise peak is centered in an ADC bin. The gain in the linear region (purple box) of the NLSR is determined and calibrated with the help of X-ray calibration spectra, as e.g. ^{55}Fe (grey box, grey curves).

In the **second step**, the NLSR is scanned with a calibrated signal charge (green box, green stars). The signal charge can be generated e.g. by laser pulses or by electrically pulsing the backside voltage.

of the effect of I_{ramp}-setting is available, it may also be sufficient to scan only a sub-range of the available setting. Sec. 5.3 proposes a method for the DSSC gain characterization and studies its accuracy. The stability of the presented method can be improved when the noise value (in digital units LSB) is known before the gain calibration. After the gain calibration, the system noise can be calculated in numbers of electrons ENC (equivalent noise charge).

- In the **second step** of the calibration, the non-linear system response is scanned either by repetitively generating a defined amount of signal charge, or by generating signal charge via an externally calibrated source.

    For the former approach it is necessary to inject a signal charge Q_1 into the detector that can be reproduced identically and repeatedly. By generating a multiple of this charge in the linear region of the NLSR, it can be determined accurately, e.g. via a linear fit. For the scan of the total dynamic range of the NLSR, the respective signal charge is then calculated via $Q_N = N \cdot Q_1$ after repeating the injection process N times. A first example of a calibration of the NLSR of a DSSC prototype using this approach was presented in [35]. The continuation of these studies will be documented in [32].

3.4 DSSC prototypes and experimental setups

This section gives an overview over the two experimental setups that were operated in preparation of this thesis. Both setups were placed in light-tight boxes as the used sensors (DEPFET, MiniSDD, sec. 3.1.2) are sensitive to optical light.

3.4.1 SPIX sensor test bench

The **SPIX**[8] **sensor test bench** ([38], fig. 3.16) is used to characterize DSSC DEPFET sensor test structures. Sensor biasing is provided by a set of laboratory power supplies. Supply nets can be switched by a FPGA-controlled main board. A read-out board using two operational amplifiers for signal amplification is attached to the device under test (DUT). For digitization, an external 14bit-ADC connected to a personal computer is used.

3.4.2 DSSC prototype setup

The **DSSC prototype setup** is predominantly developed by Jan Soldat [36] from the University of Heidelberg. Its central building block is a custom made FPGA-board that provides a fast 695 MHz clock for the sequencing of the DSSC ASIC and a USB interface for digital read-out via a personal computer.

Fig. 3.17 shows the setup in the environment that was designed for the purpose of calibration tests. It comprises a light-tight box, an automated handler for radioactive sources and a temperature control system. The latter is needed to provide a constant operation temperature

---

[8]SPIX stands for "Single PIXel setup. However, due to continuous updates and being equipped with electronic switcher banks the setup can also be employed to operate larger matrix sensors and readout chips.
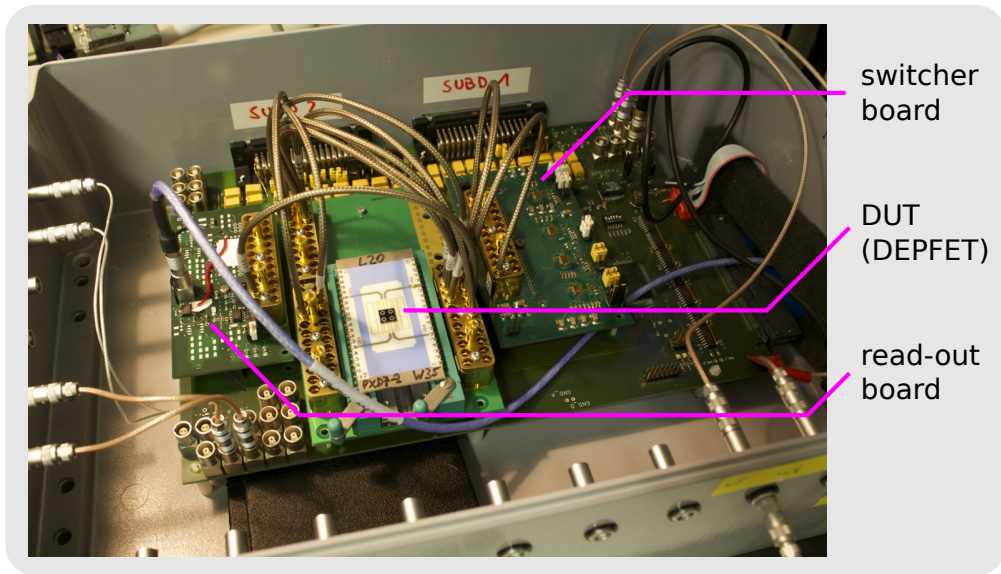
Figure 3.16: SPIX sensor test bench. The light blue and white rectangle in the middle is a ceramic that carries the prototype silicon sensor (small black square, in this case a DSSC DEPFET with four individual 7-pixel clusters). The signal is amplified on the read-out board and then fed to an external 14bit-ADC via differential signaling (blue cable).
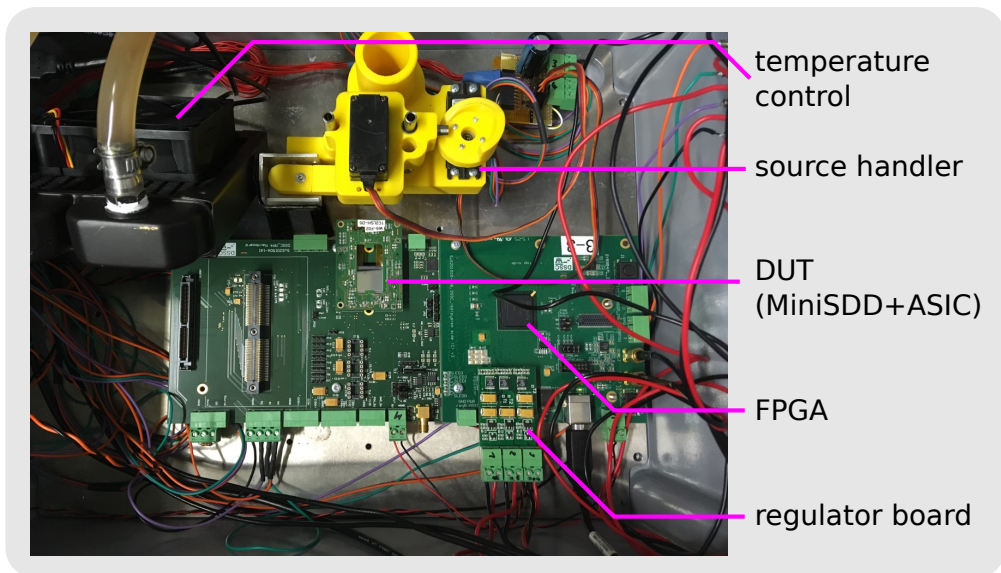

Figure 3.17: DSSC prototype setup with temperature control, automated calibration source handler, sensor test structure (64 x 64 MiniSDD) bump bonded (fig. 3.2) to a DSSC ASIC test chip, FPGA control and read-out board, and regulator board used for ASIC and sensor biasing.

within a variation of $< 0.1\,K$, as the gain and offset of the DSSC are very sensitive to temperature changes.

The goal of the DSSC prototype is to emulate all operational conditions of the components of final DSSC detector as close as possible. Two different options for equipping the setup with DSSC prototype sensors and ASICs are possible:

- For the studies in [35] and [32], DEPFET sensors first characterized on the SPIX sensor test bench were in a second step connected to the prototype ASIC via an interlink PCB. The non-linear pixel characteristic (NLPC, fig. 3.9) of the DEPFET is a sensor-intrinisic property. That means, that the change in signal current in relation to the incident signal energy only depends on the sensor biasing. By applying identical sensor biasing in both setups, the two-step calibration approach for the NLSR could be cross-checked in these studies.

- For the experiments in the scope of this thesis, the setup was equipped with a full-format 64 x 64 pixel DSSC ASIC[9] and a corresponding, bump bonded (fig. 3.2) MiniSDD sensor.

---

[9]chip generation "F1"

4. Development of the detector simulation environment

The simulation of the salient instrument properties has been an integral part of the development of the DSSC detector since the start of the project. Detailed information on the design and simulation of the read-out electronics (see sec. 3.1) can be found in [26]. For the electronic design of the read-out ASIC, industry-standard hardware description and modeling techniques such as Verilog [39] and SPICE [40], as well as Monte-Carlo techniques have been applied. This chapter focuses on the development of the physical model that was used to simulate the calibration test data sets employed in this thesis.

4.1 A simple approach to simulating the spectral response using the Monte Carlo method

An early approach to simulating the spectral response of the hexagonal DSSC pixels was performed with a simple, two dimensional Monte-Carlo simulation based on the random number generator `TRandom3` [41] from the `ROOT` framework [42]. This was done in order to provide a "toy model" that was employed to study the effects of the variation of characteristic simulation parameters used for modelling processes such as charge sharing between pixels and "out-of-time" events (explanation below). These studies were also used as a proof-of-concept for certain aspects of the simulation of the spectral response before a more refined detector simulation was adapted to the DSSC detector (see sec. 4.2). With this early approach, all salient processes in the formation of a single pixel calibration line spectrum can be simulated:

- Electronic detector noise

- Photon flux

- Different line energies and decay probabilities

- Fano noise

- Out-of-time events causing incomplete charge collection

- Charge sharing due to finite size of signal electron clouds

To do so, the simulation software performs the following steps in the given order. The algorithm is performed N times, corresponding to the number of signal read-out cycles of the detector in order to generate a spectrum with N entries.

1. The simulation starts with the generation of the electronic detector noise, measured in number of electrons. This is simulated by a random value $G_{x_\mathrm{n}, \sigma_\mathrm{n}}$ from a Gaussian distribution with mean x_n and standard deviation σ_n.

2. The photon hitting the detector with arbitrary adjustable probability $P_{\text{phot}} \in [0, 1]$ during the signal read-out window is simulated by a random number $U_{\text{Rndm}} \in [0, 1]$ from a uniform distribution. This corresponds to the ratio of the given photon flux of the calibration line source and the time frame in each read-out cycle in which the detector is "online", i.e. able to detect signal. If $U_{\text{Rndm}} < P_{\text{phot}}$, the process of signal charge generation is initiated. In order to reproduce typical DSSC calibration line spectra, P_{phot} is very low (< 0.01) due to the sensor read-out window being short in comparison to the activity of available calibration line sources (e.g. sec. 6.1). If no signal charge generation is initiated, the simulation algorithm ends and only the simulated detector noise is accumulated.

3. If charge generation is initiated, two individual calibration line peaks of a typical calibration source are simulated. For a ^{55}Fe-spectrum, the relative probability P_{K_β} for a K_β-decay in relation to K_α is about 11.7%. For a random number $U_{\text{Rndm}} \in [0, 1] < P_{K_\beta}$, a photon energy of 6.49 (K_β) keV is simulated, for $U_{\text{Rndm}} \in [0, 1] \geq P_{K_\beta}$ the energy of the simulated photon is set to 5.89 keV (K_α).

4. The number of signal electrons N_e is calculated from the incident photon energy by the pair production energy in silicon assumed to be 3.63 eV. The Fano noise (sec. 3.1.1, eq. 3.2) is simulated by generating a random value $G_{N_e,\sigma_{N_e}}$ from a Gaussian distribution with mean N_e and standard deviation $\sigma_{N_e} = \sqrt{F_{Si} N_e}$, with the Fano factor for silicon being $F_{Si} = 0.115$.

5. When a photon signal arrives late during the signal flat top (sec. 3.1), the generated signal electron charge cloud cannot be collected completely in the pixel read-out node before the filtering and digitization process is started. This is called an "out-of-time" event. This process is only relevant for photon sources that are not synchronous to the detector read-out, such as radioactive calibration line sources as ^{55}Fe.

   The model for simulating the out-of-time events is based upon the result of a synopsys[1] device simulation [43] that was performed in order to model the signal charge drift time in a DSSC pixel after the charge generation at the detector surface close to the entrance window[2]. Fig. 4.1 shows on the ordinate the fraction of the collected charge in the internal gate of a DEPFET sensor pixel, normalized to the complete charge. The time variable is given on the abscissa.

   For the simulation, an arbitrary flat top time T is assumed and a random number $U_{\text{Rndm}} \in [0, T]$ denoting the point in time of the photon event is computed. The fraction of the signal charge that has been collected at the read-out node of the detector pixel is then determined by evaluating the given characteristic.

   The shorter the flat top, the more signal charges are collected incompletely, causing the calibration lines to "bleed out" towards lower energies. This effect has been measured

---

[1] ® Synopsys, Inc. – www.synopsys.com
[2] A detailed study on the development of DEPFET pixels for the DSSC detector, comprising studies on the signal charge transport due to the electric potential in the sensor material can be found in [13].
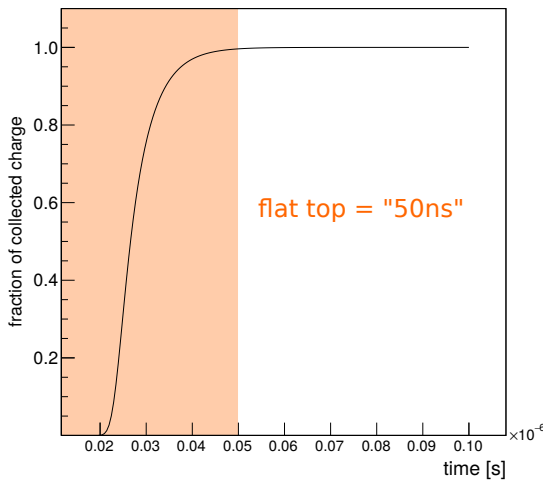
Figure 4.1: Simple approach for the simulation of out-of-time events based on a DSSC prototype device simulation [43]. A random point in time inside the orange "flat top" $U_{\mathrm{Rndm}} \in [0, T]$ is used to calculate the respective collected charge in the read-out node.

qualitatively with a prototype DSSC DEPFET pixel[3] operated in the SPIX setup (sec. 3.4.1) by gradually changing the flat top time. The result of this measurement is depicted in fig. 4.2: The longer the flat top, the higher the fraction of incident photons whose charge is collected completely in the read-out node. The calibration lines "bleed out" into the trough for decreasing flat top duration, and the ratio of trough to calibration line increases. In this example, the signal charge cannot be sampled completely for a flat top of 2 μs.

6. Due to the finite size of the signal charge cloud, charge sharing occurs, i.e. the signal charge is split between neighboring pixels. A more detailed explanation of this effect is given in 5.3.2. For the DSSC, charge sharing dominates the formation of a low energy trough between calibration lines and noise peak that can also be identified in fig 4.2. If signal charge generation was initiated in step 2., a charge cloud containing the computed number of electrons N_e is simulated. N_e depends on the electronic noise, the signal charge with or without Fano noise and out-of-time event modeling. Fig. 4.3 (a) illustrates the concept of this step. The position of the charge cloud is given by two random numbers $U_{\mathrm{Rndm}} \in [0, 2\pi[$ for the angle φ and the square root of $U_{\mathrm{Rndm}} \in [0, R]$ for the radius r from uniform distributions. At each position, a two dimensional Gaussian distribution with the standard deviation σ containing N_e elements is computed.

The simulated detector pixel is defined as a geometric shape with a surface area identical to the unit circle. In order to simulate charge sharing, R needs to be larger than the assumed pixel size in order to simulate charge clouds that are not located completely inside the pixel. This is illustrated by fig. 4.3 (b) to (c), for which σ is increased gradually. For each

---

[3]Prototype chip generation "pxd7". The time needed to collect charge in the read-out node and the respective flat top times are not comparable to the simulation depicted in fig. 4.1, as the time domain of this measurement is dominated by the frequency response of the read-out electronics.
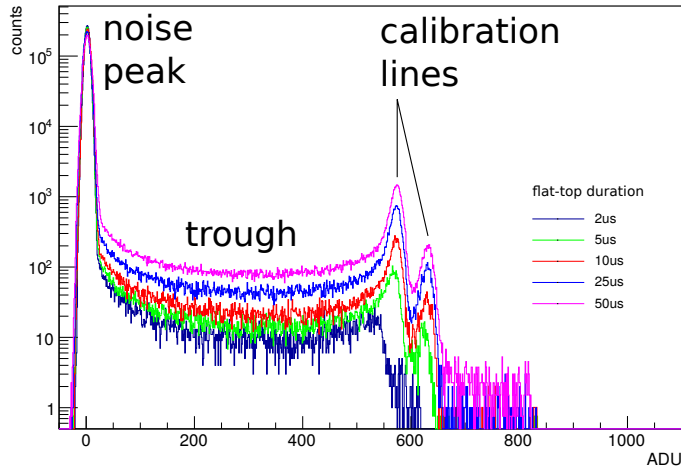
Figure 4.2: Comparison of ^{55}Fe single-pixel spectra measured with the SPIX setup and a prototype DSSC sensor chip, gradually changing the flat top time. The "trough" between calibration lines and noise peaks develops mainly due to signal charge separation to neighboring pixels.

simulation run involving signal charge generation, all simulated electrons inside the pixel boarders are summed up to generate a histogram.

By simulating different geometrical pixel shapes, the functionality of the simple Monte Carlo simulation was tested. Fig. 4.4 shows a comparison between a circular pixel, a hexagonal pixel and a square pixel, all of them covering the surface area of the unit circle. The number of so-called "split-pixel" events, i.e. events strongly influenced by charge sharing, was determined by an arbitrary chosen threshold of the signal charge simulated inside the pixel boarders. If less than 50% were "collected" inside the pixel, the event was counted as a split-pixel event. For each simulation in this study, the same random number seed for all of the employed random numbers in the simulation steps 1. to 6. was used in order to guarantee identical test conditions for the three pixel shapes. As expected, the circular pixel shows the least amount of split-pixel events, followed by the hexagon and the square – the higher the ratio between circumference and surface area, the higher the amount of split events.

An overview of the introduced options of the simple Monte Carlo simulation approach is given in fig. 4.5. Plots (d) to (f) show that the effect due to simulated out-of-time events is similar to the measurement presented in fig. 4.2. The apparent shift of the calibration line center towards lower energies for flat top times shorter than the time constant of the charge collection time is clearly visible in (f). Both out-of-time events and charge sharing contribute to the formation of the characteristic low energy trough. A combination of the two effects can be found in panel (i). It has to be noted that events occuring during the baseline and the signal integration phases (sec. 3.1.3, fig. 3.11) are also called out-of-time events but are not accounted for in this model.
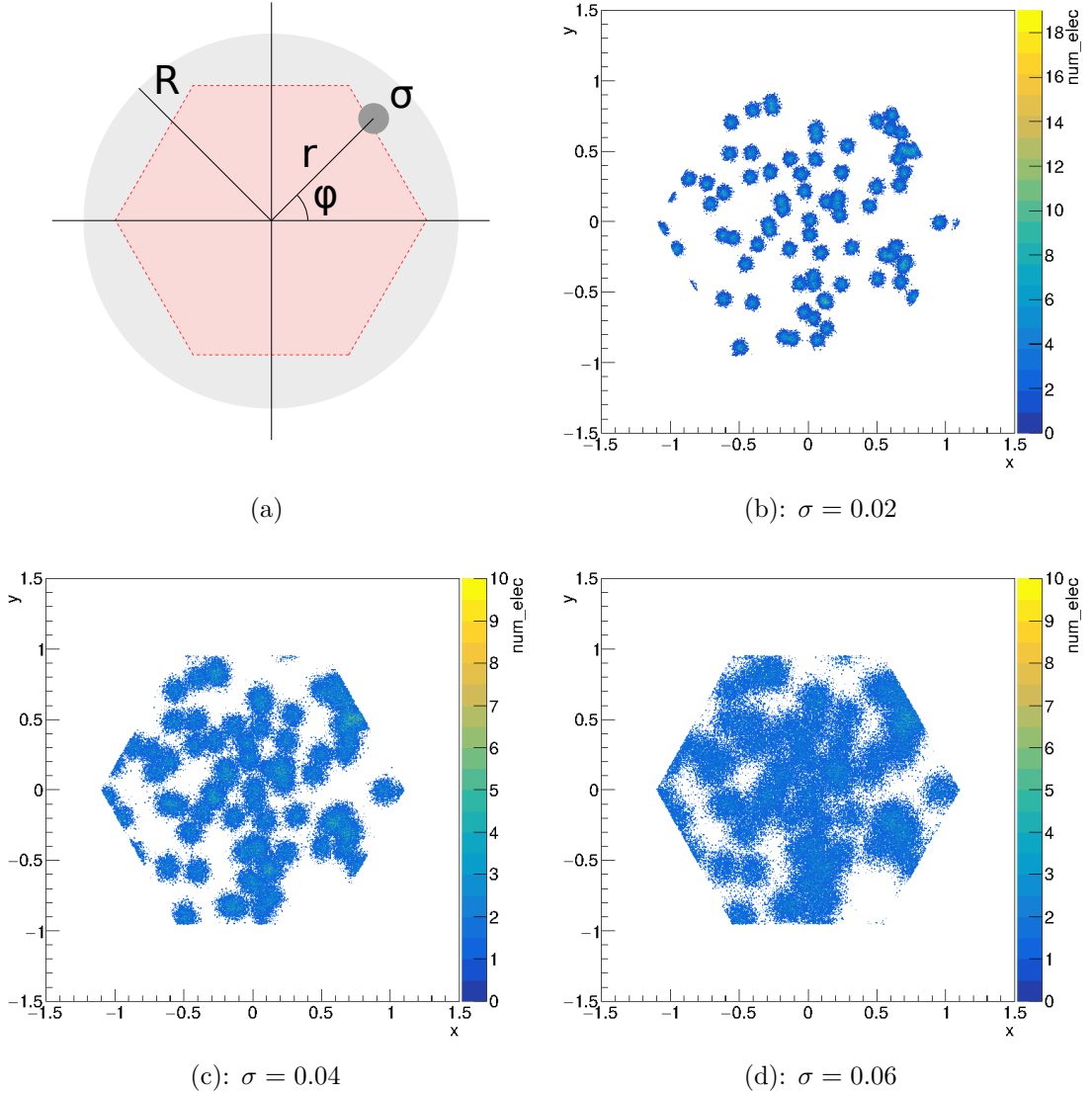
(a)

(b): $\sigma = 0.02$

(c): $\sigma = 0.04$

(d): $\sigma = 0.06$

Figure 4.3: Simple Monte Carlo simulation approach of electron charge cloud generation and charge sharing. The area with radius R is "irradiated". The charge clouds are simulated as two-dimensional Gaussian distributions with standard deviation σ and their position determined by r and φ.
Plots (b) to (d) show all simulated signal electrons located inside the hexagonal pixel for $2 \cdot 10^2$ ^{55}Mn γ-decay events with $R = 3$. For increasing charge cloud size, more and more so-called "split-pixel" events occur. The pixel shape is a regular hexagon. The size of the pixel is measured without unit, its surface area is identical to the unit circle.
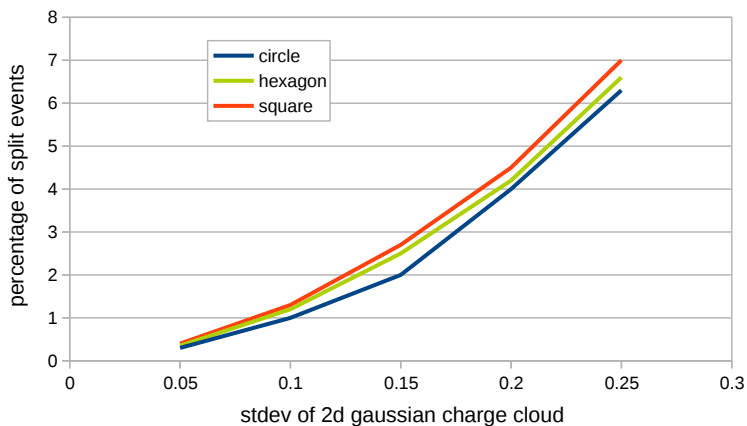
Figure 4.4: Test of the simple Monte Carlo simulation approach using different pixel geometries.

In figs. 4.6 to 4.7, a spectrum simulated with the proposed, simple Monte-Carlo approach is compared with a spectrum of ^{55}Fe measured with a DSSC (DEPFET) prototype on the SPIX detector test bench. The flat-top time of the measurement was $5\mu s$, which is much longer than the charge collection time in the sensor chip [13]. The frequency response of the the read-out electronics can also be neglected to first order (compare fig. 4.2). Out-of-time events (simulation step 5.) have been switched off in the simulation.

For better assessment of the difference D between simulation and measurement, the significance S_{bin} of the residual is calculated on a bin per bin basis by

$$S_{\text{bin}} = \frac{D}{\sigma_{\text{meas}}} = \frac{C_{\text{meas}} - C_{\text{sim}}}{\sqrt{C_{\text{meas}}}} \tag{4.1}$$

assuming Gaussian bin-wise statistics [35], with C_{meas} and C_{sim} being the respective bin contents. The expectation value of this measure is zero, "significant" deviations are usually characterized by values > 1 (i.e. "more than one σ").

The comparison between the simulated and the measured spectrum shows the most significant differences symmetrically around the noise peak (fig. 4.7, bottom left panel), signaling a mismatch of the electronic detector noise setting of the simulation. The focus however of this simple Monte-Carlo approach was the modeling of the low-energy trough between calibration lines and noise peak. In this region, the significance is around zero. This result further motivates the assumption, that the low energy trough is dominated by charge sharing. In order to simulate the measured spectrum, the standard deviation of the charge cloud was set to $\sigma = 0.24$ (compare fig. 4.3). This measure corresponds to about 13% of the diameter of the simulated pixel.

For the region around the calibration line peaks, the significance of the residual increases again. In particular for the low-energy tailing of the K_α-line, the simulated spectrum is too low (fig. 4.7, right column). This effect is related to the out-of-time event simulation being switched off in this example.
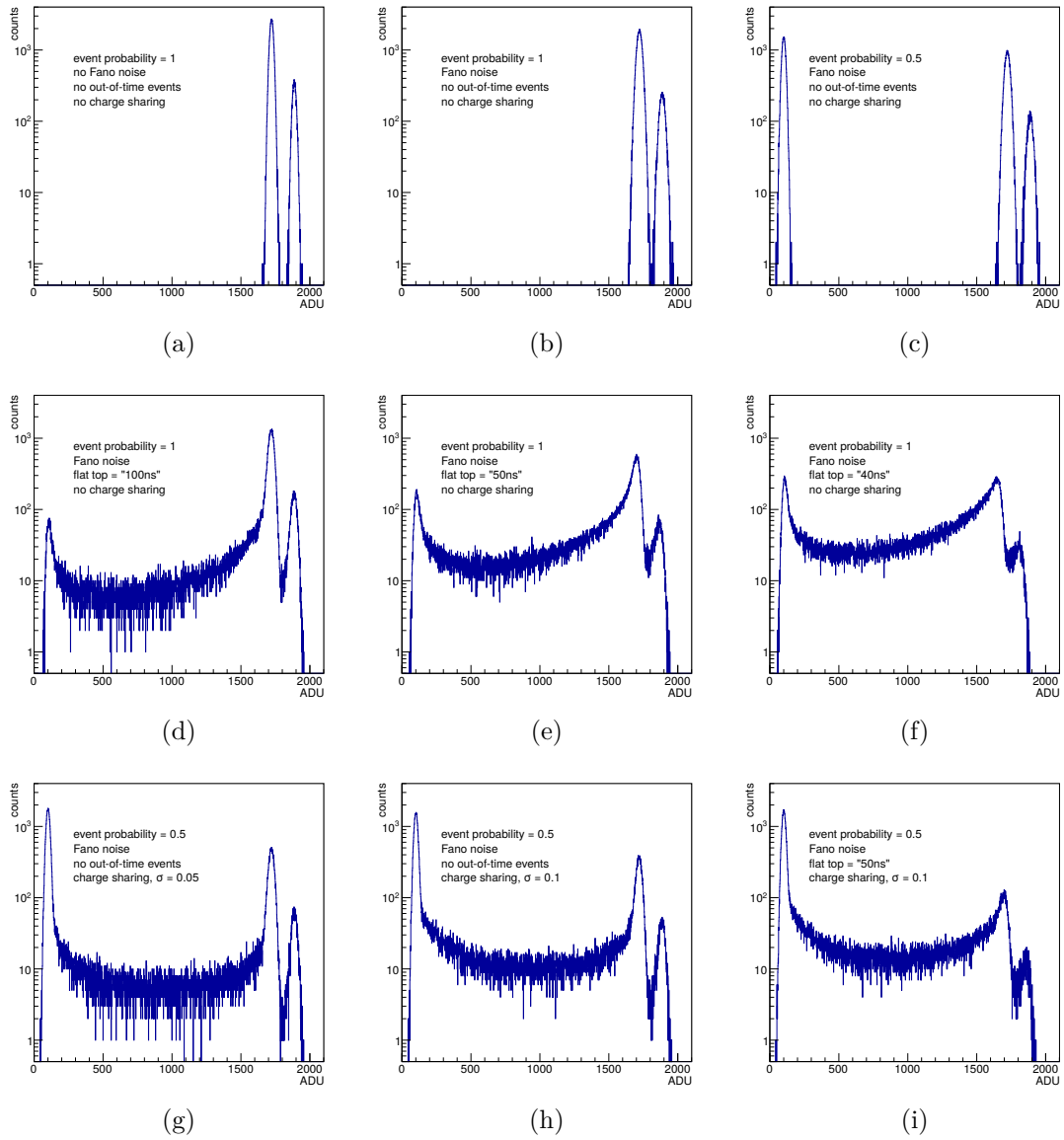
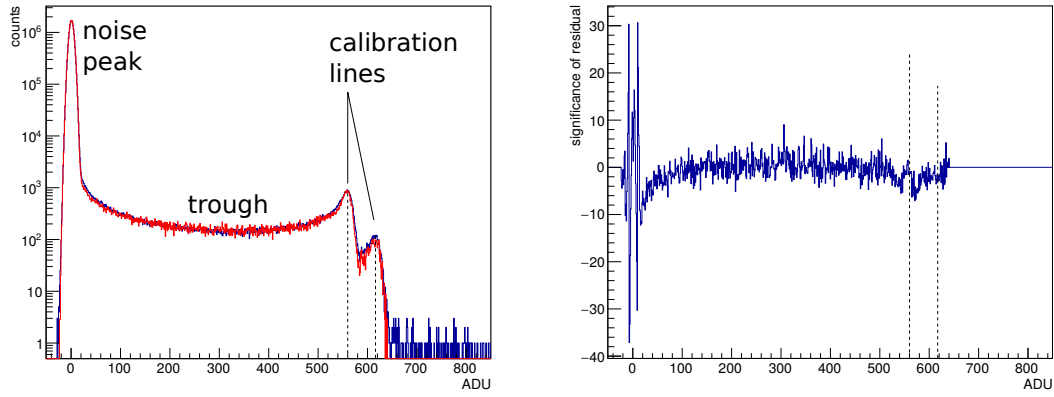**Figure 4.5:** Simulation of Fano noise, out-of-time events and charge sharing with the simple Monte Carlo method.

Figure 4.6: Comparison of a ^{55}Fe spectrum measured with a DSSC prototype pixel on the SPIX test bench (left, blue) and the output of the described simple Monte Carlo simulation (red). The strongest significance of the residual (in units of σ, right) is around the noise peak. The dashed lines marking the position of the calibration lines are given for orientation. A zoom into the critical regions close to the noise peak and the calibration lines can be found in fig. 4.7.
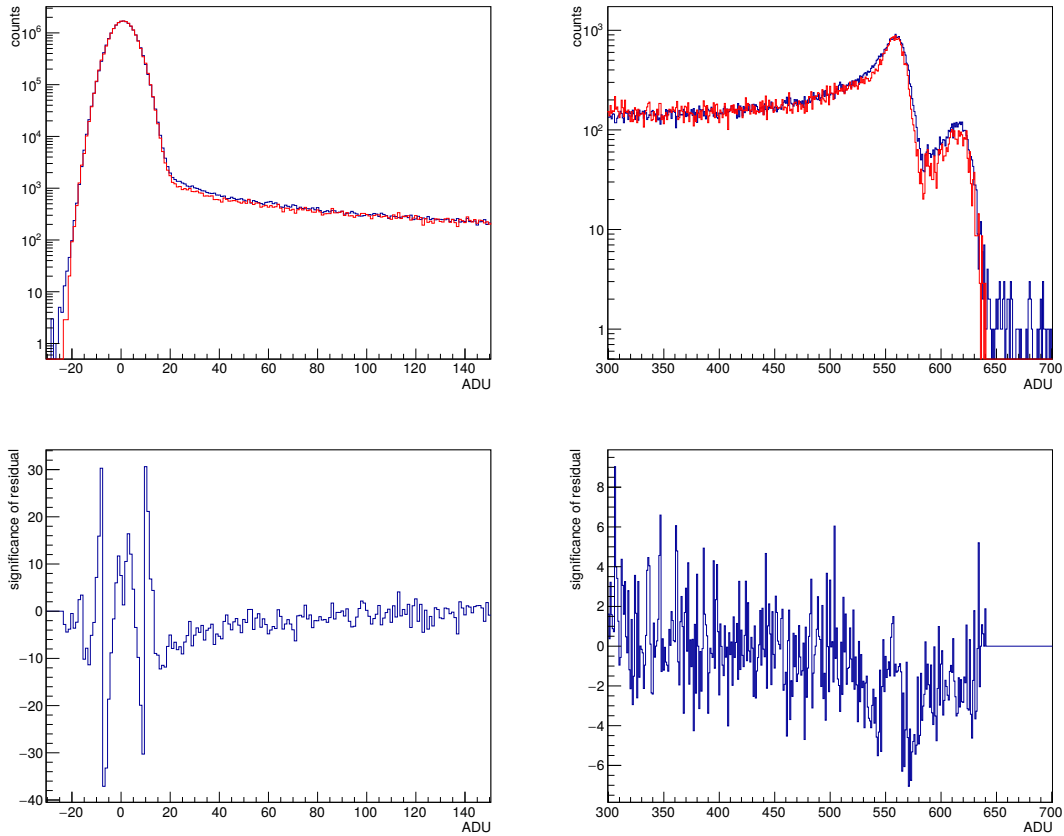
Figure 4.7: Zoom to the most critical regions of fig. 4.6 (left). Upper row: comparison of measurement (blue) and simulation (red). Below: Significance of residual in units of σ (see eq. 4.1).

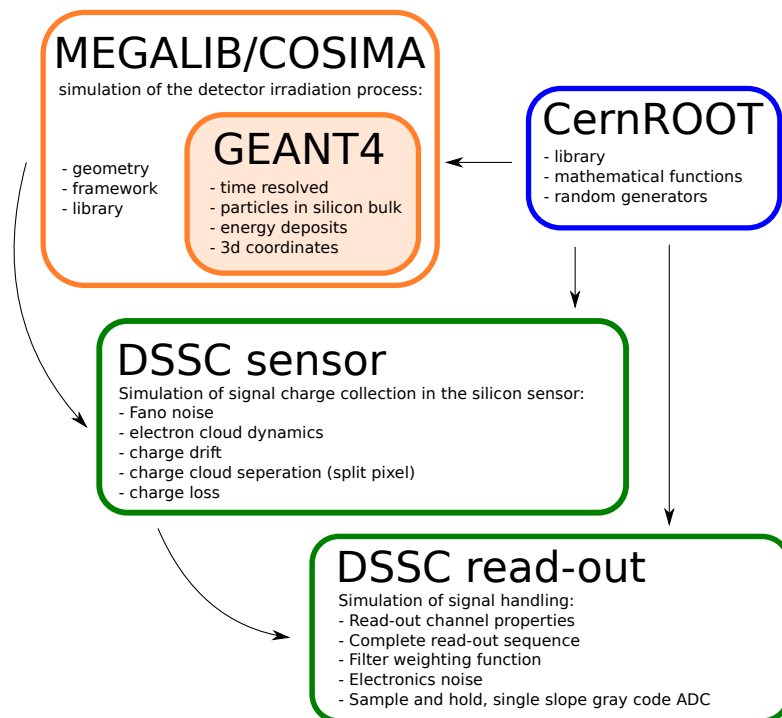## 4.2 Description of the DSSC system simulation package

Figure 4.8: Overview over the individual sub-modules of the DSSC system simulation package

In order to simulate the characteristic spectral response of the DSSC system that comprises the physical properties of the sensor as well as the signal processing chain in the read-out electronics, a dedicated software package has been developed [44]. The software is an end-to-end simulation of detector systems equipped with fully depleted, pixellated silicon sensors. All salient aspects of the generation of signal charges in the detector and the subsequent charge transport, collection and sampling can be simulated. It employs models for generating and propagating signal electrons in the silicon sensor, taking into account drift, diffusion, and electrostatic repulsion. The pixel-wise read-out electronics of the DSSC ASIC are also modeled. The list below gives an overview of the individual parts of the simulation routines that are also illustrated in fig. 4.8.

- The simulation of the energy deposits corresponding to particles (e.g. photons, electrons, protons) incident on the sensor is based upon GEANT4 ([45], [46] and [47]) which is employed by using the COSIMA/MEGALIB simulator framework [48] that provides an easy interface for defining the experiment and detector geometry. The output is a time-resolved, three dimensional map of energy deposits in the silicon bulk of the sensor. The sensor properties (e.g. thickness, surroundings, coating of the entrance window) are taken into account in this step.

- The space and time distribution of energy depositions in the sensitive sensor volume are then converted to three dimensional signal electron charge clouds, taking into account Fano

statistics.

- In the next step, various models for the drift, diffusion and electrostatic repulsion of the charge clouds can be used to compute the pixel distribution of the signal electrons once they are collected at the pixel read-out nodes. For distributing the signal charge to the individual pixels in order to simulate charge sharing (i.e. split-pixel events), the simplifying concept of a so-called charge separation depth is introduced. In this concept, it is assumed that the lateral expansion of the cloud by diffusion and electrostatic expansion is unimpeded until the cloud arrives at a certain depth (the charge separation depth) in the sensor volume. Before reaching the charge separation depth, the propagation of the cloud electrons is assumed to be determined by the presence of the potential wells of the pixels. In this approach, the lateral position of an electron at the charge separation depth determines in which pixel this electron is collected. A close study of this concept, where the charge separation depth is evaluated based on device simulations and measurements, can be found in [49].

- The final stage of the DSSC simulation package is a simulation of the sensor read-out sequencing, which is modeled according to the definitions in sec. 3.1. Due to the correlation of the time distribution of the individual energy deposits and the signal charge propagation through the sensor volume with the sequencing of the signal read-out, the simulation of out-of-time events has reached a high level of realism.

The object-oriented `C++` code of the DSSC simulation package also makes use of the `ROOT` framework [42] in order to rely on heavily tested, fundamental functions when possible.

Figs. 4.9 to 4.10 show a comparison of the simulation to a ^{55}Fe spectrum recorded in November 2014 with a DSSC (DEPFET) prototype on the SPIX test bench (sec. 3.4). The source had an activity of about 321 MBq, which corresponds to photon emission rate of $R_\gamma = 5.2 \cdot 10^6 \gamma/(s\,sr)$ according to the source data sheet. It was mounted at a distance r of about 1 cm to the detector, the solid angle equivalent S_{px} of a single DSSC pixel with a surface of $4.8 \cdot 10^{-4} cm^2$ at this distance is $4.8 \cdot 10^{-4} sr$. The expected rate $R_{px,SPIX}$ of incident photons per pixel and frame due to the signal flat-top T_{ft} of $25\,\mu s$ is then about

$$R_{px,SPIX} = R_\gamma \cdot S_{px} \cdot T_{ft} \sim 6.3 \cdot 10^{-2} \frac{\gamma}{px \cdot frame} \tag{4.2}$$

In the simulation, a rate of about

$$R_{px,SIM} \sim 6.7 \cdot 10^{-2} \frac{\gamma}{px \cdot frame} \tag{4.3}$$

was asumed in order to reproduce the measured spectrum. This rate is only about 6% larger than the experimental rate, which lies well within uncertainties (e.g. distance of the source to the detector, source activity). Both the trough from charge sharing and the pattern pile-up contribution are well reproduced in the simulation.

In the simulation, the standard deviation of the lateral extent of the signal charge cloud at the depth of the so-called charge separation depth, i.e. the depth in the sensor bulk at which
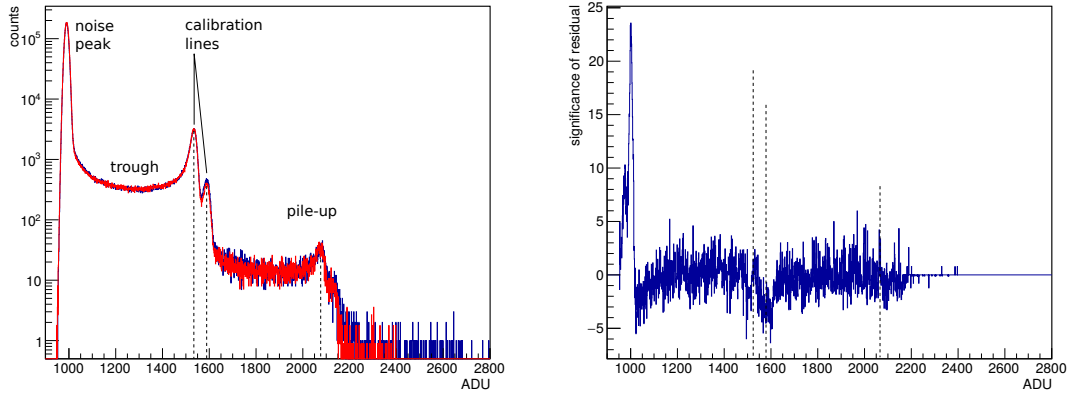
Figure 4.9: Comparison of a ^{55}Fe spectrum measured with a DSSC prototype pixel on the SPIX test bench (left, blue) and the output of the DSSC system simulation package (red). The dashed lines are given for orientation. A magnification of the critical regions close to the noise peak and the calibration lines can be found in fig. 4.10.
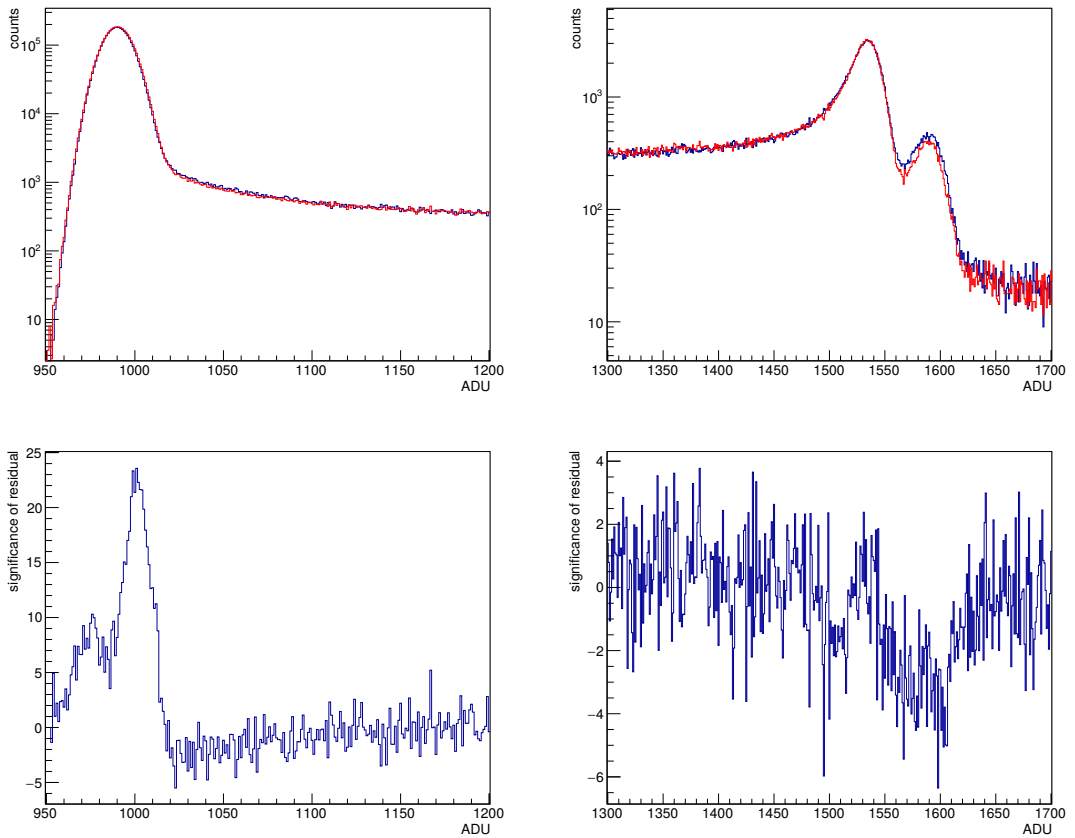

Figure 4.10: Magnification of the most critical regions of fig. 4.9 (left). Upper row: comparison of measurement (blue) and simulation (red). Below: Significance of residual in units of σ (see eq. 4.1).

44

the cloud is divided into neighboring pixels, is about $19.6\,\mu m$. This is about 10% of the pixel diameter. The simple Monte-Carlo approach (sec. 4.1) yielded a standard deviation of about 13% of the pixel diameter, which is still in good agreement with this much more refined approach. In general, the estimated charge cloud sizes for DEPFET devices analysed here are in the order of values that have been studied in [49], using classical CCD sensors.
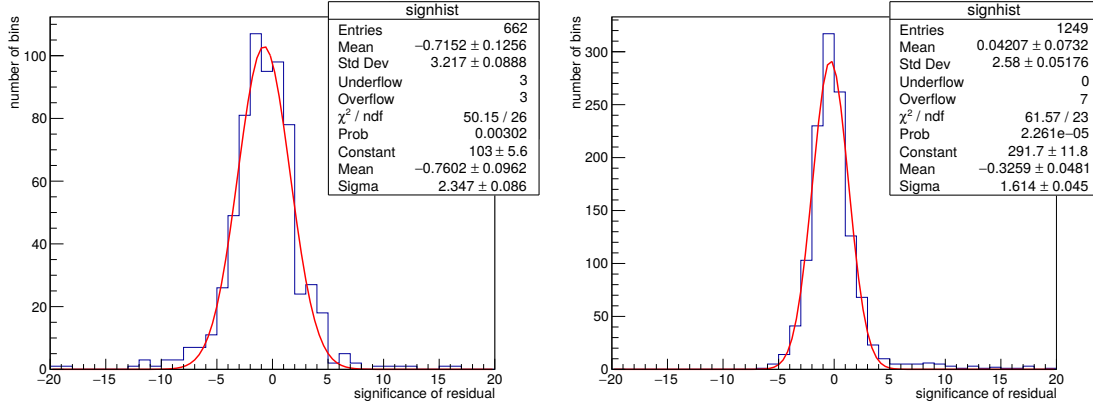

Figure 4.11: Histogram of the significance (in units of sigma) of the residual between simulation and measurement in each bin. Left: Simple Monte-Carle approach. Right: DSSC system simulation package.

Fig. 4.11 shows a comparison of the two presented simulation approaches, assessed by the histogram of the residual between simulation and measurement given by eq. 4.1, summarizing all bins of the respective spectra. It must be noted, that the focus of both models was the simulation of the low-energy "trough", with no attempt made to match the ratio between the calibration lines that depend, amongst others, on self-absorption in the source and the source window. Looking at the respective standard deviation of the histograms, it is evident, that the DSSC system simulation package provides a simulation of the DSSC detector system that is closer to reality. Nevertheless the simple Monte-Carlo approach has proven to be reliable as a quick test tool for the illustration of relevant aspects of the sensor working principle.

5. Calibration methods

As described in sec. 3.3.2, the calibration of the NLSR of the DSSC is a two-step strategy. This chapter gives a summary of the key aspects of the calibration methods used in the first calibration step and describes how exactly the data is measured and analyzed in the calibration procedure. The individual methods have been developed using simulated (ch. 4) as well as measured datasets. The simulated datasets and test procedures will be presented in sec. 5.2.5. This chapter concludes with an evaluation of the proposed calibration methods by assessing their statistical and systematic uncertainties based on the simulated datasets. In ch. 6, the proposed methods will be applied to measured datasets. In sec. 6.2, the second step of the calibration procedure is applied and the calibration of the NLSR is cross-checked with an independent, absolute energy reference.

5.1 Handling of calibration data

A central goal in the development of the calibration methods that have been studied for this thesis is to provide stability and accuracy of results and performance. The calibration of the more than one million pixels of the DSSC aims at getting the best possible settings, depending on the scientific use case, for each pixel. Each individual pixel has more than two thousand different possible calibration settings. As described in sec. 3.3.2, calibration techniques avoiding an individual characterization of each of these settings or combinations are in development. Still, the dimension of the set comprising all pixels of the DSSC and all settings that need to be characterized for the calibration procedure will be in the order of 100 million (approximately 100 individual settings per pixel). This means, that the large amount of resulting measurement data will have to be processed automatically by thoroughly tested and stable algorithms. The studies presented in this chapter are based on datasets of up to 4096 pixels, which is the number of pixels on one full frame DSSC ASIC (sec. 3.1) This represents about 0.4 percent of the final megapixel camera that will comprise 256 DSSC ASICs.

5.1.1 DSSC data output

When performing measurements with the DSSC, each configuration of a grid or a sweep can be set consecutively by automated measurement scripts [37]. A number of N individual measurements is performed at each measurement step and saved to a global results file. After the measurement is finished, the raw data is sorted into histogram format by summing up of the individual measurement results for each step. In terms of data output, a DSSC sweep or grid is therefore understood as a series S of histograms, each of which contain a number N of individual measurements.
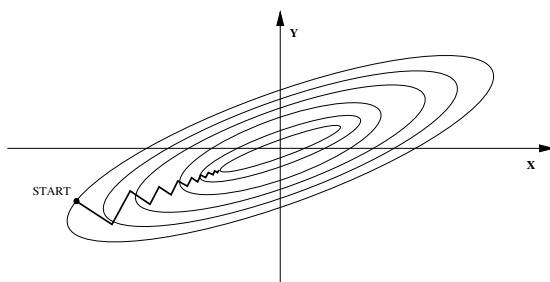
Figure 5.1: Gradient descent method used in popular fitting algorithms visualized for a two-dimensional minimization problem. Image from [50]

5.1.2 Numerical aspects

The most time-consuming sub-routine in processing the calibration data is the fitting of individual histograms. The studies presented here are based on the `MINUIT` fit algorithm by Fred James [51], which was used via the Cern `ROOT` Data Analysis Framework [42] in the scope of this work. The analysis of one typical dataset (i.e. an "$I_{ramp}-$ pixel delay" grid of a 64x64 pixel matrix prototype detector with roughly 4.2 million individual histograms) took about a day using 30 CPUs (present-day Intel Xeon[1], 2 GHz range). Clearly, more powerful machines can be used in order to speed up the process, but it becomes evident that the performance of the data handling and fitting algorithms is of high importance for the success of the calibration.

As described in sec. 3.3, measurement data gathered with the low noise DSSC sensor and ASIC are typically very narrow with respect to their binning that results from the sampling in the 8-bit DSSC ADC. As discussed in detail in [35], the aspects that dominate the process of getting the correct information from these data can be summarized in the following way:

- Due to the low ADC resolution, information is lost during sampling. This may result in systematic deviances of any mathematical respectively numerical method that is applied to the data. It impedes the determination of the original properties such as the mean or the width of the distribution of physical measurement results.

- The narrower the distribution of results is in comparison to the ADC resolution, the higher importance of linearity and determinability of the binning. Common traits of ADCs used for data sampling are dynamic and integral non-linearity (DNL and INL, see also sec. 3.1.4) which distort this binning and thereby imped the assessment of the information the result data contains. The effects of this distortion on the accuracy of results will be discussed later in this chapter.

- The binned data will often exhibit bins differing by orders of magnitude from each other. Valuable information about the distribution also can be gathered by taking into account bins with no entries.

For these reasons, the best choice in terms of stability and reliability of results for most of the fitting problems in the scope of this thesis is a so-called "maximum likelihood fit" with additional

---

[1]Intel Xeon Processor E5-2630 v3

integration of the fit-function between the bin boundaries [35]. The integral over the fit-function needs to be calculated in each step of the minimization. The `ROOT` framework employs integration algorithms from the GNU Scientific Library (`GSL`) [52] and also provides the possibility to apply its routines to histograms with non-equidistant binning caused by the DNL of the ADC.

An individual fit has finished after it has "converged". The term "convergence" used in the context of algorithm based fitting describes the process of finding the extremal value of the test statistic on its space of free parameters. Fig. 5.1 shows a visualization of such an algorithm, in this case a simple gradient descent method. `MINUIT`'s popular and advanced minimization method `MIGRAD` is also based on this idea. Poor fit convergence can result in the following effects:

- Longer duration of the fit algorithm, thereby drastically impeding the performance of the global routine.

- Erratic fit results, respectively erroneous estimation of fit errors.

- Convergence in local extrema rather which does not yield the absolute minimum residual between fit and data. This especially holds true for fits with multiple free parameters.

Both the integration and the minimization algorithm can fail under certain circumstances and thereby cause poor convergence. The minimization fails, when the n-dimensional surface that represents the minimization problem is too flat in relation to the current step size of the variation of the n free parameters, or has too many well pronounced local minima in relation to the global minimum. This effect can be further provoked by failures in the numerical integration, that typically occur when features of the fit-function are of the same order as the numerical precision of the integration algorithm.

5.1.3 Dealing with data outliers and presentation of results

Large datasets can be inherently inhomogeneous due to so-called data outliers, which can be caused by:

- Erratic measurement data.

- Errors in data processing such as non-convergent fits.

- Statistical effects.

In the calibration of the DSSC, certain data analysis and calibration steps build up on information (sec. 3.3.2) that has to be gathered automatically from previous steps. This provokes the need for methods that are robust against outliers. Various methods can be applied to cope with these effects. In addition to simple arithmetic averaging, the two following methods have been implemented in the data analysis software that was used to perform the studies at hand (see app. A for the mathematical definition):

- The median as a location measure of a sample distribution with the so-called "median absolute deviation" (`MAD`), a measure of the distribution's variance.

- The weighted arithmetic mean.

For the presentation of results and their interpretation during the development of the DSSC calibration, the median measure was used predominantly. Many overview histograms depicted in this work therefore mark the median with a green, dashed line and $\pm$`MAD` in dashed, magenta lines. The plot range is, if not otherwise noted, chosen to be $\pm$`3MAD`. For Gaussian distributions, this range would show about "2σ" respectively more than 95% of the data (eq. A.7 in the appendix). Together with the measures for histogram under- and overflow, the sample mean and the standard deviation of both the binned and unbinned dataset, it is thereby possible to quickly assess the key characteristics of most distributions without any a priori assumptions for the illustration such as pre-defined plot ranges.

5.2 Characterization of electronic noise and offset using an "$I_{ramp}-$ pixel delay" grid

"$I_{ramp}-$ pixel delay" grids (sec. 3.2.2) are used in order to characterize the system noise relevant for the calibration of the DSSC (sec. 3.3.2) for the following reasons:

- As the grid comprises a high number of individual measurements with theoretically identical noise (in units LSB), the accuracy of the noise determination can be improved due exploiting multiple measurements.

- The characterization of noise and offset can be employed to improve the calibration of detector gain (sec. 5.3).

- As a side effect, the individual pixel delay step sizes can be determined. This information can be used to improve further calibration steps.

The measurement is performed with the DSSC recording so-called dark frames, typically with at least 10^4 individual measurements comprised in each grid histogram. In an ideal situation, i.e. when no systematic artifacts are present (e.g. sec. 6.2.2), the distribution underlying the binned data should therefore be, to a very good approximation Gaussian.

Three different analysis methods have been investigated and compared using simulated data and will be described in this section. A comparison of the difference in the achievable accuracy and the robustness of the individual methods will be given in sec. 5.2.6.

5.2.1 Individual fitting and averaging

For distributions that are narrow in comparison to the bin width, the standard deviation calculated from the binned distribution has an inherent, systematic bias[2]. Therefore, in the first step of the analysis of the "$I_{ramp}-$ pixel delay" grid, each histogram is fitted individually in order to get the position and the standard deviation of the distribution, i.e. the width and offset of the

---

[2]This effect, amongst various methods to improve fitting binned distributions narrow in comparison to the histogram binning, has already been investigated in [35].

digitized electronic noise for each individual I_{ramp} and pixel delay setting of the grid. The fit of the Gaussian has two free parameters $\sigma_{j,k}$ and $x_{j,k}$, as the number N of total samples in each histogram is known. The area under the fit-function can therefore be fixed, if the function is normalized in the following way:

$$F_{\text{noise}}(x) = \frac{N}{\sigma_{j,k}\sqrt{2\pi}} \, e^{-\frac{1}{2}\left(\frac{x-x_{j,k}}{\sigma_{j,k}}\right)^2} \tag{5.1}$$

A first attempt at characterizing the mean of the width of a series of K histograms with identical I_{ramp} setting with individual fit results σ_k was performed by calculating the arithmetic mean. In addition, tests were performed with the median and the weighted arithmetic mean (app. A). A comparison of these basic averaging methods and an evaluation of their application in the characterization of the detector noise can be found in [32]. There it is shown, that under ideal conditions the weighted arithmetic mean is the averaging method suited best for characterizing the noise in an "$I_{ramp}-$ pixel delay" grid. Other more advanced methods can be used to further improve the results, as will be shown in the following.

5.2.2 Error function method

One method that can be used to determine the noise on a set of pixel delay step histograms is based on the so-called normal cumulative distribution function. As the averaging of the individual fits, it is based on the assumption, that all histograms of a "$I_{ramp}-$ pixel delay" with identical I_{ramp}-setting have the same width.

Put in words, the normal cumulative distribution function, f_{ncd}, is the integral over a Gaussian centered at x_0 and standard deviation σ, with the integration going from negative infinity up to x:

$$f_{\text{ncd}}(x) = \frac{1}{\sigma\sqrt{2\pi}} \int_{-\infty}^{x} e^{-\frac{1}{2}\left(\frac{t-x_0}{\sigma}\right)^2} dt = \frac{1}{2}\left(\text{erf}\left(\frac{x-x_0}{\sigma\sqrt{2}}\right)+1\right) \tag{5.2}$$

This relation can also be understood as the continuous shift of a Gaussian with a variable mean x towards the negative infinity over a sharp threshold at x_0, while integrating everything underneath the Gaussian which is on the negative side of the edge.

The shift induced by the pixel delay grid measurement is a discrete case of this mathematical relation. The positions of the individual distributions for each pixel delay step are separated by the series of pixel delay steps and represent the nodes of eq. 5.3 on the abscissa. The edge at x_0 is represented by an individual bin boundary, and the ordinate values are obtained by summation of all entries in the histogram below this edge for each individual pixel delay step. In the following, this method is referred to as "error function method":

$$f_{\text{err}}(x) = \frac{N}{\sigma\sqrt{2\pi}} \int_{x}^{-\infty} e^{-\frac{1}{2}\left(\frac{t-x_0}{\sigma}\right)^2} dt = \frac{N}{2}\left(\text{erf}\left(\frac{x_0-x}{\sigma\sqrt{2}}\right)+1\right) \tag{5.3}$$

with N being the norm of the normalized Gaussian with standard deviation σ. As higher pixel delay steps lead to higher mean values, the shift of the gaussian over the edge at x_0 in this particular case goes from negative to positive – "left to right", resulting in inverted integral
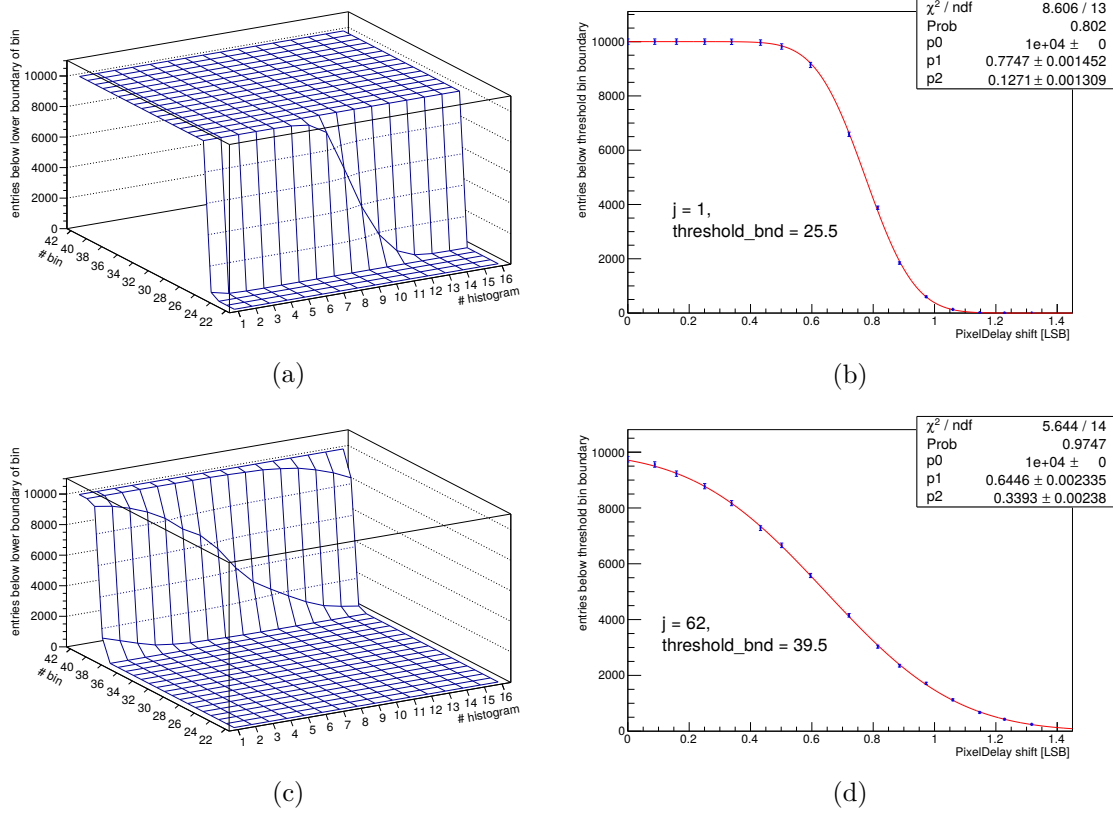
(a)

(b)

(c)

(d)

Figure 5.2: Illustration of the error function method for a low I_{ramp} setting (= low gain) in (a) and (b) and a high setting (= high gain, leading to distributions with increased width) in (c) and (d). The plots on the left intend to illustrate the program algorithm that searches for the most suitable threshold bin boundary. For (a), this is bin number 26 with its lower bin boundary being 25.5. For (c), the lower bin boundary of bin 40 at 39.5 gives the largest difference between the first and last histogram of the series. It becomes evident, that with the respectively adjacent bin boundaries much less information about f_{err} could be extracted.

On the right side, the nodes on the abscissa (the shift due to the pixel delay) are given by averaging over the individual fits of all 64 I_{ramp} settings (sec. 5.2.4), while the ordinate values are identical to the plots on the left side. Error values are available for both the counts below the threshold bin by assuming poisson statistics and the difference in the positions, i.e. the pixel delay steps, gathered from the fits. The fit result of $f_{err}(x)$ is depicted in red. The fit parameters are:

$p0 = N$, which is fixed to the total number of counts that is identical in all histograms

$p1 = x_0$, the distance of the threshold bin boundary to the offset of the first histogram

$p2 = \sigma$, the global standard deviation of the histogram series

boundaries.

In order to determine the common standard deviation σ, the following steps have to be performed in the given order to apply this method on a series of histograms from an "I_{ramp}- pixel delay" grid:

- Fit all histograms individually in order to get the positions of the noise peaks, denoted as $(x_{p0}, \ldots, x_{pn})$. Average over all available sub-series, assuming that the pixel delay stepping is independent on the I_{ramp} value, in order to obtain the pixel delay step sizes (sec. 5.2.4, eq. 5.11).

- Find an appropriate bin boundary to assign as "edge" x_0. As f_{err} is asymptotic to zero in the upper region and to the number of counts N in an individual histogram in the lower region of its domain of definition, the most suitable bin boundary is the one that leads to the largest difference between $f_{err}(x_{p0})$ and $f_{err}(x_{pn})$, as the region of maximum variation yields the most information about the parameter σ that is encoded in the curvature of the error function. See also fig. 5.2.

- Fit f_{err} to the discrete nodes. Thereby, N is fixed to the total number of counts (=number of ADC samples) in each histogram of the series. The fit parameter σ is then the global noise in a subset of histograms of an "$I_{ramp}-$ pixel delay" with identical I_{ramp} setting.

- The fit parameter x_0 is the distance of the threshold bin boundary to the offset of the first histogram. Together with the information about the pixel delay steps, this information can be used to determine the offset of all k histograms with the same I_{ramp} setting (sec. 5.2.8).

The shape of f_{err} is only based on counting entries below a certain threshold bin boundary and the information about the pixel delay step sizes. This is why the influence of wrong bin boundary information is reduced in comparison to methods based solely on histogram fitting, which will be illustrated in sec. 5.2.6. The knowledge about the pixel delay steps however can only be obtained from methods based on histogram fitting. Therefore some influence of wrong binning information cannot be excluded.

5.2.3 Simultaneous fitting

A different approach to characterizing an "$I_{ramp}-$ pixel delay" grid is the so-called simultaneous fit. It is also based on the assumption that the noise is identical for histograms with identical I_{ramp} setting. The goal of the method is to improve the stability of the fitting algorithm by combining the histograms with identical I_{ramp} setting in one single histogram, so that they can be fit simultaneously. Figure 5.3 shows an example of such a combination. The combination of the individual histograms to a composite histogram is done in the following way:

- From each histogram of the series get the first bin b_f and last bin b_l that has counts.

- Ensure that in the composite histogram each distribution will be framed with at least two empty bins, which guarantees that the (likelihood-)fit will not loose valuable information
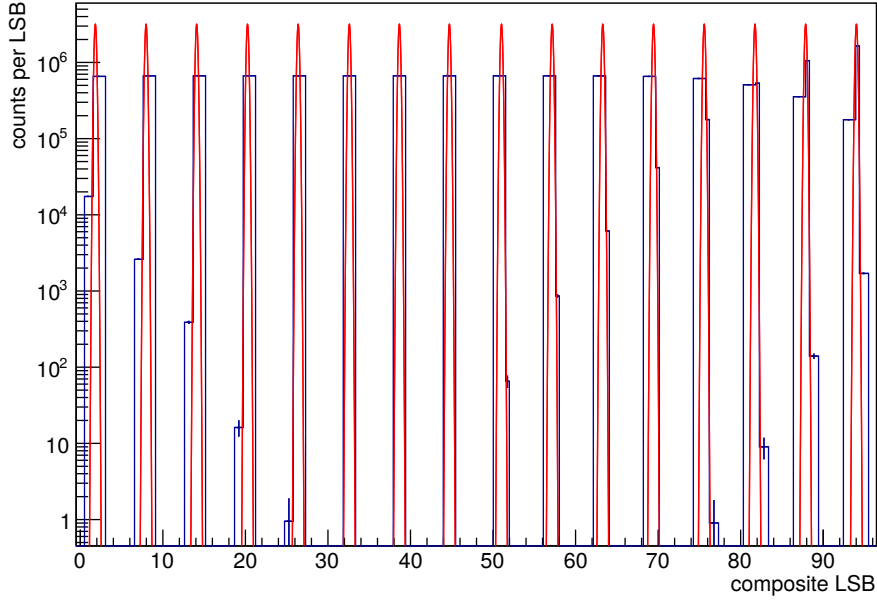
Figure 5.3: Histogram composed of sixteen individual datasets (blue), each representing a different pixel delay step of an "I_{ramp-} pixel delay" grid. The composed fit-function is depicted in red. Bin boundary information has been taken into account.

and provides a clear separation of the individual peaks. For that purpose, the smallest and largest element out of the set that contains all $b_{f,k} - 1$ and $b_{l,k} + 1$ of all K pixel-delay series histograms $\{H_1, \ldots, H_K\}$ are determined, identified as $b_{f,\text{global}}$ and $b_{l,\text{global}}$. In a typical "I_{ramp-} pixel delay" grid $K = 16$.

- As the binning information is related to the pixel, the binning for all series histograms is identical. The composite histogram will therefore be a sequence of the bins $b_{f,\text{global}}$ to $b_{l,\text{global}}$ concatenated K times, with the number B of bins in this sequence being

$$B = b_{l,\text{global}} - b_{f,\text{global}} + 1 \tag{5.4}$$

- The position (in units LSB) of the composite binning on the histogram abscissa is arbitrary. For ease of interpreting the results, one can place the center of the first bin at zero, by identifying the negative half bin width of the first global bin as the lower bin boundary of the first bin of the composite histogram. With $w(b)$ being the width of bin b in the unit

LSB, the sequence of bin boundaries S_{bb} can then be produced in the following way:

$$s_{bb,0} = -\frac{1}{2}\, w(b_{f,\text{global}}) \tag{5.5}$$

$$s_{bb,n} = s_{bb,n-1} + k\, w(b_{f,\text{global}} + i) \tag{5.6}$$

$$\text{with} \quad i \to 0, \ldots, B-1$$

$$\text{and} \quad k \to 1, \ldots, K$$

leading to a set of $K \cdot B + 1$ bin boundaries in total.

- The composite histogram is filled with the entries from the original K series histograms by mapping the original bin number b_i to the new bin number $b_{\text{cmp},i}$ in the following way: [3]

$$b_{\text{cmp},i} = b_i - b_{f,\text{global}} + k\, B \tag{5.7}$$

$$\text{with} \quad i \to 0, \ldots, B-1$$

$$\text{and} \quad k \to 0, \ldots, K-1$$

generating the composite set of total $K \cdot B$ bins.

- For each of the K sections of the composite histogram, an offset to the original series histogram $\{H_1, \ldots, H_K\}$ can be identified. For the first section, this offset is $-c(b_{f,\text{global}})$, with $c(b)$ being the center of bin b, as bin $b_{f,\text{global}}$ will be centered at the zero mark of the composite histogram abscissa. The sequence of offsets $S_{\text{off}} = \{s_{\text{off},1}, \ldots, s_{\text{off},K}\}$ therefore can be written as:

$$s_{\text{off},k} = -c(b_{f,\text{global}}) + k\, w_{\text{section}} \tag{5.8}$$

$$\text{with} \quad k \to 0, \ldots, K-1$$

with w_{section} being the total width of the section of bins $b_{f,\text{global}}$ to $b_{l,\text{global}}$. The sequence of offsets then references the original peak positions x_k from the individual fit to the peak positions $x_{\text{cmp},k}$ in the composite histogram by:

$$x_{\text{cmp},k} = x_k + s_{off,k} \tag{5.9}$$

After generating the composite histogram, the fit-function comprising the K individual peaks of one I_{ramp} setting reads:

$$F_{\text{simfit}}(x) = \sum_{k=1}^{K} \frac{N}{\sigma\sqrt{2\pi}}\, e^{-\frac{1}{2}\left(\frac{x-x_{0,k}}{\sigma}\right)^2} \tag{5.10}$$

with the $K + 1$ free fit parameters being the positions $x_{0,k}$ and σ. N is fixed to the number of entries in each individual series histogram. As start values, the average σ and the offset-corrected

---

[3]Eq. 5.7 will lead to a bin numbering starting from zero. However, in the usage of the ROOT framework [42], bin "zero" refers the so-called "underflow" bin. This has been taken into account for the implementation of the method.

$x_{\mathrm{cmp},k}$ of the K individual fits can be assigned. Using eq. 5.9, the original peak positions can be obtained and saved for later use, e.g. the determination of the pixel delay steps.

5.2.4 Pixel delay steps

The individual pixel delay step sizes can be determined based on the position information from either the individual fits or the simultaneous fitting. In both cases, averaging over the J settings of I_{ramp} can be used in order to stabilize the result, as the offset shift due to the pixel delay is assumed to be independent on the I_{ramp} setting. The k-th pixel delay step pxd_k can be calculated in the following way, denoting that the number of pixel delay settings exceeds the number of pixel delay steps by one:

$$\mathrm{pxd}_k\,[\mathrm{LSB}] = \mathrm{AVG}\left\{(x_{j=0,k+1} - x_{j=0,k}),\,(x_{j+1,k+1} - x_{j+1,k}),\,\ldots,\,(x_{J,k+1} - x_{J,k})\right\} \quad (5.11)$$

Arithmetic averaging, weighted arithmetic averaging and the median method (app. A) have been compared. This comparison will be detailed in sec. 5.2.9. It gives as a result, that the simple arithmetic average provides the most stable results for the pixel delay step determination in the tested environments. Therefore this method has been used in all following sections.

5.2.5 Test environments
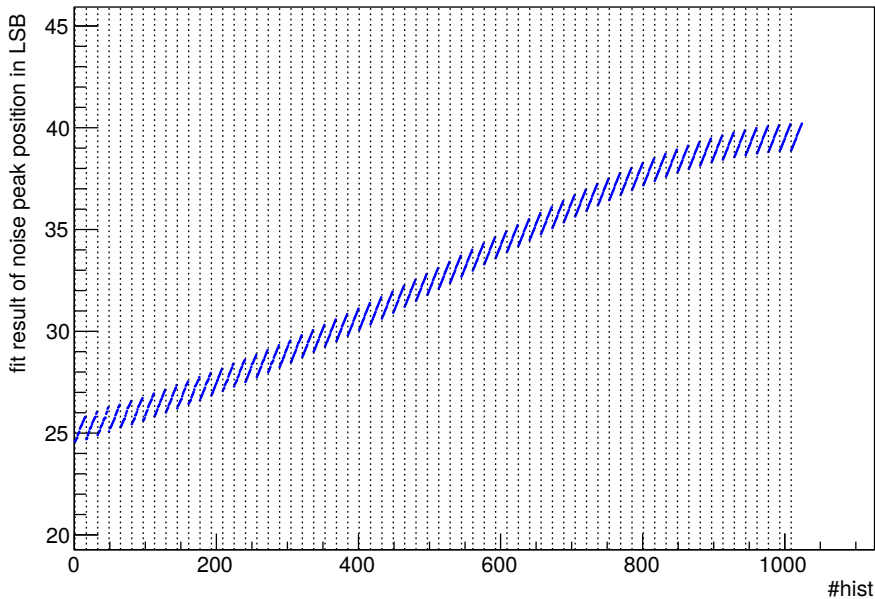
Figure 5.4: Blue dots mark the fit results to 1024 individual grid step histograms of one pixel in a full "$I_{ramp}-$ pixel delay" simulation. This figure shows the resulting positions x_k. The dashed, black lines separate the 64 I_{ramp} ($j \to 0,\ldots,63$) groups. The offset-shift caused by the pixel-delay can be clearly identified for the individual groups of 16 pixel delay step each ($k \to 0,\ldots,15$).
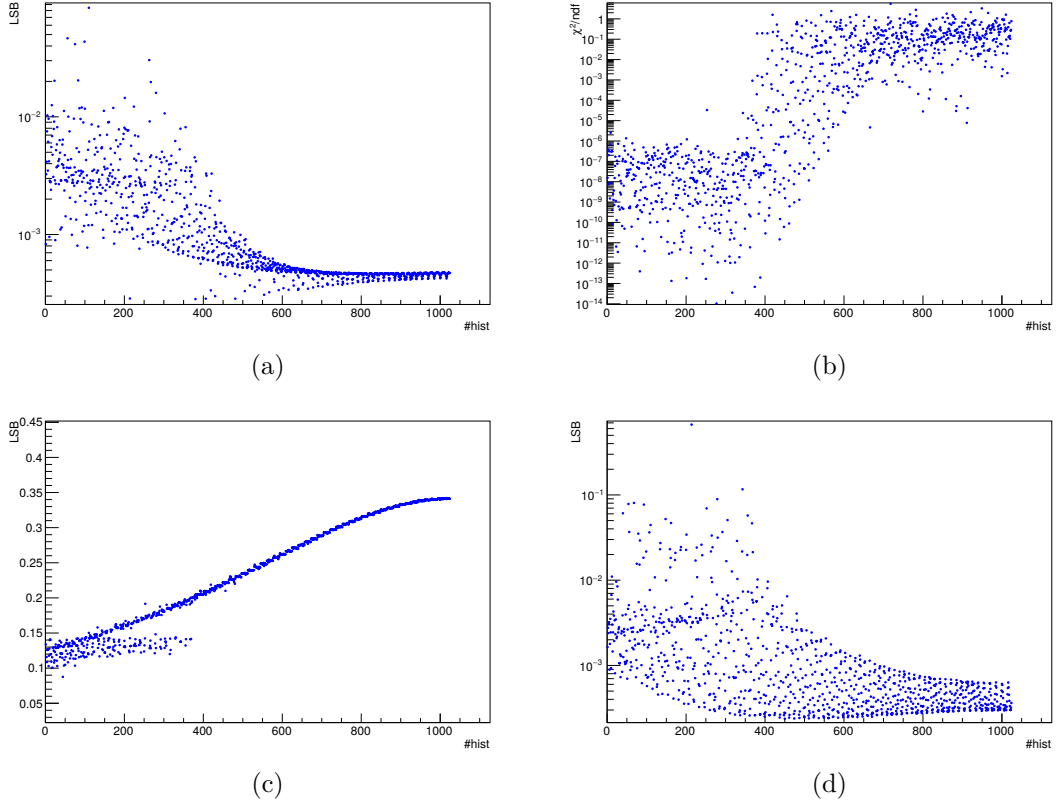
Figure 5.5: (a) fit error of the peak positions (i.e. offset) x_k, (b) reduced χ^2, (c) fit result for peak width σ_k, (d) fit error of σ_k. For each of the groups with same I_{ramp}-setting an identical peak width (sec. 3.2.2) was simulated. The scattering of the results in (c) up to approximately 0.2 LSB peak width shows the expected [35], erroneous behavior of individual fits to narrow distributions. The very low values for the reduced χ^2 and the high error values also indicate the problematic fitting of these data.
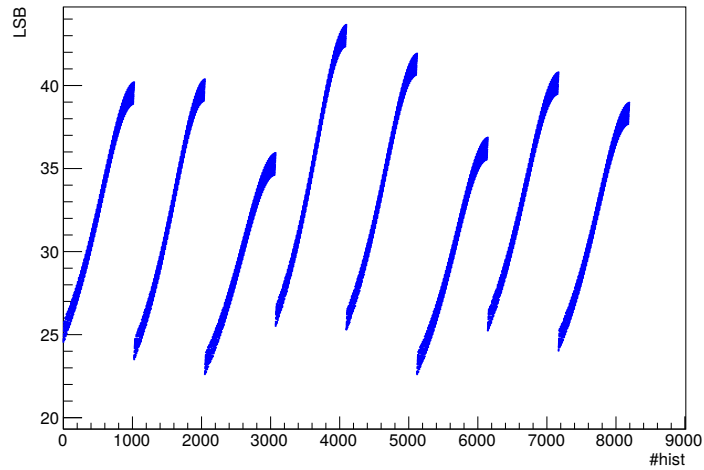
Figure 5.6: As fig. 5.4, but now the individual fit results of the positions in a full jk-grid simulation of 8 pixels are depicted.
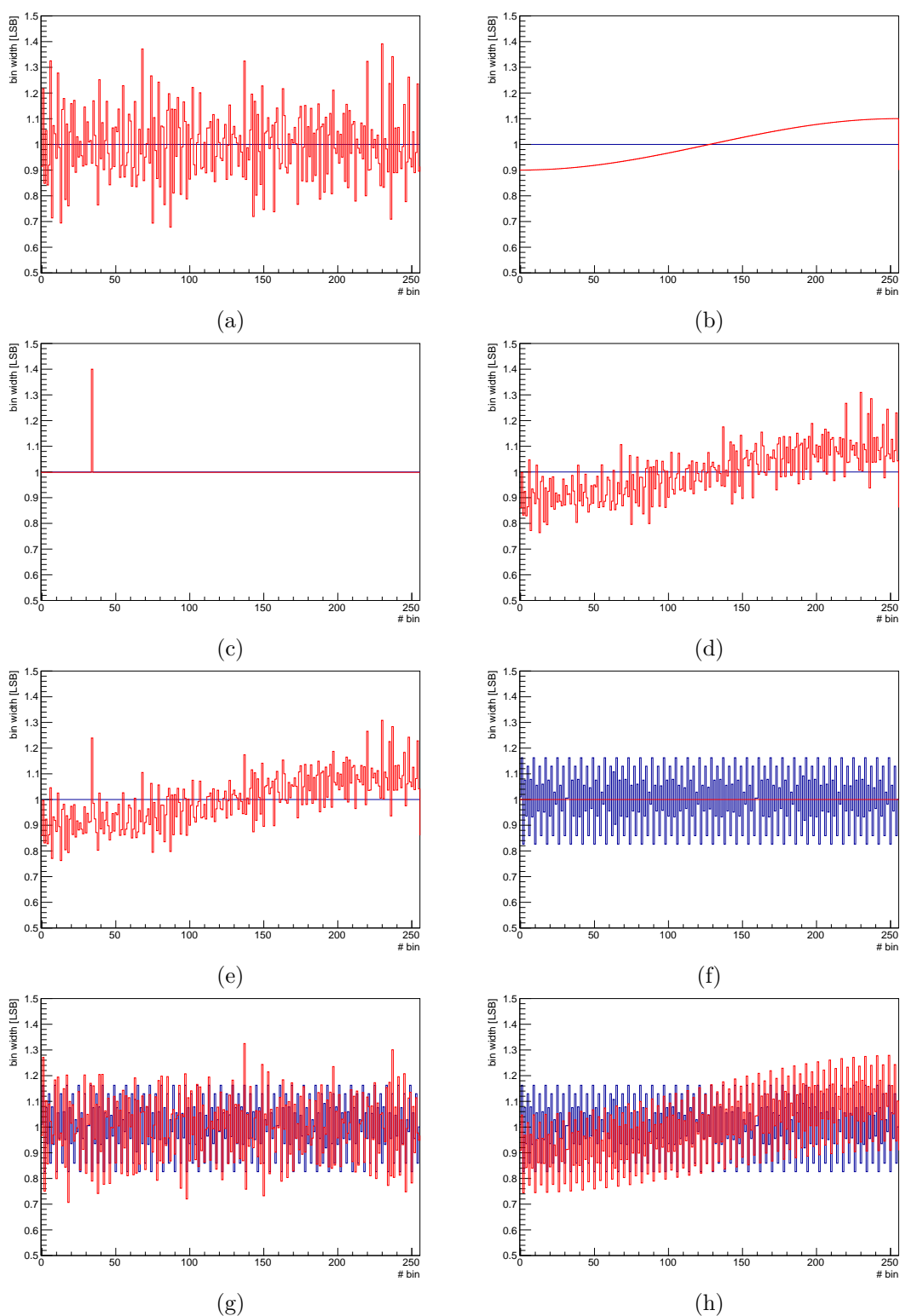
Figure 5.7: Binning manipulation. Original binning in blue, binning used in data analysis in red. (a): blurred by random values from a Gaussian distribution with $\sigma_{\text{blur}} = 0.1$ LSB. (b): sinusoidal INL. (c): bin 35 is 40% wider. (d): combination of (a) and (b). (e): combination of (a),(b) and (c). (f): simulated (cyclic) DNL with $\sigma_{\text{DNL}} = 0.1$ LSB, ignored (g): simulated DNL taken into account, additionally blurred (Gaussian, $\sigma_{\text{blur}} = 0.05$ LSB). (h): additional sinusoidal INL

One of the simulated (ch. 4) datasets that were used to develop and test the proposed methods for analyzing "I_{ramp}– pixel delay" grids is illustrated in figs. 5.4 and 5.5, where the individual fit results for one single pixel of a full jk-grid are depicted. Fig. 5.6 shows 7 further pixels of these data. The simulation truth, i.e. the individual values for the distribution offset and the noise of each histogram, is saved together with the simulated histogram data (ch. 4). By comparison to the simulation truth, the accuracy of the individual methods can be assessed. Two different categories of simulated data have been used as test environments:

- 64x64 pixels, k-grid, $K \cdot \text{pix}_x \cdot \text{pix}_y = 16 \cdot 64 \cdot 64 = 65536$ histograms, identical I_{ramp}-setting j, each pixel has individual offset and noise.

- 10x10 pixels, full jk-grid, $J \cdot K \cdot \text{pix}_x \cdot \text{pix}_y = 64 \cdot 16 \cdot 10 \cdot 10 = 102400$ histograms, each pixel has individual offset and noise values.

The first test environment category was used to study effects of the individual calibration methods at specific noise values, the second category resembles the actual calibration data measured with the DSSC. All test data sets have been generated with different ADC characteristics (sec. 3.1.4):

- ideal binning ($\sigma_{\text{DNL}} = 0$)

- $\sigma_{\text{DNL}} = 0.1$, 0.2 and 0.3 LSB, individual for every pixel

If the dataset was simulated with a DNL, the entry count in the bins of the individual histograms reflect this effect, as larger bins "count" more entries in comparison to more narrow bins – each in relation to their bin width. The simulated ADC characteristic is saved together with the simulated histogram data.

In order to study the the effect of an uncertainty in the determination of bin boundaries on the applied calibration algorithms, the data analysis software can either statistically blur or systematically distort, or even completely disregard it. For the current DSSC ASIC generation, a $\sigma_{\text{DNL}} = 0.08$ LSB has been determined (ch. 6), and it is estimated that the binning can be measured with an uncertainty of approximately 10% of the nominal bin width.

Fig. 5.7 illustrates the different manipulations that can be applied to the histogram binning during data analysis in order to simulate erroneous binning information:

- (a) Each bin boundary is shifted by a value computed from a Gaussian random seed. This manipulation is referred to as "blurring" in the following, measured by the standard deviation σ_{blur} of the Gaussian. A statistical uncertainty in the binning determination of 10% of the nominal bin width correlates to $\sigma_{\text{blur}} = 0.1$ LSB.

- (b) Bin widths distorted by a sinusoidal function. This simulates a systematic INL (sec. 3.1.4) in the determined bin boundaries, that could for example be caused by a non-linear voltage source during the bin-boundary determination. The function that has been used to generate the sinusoidal distortion is:

$$f(x) = 1 - A \cos\left(\frac{x \cdot \pi}{256}\right) \tag{5.12}$$

with A being the factor used to set the level of the distortion. For $A = 0.1$, the first bin is 10% smaller than the nominal bin-width, with the first 128 bins being shrunken and the last 128 bins being widened.

- (c) A distorted individual bin, used to study the effects of binning distortion around a specific position.

- (d), (e) A combination thereof.

- (f) Simulated cyclic DNL due to the functioning principle of the DSSC ADC (individual bit lines and Gray Code Counter, sec. 3.1.4). In this case, the binning information was ignored.

A combination possible binning manipulations on a simulated ADC characteristic is shown in fig. 5.7 (g) and (h). After applying the binning manipulations, the set of 256 bin boundaries was always checked for monotony and normalized to a nominal width of 256 LSB.

A more detailed comparison of these manipulations regarding their influence on the results of the analysis and the calibration algorithms will be presented in the following sections of this chapter. It should be anticipated here, that the two following manipulations lead to similar, qualitatively comparable results:

- artificially blurred ideal binning, as in fig. 5.7 (a).

- simulated ADC non-linearities that are ignored during the analysis, as in fig. 5.7 (f).

5.2.6 Comparison of methods: Noise characterization

The task of the noise characterization on a full DSSC jk-grid is again illustrated in fig. 5.8. There, the simulation truth as well as the result of the weighted mean method (sec. 5.2.1) are depicted together with the individual fit results. A complete view on the results of the individual peak fits of a full jk-grid of 100 pixels is given in fig. 5.9. The residual of the determined noise value relative to the simulation truth,

$$\sigma_{\text{rel.res.}} \, [\%] = \frac{\sigma_{\text{fit}} - \sigma_{\text{sim.truth}}}{\sigma_{\text{sim.truth}}} \cdot 100 \tag{5.13}$$

is displayed in two different ways: The two-dimensional histograms on the right illustrate the composition of the distributions depicted on the left, by plotting the residual as a function of the simulated peak width. The results lying well below the simulation truth in fig. 5.8 can clearly be identified in fig. 5.9 (b). The plots (c) and (d) illustrate the difficulties that arise when the binning information is erroneous. In this case, the original ideal binning has been blurred with $\sigma_{\text{blur}} = 0.1 \, \text{LSB}$, as depicted in fig. 5.7 (a). For ideal binning, the results deviate from the simulation truth predominantly for more narrow peaks, i.e. low noise values. Erroneous binning information causes large statistical uncertainties for all simulated peak widths of the jk-grid.

For the three proposed noise characterization approaches, namely
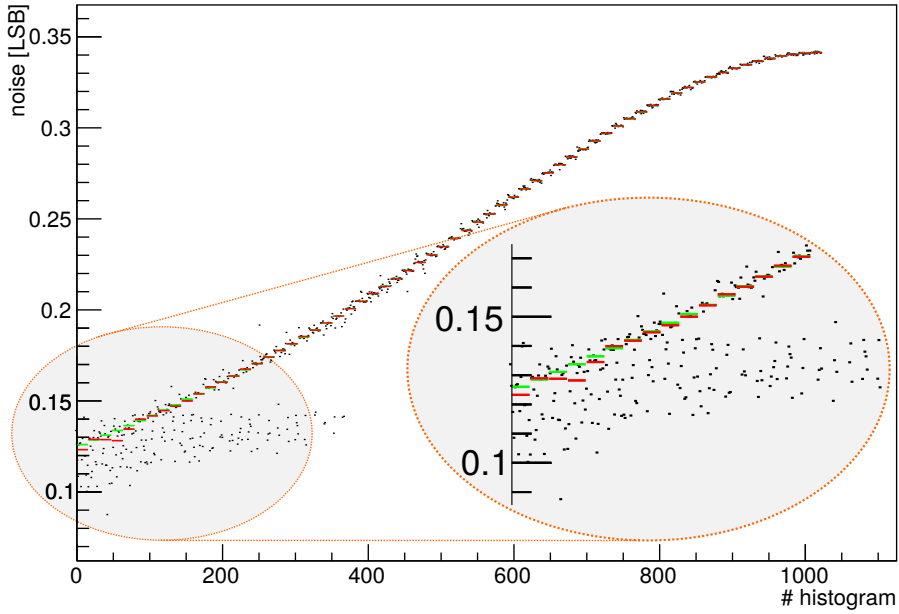
- the weighted mean method (sec. 5.2.1),

Figure 5.8: The black dots show the individual fit results for the σ of one pixel in a full jk-grid. This dataset is identical to fig. 5.5, (a). The simulation truth is depicted by the green lines. The weighted mean of each group of 16 data points is given in red. The dashed, orange section comprises the first 16 I_{ramp} settings (256 individual fit results) and is given as a zoom inlay.

- the error function method (sec. 5.2.2),

- and the simultaneous fit method (sec. 5.2.3).

the statistical uncertainties increase with decreasing noise as expected. For ideal, non-erroneous binning information and two specific peak widths, 0.2 LSB and 0.1 LSB, this effect is illustrated in figs. 5.10 and 5.11. In these plots, the mean and the standard deviation of the distributions of the residuals (as in eq. 5.13) of the three proposed methods are compared. For this comparison, a k-grid (i.e. 16 pixel delay settings) simulated for a specific I_{ramp} setting on a DSSC ASIC with $64 \cdot 64 = 4096$ pixels has been analyzed (sec. 5.2.5).

Fig. 5.10 shows the situation for a peak width of approximately 0.2 LSB. It becomes evident, that a higher number of dark frames improves the results of all three compared methods, regarding both the mean and the standard deviation of the distributions. The fitting based methods slightly outperform the error function method. For data with at least 10^5 dark frames the systematic error of either of the three methods is below 1% of the simulated peak width. The accuracy of the error function method strongly depends on the determined pixel delay steps. It particularly profits from the information that can be obtained on a full jk-grid, as the averaging over the pixel delay steps (sec. 5.2.4) improves the accuracy of the function nodes. When analyzing only a k-grid, this advantage can be simulated by granting the error function method access to the correct, simulated pixel delay step sizes. If done so, the results of error function method improve. The simultaneous fit method also provides the individual positions of the k distributions – and therefore the pixel delay steps. The error function method based on the pixel delay steps determined from the 16

(a)

(b)

(c)

(d)
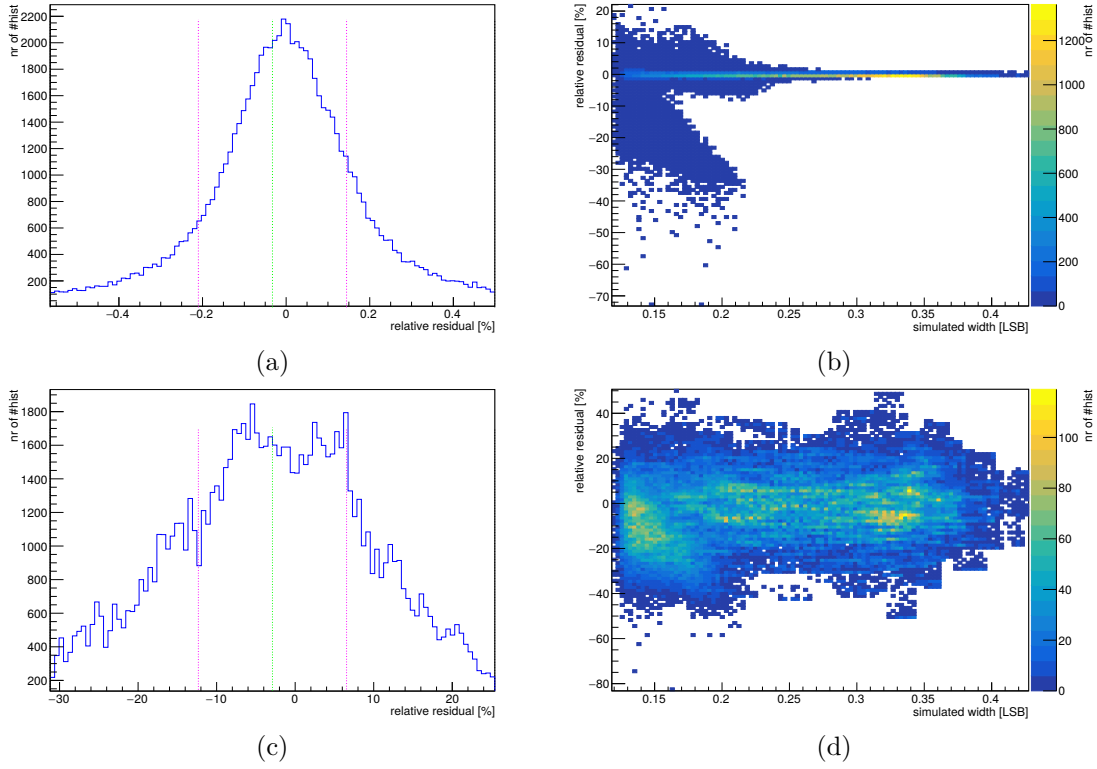
Figure 5.9: Relative residual to the simulated peak width of the individual fit results of 100 pixels in a full jk-grid. The one-dimensional histograms on the left show $\pm 3\mathtt{MAD}$. The two-dimensional histograms on the right show the full set of 102400 data points as a function of the simulated peak width.
(a) and (b): ideal binning, $\overline{m}_{arith.} = -2.2\%, \sigma = 6.6\%$.
(c) and (d): binning blurred with $\sigma_{\mathrm{blur}} = 0.1\,\mathrm{LSB}$, as in fig. 5.7 (a), $\overline{m}_{arith.} = -3.2\%, \sigma = 14.4\%$.
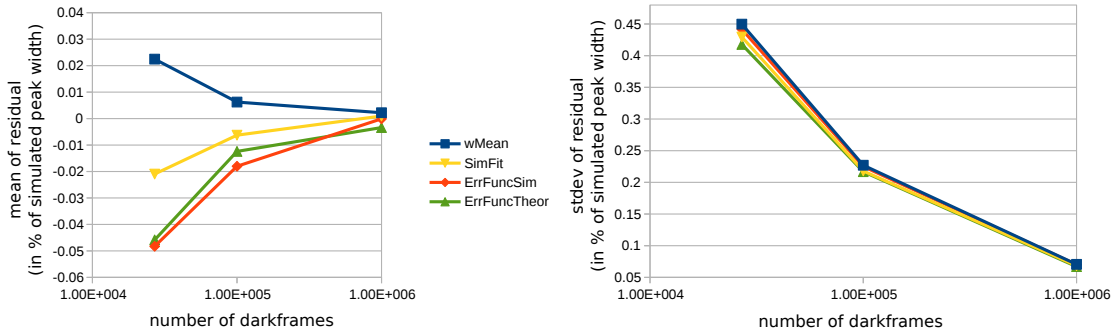
Figure 5.10: Simulated peak width: 0.2 LSB. Mean (left) and standard deviation (right) of the distributions of relative residuals to the simulated peak width of the three proposed methods. Each data point represents $K \cdot N_{\mathrm{pix}} = 16 \cdot 4096 = 65536$ individual histograms.
Results of weighted mean method (blue) and simultaneous fit method (yellow), the error function method has been applied in two different ways: Using the pixel delay step sizes from the simultaneous fit method (red), and using the correct, simulated pixel delay step sizes (green).
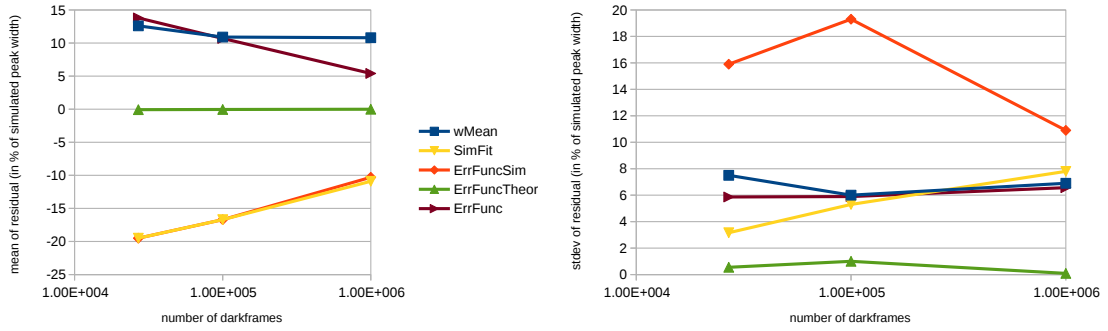
Figure 5.11: Simulated peak width: 0.1 LSB. As fig. 5.10. Three different variants of the error function method are depicted: Using the pixel delay step sizes from the simultaneous fit method (red), using the correct, simulated pixel delay step sizes (green) and using the step sizes from the K individual fits (dark mauve).

individual fits is not plotted in fig. 5.10, as its performance is strongly impeded by the poor determination of the step sizes (fig. 5.18). Nevertheless, it showed the expected improvement for an increasing number of dark frames.

Fig. 5.11 represents the results for a peak width of approximately 0.1 LSB. All three methods show large systematic uncertainties in regards to the simulated peak width. The distributions of the residuals become highly irregular at this point, nevertheless their mean and standard deviation show the expected tendency to improve for a higher number of dark frames. The results of the error function method based on the pixel delay steps determined from the individual histogram fits are also shown in this plot, as they do not deviate much from the results obtained with the pixel delay steps from the simultaneous fit method. This is due to the deteriorating position accuracy of the simultaneous fit method for lower peak widths, which will be detailed in sec. 5.2.7. It becomes clear, that for peak widths this narrow the error function method strongly outperforms the other two approaches – given it has the correct information about the pixel delay steps. For "perfect" pixel delay steps and data with at least 10^5 dark frames, the residuals of the error function method were generally not larger than 1% of the simulated peak width.

A comparison of the three proposed methods for characterizing the noise in a full jk-grid is given in fig. 5.12. The results of the weighted mean method are depicted in (a) and (b), the results of the error function method in (c) and (d). The results obtained with the simultaneous fit method are given in (e) and (f). The left column illustrates the test environment of an ADC with ideal binning. Results for erroneous binning information, using a Gaussian blur identical to the one used for the individual fits in fig. 5.9 (c) and (d), are depicted in the right column. For ideal binning (left column of fig. 5.12), the strong dependence of the two peak-fitting based methods on the simulated peak width is well noticeable. They both show increasing deviations for peak widths narrower than approximately 0.15 LSB, as already evident in fig. 5.12. As anticipated in fig. 5.10, they outperform the accuracy of the error function approach for peak widths larger than approximately 0.2 LSB. A clear advantage of the error function method in conditions with erroneous binning information is indicated in the right column of fig. 5.12.
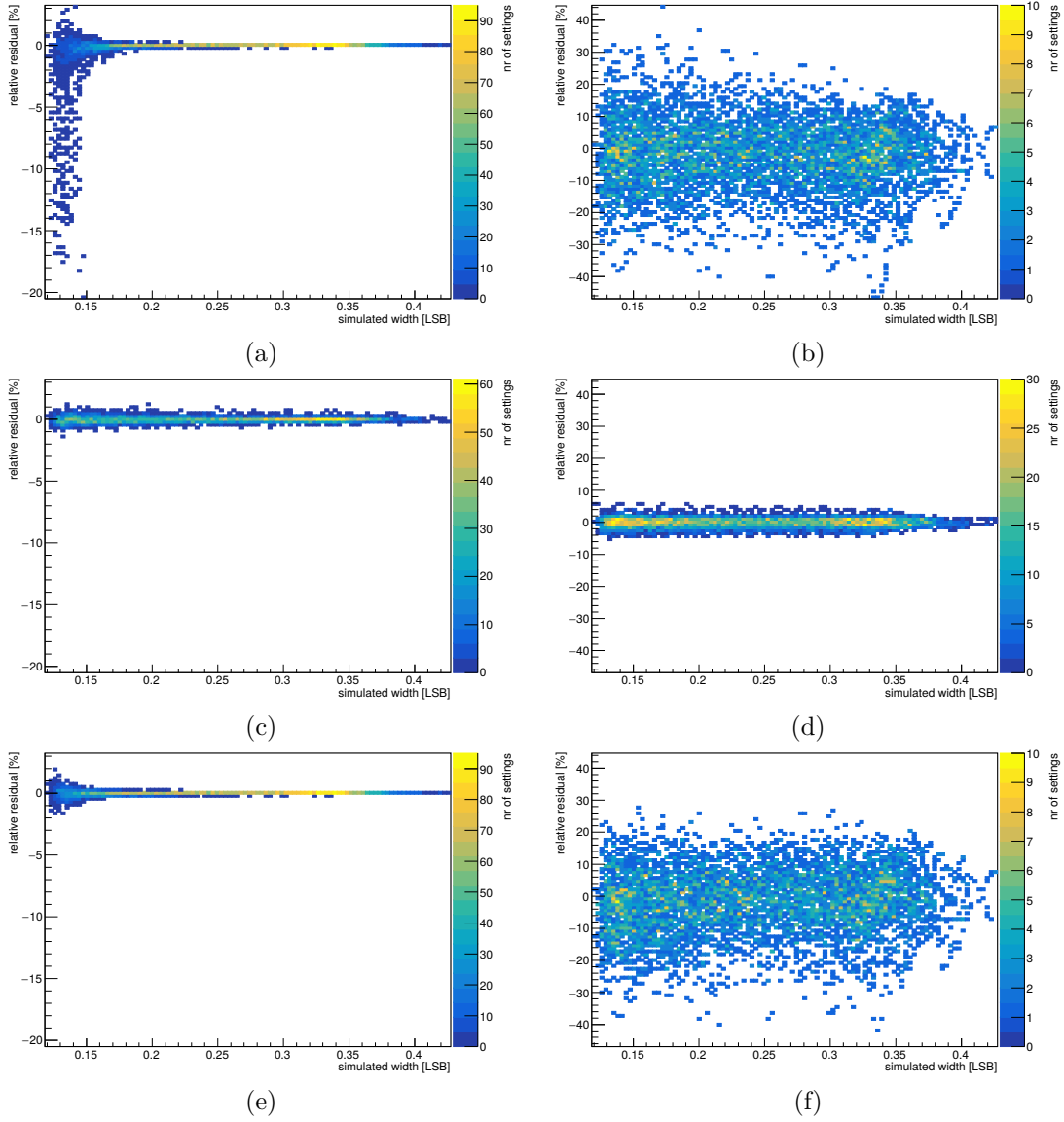
Figure 5.12: Comparison of the three proposed methods for determining the system noise from a jk-grid (full grid, 100 pixels). The distributions contain $J \cdot \mathrm{px}_x \cdot \mathrm{px}_y = 64 \cdot 10 \cdot 10 = 6400$ individual results, one for each of the 64 possible I_{ramp} settings. Results are given by the relative residual to the simulated peak width, plotted as a function of the simulated peak width.
The left column shows the results for ideal binning, for the right column, the binning has been blurred with $\sigma_{\mathrm{blur}} = 0.1\,\mathrm{LSB}$. The scale of the y-axis is identical for each sub-plot of a column, in order to make the results comparable.
(a) and (b): Weighted mean method.
(c) and (d): Error function method.
(e) and (f): Simultaneous fit method.
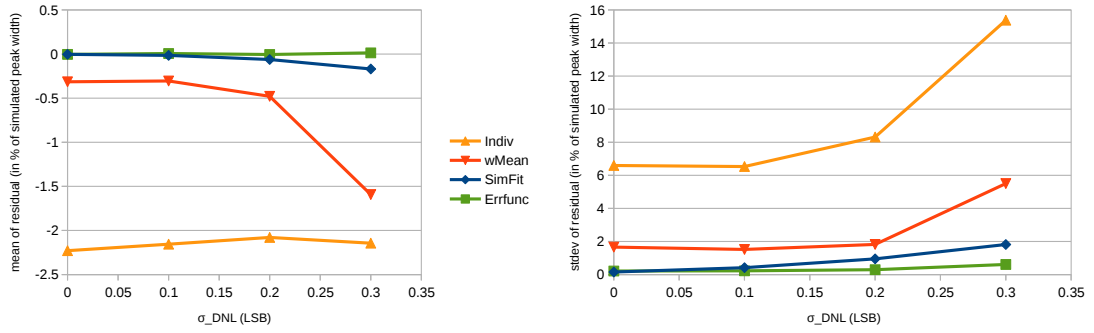
Figure 5.13: Comparison of the results of three proposed noise characterization methods applied to a full *jk*-grid of 100 pixels (102400 individual histograms) for ideally known ADC binning. The σ_{DNL} of the simulated cyclic DNL is given on the abscissa. The left plot shows the mean of the relative residuals of all I_{ramp}-settings to the simulated peak width. On the right, the standard deviation of the distribution of these residuals is given. In addition to the individual fits (yellow), the plots show the results of error function method (green), weighted mean (red) and simultaneous fit (blue).

Fig. 5.13 compares the results of all three noise characterization methods applied to a full *jk*-grid of 100 pixels for an ADC with ideal binning and three different, simulated DNL intensities. In addition, the unprocessed result of the individual fits is shown. For this study, the ADC binning was ideally known during the analysis. No significant systematic deviations could be identified for either of the three methods. As expected, the weighted mean method shows the largest systematic and statistical uncertainties – and is also affected most by increasing DNL in comparison to the other two methods. The reason for this is that it is based on individual fits to the noise peaks that are directly influenced by the binning. In contrast, the error function method shows the best stability for increasing DNL.
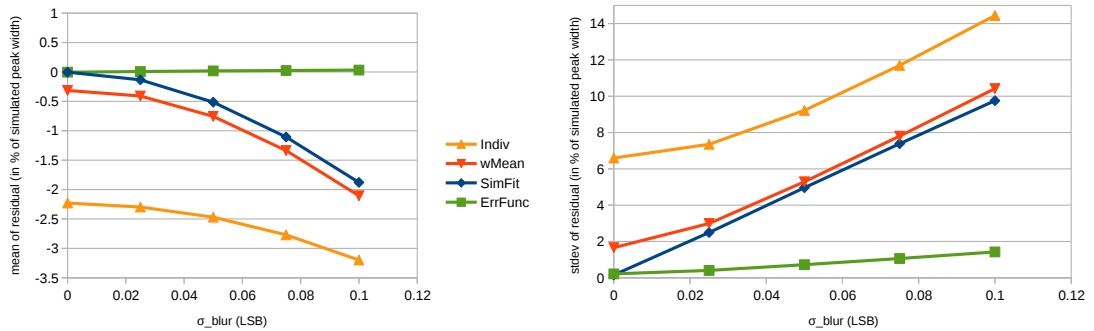
Figure 5.14: Comparison of the results of three proposed noise characterization methods applied to a full *jk*-grid of 100 pixels for different DNL values simulated by Gaussian blurring, compared with the result of the individual fits. The abscissa shows the σ_{blur} of the Gaussian distribution used for the binning manipulation. The mean of the relative residual to the simulated peak width is given on the left, the standard deviation on the right.

A comparison of the three proposed noise characterization methods regarding their performance under the influence of erroneous binning information is given in fig. 5.14. For this plot, the
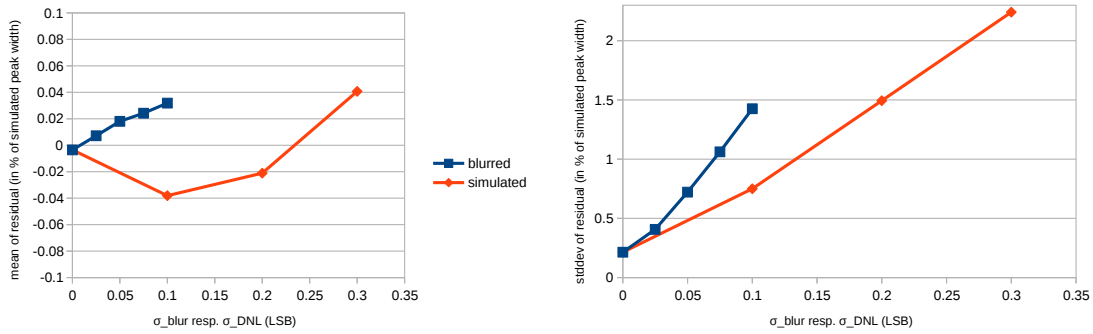
Figure 5.15: Comparision between simulated and ignored (red) and artificially blurred (blue) binning information for a full jk-grid of 100 pixels. Results have been calculated with the error function method. The results for the blurred binning are identical to the ones in fig. 5.14. The σ_{blur} of the Gaussian distribution used for the blurring, respectively the σ_{DNL} of the simulated cyclic DNL is given on the abscissa.

simulated ideal ADC binning has been manipulated with Gaussian blurring with increasing standard deviation, up to $\sigma_{\text{blur}} = 0.1$ LSB. The advantage of the error function method over the individual fit method and the simultaneous fit method is evident. Not only is the spread of the distribution of residuals much smaller, also the increasing systematic offset for higher values of σ_{blur} is less strong for the error function.

As anticipated in sec. 5.2.5, a comparison between artificially blurred, ideal ADC binning and ignored, simulated DNL shows the similarity of these two effects. Fig. 5.15 illustrates this observation by superimposing results for analyses with blurred (σ_{blur}) and ignored (σ_{DNL}) binning on the same abscissa. The statistical uncertainties (right plot) are comparable. Albeit the systematic deviations (left plot) of the individual result distributions are similar in terms of quantity, monotony is not given for both series. The reason for this is that the artificial blurring (blue) has always been performed with the same random number seed, leading to effects that only differ in magnitude as a function of σ_{blur}. The simulation of the cyclic DNL on the other hand leads to ADC binnings that do not necessarily resemble each other.
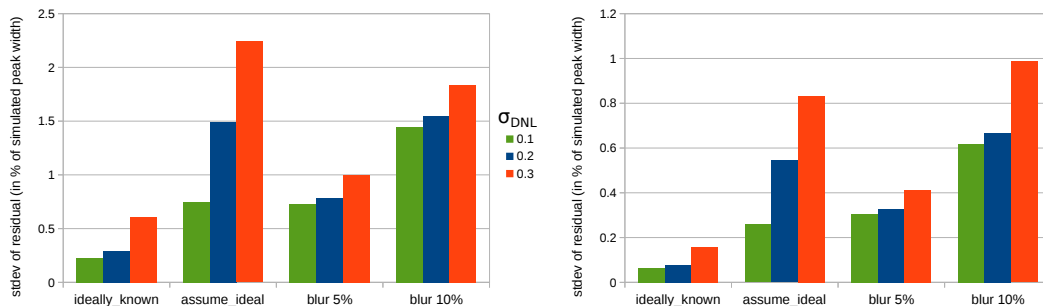
Figure 5.16: Comparison of datasets with increasing intrinsic DNL for different binning environments. Data was analyzed using the error function method. Left: Darkframe jk-grid for 1 keV/LSB system gain calibration. Right: Darkframe jk-grid for 0.5 keV/LSB system gain calibration.

In practice, it is not possible to determine the binning of the DSSC ADC with arbitrary

accuracy (sec. 3.1.4 and sec. 5.2.5). Studies show [32], that for the current DSSC ASIC generation (F1 prototype) an accuracy of 10% in the binning determination can be expected. In fig. 5.16 the statistical uncertainty of the noise determination using the error function method is compared for different test cases of binning manipulation, in order to simulate this uncertainty. Increasing intensities of intrinsic DNL, that are $\sigma_{\mathrm{DNL}} = 0.1\,\mathrm{LSB}$, $0.2\,\mathrm{LSB}$ and $0.3\,\mathrm{LSB}$, have been analyzed with:

- Ideally known binning.

- Ignored binning information, i.e. assumed to be "ideal", equidistant binning.

- Artificially blurred binning with $\sigma_{\mathrm{blur}} = 0.05\,\mathrm{LSB}$ and $0.1\,\mathrm{LSB}$, corresponding to the situation of an uncertainty in the determination of the binning of 5% respectively 10% of a standard ADC bin width.

The study has been performed on simulated dark frame datasets comprising a full jk-grid of 100 pixels, configured for a later calibration of the system gain (sec. 5.3) to 1 keV/LSB (left panel), and to a system gain of 0.5 keV/LSB (right panel). These jk-grids cover system gain ranges of about 1.7 keV/LSB up to 0.5 keV/LSB (respectively 0.8 keV/LSB up to 0.25 keV/LSB). This leads to noise values from approximately 0.1 LSB up to about 0.35 LSB (respectively 0.2 LSB to 0.8 LSB). The plots show the standard deviation of the distribution of the relative residuals to the simulated peak width:

- It is evident that the best results can be achieved with ideally known binning.

- As expected, the 0.5 keV/LSB grids (right panel) lead to a more accurate determination of the noise value (note the different scale on the ordinate). This is due to the better determination of the pixel delay steps. This analysis step, that relies on the individual fit results for the noise peak positions, profits from the peaks being broader in relation to the binning.

- For the 1 keV/LSB jk-grids and $\sigma_{\mathrm{DNL}} = 0.1\,\mathrm{LSB}$ (green), ignoring the binning information and assuming ideal (equidistant) binning results in a statistical uncertainty similar to what can be achieved, when the binning can be determined with an uncertainty of 5% of the nominal bin-width. The statistical uncertainty increases, when the binning can only be determined with a higher uncertainty of 10%. A similar result was achieved for the 0.5 keV/LSB jk-grids.

- For $\sigma_{\mathrm{DNL}} = 0.2\,\mathrm{LSB}$ (blue), the best results can be achieved when the binning can be determined with 5% accuracy. For a 1 keV/LSB system gain configuration the results for ignored binning information and binning determined with 10% accuracy are "on par". For the 0.5 keV/LSB jk-grid the result leads to the conclusion, that it is better to assume ideal bin boundaries, when the binning can not be determined with a better accuracy than 10%.

- For $\sigma_{\mathrm{DNL}} = 0.3\,\mathrm{LSB}$ (red) and the 1 keV/LSB jk-grid configuration, determining the ADC binning leads to an improvement of the statistical uncertainty for both binnings

determined with 5% respectively 10%. For the broader noise peaks in the 0.5 keV/LSB jk-grid configuration, the binning determination is not profitable regarding the noise determination accuracy, when it can not be done with an accuracy better than 10% of a bin-width.

For either of the results, the systematic uncertainty (not shown) generally does not exceed 1‰.

5.2.7 Comparison of methods: Offset calibration

An initial determination of the offset positions in a dark frame jk-grid can either be given by the individual fits (sec. 5.2.1) or by the simultaneous fit method (sec. 5.2.3). After this initial determination, the pixel delay step sizes can be calculated, as described in sec. 5.2.4. More detail on the pixel delay step averaging will be given in sec. 5.2.9.
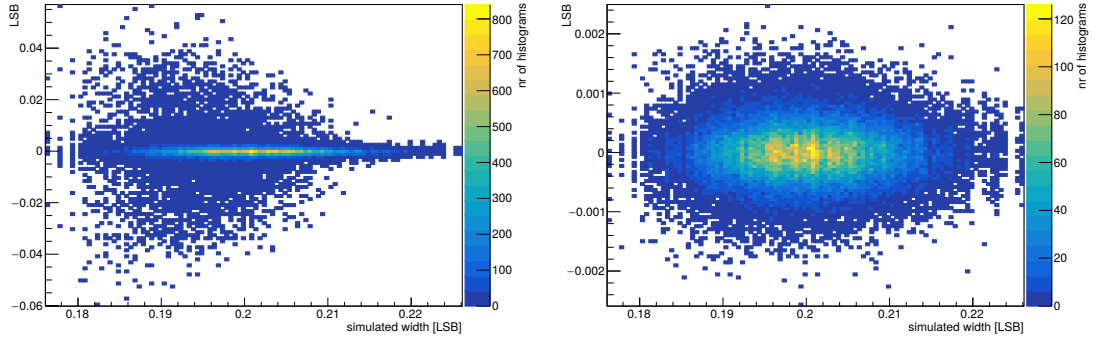
Figure 5.17: Comparison of the absolute residual of all position results of a k-grid simulated on a DSSC ASIC ($K \cdot N_{\mathrm{pix}} = 16 \cdot 4096 = 65536$ individual histograms with 10^6 dark frames each), plotted as a function of the simulated peak width. Left: Individual fits. Right: Simultaneous fit method.
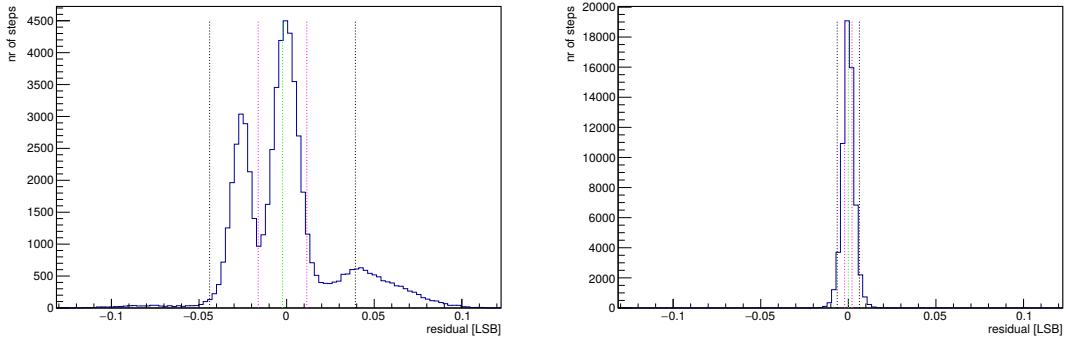
Figure 5.18: Absolute residual of the determined pixel delay steps of a k grid with 16 pixel delay steps simulated on a DSSC ASIC with $64 \cdot 64 = 4096$ pixels. Individual histograms had been simulated with an approximate noise of 0.2 LSB. Left: Pixel delay steps from individual fits. Right: Pixel delay steps from simultaneous fit method. Each distribution contains $(K - 1) \cdot N_{\mathrm{pix}} = 15 \cdot 4096 = 616440$ individual pixel delay steps.

One measure for the accuracy of the offset determination is the absolute residual to the simulated peak position. When the binning information is not altered, this measure assesses the deviance caused solely by the fit method. An example of the absolute residual is given in fig. 5.17, where the individual fit method and the simultaneous fit method are compared using a dataset with ideally known binning. In this case, the individual fits (left) generate more outliers than the simultaneous fit method (right), leading to a standard deviation that is higher by approximately

one order of magnitude. Calculating the pixel delay steps from the position information of these two datasets, the clear advantage of the simultaneous fit method over the individual histogram fits in this specific case can be identified, as is illustrated in fig. 5.18.
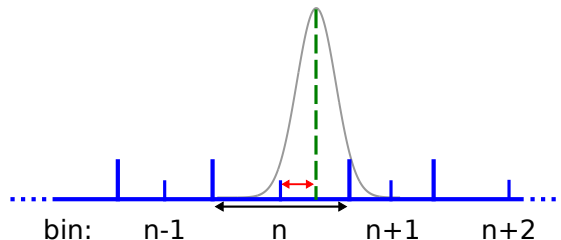
Figure 5.19: The relative bin-wise offset of a position (green) is determined based on the underlying binning information (blue). The distance (red) to the bin center (small blue mark) is divided by the bin-width (black), which is the distance between the lower and the upper bin-boundary (large blue marks).

If the binning information is altered (and therefore erroneous, see sec. 5.2.5), the absolute residual to the simulated peak position also includes any offset caused by the binning itself, as the simulated peak position is defined in relation to the simulated binning. If, for example, the bins below the center of the sample distribution are systematically smaller than the actual, simulated bins (as in fig. 5.7, (b) up to bin number 124), this integrated non-linearity (INL) would cause an additional, negative residual of the determined to the simulated peak position. One goal of the DSSC calibration procedure (ch. 3.3.1) is to place the position of the noise peak on the center of an ADC bin. It is therefore necessary to assess the uncertainty of the position determination method in regards to this requirement, irregardless of the binning. This measure, the so-called "offset residual", is the difference between the relative bin-wise offset (fig. 5.19) of the determined position and the relative bin-wise offset of the simulated peak position:

$$\text{offs}_{\text{res}} = \text{rel.offs}_{\text{bin-wise, det.}} - \text{rel.offs}_{\text{bin-wise, sim.}} \tag{5.14}$$

measured in percent of LSB. Based on this measure, the accuracy and stability of the methods can be compared.

Examples of this comparison can be found in figs. 5.20 and 5.21. The former shows, as already evident for the noise determination, the advantage of a higher number of dark frames. In the latter, the stability of the individual fit method is compared to the simultaneous fit method for different DNL situations. The plots in 5.21 use the median and the median absolute deviation as a measure of comparison, which is more robust against the increasing number of outliers for datasets with higher DNL. As long as the binning is known, the performance of the simultaneous fit excels the individual fit method, which can be seen in (a) and (b). The systematic uncertainty of both methods is on par for "blurred" binning (c), whereas the statistical uncertainty of the simultaneous fit method for blurred (d) respectively ignored (f) binning information shows a clear disadvantage in comparison to the individual fits. This disadvantage is also evident (e) for the systematic uncertainty for datasets with ignored DNL.

The individual fits outperform the more complex simultaneous fit method whenever the binned

data is subject to "wrong" binning, i.e. either blurred or ignored binning information. A reason for this is likely its inflexibility due to the common peak width σ (eq. 5.10) for all pixel delay series noise peaks. Although the individual fits cannot reach the accuracy of the simultaneous fit method regarding the determination of this common peak width (sec. 5.2.6), they seem to "override" the erroneous binning information by altering the width, which gives this method an advantage regarding the position determination.
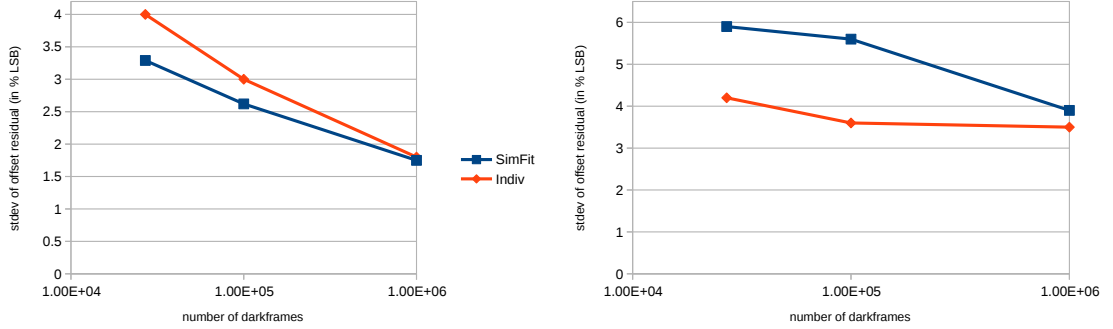
Figure 5.20: Comparison of the standard deviation of the distribution of the bin-wise "offset residuals" for simultaneous fit method (blue) and individual fits (red). The plots show the results for a k-grid simulated on a DSSC ASIC with $64 \cdot 64 = 4096$ pixels with a noise of approximately 0.2 LSB (left) and 0.1 LSB (right). For both noise levels, a higher number of dark frames improves the accuracy of the two compared methods.

A more detailed assessment of the performance of the individual fit method for offset characterization is given in fig. 5.22, where the offset residual for a full jk-grid of 100 pixels is compared for different binning scenarios. The left column depicts the 102400 individual results in form of a histogram, illustrating the innermost ($\pm$3MAD) of the distributions. In the right column, the results are plotted as a function of the simulated peak width. For ideal binning (fig. 5.22, upmost row), the offset characterization works best for simulated peaks not narrower than 0.2 LSB. For erroneous binning (fig. 5.22, all other rows), the offset residual distributions widen and more outliers show, with offset residuals of up to 100% of the bin width. These far outliers form, when the simulated true center of a peak is close to a bin boundary and the fit result for the position is in the adjacent bin. These outliers are insignificant, as they to not refer to peak positions close to the bin center (sec. 3.3.2).

The best pixel delay setting, or in short "k-value", is defined by the pixel delay series histogram with the peak position that is closest to the center of its respective bin. This value can both be identified for the peak positions determined by the fits as well as from the simulation truth, both based on their respective binning information: The possibly erroneous binning information that has been altered e.g. by blurring or has been falsely assumed to be ideal, and the simulated true binning respectively.

The residual of the pixel delay setting determined from the individual fits to the "optimal" setting given by the simulation truth is shown in fig. 5.23[4] for different binning environments.

---

[4]Figs. 5.23, 5.25 and 5.26 have been generated by assigning the selected "optimal" value resp. the resulting residual to all of the $k = 16$ histograms of the respective pixel delay series.
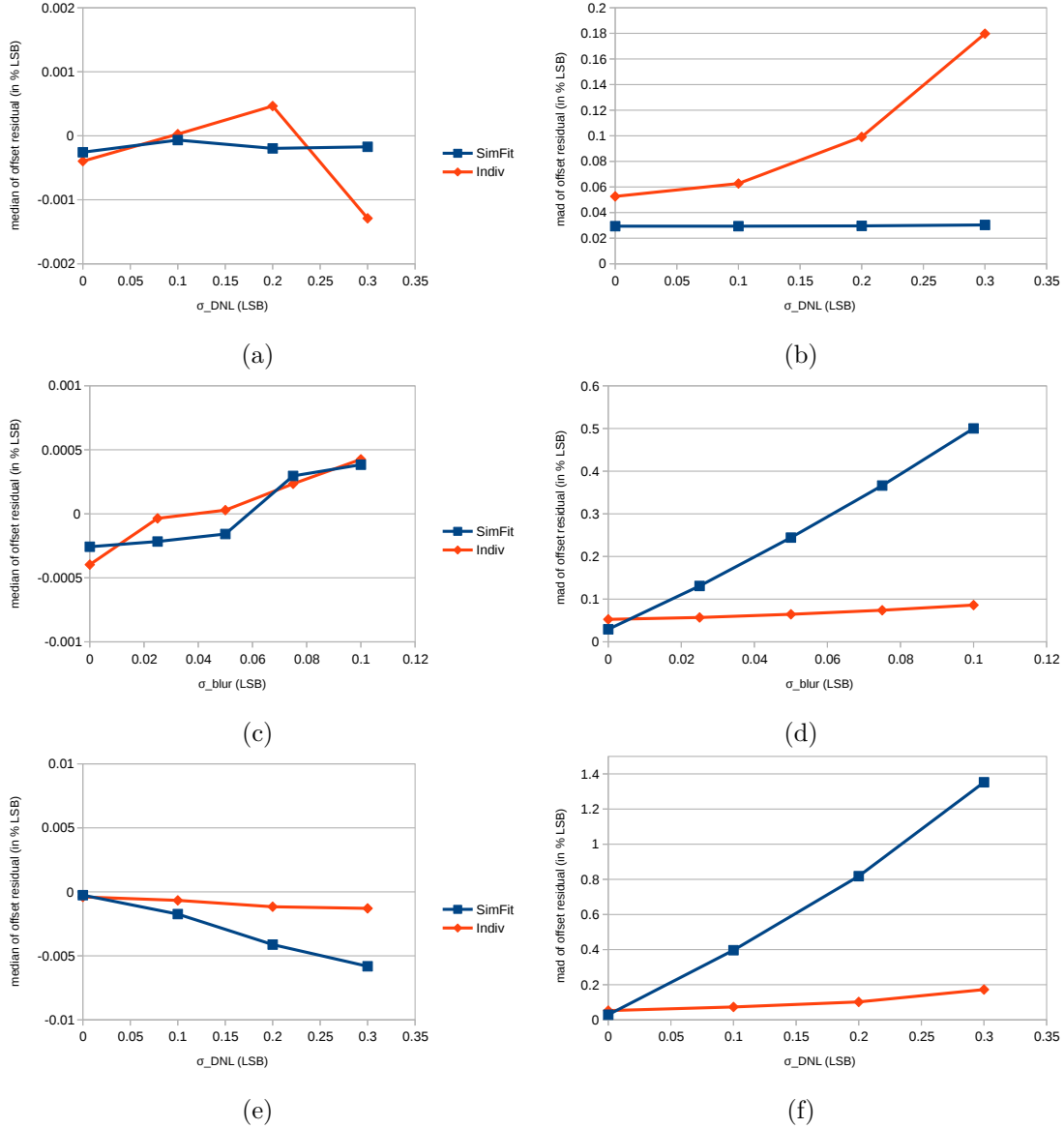
Figure 5.21: Systematic (left column) and statistical (right column) uncertainty of simultaneous fit method (blue) and individual histogram fitting (red) for different DNL situations:
(a) and (b): Ideally known DNL.
(c) and (d): Blurred binning information.
(e) and (f): Simulated DNL, ignored binning information.
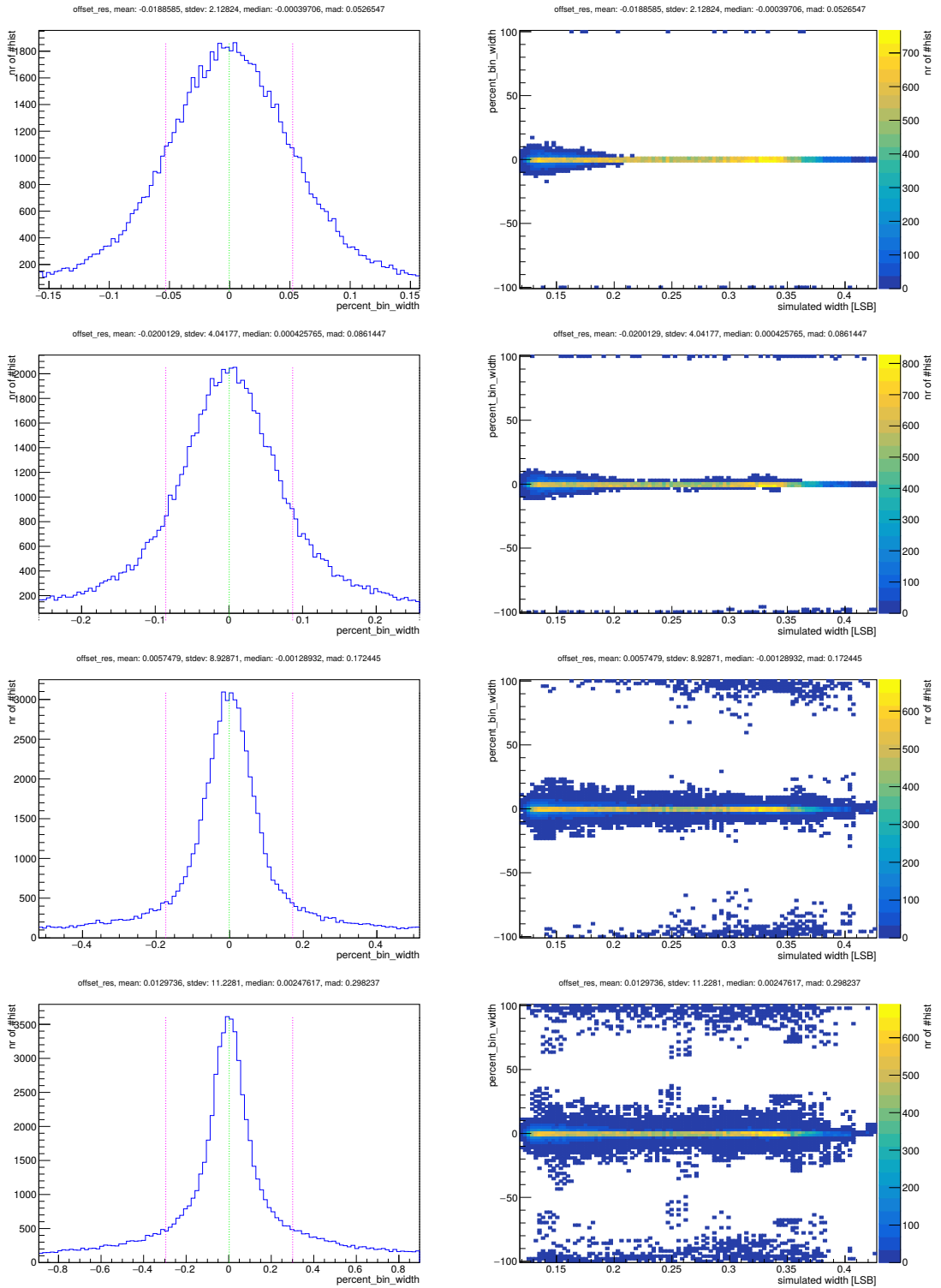Each data point is based on the analysis of a full jk-grid dataset of 100 pixels.

Figure 5.22: Offset residual results for a full jk-grid of 100 pixels. 10^6 dark frames have been simulated. The right column depicts the results as a function of the simulated width, the respective histograms are shown on the left.
First row: Ideal binning.
Second row: $\sigma_{\mathrm{blur}} = 0.1\,\mathrm{LSB}$.
Third row: $\sigma_{\mathrm{DNL}} = 0.3\,\mathrm{LSB}$. Binning ignored (ideal binning assumed).
Last row: $\sigma_{\mathrm{DNL}} = 0.3\,\mathrm{LSB}$. Binning known, but blurred with $\sigma_{\mathrm{blur}} = 0.1\,\mathrm{LSB}$.
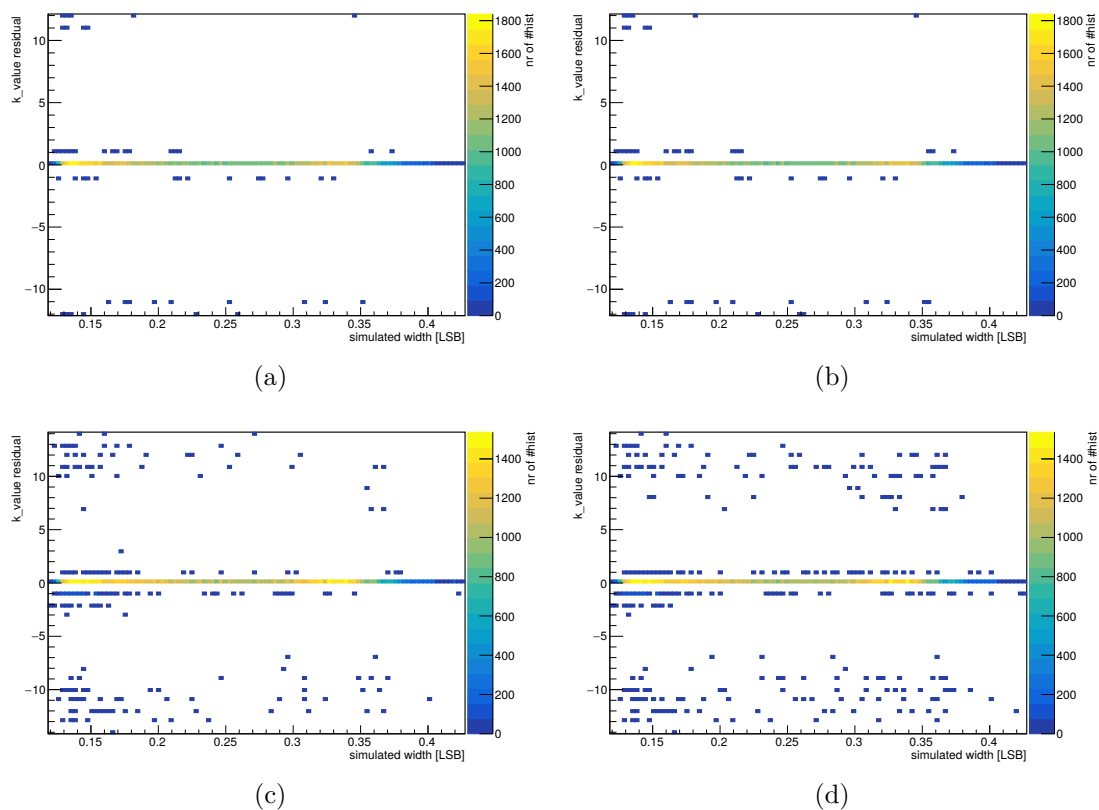
Figure 5.23: Offset characterization with individual fit method. Difference of chosen k-value to "ideal" k-value calculated from simulation truth.
(a) ideal binning.
(b) $\sigma_{\text{blur}} = 0.1\,\text{LSB}$.
(c) $\sigma_{\text{DNL}} = 0.3\,\text{LSB}$. Binning ignored (ideal binning assumed).
(d) $\sigma_{\text{DNL}} = 0.3\,\text{LSB}$. Binning known, but blurred with $\sigma_{\text{blur}} = 0.1\,\text{LSB}$.

73

The groups of far outliers showing a difference of more than five pixel delay steps to the optimal setting occur, when the selected pixel delay setting refers to a dark frame peak that is centered in an adjacent bin (fig. 5.24). As expected, the frequency of this effect increases for examples with higher intrinsic DNL as well as for increasingly erroneous binning information. As one goal of the calibration procedure (sec. 3.3.2) to center the offset of the DSSC pixel in an ADC bin – any bin – these outlier groups are of no major concern.
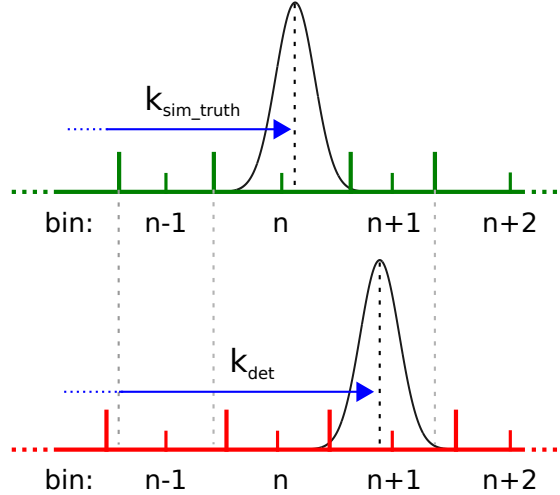
Figure 5.24: Due to erroneous binning information (red) and the limited accuracy of the peak determination method, the pixel delay series peak determined to be most centered can lie in a different bin than "optimal" peak given by the simulation truth. The calibration algorithm then determines a pixel delay setting (k_{det}) larger or smaller than the optimal "simulation truth" setting $k_{\text{sim\_truth}}$, with a typical residual of more than five pixel delay steps.

The highest achievable accuracy of the offset calibration is illustrated in fig. 5.25. The left plot shows the bin-wise offset to the respective bin center of the peak generated by the "optimal" setting given by the simulation truth for ideal binning. The data for a binning with a cyclic DNL with $\sigma_{\text{DNL}} = 0.3\,\text{LSB}$ is basis of the right plot. The accuracy is limited by the step size of the pixel delay setting. For increasing DNL, the occurring smaller bin widths cause larger bin-wise offsets (eq. 5.14), which is reflected in the outliers fig. 5.25 (b).

Substracting the bin-wise offset of the optimal setting given by the simulation truth from the bin-wise offset of the setting selected by the calibration algorithm assesses the total loss in accuracy, which is again illustrated for four extremal binning environments in fig. 5.26. Even for the most adverse conditions in this study, that are cyclic DNL with $\sigma_{\text{DNL}} = 0.3\,\text{LSB}$ and additional blurring with $\sigma_{\text{blur}} = 0.1\,\text{LSB}$, approximately 99% of the results show a loss in accuracy not greater than 3‰, with none exceeding 25% of a bin-width compared to the highest achievable offset calibration accuracy.

5.2.8 Error function based offset calibration

An additional determination of the offset positions in a jk-grid is a result of the error function method (sec. 5.2.2), based on the averaging of the pixel delay step sizes determined from the
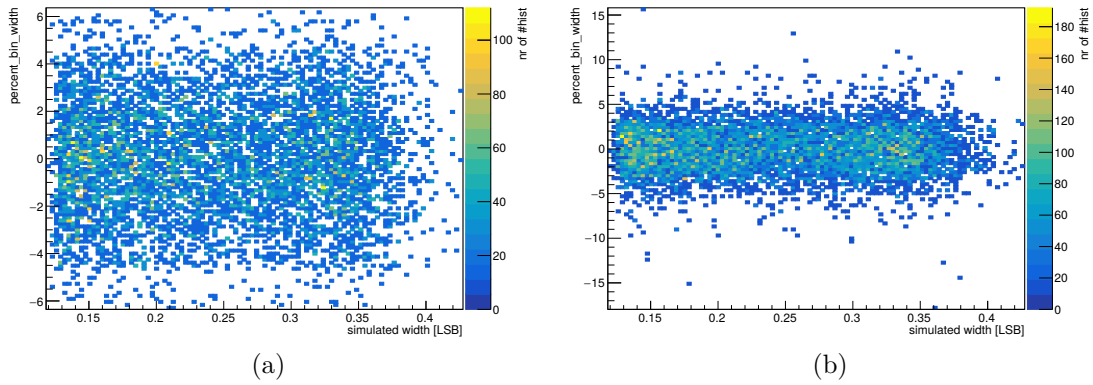
Figure 5.25: Highest achievable accuracy of the offset calibration given by the simulation truth of two different datasets of a full jk-grid for 100 pixels: Ideal binning (a) and cyclic DNL with $\sigma_{\mathrm{DNL}} = 0.3 \, \mathrm{LSB}$ (b).
left: $\sigma = 2.4 \, \%$ LSB, MAD $= 1.66 \, \%$ LSB
right: $\sigma = 2.6 \, \%$ LSB, MAD $= 1.73 \, \%$ LSB
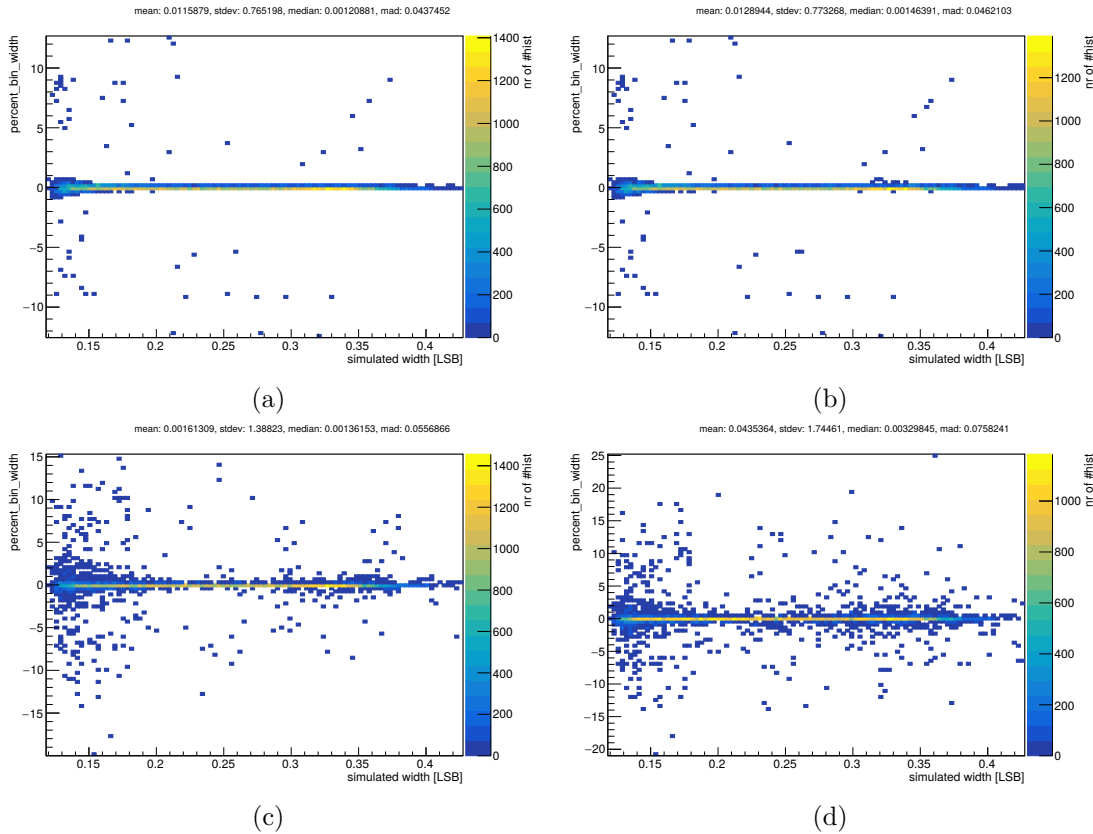
Figure 5.26: Offset characterization with individual fit method. Residual of bin-wise offset of selected pixel-delay setting to the respective optimal setting from the simulation truth.
(a) ideal binning.
(b) $\sigma_{\mathrm{blur}} = 0.1 \, \mathrm{LSB}$.
(c) $\sigma_{\mathrm{DNL}} = 0.3 \, \mathrm{LSB}$. Binning ignored (ideal binning assumed).
(d) $\sigma_{\mathrm{DNL}} = 0.3 \, \mathrm{LSB}$. Binning known, but blurred with $\sigma_{\mathrm{blur}} = 0.1 \, \mathrm{LSB}$.

75

individual fits. As the free fit parameter x_0 in eq. 5.3 is the distance of the threshold bin boundary to the center of the noise peak in the first histogram of the pixel delay series, the other noise peak positions can be calculated using the pixel delay step sizes. For the three most extremal cases of binning environments from the comparison in fig. 5.21, a detailed depiction of the offset residual of the simultaneous fit method and the error function method can be found in the appendix in figs. B.1 to B.3. Whereas for ideal binning information the error function method performs on par with the other methods, it quickly becomes evident that for erroneous binning information its results can not reach the accuracy of neither simultaneous nor individual fit method – even, when it is given the "perfect" pixel-delay step size information from the simulation truth (last row of the plots). Similar to the simultaneous fit method used for offset determination, the reason for the low robustness of this method against erroneous binning information lies in its stiffness that is based on the fixed offset shift between the individual peaks.

5.2.9   Improvement of pixel delay step averaging

<div align="center">(a)   (b)</div>
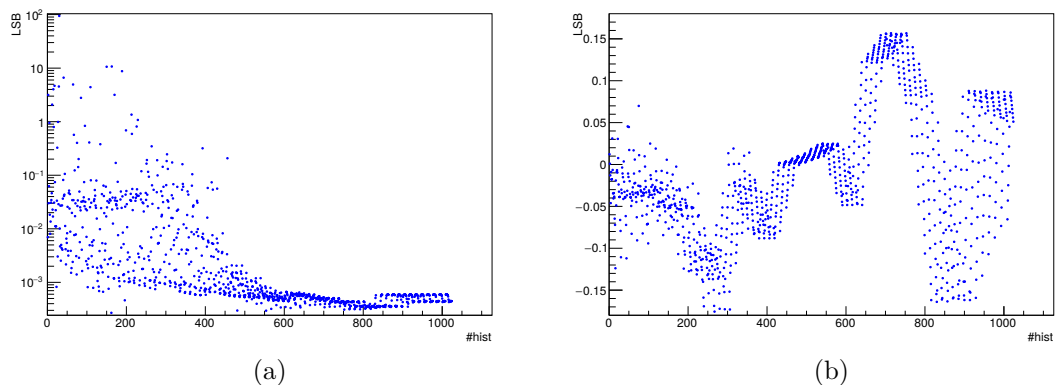
Figure 5.27: Left: Fit error of positions of one pixel in a complete jk-grid. The dataset is identical to fig. 5.5, but in this case, the binning was blurred with $\sigma_{\text{blur}} = 0.1\,\text{LSB}$ (as in fig. 5.7, (a)). Right: Absolute residual of the respective fit results relative to the simulation truth.

As the error function method depends heavily on the accuracy of the determination of the pixel delay steps (sec. 5.2.4), significant improvements in the noise determination could be achieved after a comparison of the different averaging methods for the pixel delay step determination. At first, weighted averaging was assumed to provide the most stable results due to its supposed robustness against data outliers. A comparison with the median and simple arithmetic averaging did prove the contrary.

Although a difference in the performance can already be observed for ideally known binning, the choice of the averaging method becomes even more crucial for erroneous binning information. Figs. B.4 and B.5 in the appendix of this document show a comparison of the individual averaging methods by means of the determined pixel delay steps (left column) and the noise determination results of the error function method (right column). Fig. B.4 shows an originally ideal binning, blurred with $\sigma_{\text{blur}} = 0.1\,\text{LSB}$ (fig. 5.7, (a)), fig. B.5 an ADC with a simulated, cyclic DNL of $\sigma_{\text{DNL}} = 0.1\,\text{LSB}$ of the bin width, additionally blurred by $\sigma_{\text{blur}} = 0.1\,\text{LSB}$ (fig. 5.7, (g)).

A close study of the low outliers in the sub-plots (a) and (b) of both figs. B.4 and B.5, that show the results of the weighted mean based pixel delay step determination, could trace the their origin back to individual pixels of the simulated datasets. In those pixels, specific binning conditions caused individual position fit results of the jk-grid to have exceptionally low fit error values, over-pronouncing them in the pixel delay step determination due to their higher weighting in the weighted average. Fig. 5.27 illustrates, that in this case the accuracy of the fit result in relation to the simulation truth can not be reliably assessed by the fit error.[5].

A comparison between the median and the simple arithmetic mean for computing the pixel delay steps can also be found in figs. B.4 and B.5. Using the mean has an advantage over the median, measured by the significantly smaller standard deviation of the relative residuals.

5.2.10 Summary

Three different methods for characterizing noise and offset (i.e. standard deviation and position) of noise peak (i.e. dark frame) distributions in a DSSC jk-grid have been compared. All three methods have been tested in various simulated environments. For ideally known ADC binning, they show no significant systematic uncertainties. As expected, the statistical uncertainty of all methods can be improved with a higher number of dark frames. It was shown that the desired accuracy can be achieved with a number of 10^6 dark frames. Due to the high sampling rate of the DSSC (sec. 2.3), the measurement time of this calibration step is unproblematic. For the data processing the raw data (i.e. each individual sample) can be compressed by categorizing (histogram representation, see also sec. 5.1 for estimations on the process time).

For the noise characterization, the error function method shows the best robustness against effects of the ADC DNL, low statistics and noise peaks that are narrow in comparison to the bin widths. The simultaneous fit method described in sec. 5.2.3 has advantages regarding its accuracy in situations with wide peaks (σ at least 0.2 LSB), as long as the ADC binning is determined well enough. It has to be noted though that this method exceeds the computation time of the error function method roughly by a factor of 10. This is due to the computationally costly focus of the method on the binned likelihood fit of the composite peak function (eq. 5.10), that includes an integration over the k (usually 16) narrow Gaussian peaks in each minimization step of the $k + 1$ free parameters. In contrast, the error function method only depends on a χ^2-fit of a relatively simple function (eq. 5.3) of only 2 free parameters, with no integration needed.

The offset can be determined either with the individual fits or with the simultaneous fit method. An addional – yet, due to its low accuracy, neglebile – determination of the offset is a result of the error function method (sec. 5.2.8). The most robust and accurate results in determining the offsets and calibrating the best pixel delay value in a jk-grid can be achieved with individual likelihood-fits to all grid histograms.

---

[5]using the standard error output from Minuit[51]

5.3 Calibration of the detector gain using X-ray line sources

As proposed in sec. 3.3.2, the system system offset (or pedestal) and noise as well as the system gain in the linear region of the NLSR are determined in the first step of the calibration of the DSSC. The gain calibration is based upon fitting calibration line spectra recorded with the individual pixels of the DSSC detector. First, a series of spectra is recorded by varying the ADC gain with help of the I_{ramp}-setting. After determining the system gain of each spectrum with help of a pre-defined fit function (sec. 5.3.1), the best setting can be selected.

For the technique described in this section, the system is assumed to provide a linear system response in the lower region of the dynamic range of the detector, i.e. a linear dependence between the number of incident photons respectively the incident amount of energy and the digital output. If this were not the case, the non-linearity in the spectral response would have to be characterized before the gain calibration in order to be taken into account in the fit algorithm. All calibration measurements with DSSC prototypes and DSSC prototype sensors[6] so far show, in first order, a linear system response for low energies. A closer investigation of the detector linearity will be conducted once prototypes closer to the final detector system are available.

The system offset and noise (in units of LSB) can be determined with dark frames (sec. 5.2). After a successful determination of the system gain, the system noise can then be given in units of "equivalent noise charge" (ENC). As the ADC gain setting also influences the system offset (sec. 3.1 and 3.2.2), the default measurement for the offset and noise characterization is a complete jk-grid.

As this study is focused on the evaluation of the accuracy of the gain determination method, only full jk-grids that comprise a broad range of system offset and gain configurations have been analyzed here. The study will conclude in an assessment of the achievable accuracy of the proposed method, together with a comparison of the influence of different test environments (sec. 5.2.5) of ADC binning. The actual calibration of the gain of a real detector system – i.e. the selection of the correct gain setting – is trivial, as long as the accuracy of the gain determination is better (smaller) than half the granularity of the setting.

As sec. 5.2, this section will first present the applied method and then assess the achievable accuracy and stability based on analyses performed on simulated datasets.

5.3.1 The fit-based approach for system gain determination

The initial gain characterization of the DSSC is based on determining the position of characteristic X-ray lines in the output spectra of individual pixels. The inherently poor ADC resolution of the DSSC detector (sec. 3.1) due to its 8-bit read-out ADC combined with requirements regarding the dynamic range (sec. 3.3.1) makes this task challenging. The following reasons motivate the development of a DSSC-specific approach for the gain characterization based on fitting the DSSC calibration line spectra with a custom, parameterized and global fit function:

- When calibrating with calibration line sources not synchronized to the read-out cycle of the DSSC, photon events taking place shortly before the end of the signal flat top (sec. 3.1

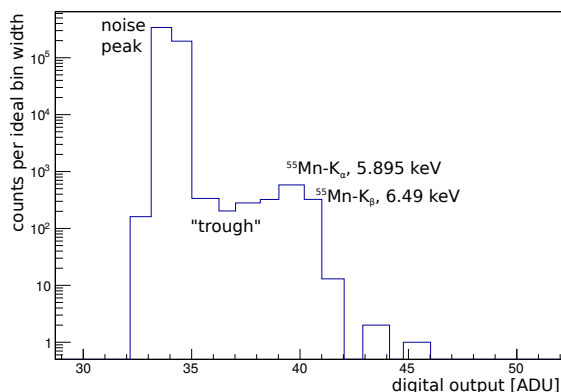[6]i.e. DSSC DEPFET sensor chips measured on the SPIX (sec. 3.4.1) sensor characterisation test bench

Figure 5.28: A typical calibration line spectrum recorded with a DSSC prototype that has been irradiated with ^{55}Fe, a standard X-ray source. The two characteristic line energies of the daughter nuclide ^{55}Mn are annotated in the plot. The given K_α line energy is calculated as the weighted mean of the two characteristic K_α lines of ^{55}Mn (for details, see sec. 5.3.4).
The binning information, the so-called DNL of the ADC, has been taken into account by scaling the bin entries according to their respective bin-widths. This reflects the respective individual probability for counts in the bins due to the differently sized ADC steps (sec. 3.1.4).

and 4.1) generate signal charges that can not be collected and digitized completely. These so-called "out-of-time" events "smear" the calibration line towards its low-energy side and thereby contributes to the trough. For most of the time during the development phase of the DSSC detector, no synchronized calibration sources were available.

- Mainly due to charge sharing between pixels, so-called "split pixel events", spectra recorded with DSSC pixels show a so-called low-energy "trough" between the calibration lines and the pedestal, which is illustrated in fig. 5.28. This trough impedes the determination of the calibration line positions. The desired accuracy of the gain determination is given by the granularity of the gain setting (sec. 3.1), which is about 2%. It has been shown [35], that fitting these spectra with pure Gaussians can lead to errors on the order of 10% of the actual system gain. In conclusion, fitting with pure Gaussians does not yield sufficient accuracy for the calibration.

- Certain characteristics of DSSC calibration spectra severely impede common techniques used for conventional, multi-pixel X-ray detectors such as split event filtering or recombination. Studies of these techniques can be found in [53], [22] and [54]. One possible approach applied successfully for the gain calibration of X-ray detectors used in astronomy [55], is to consider only "single events" for the calibration, i.e. events that are not subject to charge sharing.

  As the width of a DSSC bin corresponds to a relatively large fraction of the photon energy due to the poor ADC resolution, this approach would lead to well pronounced "false single events", as is explained in more detail in fig. 5.29. Also, at the start of the calibration routine, measurements results show a variation of the energy gain of individual DSSC pixels in the order of 10% (sec. 6.1), even after applying internal detector trimming techniques. This additionally impedes the effectiveness of signal thresholds for single events, as the

threshold energy is not well defined.

- During a significant part of the development of the DSSC detector, prototypes available for calibration studies only provided single-pixel read-out functionality, which excludes any techniques relying on the information gathered in neighboring pixels.

- The DNL of the DSSC ADC is non-negligible in comparison to the calibration accuracy (sec. 3.1). The method for the gain calibration therefore has to be robust against binning effects, in particular overly large or small bins that lie between the noise peak and the calibration lines.

As the calibration of the DSSC must be performed under XFEL beam conditions (sec. 3.3.2), providing only spectra with poor (8-bit) ADC resolution, the strategy for determining the system gain in these DSSC calibration line spectra is as follows:

1. Use a DSSC sensor pixel spectrum with high ADC resolution (e.g. 14-bit SPIX spectrum) in order to characterize the shape of the spectral response to a specific calibration line source (e.g. ^{55}Fe, ^{109}Cd, Roentgen tube with metal filter). The shape is determined by fitting the measured high-resolution spectrum with a global fit function proposed in the following section 5.3.2.

2. By defining a certain set of fit parameters this shape can be "fixed", so that the ratio of the calibration line peaks to the trough and the salient trough features (smoothness, asymmetry) are conserved.

3. With only a low number of free fit parameters, the global shape can then be fitted to the spectra with poor ADC resolution in order to determine the gain, or also the offset and noise (sec. 5.3.3) if desired. Thereby, the information about the spectral response gathered in step 1. is used to improve the accuracy and stability of these analyzes.

This approach is based on the idea that the spectral response of the DSSC sensor pixels, mainly dominated by charge sharing, is identical for different forms of signal processing, regardless of e.g. ADC resolution and DNL and depends only on the sensor biasing. The differences in the signal read-out (filtering, sequencing, digitization) of spectra with high ADC resolution and the 8-bit spectra used for the gain calibration can nevertheless cause variations in the electronic noise and, for radioactive calibration line sources, also the portion of out-of-time events (compare sec. 4.1) contributing to the trough. Thereby also the ratio of counts in the trough in comparison to the calibration line(s) changes. The parameterization of the global fit function provides additional flexibility that can be applied after the initial spectral response shape has been fixed, in order to improve the fit results (sec. 5.3.3).

5.3.2 A parameterized fit function for the spectral response of single pixels

Extending the findings in [35], a continuous fit function for the typical spectra measured with DSSC pixels has been developed [56] [57], basing on shapes presented in [58]. The proposed fit
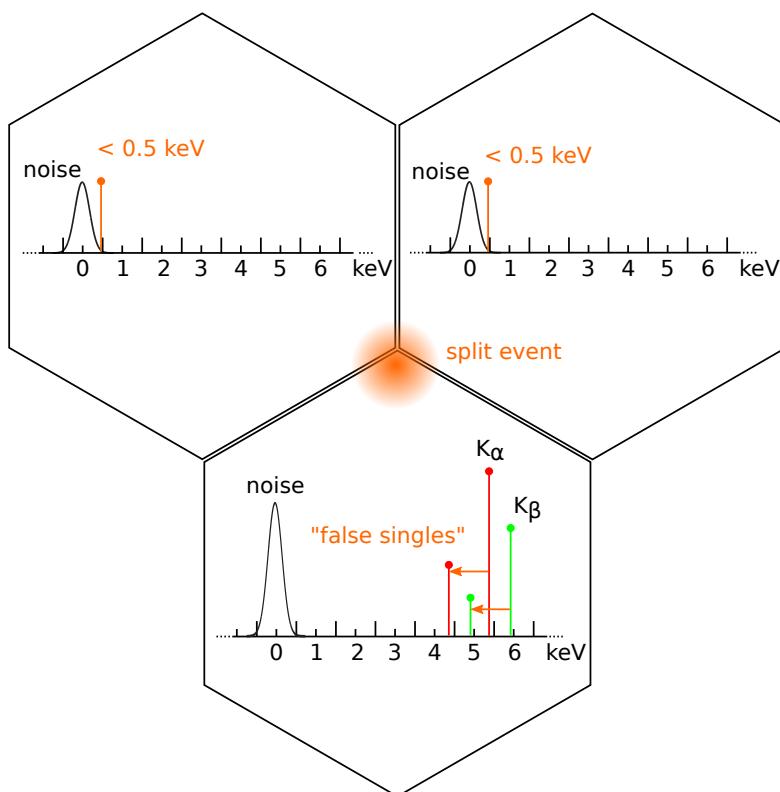
Figure 5.29: Considered is a cluster of three hexagonal pixels of the DSSC detector that are already configured in an ideal offset and gain calibration, in this case for photon counting with a pixel gain of 1 keV/ADU. In this example, a gain calibration is performed with ^{55}Fe as a calibration line source. The emission is dominated by K_α photons at approximately 5,9 keV (red), followed by K_β photons at about 6,5 keV (green).

Setting a threshold for single events is dictated by the granularity of the ADC resolution. The smallest increment discerning measured signal from the electronic noise background is $1 \text{ ADU} \equiv 1 \text{ keV}$, which is set as a threshold value: Measured signals are only considered, if all surrounding pixels show no counts above the noise bin.

Using this "single event" condition, a calibration spectrum is recorded for the lower pixel. If now a split event occurs due to charge sharing between the three pixels, signal charge that corresponds to a photon energy of up to < 1 keV can be collected in the neighboring (upper) pixels without violating the condition. The resulting "false single events" in the lower pixel would lead to a prominent shoulder in bin 4 and 5 of the calibration spectrum which would have to be considered in the fit-based gain determination.

It is evident that using single-event filtering would be even more problematic for the real, still uncalibrated detector – even more so due to different bin-widths caused by the DNL of the ADC.

function is an analytical model for the shape of a typical calibration line spectrum for single detector pixels (see again fig. 5.28). The focus of this approach lies on the determination of gain, offset and noise and not on a detailed, physical description of the spectral response. A central objective is also ease of usage and stability of the fit in various environments such as low ADC resolution and non-ideal ADC-binning.

The global fit function comprises the noise peak and an arbitrary number of calibration lines. In addition, it provides features modeling the signal-related, so-called "trough" between the calibration lines and the noise peak. The components of the fit function describing the trough include scaling parameters that determine the ratio to their respective calibration lines. All features of the fit function are normalized, so that the areas underneath the individual components can be compared with the help of their respective scaling parameters. The fit function with its parameterized components is meant to be fitted globally in "one go" to the spectrum, either determining all parameters at once or an arbitrary subset of parameters.
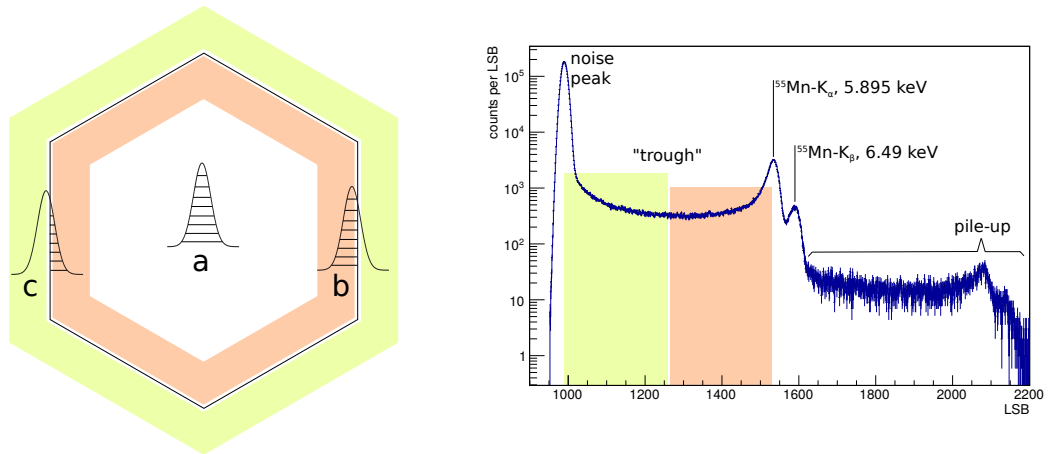
Figure 5.30: Left: Simplified, qualitative illustration of split events (b and c) and completely collected charges (a) on a hexagonal pixel.
Right: ^{55}Fe spectrum measured with a hexagonal DSSC (DEPFET) pixel on a dedicated sensor test bench.

The shape of the trough in typical DSSC pixel spectra is asymmetric, featuring lower count rates near the calibration lines and higher count rates approaching the noise peak. This is related to the generation of signal charges in the detector (sec. 3.1). Fig. 5.30 gives a simplified, qualitative explanation for this relation. There, the signal charge clouds are visualized as Gaussian distributions. The hatched areas underneath the Gaussian distributions symbolize charge collected in the pixel readout node. Charge sharing occurs in the colored regions. The width of these regions is related to the signal charge cloud size. Depending on where the charge cloud is generated, different portions of the signal charge will be collected in the pixel:

- Photons hitting the detector pixel with enough distance to the pixel boundary do not suffer from charge sharing (a).

- Photons incident on the detector close to the pixel boundary (red), but still inside the pixel

(b) will lead to less than 100%, but more than 50%, of the signal charge being collected in the read out node.

- Events outside of the pixel (green area) will result in less than 50% of the signal charge being collected in the pixel (c).

It is geometrically evident, that the green area is larger than the red area. For homogeneous irradiation, the probability for events in the green area that deposit less than 50% of the charge in the considered pixel is therefore higher than for events in the red area. The fit function models both the high-energy side of the trough close to the calibration lines as well as its low-energy counterpart underneath the noise.
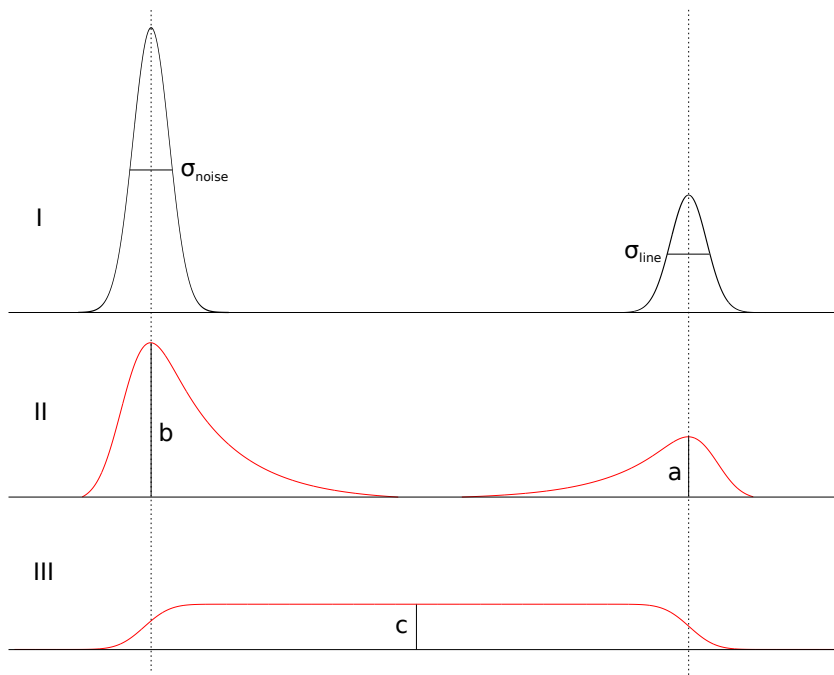
Figure 5.31: Individual components of the global fit function. Noise peak and calibration line peak are modeled as Gaussians (I) with individual widths. The two "tail" components (II) provide an exponential decay towards the middle of the trough. An additional "shelf" (III) completes the model for the trough.

A schematic illustration of the composition of the fit function for a single calibration line can be found in fig. 5.31. The trough model for each calibration line (I, right) consists of the so-called "tail" (II) and the "shelf" (III). The tail components are exponential functions folded with Gaussians with the same standard deviation σ_{line} as the calibration line, using the shape introduced in [58]. The shelf is constructed out of normal cumulative distribution functions. The smoothness of their edges is also defined by σ_{line}. The scaling of the tail component underneath the calibration line (a) and underneath the noise peak (b) and of the shelf component (c) are given for illustration. Eq. 5.15 to 5.21 give the definition of the individual components of the fit function $F_{\text{global}}(x)$, as they were published in [57]:

- Eq. 5.15: The global fit function is a combination of the noise peak $F_{\mathrm{noise}}(x)$ and an arbitrary number of calibration lines $F_{\mathrm{i,line}}(x)$.

- Eq. 5.16: The noise peak is assumed to be of Gaussian shape with standard deviation σ_{noise} and position x_{noise}. The area underneath the noise peak is given by N_{noise}.

- Eq. 5.17: Each calibration line is defined as a combination of Gaussian peak, high-energy and low-energy tail feature and a shelf component, the latter composing the trough.

- Eq. 5.18: The calibration line peak of line i is assumed to be a Gaussian with standard deviation σ_i and position x_i. The area underneath the calibration line peak is given by N_i.

- Eq. 5.19: An exponentially decaying function folded with a Gaussian of standard deviation σ_i models the high-energy tail feature. It is positioned at x_i. The steepness of its decay is given by β_t. The area underneath this feature is given as a ratio to the calibration line peak with N_t. The normalization of this component is given in the appendix in sec. A.4.

- Eq. 5.20 defines a mirrored duplicate of the high energy tail underneath the noise peak. Its ratio to the high-energy tail is given by S_{tnoise}. With α_t, an additional asymmetry for the shape of the tail underneath the noise peak in comparison to the calibration line tail can be achieved. $\alpha_t > 1$ leads to a tail that decays faster, $\alpha_t < 1$ lets the tail decay on a longer scale.

- Eq. 5.21 models the shelf. The "smoothness" of the slopes underneath the calibration line at position x_i and underneath the noise peak at position x_{noise} is given by σ_i. The area underneath the shelf is given as a ratio to the calibration line peak with N_s. The normalization of the shelf is motivated geometrically, by the definition of the error function.

All individual components are differentiable, therefore their sum is also differentiable [59]. Each component is either zero or asymptotically approaches zero for $x \to \pm\infty$. This ensures, that fitting the function is unproblematic: There are no singularities or "kinks", that could impede e.g. the numerical integration over the fit function. Also, the fit range can be defined freely. A summary of all parameters can be found in table 5.1.

$$F_{\text{global}}(x) = F_{\text{noise}}(x) + \sum_i F_{\text{i,line}}(x) \tag{5.15}$$

$$F_{\text{noise}}(x) = \frac{N_{\text{noise}}}{\sigma_{\text{noise}}\sqrt{2\pi}}\ e^{-\frac{1}{2}\left(\frac{x - x_{\text{noise}}}{\sigma_{\text{noise}}}\right)^2} \tag{5.16}$$

$$F_{\text{i,line}}(x) = F_{\text{i,peak}}(x) + F_{\text{i,tail\_high}}(x) + F_{\text{i,tail\_low}}(x) + F_{\text{i,shelf}}(x) \tag{5.17}$$

$$F_{\text{i,peak}}(x) = \frac{N_i}{\sigma_i\sqrt{2\pi}}\ e^{-\frac{1}{2}\left(\frac{x - x_i}{\sigma_i}\right)^2} \tag{5.18}$$

$$F_{\text{i,tail\_high}}(x) = \frac{N_t\ N_i}{\beta_t e^{-\left(\frac{\sigma_i}{2\beta_t}\right)^2}}\ \frac{1}{2} e^{\frac{x - x_i}{\beta_t}} \operatorname{erfc}\left(\frac{x - x_i}{\sigma_i} + \frac{\sigma_i}{2\beta_t}\right) \tag{5.19}$$

$$F_{\text{i,tail\_low}}(x) = S_{\text{tnoise}}\ \frac{N_t\ N_i}{\alpha_t\beta_t e^{-\left(\frac{\sigma_i}{2\alpha_t\beta_t}\right)^2}}\ e^{\frac{-(x - x_{\text{noise}})}{\alpha_t\beta_t}}\ \frac{1}{2}\operatorname{erfc}\left(\frac{-(x - x_{\text{noise}})}{\sigma_i} + \frac{\sigma_i}{2\alpha_t\beta_t}\right) \tag{5.20}$$

$$F_{\text{i,shelf}}(x) = \frac{N_s\ N_i}{(x_i - x_{\text{noise}})}\ \frac{1}{2}\left(\operatorname{erfc}\left(\frac{x - x_i}{\sigma_i}\right) - \operatorname{erfc}\left(\frac{x - x_{\text{noise}}}{\sigma_i}\right)\right) \tag{5.21}$$

Symbol	Description
N_{noise}	area underneath the noise peak
x_{noise}	position of the noise peak
σ_{noise}	standard deviation of the noise peak
N_i	area underneath the calibration line peak
x_i	position of a calibration line peak
σ_i	standard deviation of a calibration line peak
N_t	relative factor for area underneath the peak tail
β_t	steepness of the peak tail
α_t	asymmetry of steepness of decay for tails underneath noise peak
S_{tnoise}	scale factor for the tail component underneath the noise peak
N_s	relative factor for area underneath the peak shelf

Table 5.1: Summary of the parameters of the global fit function.

As the shape of the trough in the calibration line spectra is dominated by effects related to charge collection in the detector pixel (sec. 3.1), the shape of the individual trough components also depends on the photon energy. As a simplification, parameters N_t, β_t, S_{tnoise} and N_s are assumed to be identical for all calibration lines of similar energy (about $\pm 4\,\text{keV}$). An example of a fit with the global fit function to experimental data is provided in fig. 5.32, illustrating again the composition of the trough and its individual components.

5.3.3 Application of the global fit function to spectra with poor ADC resolution

In order to simplify the application of the fit function for spectra with poor ADC resolution, a few modifications to the original equations (sec. 5.3.2, eq. 5.15 to 5.21) are applied:

1. As long as the electronic noise does not depend on the input signal level, the width of the
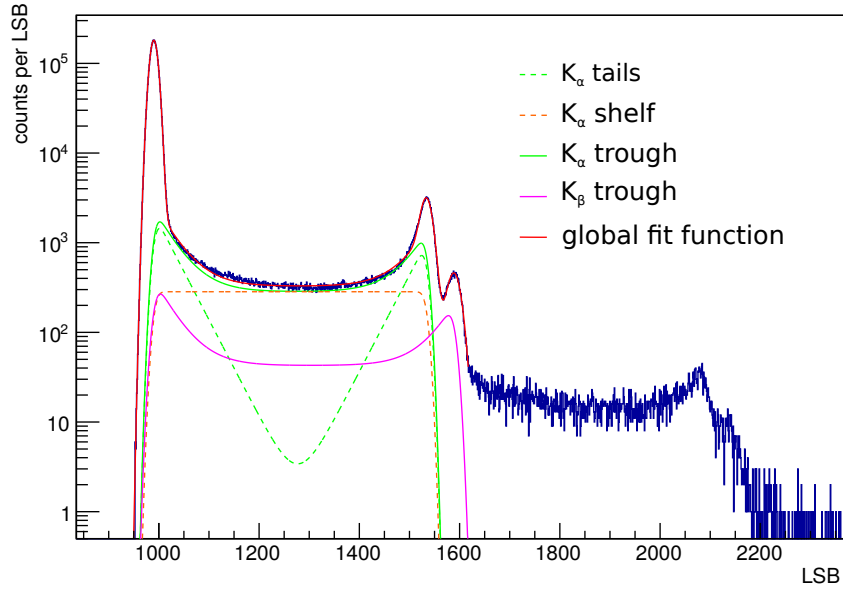
Figure 5.32: ^{55}Fe spectrum measured with a hexagonal DSSC (DEPFET) pixel on a dedicated sensor test bench (SPIX). The individual trough components of the fit function are illustrated in color coded lines. The Gaussian distributions for the noise peak and the calibration lines are not shown. The fit is performed only for the two prominent K-lines, the fit-range excludes the pile-up region. Published in [57].

calibration line peaks differ from the width of the electronic noise peak only in the presence of Fano noise. In order to implement this, the fit function needs to have the information about the mean number of signal electrons $N_{e,i}$ generated by each photon of the respective energy E_i. The width parameter of the respective calibration line can then be fixed to:

$$\sigma_i = \sqrt{\sigma_{\text{noise}}^2 + (F_{Si}\ N_{e,i})^2} \tag{5.22}$$

with

$$N_{e,i} = \frac{E_i}{E_{Si,e/h}} \tag{5.23}$$

and $F_{Si} = 0.115$ being the Fano factor, $E_{Si,e/h} = 3.63\frac{\text{eV}}{\text{e/h}}$ being the average pair production energy in silicon (sec. 3.1.1).

2. As the functional principle of the DSSC analog signal filtering stage (sec. 3.1.3) is based on the integration of a varying signal current, the electronic noise level increases with larger signal amplitudes [26]. An additional parameter n_{add} is introduced in order to comply with spectra that show additional, signal dependent noise. This parameter can either be determined during the definition of the shape of the fit function at high ADC resolution or used for additional flexibility when fitting at low resolution. Eq. 5.22 that defines the σ_i of

each individual calibration line becomes:

$$\sigma_i = \sqrt{\sigma_{\text{noise}}^2 + (F_{Si}\ N_{e,i})^2 + (n_{\text{add}}\ N_{e,i})^2} \tag{5.24}$$

By applying modification 1. and 2. the number of "noise parameters" describing the width of the noise peak and of the arbitrary number of calibration line peaks is not larger than two (σ_{noise} and n_{add}). In this work, this effect is considered negligible, as the added signal dependent noise is low even in comparison to the Poisson statistics of the photon generation [26]. $n_{\text{add}} = 0$ in all presented fits.

3. Instead of using the individual positions x_i of the calibration lines as fit parameters, it is convenient to define as "gain parameter" the distance $D = x_0 - x_{\text{noise}}$ of the most prominent calibration line located at x_0 to the noise peak located at x_{noise} as "gain parameter". Thereby, the system gain (in units of LSB per keV) can be calculated easily. With knowledge of the energy E_i of the respective calibration line i, its position relative to the most prominent calibration line (with position x_0 and energy E_0) can be fixed using the relation:

$$x_i = \frac{x_0 - x_{\text{noise}}}{E_0} E_i = D\frac{E_0}{E_i} \tag{5.25}$$

Linking the individual calibration lines in this way further reduces the number of free fit parameters and increases the stability of the fit, as the area underneath the fit function in relation to the number of available data points (i.e. bins) is increased in comparison to fitting pure Gaussians [35].

4. As an additional parameter, a ratio of individual calibration lines, or groups of calibration lines, is introduced. Although a good start value for this ratio can be determined due to the known probabilities of individual decay channels of typical calibration line sources and their respective quantum efficiency, it is necessary to adapt the composition of the global fit function. On the one hand, this is due to its limited abilities describing the actual physical context, leading to unavoidable interdependencies of the fit features and their respective parameters. On the other hand an adaption is necessary due to the characteristic spectral response of the DSSC detector: Specific hardware properties such as the composition of the sensor entrance window can influence the quantum efficiency ([60]) for certain photon energies and thereby the spectral response. The ratio $S_{l,i}$ acts directly upon the Gaussian (eq. 5.18) of the respective calibration line:

$$F_{\text{i,peak}}(x) = \frac{S_{l,i}\ N_i}{\sigma_i\sqrt{2\pi}}\ e^{-\frac{1}{2}\left(\frac{x-x_i}{\sigma_i}\right)^2} \tag{5.26}$$

All other trough features are scaled in relation to the respective calibration line. The ratio $S_{l,i}$ can be conserved easily when fixing the shape for its application to spectra with poor ADC resolution.

5. The parameter β_t in eqs. 5.19 and 5.20 works similar to a decay constant and by that

stands in relation to the scale on the abscissa. In order to ensure that the shape of the fit function does not change during fitting when β_t is fixed to a specific value, the parameter must be independent of the system gain. This can be achieved by combining the parameter β_t in a product with the distance of the calibration line to the noise peak $D = x_i - x_{\text{noise}}$. Eqs. 5.19 and 5.20 become:

$$F_{\text{i,tail\_high}}(x) = \frac{N_t \, N_i}{D\beta_t e^{-(\frac{\sigma_i}{2D\beta_t})^2}} \; \frac{1}{2} e^{\frac{x-x_i}{D\beta_t}} \operatorname{erfc}\left(\frac{x - x_i}{\sigma_i} + \frac{\sigma_i}{2D\beta_t}\right) \tag{5.27}$$

$$F_{\text{i,tail\_low}}(x) = \frac{S_{\text{tnoise}} \, N_t \, N_i}{D\alpha_t\beta_t e^{-(\frac{\sigma_i}{2D\alpha_t\beta_t})^2}} \; e^{\frac{-(x-x_{\text{noise}})}{D\alpha_t\beta_t}} \frac{1}{2}\operatorname{erfc}\left(\frac{-(x - x_{\text{noise}})}{\sigma_i} + \frac{\sigma_i}{2D\alpha_t\beta_t}\right) \tag{5.28}$$
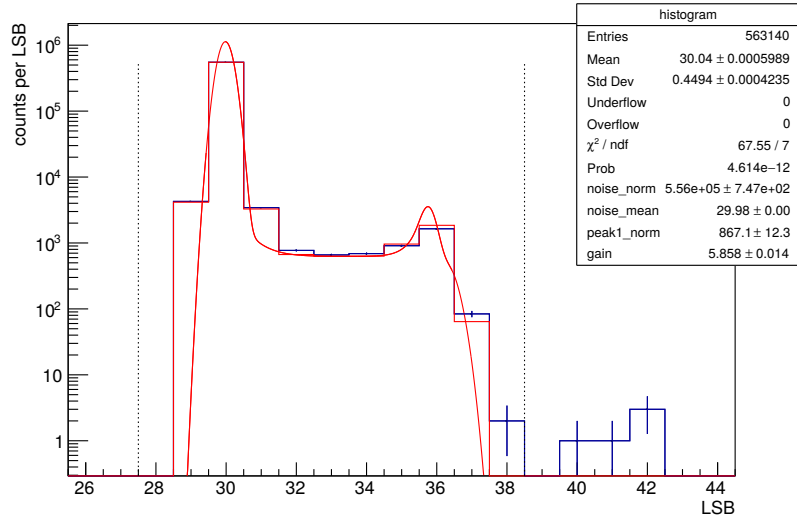
Figure 5.33: Simulated ^{55}Fe spectrum with low ADC resolution that has been fitted with the proposed global fit function. The histogram was simulated using ideal binning. The fit function is given in red, the binned fit function is plotted for comparison with the simulated data. The fit range is given by the dashed lines. The "gain"-parameter corresponds to the distance of the calibration line peak to the noise peak, as defined in eq. 5.25.

In order to preserve the general shape of the fit function regardless of system gain, offset or noise, the parameters N_t, β_t, S_{tnoise}, N_s, $S_{l,i}$ and n_{add} need to be fixed. Thereby, only the system noise, offset, gain and the area underneath the noise respectively the calibration line peaks remain as free parameters. An example of such a fit can be found in fig. 5.33. This fit was performed under the assumption, that also the system noise was already known, e.g. by a previous noise characterization with dark frames (sec. 5.2). The ratio of the counts attributed to each set of K-lines of ^{55}Mn was determined using a spectrum with 14 bit resolution. By that, the only free fit parameters are N_{noise}, x_{noise}, N_1 (the area underneath the K_α line) and the peak distance D.

5.3.4 Analysis of simulated calibration spectra with high ADC resolution

Using the DSSC detector simulation package (sec. 4.2), "SPIX-like" spectra of the calibration line sources ^{55}Fe and ^{109}Cd have been generated with the following proporties:

- linear system response

- no signal dependent additional noise component

- no significant charge loss due to out-of-time events

- charge collection effects (charge loss) and charge sharing using parameters evaluated on the basis of spectra measured with DSSC DEPFET pixels at the SPIX setup (sec. 3.4.1)

Simulated spectra with these properties with a high ADC resolution (14-bit ADC) were used as templates in order to evaluate a set of parameters of the global fit function (sec. 5.3.2). Figs. 5.34 to 5.37 show the fits to these template spectra. The fits were performed after applying the modifications to the global fit function introduced in sec. 5.3.3. The "gain"-parameter corresponds to the distance of the calibration line peak to the noise peak, as defined in eq. 5.25. An overview of the parameters used in the plots is given in table 5.2, which is an expansion of table 5.1, summarizing all parameters introduced in sec. 5.3.3.

Name	Symbol	Description
noise_norm	N_{noise}	area underneath the noise peak
noise_mean	x_{noise}	position of the noise peak
noise_sigma	σ_{noise}	standard deviation of the noise peak
peak1_norm	N_1	area underneath the calibration line peak
peakt_amp	N_t	relative factor for area underneath the peak tail
peakt_beta	β_t	steepness of the peak tail
peakp_amp	N_s	relative factor for area underneath the peak shelf
line_ratio	S_l	scale factor of individual sets of calibration lines
kbeta_nratio	S_l	calibration line scale factor, only used for ^{109}Cd fit
gain	$D = x_i - x_{\text{noise}}$	gain of spectrum in units of LSB
noise_tails	S_{tnoise}	scale factor for the tail component underneath the noise peak
through_asym	α_t	asymmetry of steepness of decay for tails underneath noise peak

Table 5.2: Summary of the parameters of the global fit function.

Making the following assumptions regarding the composition of calibration lines in the individual spectra, these fit results could be achieved for the simulated template spectra:

1. For the ^{55}Fe spectrum, the following calibration line energies have been simulated [61]:

- $K_{\alpha,1}$ at 5.888 keV with a relative event probability of 0.2994.

- $K_{\alpha,2}$ at 5.889 keV with a relative event probability of 0.5953.

- K_{β} at 6.49 keV with a relative event probability of 0.1053.

For the fit, the two K_α-lines were treated as a single line at the weighted average of 5.895 keV. The event probability of K_β in relation to this combined line is about 0.12. In the fit, this was used as a start value for the free line ratio parameter S_l. The fit result for S_l is about 0.14, which is expected due to the slightly lower quantum efficiency of the K_β photons. Figs. 5.34 and 5.35 show the fit to the simulated ^{55}Fe spectrum with high ADC resolution.

The standard deviation of the significance of the residual of the fit function to the simulated data in each bin is about 1.5 (fig. 5.34, histogram on the lower right). This, together with the plots showing a zoom into the most critical regions of the fit (fig. 5.35), indicates that a good agreement of the fit model with the simulated spectral response can be achieved. The deviation of the determined gain is about 0.01% in relation to the simulation truth, the relative deviation of the determined noise is about 0.42%.

2. For the ^{109}Cd spectrum, the following calibration line energies were simulated [61]:

- $K_{\alpha,3}$ at 21.708 keV with a relative event probability of 0.0000122.
- $K_{\alpha,2}$ at 21.99 keV with a relative event probability of 0.295.
- $K_{\alpha,1}$ at 22.163 keV with a relative event probability of 0.557.
- $K_{\beta,3}$ at 24.912 keV with a relative event probability of 0.0476.
- $K_{\beta,1}$ at 24.943 keV with a relative event probability of 0.092.
- $K_{\beta,5}$ at 25.144 keV with a relative event probability of 0.00067.
- $K_{\beta,2}$ at 25.455 keV with a relative event probability of 0.023.
- $K_{\beta,4}$ at 25.511 keV with a relative event probability of 0.00487.

For the fit, the eight individual lines were combined to a model comprising four lines as follows:

- $K_{\alpha,1}$ is treated as an individual line.
- $K_{\alpha,3}$ and $K_{\alpha,2}$ were combined to a single line at the weighted average of 21.990 keV. Their relative probability in relation to $K_{\alpha,1}$ is 0.5296. This was used in the fit as a fixed line ratio $S_{l,\alpha}$. It would not have been possible to determine this ratio via a fit, as the lines lie to close together. Also, this ratio is expected to be close to the actual event probability because of the very similar quantum efficiency of the the respective photons.
- $K_{\beta,3}$, $K_{\beta,1}$ and $K_{\beta,5}$ were combined to a single line at the weighted average of 24.933 keV. The combined relative probability of the $K_{\beta,3+1+5}$-line in relation to $K_{\alpha,1}$ is about 0.25. This was used as the start value for the free fit parameter S_l. As the energy of this K_β group is considerably different from the K_α lines, the ratio is expected to differ from the calculated event probability due to lower quantum efficiency.
- The weighted average of $K_{\beta,2}$ and $K_{\beta,4}$ is at 25.465 keV. Their combined relative probability in relation to the combined line $K_{\beta,3+1+5}$ is 0.1987. This was used in the fit as a fixed line ratio $S_{l,\beta}$.

Given the specific photon energy of each calibration line and the fixed line ratios $S_{l,\alpha}$ and $S_{l,\beta}$, the fit to this more complex spectrum can be performed with the same number of free parameters as the ^{55}Fe-fit. Figs. 5.36 and 5.37 show the fit to the simulated ^{109}Cd spectrum with high ADC resolution. The fit result for the line ratio S_l (sec. 5.3.3, 4.) is about 0.19, which shows a small deviation from the theoretical value of about 0.25, again expected by the different quantum efficiency of individual energies.

The fit function shows stronger deviations modeling the through shape of the simulated ^{109}Cd, especially close to the noise peak (fig. 5.37). However, the standard deviation of the significance of the residual to the data in all bins inside the fit range is, as for the ^{55}Fe-fit, around 1.5 (fig. 5.36). The deviation of the determined gain is about 0.08% in relation to the simulation truth, the relative deviation of the determined noise is about 0.53%.

In summary, the proposed global fit function for characteristic single-pixel calibration line spectra can be applied to fit spectra with a high ADC resolution in order to determine properties such as system noise and gain. The fit results show good agreement with the simulated data. The simulated gain values can be reproduced with an accuracy in the per mill range, the simulated noise values with an accuracy of approximately 0.5%. As the simulation agrees well with experimental data (ch. 4), the fit function can therefore be expected to accurately describe measured spectra with the given properties.

5.3.5 Study of the gain determination accuracy

In sec. 5.3.4, the shape of the spectral response of simulated DSSC sensor pixels has been characterized by fitting the global fit function to simulated template spectra with high (14-bit) ADC resolution, for two typical calibration line sources that are ^{55}Fe and ^{109}Cd. The shape of the fit function was then fixed as described in sec. 5.3.3 in order to be applied to simulated jk-grids (sec. 3.2.2) of calibration line spectra with poor (8-bit) ADC resolution, that were generated with similar properties as the spectra with high (14-bit) resolution. The only difference between the spectra with low and high ADC resolution are the properties of the (linear) read-out electronics, which causes the following two effects:

- Due to different read-out sequences, the charge collection efficiency (sec. 3.1) varies. This results in different ratios of the actual photon signal (or "count rate" when divided by the total number of frames) to the noise peak. The proposed fit function can adapt to this by variation of the scaling parameters "noise_norm" and "peak1_norm" (N_{noise} and N_i in table 5.2).

- The two read-out electronic simulations show different signal-to-noise ratios. Also, the system noise in units of LSB varies over the full jk-grid due to the change of the ADC gain (sec. 3.2.2). As the fit parameter for the system noise (σ_{noise} in table 5.2) is given in these units, it needs to adapt as soon as the system gain changes. Also, the system offset of the spectra with low ADC resolution shifts for changes of the pixel delay and the ADC gain setting.

Figure 5.34: Fit of the proposed global fit function to a simulated ^{55}Fe with high ADC resolution. The fit range is indicated by the dashed lines. The results for the parameters are given in the box on the upper right. The lower plots show the significance of the residual of the fit function to the data.
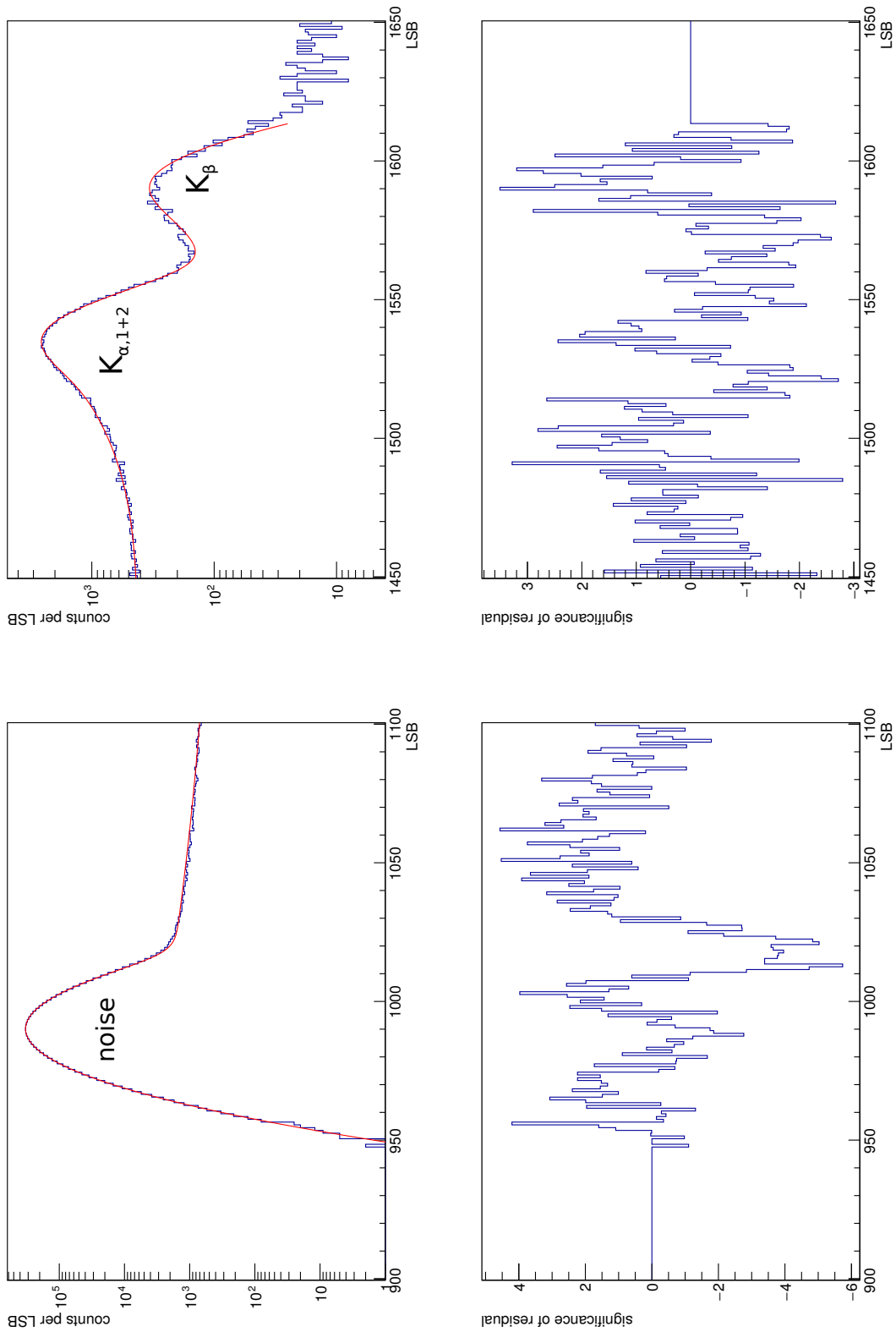
Figure 5.35: Zoom into critical regions of the fit to the ^{55}Fe spectrum given in fig. 5.34.

Figure 5.36: Fit of the proposed global fit function to a simulated ^{109}Cd with high ADC resolution. The fit range is indicated by the dashed lines. The results for the parameters are given in the box on the upper right. The lower plots show the significance of the residual of the fit function to the data.
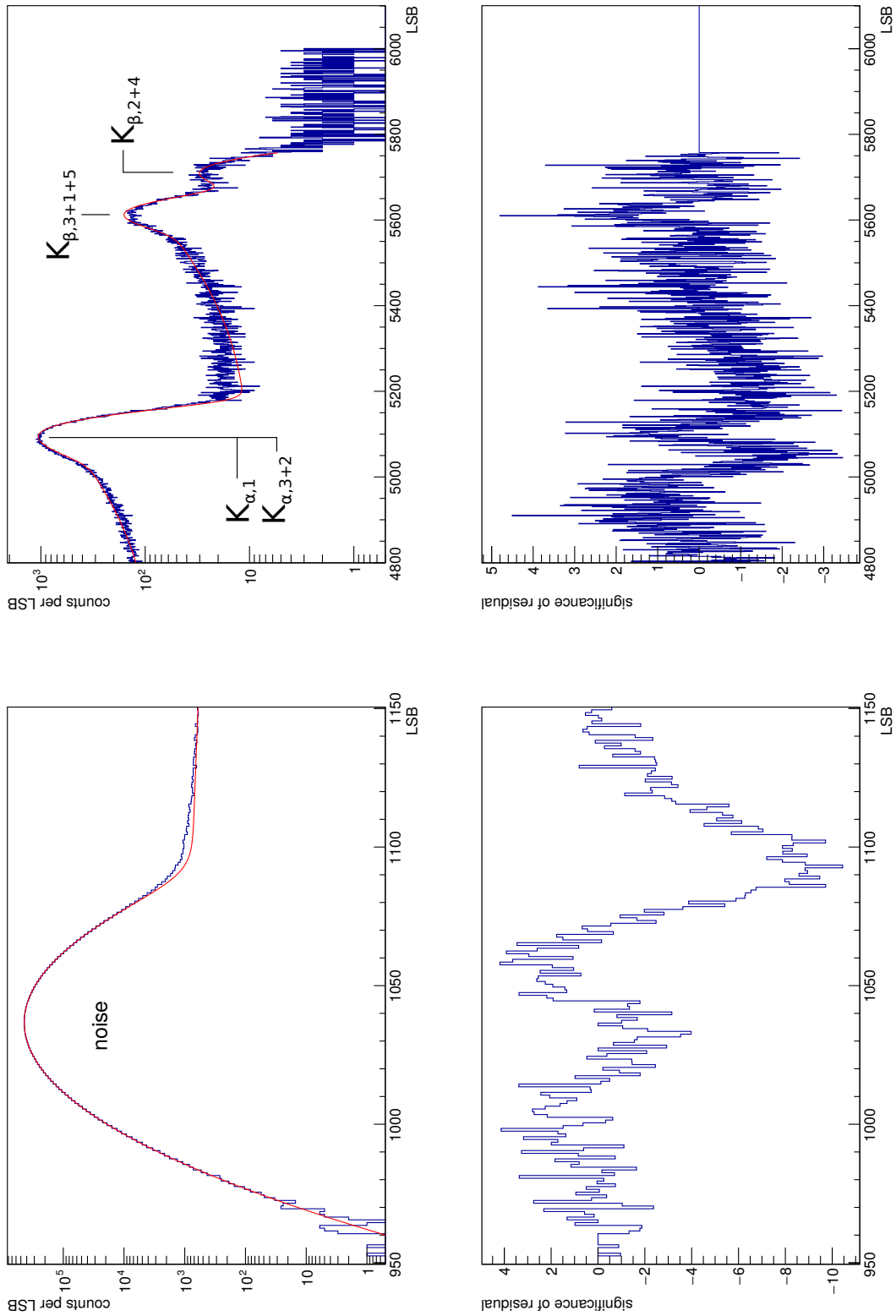
Figure 5.37: Zoom into critical regions of the fit to the ^{109}Cd spectrum given in fig. 5.36.

In this study, the fits of the individual histograms are therefore based on pre-defined values for the system noise and offset. These were either given by the simulation truth or determined by application of the error function method to corresponding dark frame jk-grids as presented in sec. 5.2.

With focus on the fit of the "gain"-parameter and the scaling parameters, this section will evaluate the achievable accuracy of the gain determination method.

5.3.6 Determination of start values, parameter limits and possible outliers
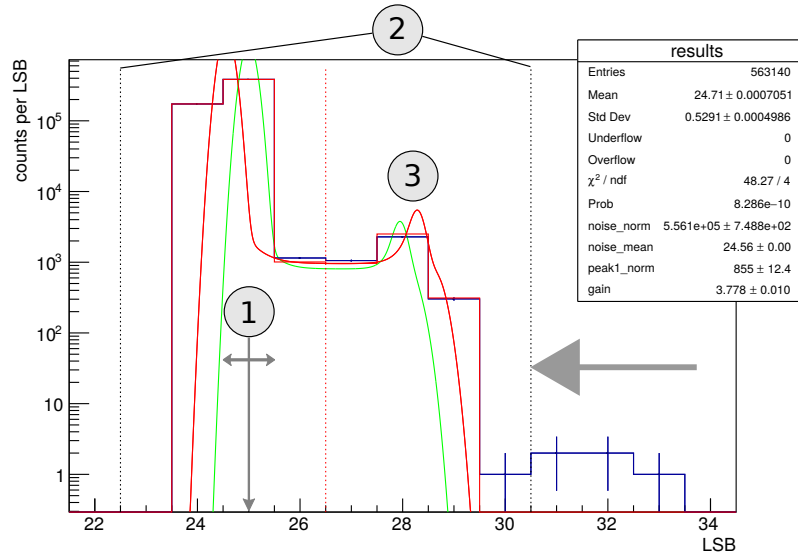
Figure 5.38: Illustration of the algorithm determining the fit start values. The gray markings refer to the proposed algorithm steps. The green curve shows the fit function with applied start values before the fit. For comparison, the result of the fit is given in red in both in continuous and binned representation.

Fig. 5.38 illustrates the algorithm that was used to find the start values for the fit of the global fit function when applied to spectra with low ADC resolution. The algorithm performs the following three steps that are marked in the plot in gray encircled numbers:

1. If the values for the offset of the spectrum and the system noise in units of LSB (x_{noise} and σ_{noise} in table 5.2) are not given at this point, these values can be evaluated by one of the three following methods, ordered by increasing complexity:

   - Set the offset start value to the center of the bin with the highest content and set the start value of the noise to the width of the highest bin or a predefined default value.

   - Calculate the offset and noise start value from a predefined number i of bins adjacent to the highest bin. The system offset is then the mean value μ of the selected bins

that can be calculated by

$$x_{\text{noise}} = \mu = \sum_i X_i p_i \qquad (5.29)$$

with p_i being the bin-wise relative probability of the distribution according to the number of counts C_i in each bin, with $p_i = C_i / \sum_i C_i$. The system noise or standard deviation σ_{noise} of this distribution is then the square root of the variance:

$$\sigma_{\text{noise}} = \sqrt{\text{Var}(X)} = \sqrt{\sum_i \left(X_i - \mu\right)^2 p_i} \qquad (5.30)$$

- Perform a Gaussian fit to a range of a predefined number of bins adjacent to the highest bin.

In [35] the advantage of a Gaussian fit with integration over the "basic" calculation of mean and standard of a binned distribution has been studied in detail. The accuracy of both the (Gaussian) fit and the calculation of μ and σ are impeded by the characteristic low-energy through between noise peak and calibration lines. Depending on the combination of count rate, system gain and noise one of the three proposed methods is suited best for the determination of the respective start values. For highly irregular spectra (e.g. caused by high DNL), the usage of a predefined default noise value prevents erroneous start values that impede the subsequent process steps. For spectra with higher resolution and less adverse conditions, the results of a Gaussian fit to the noise peak can improve the stability and thereby reduce the run-time of the fit of the global fit function.

An estimate of the start value for the scaling parameter of the noise peak "noise_norm" (N_{noise} in table 5.2) is given by the width of the highest bin multiplied by the bin content in units of "counts per LSB", assuming that in most of the calibration line spectra the noise peak is dominated by a single bin.

2. In the second step, the fit range is determined. The low boundary of the fit range is set to be the lower bin boundary of the first bin below the spectrum that has no entries. As the global fit function is fitted with a likelihood fit that is based on the assumption of Poissonian bin-wise statistics, the information content of the empty bin is correctly taken into account, which would not be the case with standard χ^2-fitting [35].

The upper boundary of the fit range is more difficult to determine due to possible "outliers" from the main spectral distribution, that can be caused e.g. by signal pile-up as can be seen for example in fig. 5.41. The global fit function in the version given in sec. 5.3.2 does not support this spectral feature. Therefore the fit range has to be limited to the main portion of the spectrum. The approach used in this study is illustrated by the large gray arrow in fig. 5.38:

The bins are examined consecutively with decreasing bin number, starting from the last bin that has entries. In each step, the median number of entries of all bins examined so far is calculated. If this median is higher than a certain threshold, e.g. the MAD (eq. A.6 in app. A) of the distribution of the bin entries examined so far, and in addition the next,

lower bin has a higher number of entries than the current bin B_i, the upper boundary of the fit range is set to the upper boundary of the bin B_{i+1}.

3. The start value for the "gain"-parameter is then determined by separating the fit range in two halves (red dashed line in fig. 5.38): With the bin center of the highest bin c_h in the upper half and the start value for the offset x_{noise} from the first step, the "gain"-parameter start value can be calculated by $D = c_h - x_{\text{noise}}$.

   Taking into account the normalization in eq. 5.18, the start value for the scaling parameter of the calibration line peak (N_i in table 5.2) is calculated by $N_i = \sqrt{2\pi} \cdot \sigma_{\text{noise}} \cdot C_{B_i}$ with C_{B_i} being the number of entries in bin c_h.

An example of the resulting fit function with applied start values is given in fig. 5.38 in green. In this example, the start value for σ_{noise} was given by the simulation truth. All other start values have been determined as described.

For additional stability of the fitting process, limits can be set for the fit parameters. This technique is usually discouraged in the usage of the `MINUIT` fitter [51] due to numerical disadvantages but can be motivated by physical constraints: For example the scaling parameter of the calibration line N_i cannot be negative and should also not be higher than the scaling parameter of the noise peak N_{noise}. Another motivation for such a constraint is the experience, that the correct result of the "gain"-parameter given by the simulation truth does not deviate more than one or two bin-widths from the start value that places the calibration line peak in the highest bin in the upper half of the fit range. The latter constraint will inhibit fit results in which the "gain"-parameter "runs off" to very high values locating the calibration line peak out of the defined fit range. This would otherwise occur often, when the ratio of the calibration peak to the trough is low, as illustrated in an example in fig. 5.39.

The setting of parameter limits for the "gain"-parameter comes with the disadvantage, that the fit-based determination of this measure is bound strictly to the region near the highest bin in the upper half of the histogram. If the binning information of the ADC is erroneous, the occurrence of bins whose width is severely underestimated lead to "spikes" in the spectra that will cause a faulty determination of the start value of the "gain"-parameter, as is illustrated in fig. 5.40.

It has to be noted though, that this effect is caused predominantly by the chosen approach for the simulation of erroneous binning information that was used in this study: The "blurring" of the bin-boundaries (sec. 5.2.5) by a Gaussian distribution can lead to very narrow bin widths due to statistical outliers. It is highly unlikely, that this effect occurs in the real detector. There, the bin-boundary determination algorithm [32] can be based on the assumption that the ADC bin-widths are cyclical (sec. 3.1.4), which prevents overly narrow bins. Up to now, no experimental determination of the binning of DSSC prototypes did result in overly narrow bins [62]. In the presentation of the results of this study the median and the median absolute deviation (`MAD`, see app. A eq. A.5 to A.7) are used in order minimize the impact of outliers due to overly narrow bins.

results	
Entries	563140
Mean	25.96 ± 0.0004737
Std Dev	0.3555 ± 0.0003349
Underflow	0
Overflow	0
χ^2 / ndf	2.14e+05 / 5
Prob	0
noise_norm	5.555e+05 ± 7.480e+02
peak1_norm	660.5 ± 29.3
gain	7.39 ± 0.53
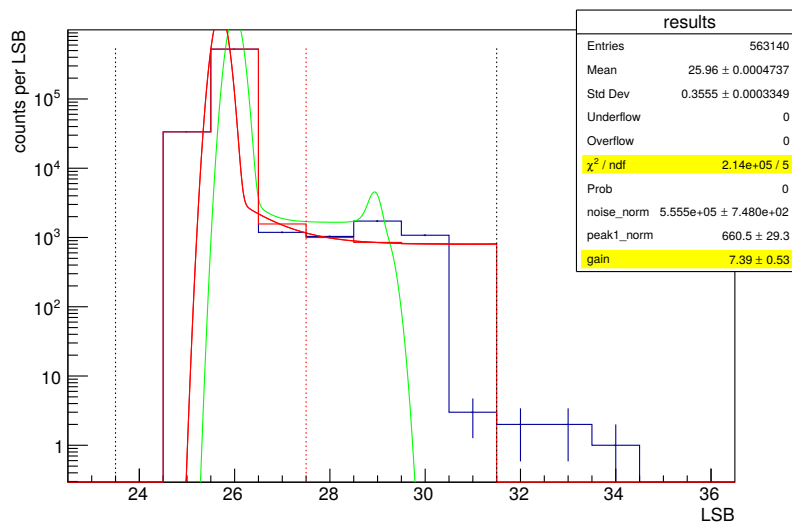
Figure 5.39: Fit result for a spectrum simulated with ideal binning. The start values (green) have been determined with the proposed algorithm. The parameter for the system noise was given by the simulation truth. In this case, no parameter limits have been set for the "gain"-parameter. The very high χ^2 value can help identify such a "misfit". Here, the "gain"-parameter was determined to be 7.39 LSB. The simulation truth would have been 3.85 LSB – a relative deviation of nearly 100%.
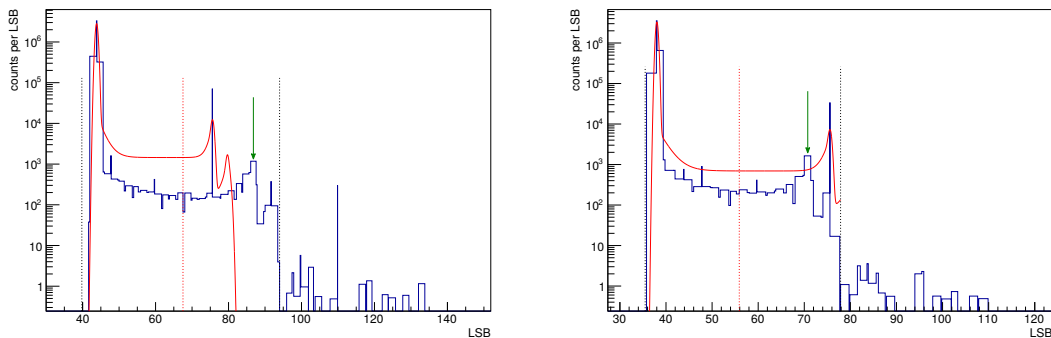
Figure 5.40: Illustration of faulty determination of the "gain"-parameter. In the depicted spectra individual bins show a very small width due to a combination of simulated intrinsic DNL with $\sigma_{\mathrm{DNL}} = 0.3$ LSB and additional bin-boundary blurring with $\sigma_{\mathrm{blur}} = 0.3$ LSB.

If one of these very narrow bins lies in the upper half of the fit range, its bin content, scaled to the bin width, can be very high in comparison to the other bins – even higher than the actual K_α-line (green arrows). Due to the start-value algorithm and the parameter limits the fit is then limited to the near region of this "spike".

5.3.7 Overview over the test field

For both sources ^{55}Fe and ^{109}Cd two individual groups of complete jk-grids of 100 pixels have been simulated, aimed at a calibration with a gain of 2 LSB/keV and 1 LSB/keV respectively. For each combination of calibration line source and detector gain setting, jk-grids with varying DNL (ideal, $\sigma_{\mathrm{DNL}} = 0.1$, 0.2 and 0.3) were simulated. This leads to a test field of 16 individual datasets. Fig. 5.41 shows four exemplary fit results with ideal ADC binning, one for each combination of detector gain and calibration line source.

As for the study evaluating the accuracy of the offset and noise determination method (sec. 5.2), the stability of the fit based approach has been tested under the influence of four different ADC binning environments:

- Ideally known binning.

- Disregarded binning information. The binning was assumed to be "ideal", i.e. neither showing DNL and INL.

- Blurring of the bin boundaries with $\sigma_{\mathrm{blur}} = 0.05$ LSB and 0.1 LSB, i.e. 5% and 10% of the ideal bin-width.

The 12 datasets simulated with an intrinsic DNL of the ADC (σ_{DNL}) have been studied in these four environments, which leads to additional 48 jk-grids of 10x10 pixels each. In summary, this leads to a test field of $(16 + 48) \cdot 100 \cdot 1024 \sim 6.5 \cdot 10^6$ individual histograms in total.

5.3.8 Results

Fig. 5.42 shows a comparison of the relative residual of determined start values of the "gain"-parameter and the respective fit results of complete jk-grids analysed in this study. The nearly vertical streaks in the plots on the left side are caused by the start value algorithm (sec. 5.3.6) that defines the center of the highest bin in the upper half of the spectrum as the position of the calibration line peak.

Plots (a) to (d) of fig. 5.42 show the start values and fit results of a grid which was aimed at a calibration with a gain of 2 LSB/keV, simulated with ^{55}Fe as a calibration line source and ideal ADC binning. In (a) and (b) the values are plotted as a function of the simulated gain, in (c) and (d) as a function of the simulated width, which corresponds to the system noise. This illustrates again the broad range of detector parameter variation featured by the jk-grid measurement (sec. 3.2.2).

Plots (b) and (d) are almost indistinguishable, but the vertical streaks are perceptibly broader in (a) than in (c): Given ideal binning, the residual of the start value to a specific simulated gain is identical for all histograms due to the start value algorithm – causing the narrow streaks in (a). On the other hand, histograms sharing the same residual to the simulated gain can exhibit different, individual system noise values (i.e. simulated width) due to pixel inhomogeneities – causing the broader streaks in (c).

Plots (e) and (f) of fig. 5.42 show the relative residual of start values and fit results of a full jk-grid aimed at a calibration with a gain of 2 LSB/keV, but simulated with ^{109}Cd as a
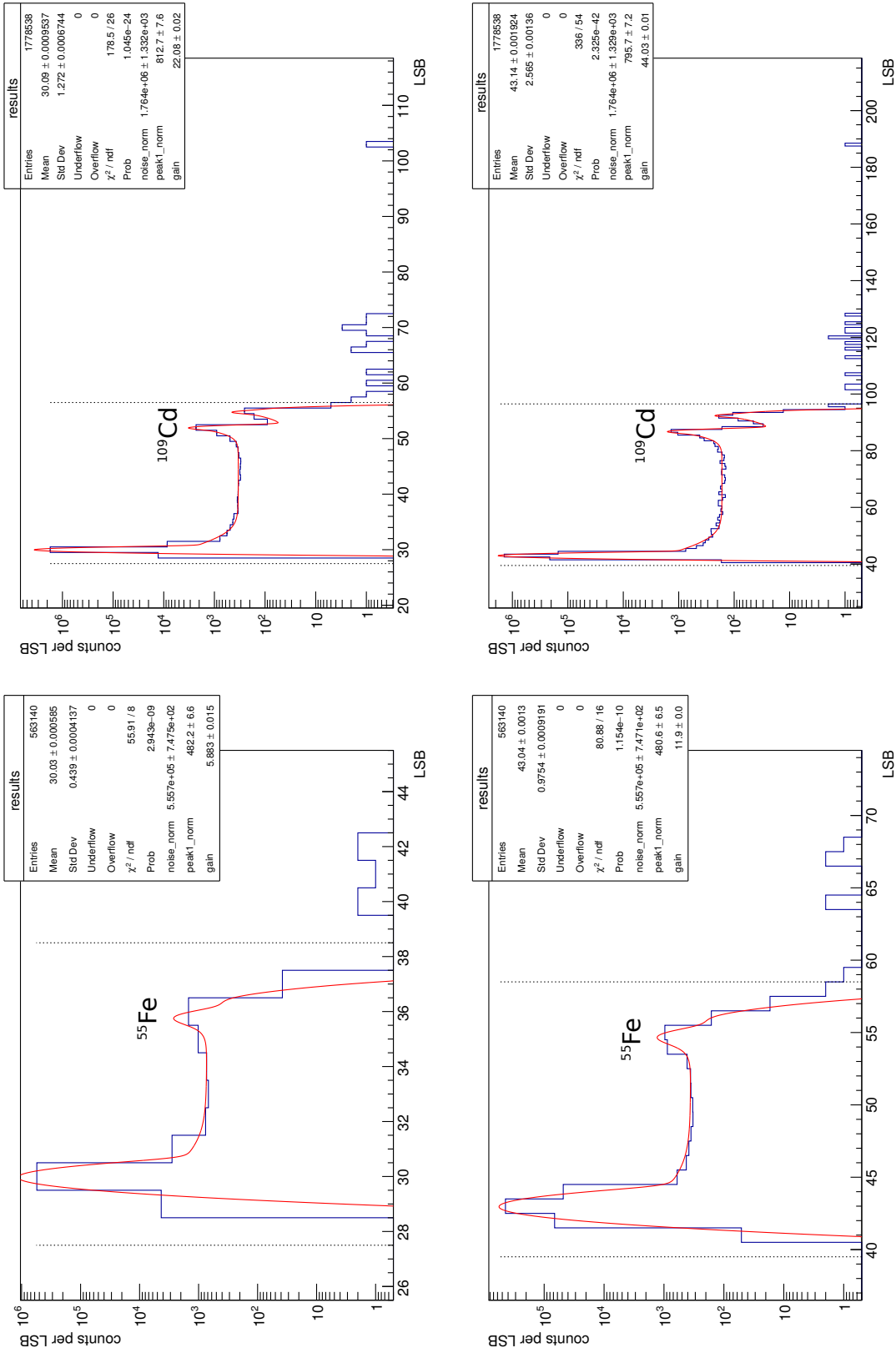
Figure 5.41: Exemplary, simulated spectra of ^{55}Fe and ^{109}Cd with low 8-bit ADC resolution. Upper row: Calibration suited for counting 1 keV X-ray photons. Lower row: calibration suited for 0.5 keV photons. The dashed black lines mark the fit range that has been determined automatically. The "gain"-parameter corresponds to the distance of the K_α-line to the center of the noise peak, measured in units of LSB.
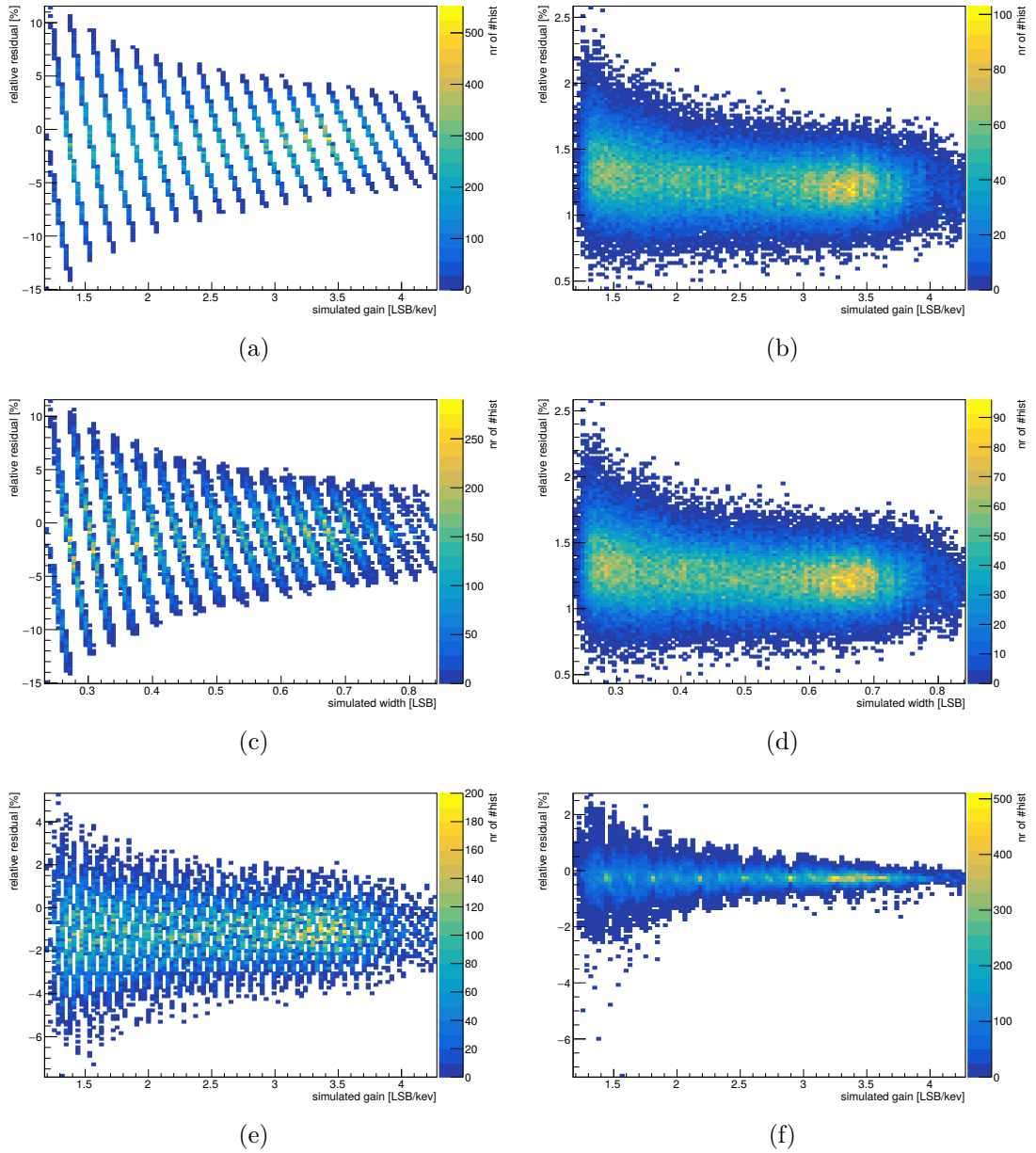
Figure 5.42: Relative residual to the simulation truth of start values (left side) and fit results (right side) for the gain determination of simulated full jk-grids of 100 pixels. Each plot depicts the results of 102400 individual histograms. The plots show examples of the test field that is described in sec. 5.3.7.

Plots (a) to (d) depict the start values and results of a jk-grid aimed at a calibration with a gain of 2 LSB/keV, simulated with ^{55}Fe as a calibration line source and ideal ADC binning. Panels (c) and (d) represent the same data, presented in a different way. More explanation can be found in the text. Plots (e) and (f) show the relative residual of start values and fit results of a jk-grid aimed at a calibration with a gain of 2 LSB/keV, but simulated with ^{109}Cd as a calibration line source and an intrinsic DNL of the ADC with $\sigma_{\mathrm{DNL}} = 0.3$. In the analysis, ideal binning was assumed.

calibration line source and an intrinsic DNL of the ADC with $\sigma_{\mathrm{DNL}} = 0.3$. In the analysis, ideal binning was assumed. Due to the higher ADC resolution of the calibration line peak, the "streaks" of start values show a finer granularity. The fit result has a lower mean systematic deviation as with ^{55}Fe as source, but exhibits a generally more "twitchy" behaviour with more prominent outliers due to the DNL not being taken into account correctly.
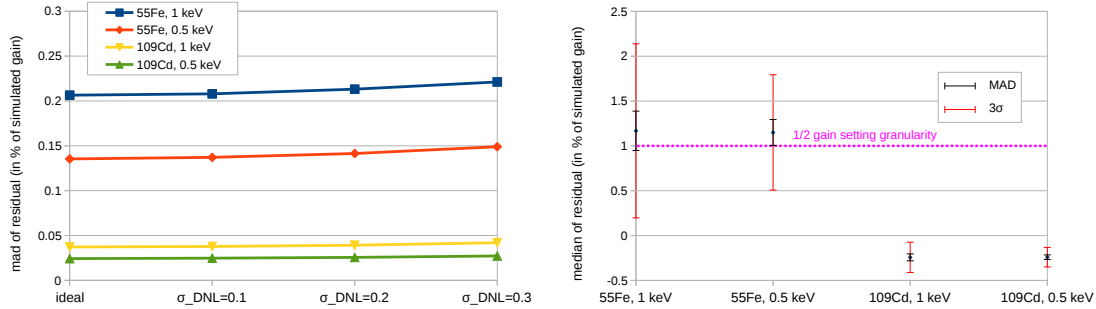
Figure 5.43: Statistical uncertainty (left) and systematic deviation (right) of the gain determination for 16 individual jk-grids of 100 pixels, aimed at calibrations suited for counting 1 keV and 0.5 keV X-ray photons, simulated with the calibration line sources ^{55}Fe and ^{109}Cd. Analyses based on ideally known binning, using system noise and offset from the simulation truth.

Fig. 5.43 summarizes the results of the analyses that were performed with ideally known DNL and using the "correct" system noise and offset values given by the simulation truth. The plots show the relative residual of the determined gain to the simulation truth in percent:

- The statistical uncertainty (left panel) is given as the median absolute deviation (`MAD`) of the distribution of results of all $J \cdot K \cdot \mathrm{pix}_x \cdot \mathrm{pix}_y = 64 \cdot 16 \cdot 10 \cdot 10 = 102400$ individual fits for each of the 16 data points. The results show, that for an increasing number of bins into which the spectrum is resolved (analyses of jk-grids with a gain around 2 LSB/keV, suited for counting photons with an energy of 0.5 keV), the statistical uncertainty is lower than for analyses of jk-grids with a gain of approximately 1 LSB/keV, suited for counting photons with an energy of 1 keV. Also, the higher calibration line energy of ^{109}Cd leads to a lower statistical uncertainty in the gain determination because of the higher relative resolution. In comparison, the analyses based on fits to the K_α-line of ^{55}Fe show a higher dependency on the DNL of the ADC: As expected, the statistical uncertainty of ^{55}Fe-based fits increases distinctly for datasets with higher DNL values.

- Assuming, that the gain of the read-out ASIC can be set with a granularity of 2% (sec. 3.1.4 and 3.2.2), the systematic deviation of the gain determination must be lower than half of this granularity in order to be able to calibrate the system to the best possible setting. Also, the statistical uncertainty must be small enough so that the magnitude of gain determinations are below that threshold.

  Each data point in the the right panel of fig. 5.43 shows the median of the four datasets that were analyzed for each combination of calibration line source and detector gain setting, using ideally known binning. As the decision for the applicability of the method must be

based on the combination of both the systematic deviation and the statistical uncertainty, the median of the statistical uncertainty given by the left panel is used as an error bar. In addition, error bars representing a 3σ range (conversion by eq. A.7 in the appendix) are plotted in red. This result shows, that in the gain determination approaches using ^{109}Cd the gain could be determined with a deviation less than 1% (half of the setting granularity) to the simulation truth in more than 99% of all individual histograms.

Fig. 5.44 shows an overview of the results of the analyses of jk-grids of calibration line spectra with varying intrinsic ADC DNL under the influence of the four described (sec. 5.3.7) binning environments. For this part of the study, the gain determination was based on offset and noise values determined by the analysis (sec. 5.2) of dark frame grids simulated with DNL properties and jk-grid settings identical to the respective grids of calibration line spectra. The plots show the statistical uncertainty of the gain determination, measured by the median absolute deviation (MAD) of the distribution of the relative residuals of the determined gain to the simulation truth.

- The "worst case" is when a calibration to 1 keV photons is approached with ^{55}Fe, an intrinsic DNL with $\sigma_{DNL} = 0.3$, but ideal bin boundaries are assumed (upper left panel, blue line): In that case, the median absolute deviation of all results is about 1.6% of the simulated gain, which approximates to a 3σ-span of the result distribution of 7.2%. In other words (and assuming that the result distribution is Gaussian in first order): More than 50% of the results show a deviation of at least 1.6% (0.675σ) from the median of all results. Considering the higher systematic uncertainty of ^{55}Fe-based calibrations (see above), this would in many cases lead to a selection of a sub-optimal ADC gain setting.

- With decreasing DNL and increasing relative resolution (higher ADC gain setting, higher calibration line energy) the statistical uncertainty decreases in all test cases. The gain determination accuracy is sufficient for the gain calibration in this example: For the combination of ^{109}Cd as source and a gain of 1 kev/LSB as target, a high intrinsic DNL ($\sigma_{DNL} = 0.3$) determined with an accuracy of 5% (lower left plot, blue line, second to last data point), the gain can be determined with an accuracy better than 1% in about 99% (3σ) of the individual histograms – taking into account also the smaller systematic uncertainty.

- Similar to the result presented in fig. 5.16 in sec. 5.2.6, in all cases with an instrinsic DNL with $\sigma_{DNL} > 0.1$ a determination of the ADC bin boundaries can improve the accuracy as long as the uncertainty on the binning determination is in the order of 5%. If the DNL of the ADC is small ($\sigma_{DNL} = 0.1$ or smaller), than the binning must be determined with an uncertainty better than 5% in order to obtain results better than with simply assuming ideal binning.

5.3.9 Summary

The fit-based approach for the gain calibration of the DSSC detector has been tested using various combinations of calibration line sources and ADC binning environments. The first part of the
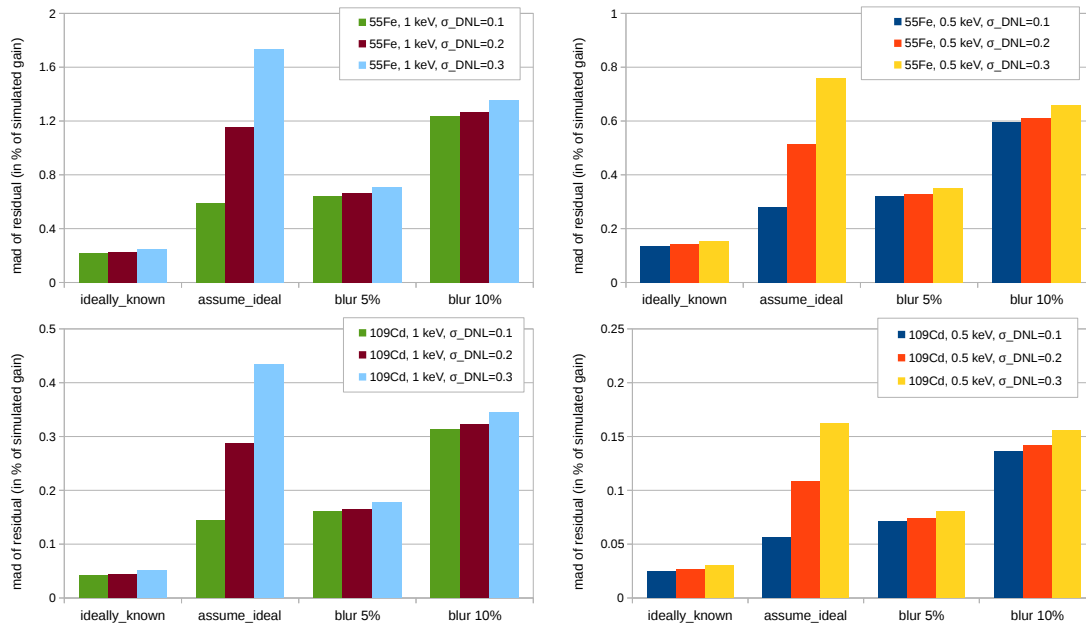
Figure 5.44: Overview of the statistical uncertainty of different combinations of calibration line source, intrinsic (simulated) DNL, knowledge of ADC binning and gain setting. The statistical uncertainty is assessed by the median absolute deviation (`MAD`). All results are based on offset and system noise values pre-determined by applying the proposed methods (sec. 5.2) using dark frame jk-grids with identical settings and DNL properties.

study was performed under "ideal conditions", i.e. ideally known ADC binning and offset and system noise values given by the simulation truth. In a second step, the gain determination algorithm was based on offset and system noise values pre-determined by the analysis of dark-frame jk-grids, that were also under the influence of various ADC binning manipulations. Thereby the conditions and the approach for the calibration of the DSSC detector proposed in in sec. 3.3.2 were reproduced and it was demonstrated, that the concept is applicable: The information that can be gathered with dark frame grids can be applied to the system gain characterization. The statistical uncertainty of the results of the gain determination study can be seen as a measure of the overall accuracy of the calibration approach.

It has to be noted, that this study only assesses the accuracy of the gain determination algorithm on a very broad range of gain settings (sec. 3.2.2) and does not compare the final selection of the gain setting (i.e. the gain calibration) with the best possible gain setting given by the simulation truth, as was done so in sec. 5.2.7 for the offset calibration. Also, the study is not based on actual results of the ADC binning determination algorithm ([31, 32]) – the uncertainty of the binning determination has been simulated by Gaussian blurring as described in sec. 5.2.5. As soon as the DSSC calibration algorithms will be integrated in the framework of the XFEL detector operation software ([63]), these studies will be revisited and also applied to experimental data.

Examples with ^{109}Cd as a calibration line source show a low systematic deviance ($< 0.3\%$) and in many cases the achievable statistical accuracy is sufficient for the calibration of the gain

setting that has a granularity of approximately 1%.

The results obtained with ^{55}Fe are heavily impaired by the lower relative ADC resolution of the calibration line peak causing significantly higher statistical uncertainties. It also noteworthy, that the determined systematic deviation remains very stable for each combination of calibration line source, detector gain setting and knowledge of the ADC binning. It is possible, that the higher systematic deviation of the gain determination approaches based on the ^{55}Fe is not only due to the lower relative ADC resolution of the ^{55}Fe-lines, but due to a worse adaption of the global fit function to the spectral response. If calibration line energies this low (< 10 keV) should be used for the calibration of the DSSC, a refinement of the composition of the global fit shape (sec. 5.3.2) taking into account the signal pile-up and improving the model of the low-energy trough between calibration line and noise peak as well as a further revision of the start value algorithm could lead to an improvement.

In total $(16 + 48) \cdot 100 \cdot 1024 \sim 6.5 \cdot 10^6$ individual histograms have been analyzed in this study. For each individual histogram, a likelihood-fit together with numerical integration over the fit-function was performed. Due to the low number of parameters in the fit function the pure processing time for the entire test field was not more than 36 hours on 32 CPUs[7]. From current experimental results it can be estimated that after the determination of offset and system noise with a dark frame '$I_{ramp}-$ pixel delay' grid, about 100 different gain and offset setting combinations will remain as "candidates" for the final calibration and will have to be characterized with the proposed method. For the 10^6 pixels of the DSSC the total computing time of the calibration would therefore be about 23 days. Of course, the process can be sped up easily by parallelization. Using the synchrotron radiation of the PETRA III facility (Hamburg, Germany) or the even higher energy of the EU.XFEL FXE beamline and an X-ray fluorescense target, an individual spectrum with every pixel illuminated can be recorded in about 1-2 minutes [62].

The fit-based method for the gain determination allows for two different approaches:

- The results of the offset and noise characterization be taken into account by fixing the respective fit parameters to the determined values. This approach has been used in the study based on the analysis of simulated spectra in this chapter. By reducing the number of free fit parameters in this way, a high fit accuracy and stability can be achieved.

- The fitting of the calibration line spectra measured with the DSSC can also be performed without prior knowledge of noise or offset. Examples for this approach can be found in the experimental part of this work in ch. 6.

The typical spectral response of DSSC sensor pixels to individual calibration line sources has been measured with high ADC resolution so far with the SPIX setup (e.g. fig. 5.32), operating prototype DSSC DEPFET pixels. The MiniSDD sensor pixels foreseen for Day0-operation have similar properties regarding their spectral response in the lower energy range that is relevant for the gain calibration. The reason is that the characteristic shape of the low-energy trough between noise peak and calibration lines is mainly dominated by charge sharing due to the size and shape of the pixel and its internal electrical potential structure. The separation of the signal electron

---

[7]Intel Xeon Processor E5-2630 v3

charge cloud between the pixels is dominated by the potential due to the drift rings (sec. 3.1.2). These structures are implemented almost identical on the two different DSSC sensor concepts.

Currently, the possibility to record calibration line spectra with high ADC resolution with DSSC prototypes and the final DSSC detector ladder systems (sec. 3.1) is being investigated. With this approach, the characteristic spectral response of the DSSC sensor pixels could be characterized without the need for additional, isolated sensor measurements.

6. Experimental calibration studies

6.1 Application of the proposed fit function data measured with 10 x 64 pixels of a DSSC prototype
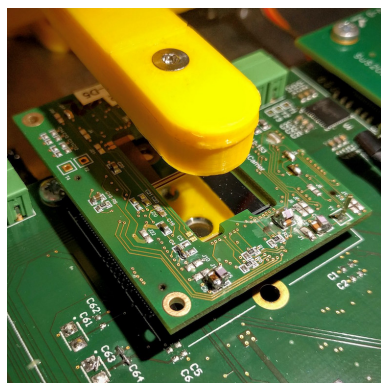
(a)
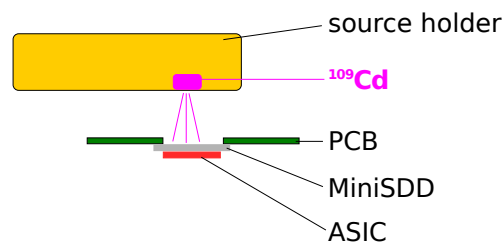
(b)
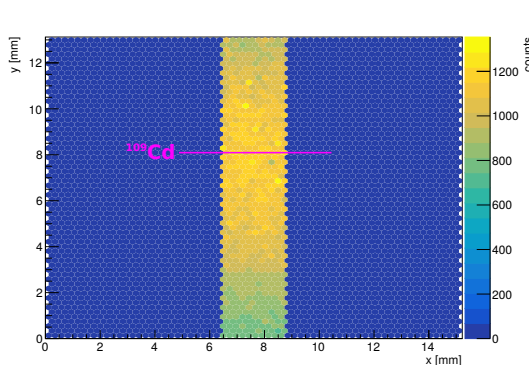
(c)
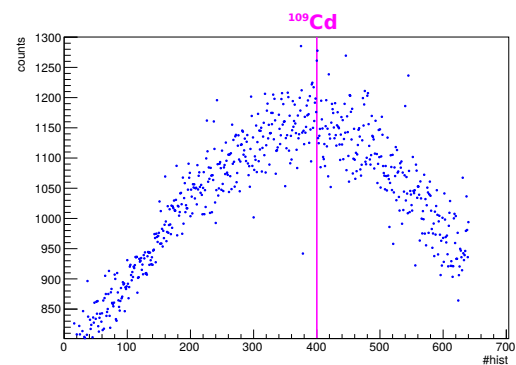
(d)

Figure 6.1: Measurement with an DSSC prototype ASIC (F1) and a MiniSDD sensor. The active sensor is the reflective surface in the center of the photo in panel (a). The reflection is due to the aluminum entrance window of the detector. In the reflection, the radioactive calibration line source, a ^{109}Cd pellet, can be seen. For this test, the source was mounted slightly off-center of the quadratic pixel matrix, as is illustrated in a sketch in panel (b).
Panel (c) shows a 2d-map of the stripe of 10x64 hexagonal pixels in the middle of the detector that were active during this measurement. Depicted are the number of "counts" in the K_α-line of the global fit function, i.e. parameter "peak1_norm" in table 5.2 in sec. 5.3.4. Panel (d) is a row-wise (left to right) representation of the plot in panel (c), starting from the lowest row.

In order to test the adaption of the proposed global fit function for single pixel calibration line spectra (sec. 5.3.2), a measurement was performed with a 64x64 pixel DSSC prototype (sec. 3.4.2) and then analysed. For the measurement, only one specific setting of the pixel read-out ASIC

was chosen, specified by the following properties (see sec. 3.1.3 and 3.1.4 were the DSSC read-out system is presented in detail):

- A strip of 10x64 pixels in the middle of the detector was operated. All other pixels readout chains were powered down.

- 2000 bursts of 800 frames each have been recorded. The signal flat top had a length of about 580 ns.

- The analog signal front-end of the read-out ASIC has been set to a medium feedback capacitor setting. A long signal integration time of about 90 ns has been selected.

- A pixel delay has not been set. The mean ADC gain was set relatively low, to a gain of about 0.5 LSB/keV (I_{ramp} setting 16, double ramp current).

- The ADC binning has been determined before the measurement with the help of a DAC-sweep.

- The ADC gain setting and the current compensation setting have been trimmed before the measurement in order to provide as much homogeneity between the individual pixels as possible.

Fig. 6.1 shows an overview of the measurement, together with a photo of the source holder and a sketch illustrating the spatial arrangement. The most relevant result from the data analysis is given in panel (c) and (d): By applying the measured binning information and with help of the global fit-function, the asymmetric distribution of photon signal on the detector surface could be assessed. The asymmetry is expected due to the slightly off-center position of the radioactive source.

The detector was irradiated with a ^{109}Cd source with an activity of about 1.6 ± 0.2 GBq in reference to the data sheet ([64], [65]) at a distance r of about 1.3 cm from the detector, assuming a fluorescence yield of about 85%. Each detector pixel has a surface A_{px} of about $4.80 \cdot 10^{-4}\,\mathrm{cm}^2$. The expected incident photon rate R_{px} in each pixel per second can be calculated with

$$R_{\mathrm{px}} = 0.85 \cdot 1.6 \cdot 10^9 \frac{\gamma}{s} \cdot \frac{1}{4\pi} \cdot \frac{A_{\mathrm{px}}}{r^2} \sim 3.0 \cdot 10^4\,\gamma/\mathrm{px}/s \tag{6.1}$$

with r being the distance between radioactive source and detector. The total measurement time T_{meas} can be calculated by multiplying the flat-top time with the number of frames and the number of bursts. With this calculation, the number N_γ of detected X-ray photons in each pixel for the complete measurement can be estimated to be

$$N_\gamma = q_e \cdot R_{\mathrm{px}} \cdot T_{\mathrm{meas}} = 0.3 \cdot 3.0 \cdot 10^4\,\gamma/\mathrm{px}/s \cdot 2000 \cdot 800 \cdot 580 \cdot 10^{-9} s = 8.4 \cdot 10^3\,\gamma/\mathrm{px} \tag{6.2}$$

with a detection efficiency q_e of about 30% for the given energy levels.

Fig. 6.2 shows a fit to the spectrum of the most upper right of the 640 individual pixels that have been analyzed. As a simplification, the fit has been performed with a fit-function with only
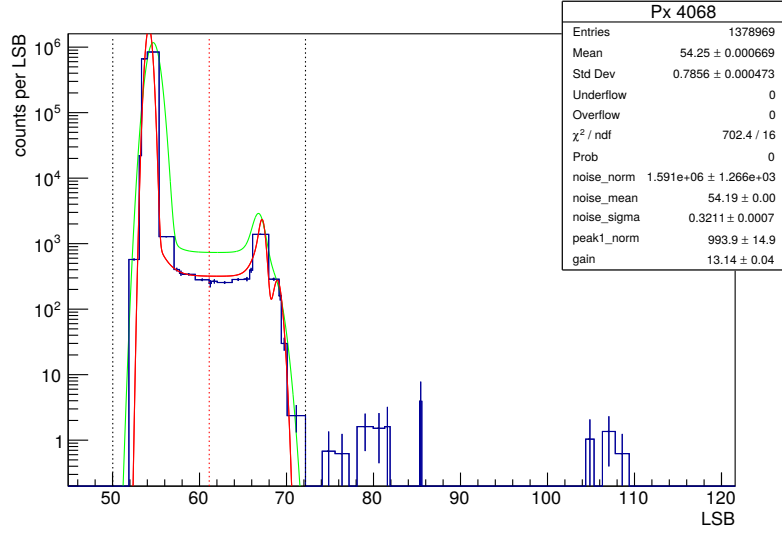
Figure 6.2: Example of one of the 640 individual fits performed for this measurement. The start values are given in green, the fit function is given in red. The black dashed lines mark the fit range, the red dashed line marks the middle of the fit range.

two discrete calibration lines as proposed in sec. 5.3.4 for ^{55}Fe spectra. In this case, (rounded) line energies of 22 keV and 25 keV for the combined K_α and K_β lines have been applied with a fixed line_ratio S_l of 0.14. The shape of the fit function was determined with shaping and scaling parameters (table 6.1) that have been determined on the basis of an older ^{55}Fe measurement performed with the SPIX setup (sec. 3.4.1). The scaling parameters are:

Name	Symbol	value
peakt_amp	N_t	1.4
noise_tails	S_{tnoise}	0.8
peakp_amp	N_s	3.7
line_ratio	S_l	0.14

Table 6.1: Scaling parameters of the fit-function used for fitting the ^{109}Cd measurement. In accordance to the applied global fit function (sec. 5.3.2), these parameters are without unit. They are the scaling factors and describe the quantity of photons in the respective spectral features in reference to the number of photons in the K_α peak $N_1 =$ peak1_norm.

The highest photon count in fig. 6.1 panel (c) and (d) is around 1200 for the parameter N_1 or "peak1_norm" (table 5.2 in sec. 5.3.4). The number of X-ray events $N_{\gamma,\text{spec}}$ in each individual spectrum can be calculated by referring to equations 5.15 to 5.21 and eq. 5.26 by:

$$N_{\gamma,\text{spec}} = \left(N_1 \cdot \left(1 + N_t + S_{\text{tnoise}} N_t + N_s\right)\right)\left(1 + S_l\right) \sim 1 \cdot 10^4 \gamma \qquad (6.3)$$

This result is in good agreement with the expected photon count (eq. 6.2), considering the large error margin on the activity of the ^{109}Cd source and the measurement of the distance to the detector. It has to be noted though that this study was intended to be a proof of concept, both

for the setting into service of a copy of the prototype detector setup (sec. 3.4.2) and irradiation of the detector with ^{109}Cd, as well as the application of the global fit function could be tested on the measured dataset. In this case it was used to determine system offset, noise and gain "in one go" as described in sec. 5.3.9.

Fig. 6.3 shows additional results from the analysis of the spectra with the global fit function. The following effects ([66]) can be identified in the dataset:

- The offset (panels a and b) shows a mostly homogeneous distribution over the active part of the detector. The mean is approximately 56 LSB. Down the center, a column of pixels is showing a slightly higher offset. For this chip generation, such an effect can be caused by an error in the setting of the ADC start value.

- The gain (panels c and d) can be assessed both in units of LSB, i.e. the distance between the noise peak and the K_α line, and in units of LSB/keV. It shows a sligth decline starting from lower pixel rows towards upper rows. This is expected due to the inevitable supply voltage drop across the detector matrix. The voltage supply lines start at the lower rows of the detector, providing these rows with a slightly higher operation voltage. The gain of the input transistor of the analog signal front-end is correlated directly to this voltage: The higher it is, the higher the pixel gain.

- The system noise (panels e and f) is given in electrons ENC. This calculation includes both the fit providing the width of the noise peak in units of LSB and the pixel gain in units of LSB/keV. Using $\epsilon_{e/h} = 3.63\,\text{eV}$ (sec.3.1.1) the energy equivalent of the noise peak can be converted to this measure. The noise increases slightly for higher pixel rows. As the electronic system noise is dominated by the input transistor, this behavior can also be explained by the supply voltage drop: The lower the supply voltage for the analog front-end of the read-out ASIC, the higher the electronic noise.

This example shows that the offset, gain and noise value of the DSSC detector can in principle be determined by applying the global fit function. For this study only one specific ASIC setting was measured. A calibration as proposed in sec. 3.3.2 based on the comparison of multiple gain and offset settings was not performed, as a method to experimentally cross-check the resulting calibrated setting was not available for the setup configuration employed in this measurement. The following chapter will provide the result of such a cross-check, performed with the configuration the system proved to operate most stable in.
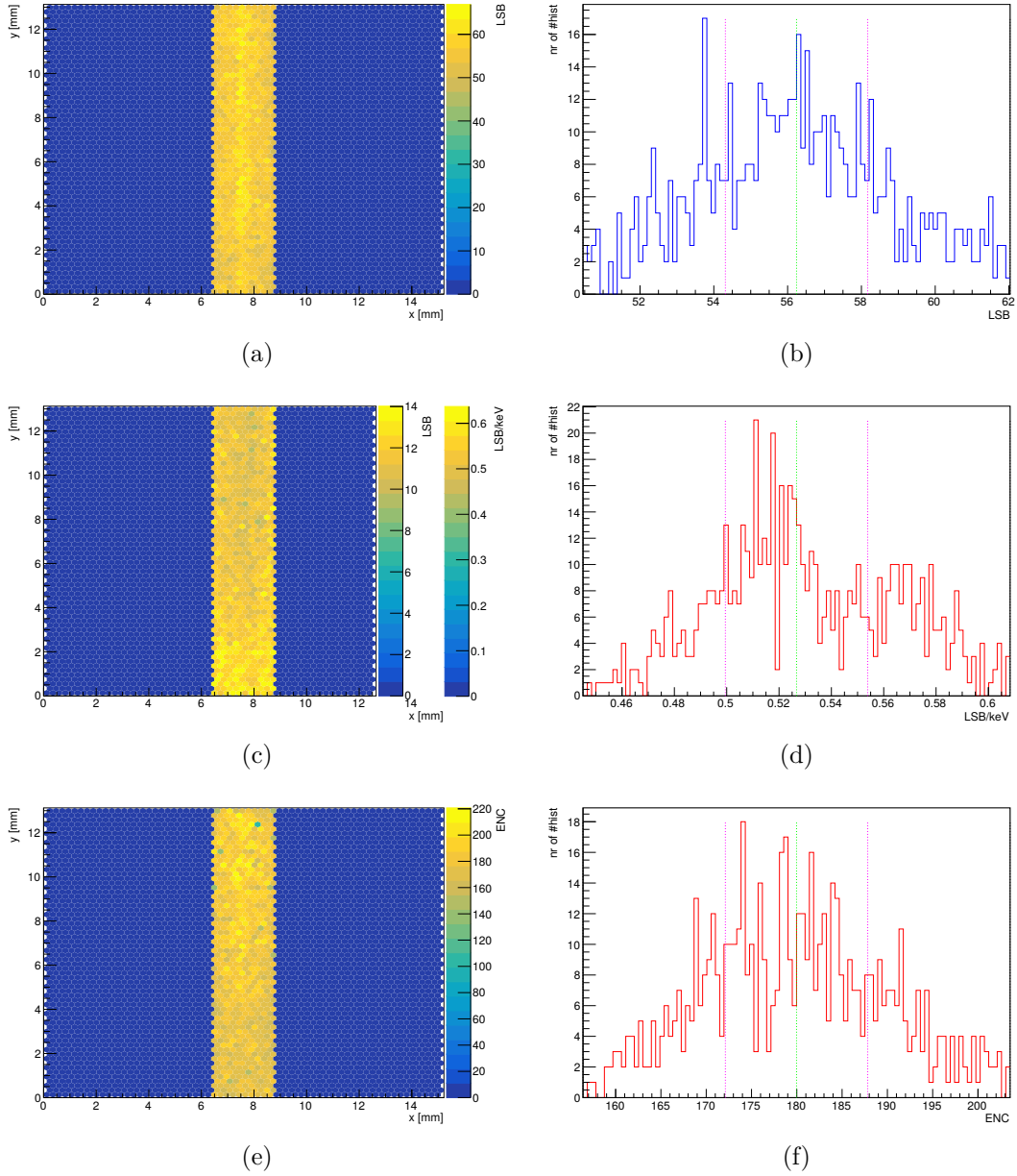
Figure 6.3: Results obtained with the global fit-function, plotted pixel-wise in a 2d map (left column) and as histograms (right column):
(a), (b): offset
(c), (d): determined gain in LSB and LSB/keV
(e), (f): system noise in ENC

6.2 Cross-check of the NLSR calibration with protons

A proof-of-concept of the two-step calibration approach for the non-linear system response (NLSR) has been performed in November 2016[1] at the INFN LABEC[2] proton beam line "DEFEL" (**DEF**lettore **EL**ecttrostatico = **EL**ectrostatic **DEF**lector, [67]) in Florence, Italy.

Irradiating the DSSC with protons with a momentum in the low MeV/c range provides a well determined energy deposition close to the surface of the silicon sensor material (sec. 3.1.1, fig. 3.5). The ensuing signal charge cloud is therefore similar to irradiation with X-rays of a low energy (keV range) and a high intensity. Thereby, the conditions of the foreseen scientific experiments at XFEL can be simulated experimentally.

For the experiment, protons with a kinetic energy in the order of 1 MeV were generated. Using nominal detector settings, this energy is in the upper range of the linear section of the non-linear system response of the F1 MiniSDD prototype detector that was operated at the beam line. The motivation of the experiment at LABEC is to cross-check this approach by assessing the accuracy of the resulting calibration at high energies using an independent absolute energy reference.
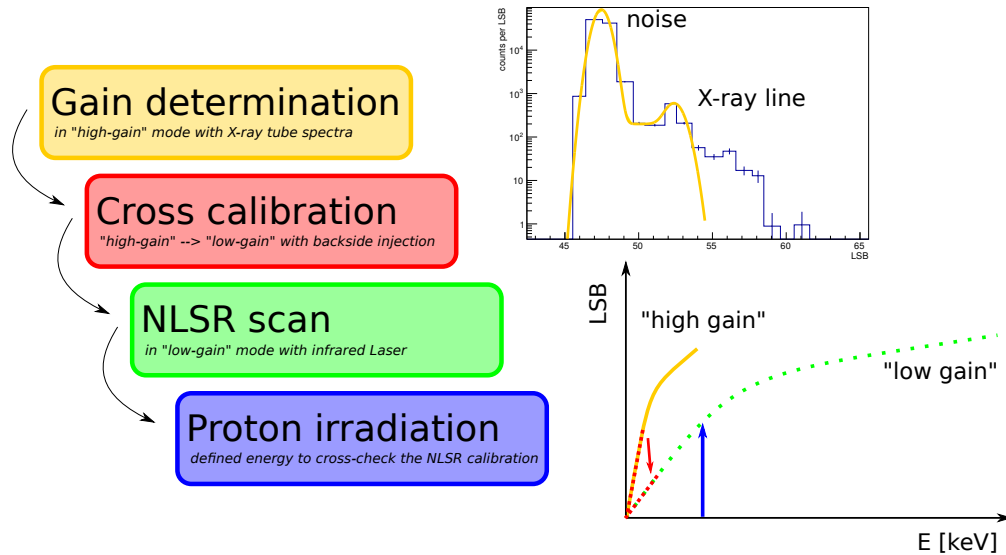
Figure 6.4: Overview over the individual steps performed at the INFN LABEC proton source in order to cross-check the NLSR calibration of the DSSC detector prototype.

Fig. 6.4 gives an overview of the individual measurements that were performed in order to assess the accuracy of the NLSR calibration approach in form of a cross-check.

- In order to determine the detector gain at low energies as explained in detail in [68], the spectrum of an X-ray tube with a Molybdenum anode, equipped with filter foils of Molybdenum and brass was employed. The gain determination was based on the position of fluorescence lines of the X-ray tube anode respectively the resulting, filtered Bremsstrahlung spectrum featuring the K-edge of the filter material in individual pixel spectra (sec. 6.2.2).

---

[1]Participants of the experiment were A. Castoldi, C. Guazzoni and S. Maffessanti (all Politecnico di Milano), J. Soldat (Univ. Heidelberg) and G. Weidenspointner and the author of this thesis (both European XFEL GmbH)

[2]Instituto Nazionale di Fisica Nucleare - Laboratorio di Tecniche Nucleari per l'Ambiente e i Beni Culturali

- To scan the non-linear system response (NLSR), a combination of so-called backside pulsing and an external infrared laser system were used (sec. 6.2.3). The backside pulsing is a method of sensor-internal signal charge generation. It was used to perform a cross-calibration between the "high-gain" setting of the detector suitable for the gain determination with the X-ray tube and a "low-gain" setting used for the proton measurement. This cross-calibration was necessary, as the dynamic range of the prototype detector in the "high-gain" setting did not suffice for recording the proton signal due to the earlier onset of system saturation.

- The proton beam was extracted from the high-vacuum beam line into ambient air by means of a beam window, due to the DSSC prototype setup not being vacuum proof. The energy loss of the protons due to straggling in the window and traveling through the air has been characterized in a previous measurement [69]. A calibrated reference diode detector was aligned such that its distance in direction of the beam from the beam window was identical to the distance of the prototype detector within measurement uncertainties. Thereby, the effective energy deposition by the protons could be characterized with a high degree of accuracy.

Fig. 6.5 illustrates the experimental setup used at the beam line. Due to stability constraints (sec. 6.2.2) of the prototype setup, a grid-search for the ideal calibration setting as proposed in ch. 5 was not performed.

6.2.1 The proton beam

The key properties of the proton beam at LABEC that motivated the experiment with the DSSC prototype are the following:

- The kinetic energy of the proton beam is tunable in the range of 1 to 5 MeV. Protons with a low kinetic energy are suitable for cross-checking the calibration of the non-linear system response, as they deposit all their kinetic energy in the sensor due to their low range and thereby generate an electronic signal.

- Due to its electrostatic beam steering the LABEC DEFEL beamline provides the possibility to finely control the number of particles in each pulse and can provide a highly focused beam spot of the size of 100x100 μm. For the experiment performed with the DSSC prototype, the beam line was tuned to provide one proton per pulse on average. Unfortunately, the quality of the focus at the time of the measurement was degraded slightly due to a recent maintenance of the accelerator.

- With the help of slit apertures and a fast electrostatic chopper it is possible to create a pulsed proton beam [67]. By synchronizing the DSSC sequencing to the proton beam it can be ensured that the resulting signal is processed correctly by the DSSC ASIC. In the experiment, the synchronization was done such that the proton beam hit the detector at one of the 800 frames of a read-out burst, i.e. a frequency of 10 Hz.

(a)

(b)

(c)

(d)
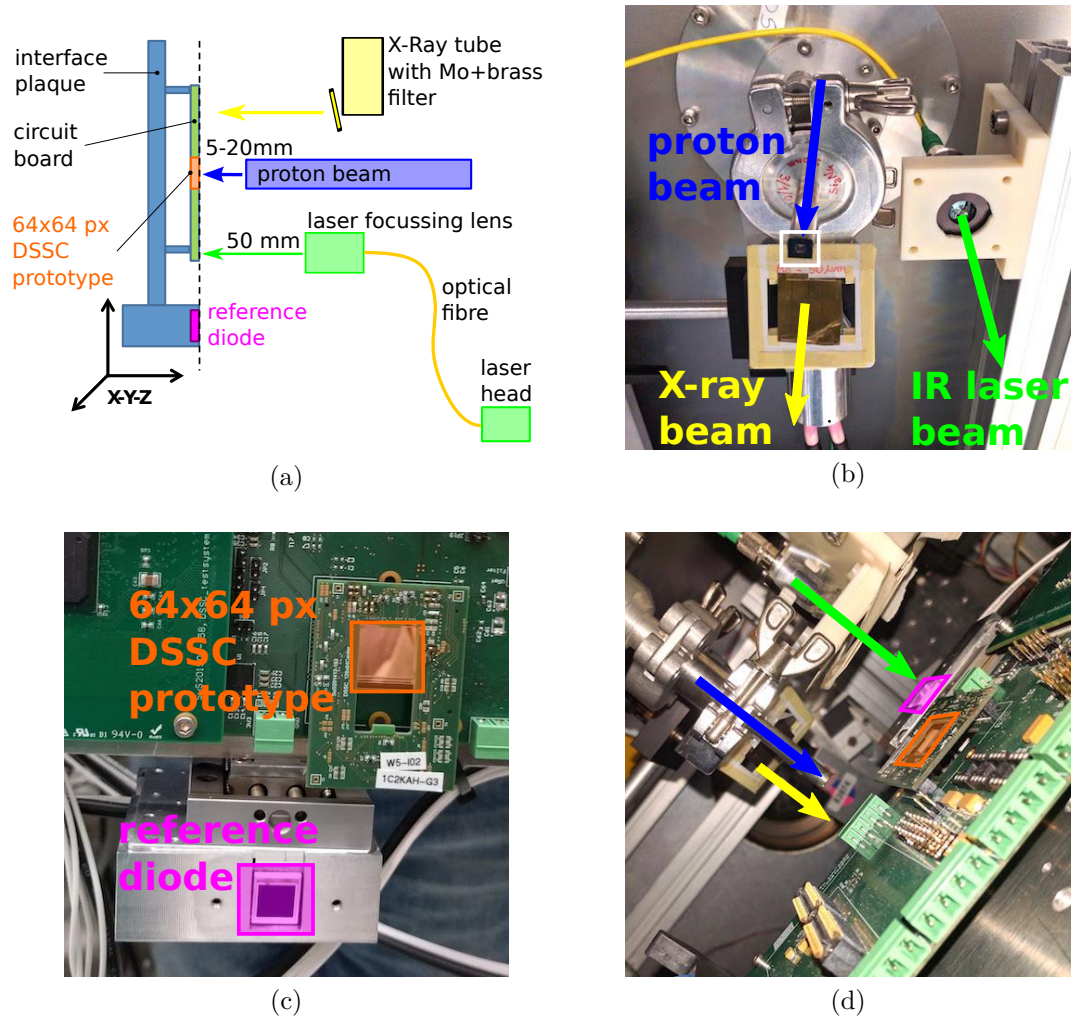
Figure 6.5: Overview over the orientation and geometry of the calibration experiment performed at LABEC:

(a) Prototype detector and the reference diode were aligned (dashed line) and mounted on a common steel interface plaque (light blue) that could be moved parallel and perpendicular to the proton beam by moving stages. Thereby, the combination of irradiation source and detector could be chosen freely from a remote terminal.

(b) The three individual irradiation sources as seen from the viewpoint of the detectors. The white square marks the beam window used to extract the proton beam.

(c) DSSC prototype and reference diode aligned and mounted on the interface plaque.

(d) View from above showing detectors and irradiation sources.

115

A sub-matrix of 10x10 pixels of the 64x64 pixel matrix detector was activated and irradiated. In order to identify the pixels with the highest signal due to incident protons, the difference between the frame isochronal to the proton pulses and the mean of the 799 other frames of each burst was calculated, as illustrated in fig. 6.6. This offset-corrected signal is then integrated for all bursts of the measurement. A visualization of the proton beam based on this calculation is given in fig. 6.7. The beam profile can be assessed by the integrated signal in each pixel by a correlation with the pixel coordinates. Fig. 6.8 shows the result of Gaussian fits to projections of the pixel rows (direction x) and columns (direction y) on the respective axis.
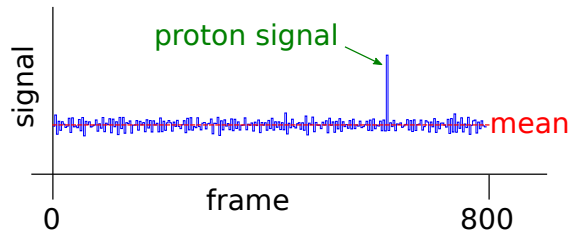
Figure 6.6: Schematic illustration of the method used for assessing the signal due to irradiation with protons. The number of the frame isochronal to the proton pulse is known due to the synchronization of the setup with the proton source. The mean of all other frames is subtracted from the output value of this frame.
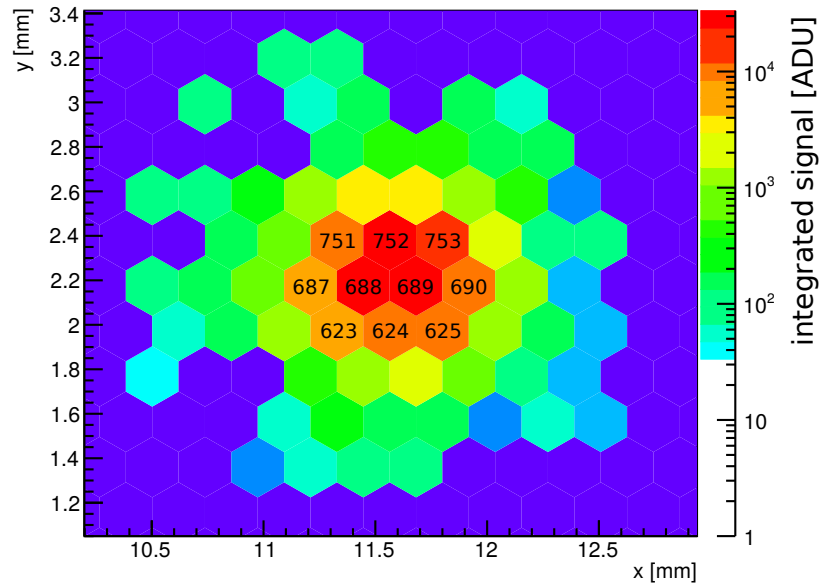
Figure 6.7: 10x10 pixel sub-matrix of the DSSC detector prototype irradiated with protons in the low MeV range at LABEC. The numbers 623-753 indicate the sub-set of 10 pixels that show a high enough signal for later analysis (Coordinate model for hexagonal pixels provided by University of Heidelberg).

At LABEC, three individual measurements with protons could be conducted, each comprising 7000 bursts, correlating to a measurement time of approximately 12 minutes each. In two of
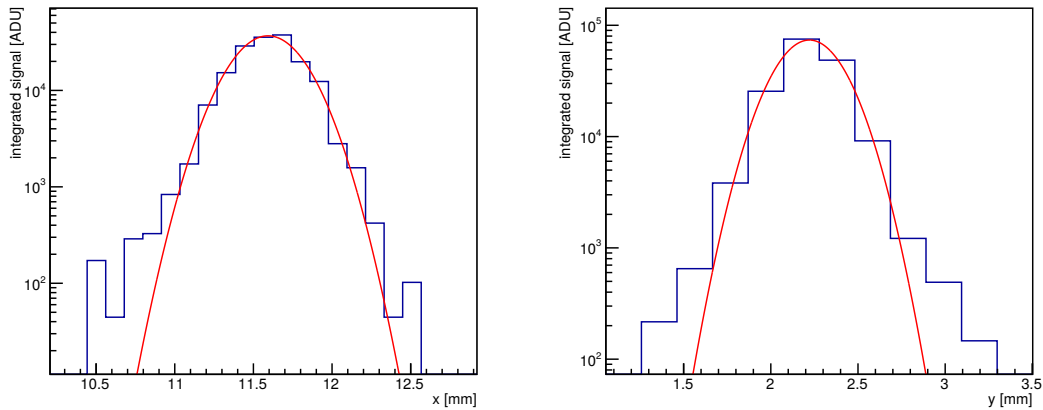
Figure 6.8: Quantification of the spatial distribution of the proton signal of fig. 6.7. The standard deviation of the (roughly) Gaussian beam profile is approximately 0.2 mm in direction x and 0.18 mm in direction y.

the measurements the distance of the detector to the beam pipe exit window was approximately 20 mm. In a third measurement, the distance was reduced by 2 mm in order to provide a different proton energy due to less straggling of the protons in the ambient air. Fig. 6.9 shows the three resulting proton spectra of one of the central pixels (688). In order to determine the position of the proton signal in the spectra, the proposed global fit function (sec. 5.3.2) has been applied to cope with the low energy trough that originates from charge sharing.

For the fits, most of the parameters of the global fit function were not fixed to predefined values, as the relative resolution of the proton peak is high enough. Also, defining a predefined shape for the "proton"-trough as described in sec. 5.3.1 is complicated for the following reasons:

- The characteristics of charge sharing between the pixels depends on the process generating the signal charges ([53]), such as the interaction depth in the silicon bulk or the amount of deposited energy. These effects alter the shape of the signal charge cloud, leading to a different propagation in the potential field of the detector.

- The irradiation with the proton beam is too inhomogeneous for the group of pixels that have been analyzed (fig. 6.7). The individual pixels show different trough shapes depending on their position in the group.

In addition, the proton measurements at LABEC were limited by time constraints and the stability of the prototype DSSC setup. Due to the low number of counts caused by proton irradiation, the unclear spectral response of the individual pixels and the high number of free fit parameters, the calculation of the error matrix by `MINUIT` fails in some cases, signifying a fit with poor convergence (sec. 5.1.2). The fit must therefore be taken as a rudimentary approach for the determination of the proton peak positions in the DSSC output data.

Figs. C.1 to C.3 in the appendix show the complete set of fits to the proton spectra recorded at the beam line for all 10 pixels. Based on the fit results, the error on the determination of the position of the proton peaks can be assessed by the following individual considerations:
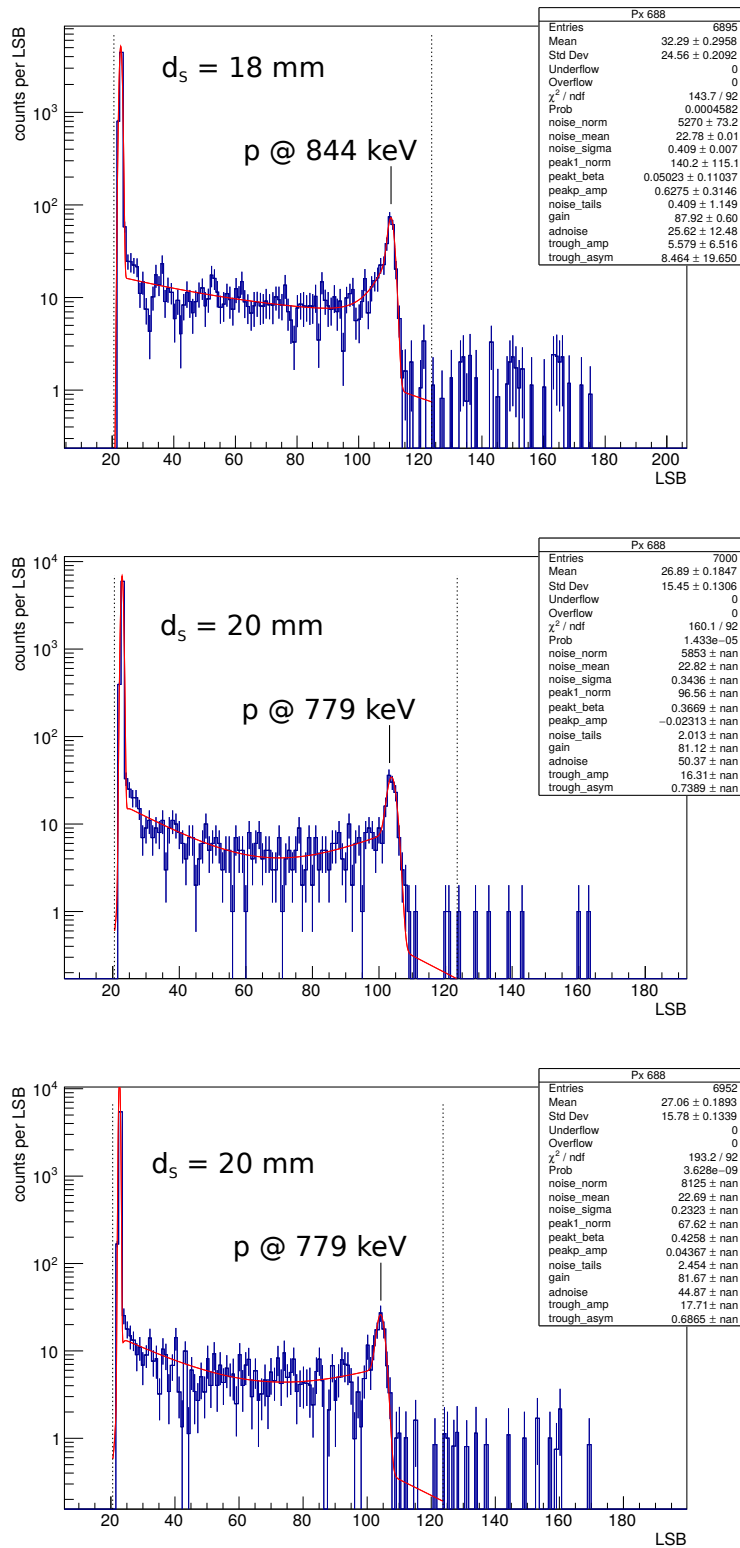
Figure 6.9: Spectra of pixel 688 after irradiation with the proton beam. Each plot represents the result of one of the three individual proton measurements. The "gain"-parameter is in units of LSB and corresponds to the distance of the proton peak to the noise peak. The fits have been performed after applying bin-boundaries determined in a previous step by an internal DAC sweep (sec. 3.2.1).

- The median fit error (result of `MINUIT`) of the "gain"-parameter is approximately 0.5 LSB.

- The median difference in the "gain"-parameter between the two proton measurements with identical distance to the beam window and therefore identical proton energy is approximately 0.5 LSB.

- The uncertainty due to ADC binning effects can be assessed by comparison of fits with and without binning information taken into account. The median difference in the "gain"-parameter of this comparison is also approximately 0.5 LSB.

The error of the fit-based position determination of the proton peaks is therefore expected to be slightly higher than 0.5 LSB.

6.2.2 Pixel gain determination with X-ray tube
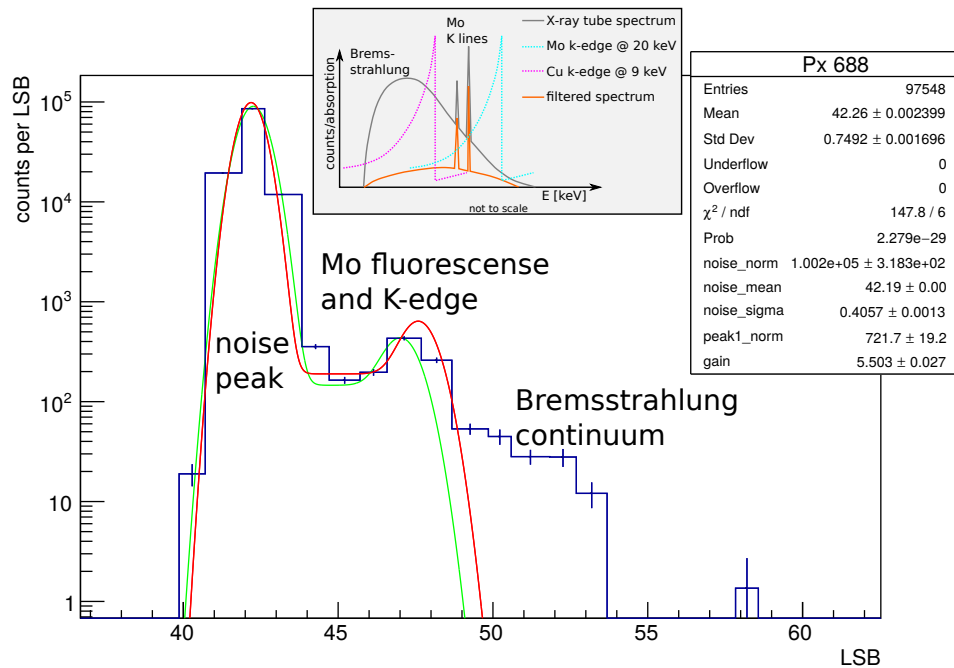
Figure 6.10: X-ray tube spectrum recorded with pixel 688 of the DSSC prototype. The applied fit model is based upon a simulation of molybdenum fluorescence as given in fig. 6.11 (c). The "gain"-parameter in units LSB relates to the distance of the combined K-line peak to the noise peak. In this example, the peak energy of 17.78 keV results in a pixel gain of approximately 3.2 keV/LSB. Together with the result of "noise_sigma", the system noise calculates to approximately 360 ENC.

The pixel gain calibration in the lower region of the dynamic range of the pixel characteristic has been performed by analyzing calibration line spectra generated by irradiation of the DSSC detector prototype with an X-ray tube. The tube was equipped with a Molybdenum target anode, its output was additionally filtered (so-called "beam hardening") by a brass and a Molybdenum filter. Fig. 6.10 shows an example of a fit to the measured data. The small inlay plot visualizes the effect of the filtering of the X-ray beam: Due to the high absorption at the K-edges of copper (brass) and molybdenum, the Bremsstrahlung continuum is attenuated which increases the line-to-continuum ratio.

Due to stability problems with the detector prototype, the intrinsic detector noise was dominated by a non-statistical effect (a sinusodial, electronic oscillation). A value of approximately 470 ENC mean system noise of all analyzed spectra at the time of the measurement was determined, which is very high in comparison to most of the preceding theoretical and experimental studies. In order to cope with this problem, the following method was used to assess the detector gain:

1. In a first step, spectra representing the two main components of the filtered X-ray tube spectrum have been simulated: The molybdenum fluorescence and the Bremsstrahlung continuum with the absorption at the K-edge of molybdenum. Histograms with a high ADC resolution (similar to the SPIX setup, sec. 3.4.1) are given in fig. 6.11 (a) and (b). In

order to resemble the DSSC single pixel spectra, the characteristic charge sharing properties have been applied in the simulation leading to the low-energy trough known from measured spectra.

2. In the next step, the simulation has been modified by changing the system noise to 470 ENC (panels (c) and (d) of fig. 6.11). These spectra with high ADC resolution were then used to determine the characteristic shape of the global fit-function as described in sec. 5.3. As the individual features (fluorescence lines, K-edge) disappear due to the high detector noise, the complexity of the fit-function was reduced:

   - Only one calibration line peak has been included.
   - The trough components described as "tails" (sec. 5.3.1, eq. 5.19 and eq. 5.20) have been omitted.

   The information that can be gathered from the spectra with the high detector noise would not suffice to determine the respective parameters of the through components and the second calibration line tail.

   The resulting fits are also given in panels (c) and (d) of fig. 6.11. As the "gain" of the simulated spectra and the offset position are known (keV/ADU), a "virtual" calibration line energy can be assigned to the fitted peak of the respective spectrum. This peak energy is 17.78 keV for the molybdenum fluorescence lines and 18.42 keV for the Bremsstrahlung k-edge, as indicated in the plots.

3. The gain of the individual pixels was then determined by fitting the characteristic spectral shape assessed in step 2 to the measured spectra. By applying the corresponding energy of the peak of the global fit function, the gain value units of LSB/keV can be determined.

Three measurements with identical properties and settings have been conducted with the X-ray tube at the LABEC beam line. To evaluate the system stability, two different observations based on the recorded data can be made:

- **The mean SRAM content**: For each of the 800 SRAM cells, the mean value of all bursts of the measurement can be calculated. This concept is explained in fig. 6.12. With this technique, intra-burst instabilities in the sub-ADU range can be resolved. These instabilities are mainly due to settling behavior of the building blocks of the read-out ASIC, due to the ASIC biasing being turned off between bursts.

- **The burst mean value**: By calculating the mean output value of each burst, a drift of the overall system offset from burst to burst (so-called "inter-burst", long-term variation) can be visualized.

The methods used for the stability assessment of the prototype setup operated at LABEC are detailed for the central pixel with number 688 in fig. 6.13. Intra- and inter-burst instabilities cause strong deviations from an ideal system behavior which impedes further data analysis. Panel (c) shows the main cause for the very high detector noise: The prototype shows strong oscillations
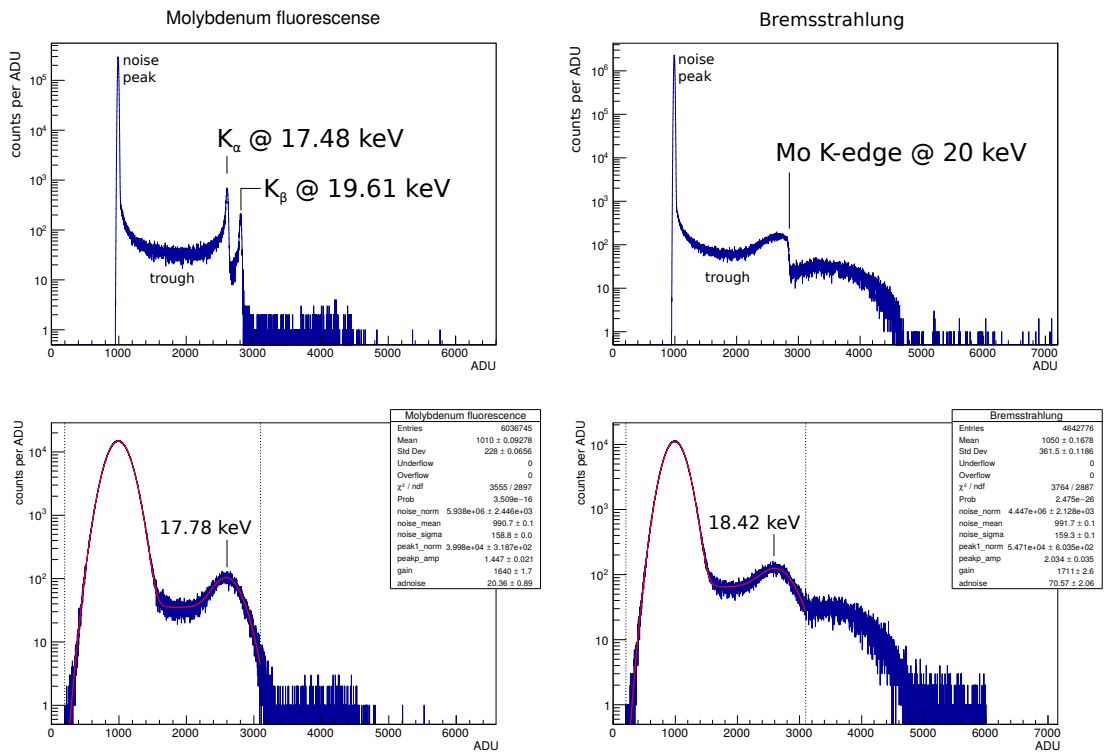
Figure 6.11: Simulated template spectra used for the determination of the fit shape applied to the recorded X-ray tube spectra. Above: Spectra with low detector noise (similar to SPIX). Below: Detector noise of 470 ENC.
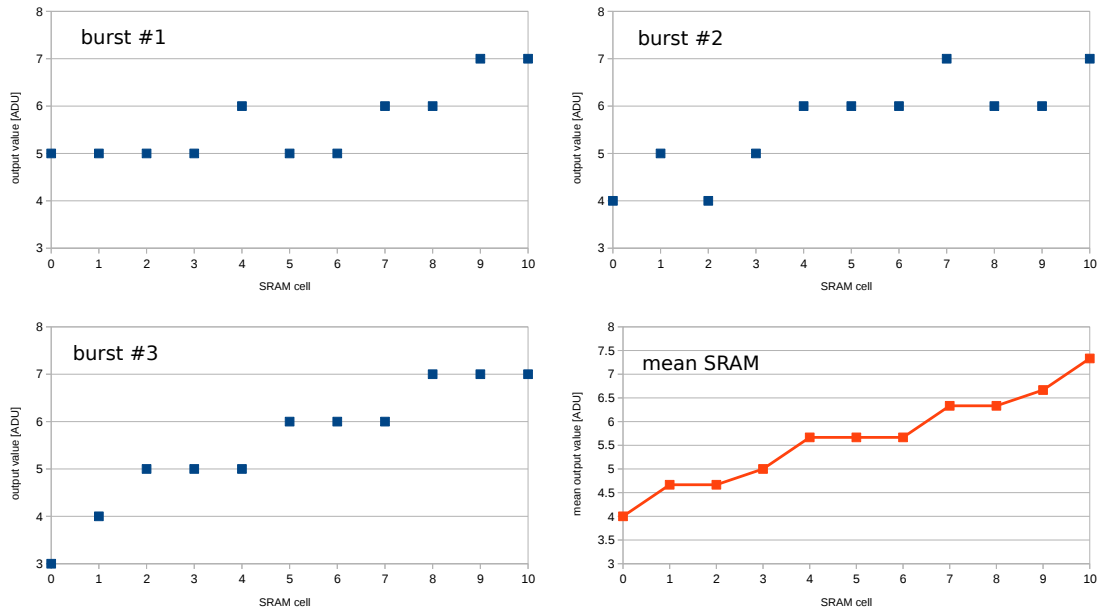
Figure 6.12: Calculation of the mean SRAM: In this example, three individual bursts with 10 SRAM values each have been recorded. As the system records only integer ADU values, the mean of each SRAM cell can be used to visualize intra-burst trends due to settling behavior.

(~ 1 ADU) with a periodicity of about 20 individual frames. In order to assess the stability of the system gain and offset over the course of one SRAM burst, two individual data ranges have been selected. An overview of the results based on this selection is given in fig. 6.14. There the mean offset and gain values of all 100 active pixels evaluated from the measured spectra with help of the two different spectral shapes (Molybdenum fluorescence and Bremsstrahlung with K-edge) are compared for each of the three identical measurements with the X-ray tube:

- Both spectral shapes lead to a nearly identical determination of the system offset. This is expected, as the dominating portion of the spectra is given by the high number of counts in the noise-peak (compare fig. 6.10), and the correct position determination of the noise peak is improved by the trough-model given by the global fit-function.
  The intra-burst drift of the offset visible in fig. 6.14 panel (b) leads to the shift of approximately 1.5 ADU between the two selected SRAM ranges. The slow drift of the global offset that is already visible in fig. 6.14 panel (d) continues over the course of the three individual measurements.

- The system gain determination shows a dependency both on the selected SRAM range and the fit model. The gain determined with data from SRAM range A is slightly lower than for SRAM range B (difference in the order of 1%). A bigger difference can be assessed between the two different fit model: The gain determined with the shape based on Molybdenum fluorescence lines is about 5% higher than the gain determined with the Bremsstrahlung k-edge shape. The system gain remains relatively stable over the course of the three individual measurements.

To summarize, it must be noted that the gain determination based on the X-ray tube calibration line spectra in this study is impeded by three main detrimental effects:

- Due to stability constraints of the detector prototype, only a comparatively low gain could be selected for the gain calibration in the linear region of the NLSR. As sec. 5.3 has shown, a lower resolution always leads to a loss of accuracy.

- Due to time and stability constraints of the detector prototype operated at the LABEC beam line, the spectrum of the X-ray tube could neither be measured with high resolution nor with a reference detector. As a result, the line-to-continuum ratio is not known, nor the exact shape of the Bremsstrahlung continuum. Therefore, the global fit function could not be adapted ideally to the calibration energies. As an approach, a comparison of two fit-models (Molybdenum fluorescence, Bremsstrahlung k-edge) was performed.

- The high width of the noise peak caused by periodic oscillations of the setup reduces the accuracy of the gain determination.

It should be possible to reduce the error margin on the gain determination of the experiments conducted at LABEC by assessing the output spectrum of the X-ray tube with a measurement with a reference detector. Then the global fit-function could be adapted to this shape after a repetition of the simulation of the spectral response of individual DSSC pixel to this calibration source.
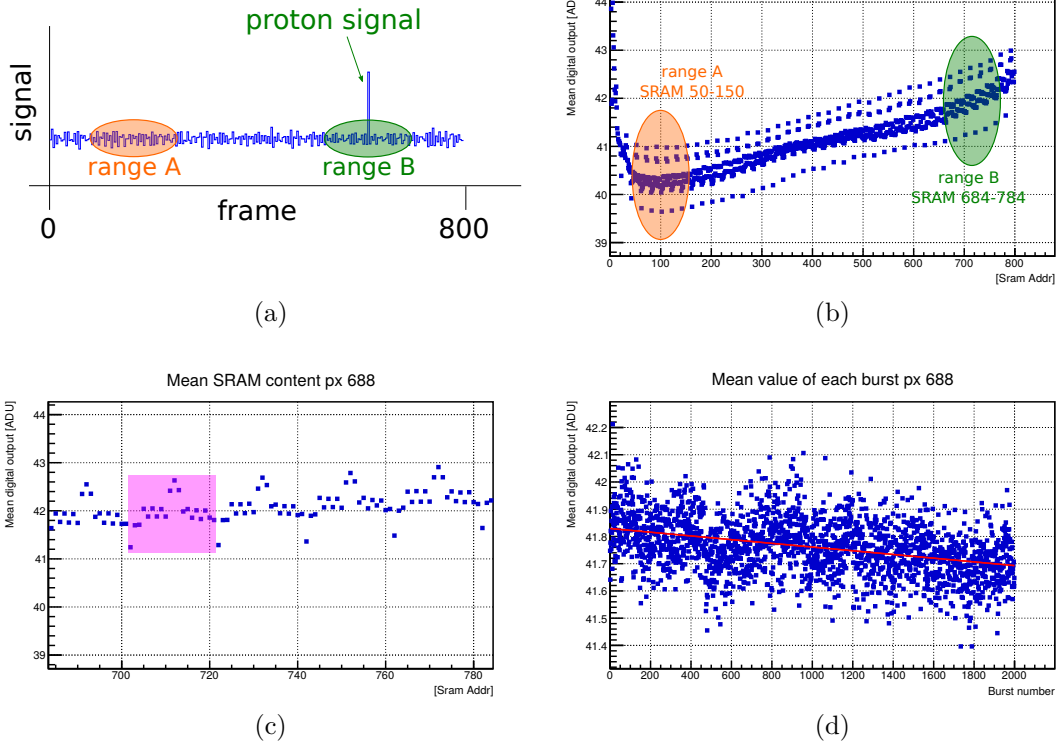
Figure 6.13: Measurements performed with the DSSC prototype at the LABEC beam line are affected by the poor system stability:

(a) Two different data ranges were selected for the gain determination. Range A (orange) is at the beginning of the burst, range B (green) is centered around the frame isochronal to the proton interaction.

(b) The mean SRAM content of each individual SRAM cell shows a distinct slope of over 2 ADU due to settling behavior.

(c) A zoom into "range B" of the mean SRAM content shows the strong periodic oscillations which are the reason for the high detector system "noise".

(d) The offset stability over the measurement duration can be assessed by the mean burst value. Over the course of 2000 bursts, the system drifted more than 0.1 ADU.
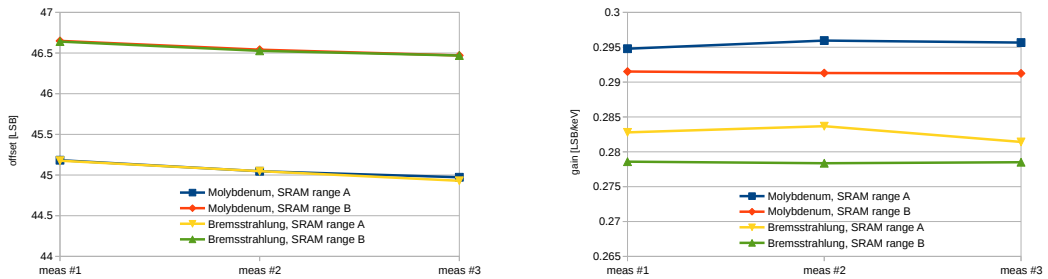
Figure 6.14: Fit-based offset and gain characterization for different fit models and SRAM ranges for three measurements performed with identical settings.

6.2.3   Cross-calibration and scan of the NLSR

The DSSC prototype detector was operated at the LABEC beam line in two different gain modes: A "high gain" mode suitable for recording spectra of the X-ray tube for the gain determination in the linear region of the NLSR, and a "low gain" mode suitable for proton irradiation. This was necessary, as the dynamic range of the "high gain" mode would not have been sufficient to record the protons generating approximately 800 keV energy equivalent per event.

After the determination of the pixel gain with the X-ray tube (sec. 6.2.2), the a part of the NLSR was scanned with the so-called "backside-injection" technique. Fig. 6.15 illustrates this technique in a (simplified) electrical circuit diagram: The negative (for depletion of the sensor, sec. 3.1.2) backside contact is connected to a pulse generator via capacitive coupling. By inducing a voltage pulse dV during the signal flat-top of the DSSC read-out sequence (sec. 3.1.4), a signal charge $dQ_{\text{sig.}}$ is generated inside the pixel. The size of the charge is relative to the equivalent capacity $C_{\text{eq.}}$ of the sensor pixel.
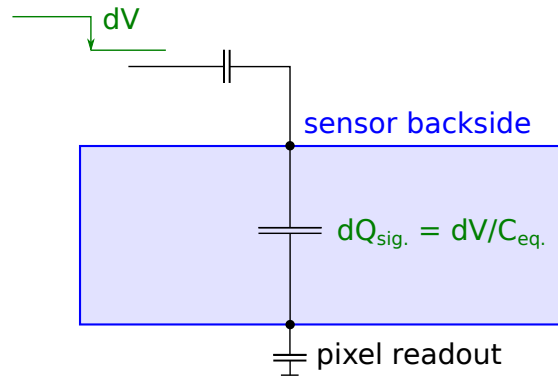
Figure 6.15: Schematic circuit diagram explaining electrical DSSC backside injection.

The upper two panels of fig. 6.16 show the results of backside-injection measurements for detector pixel 688, central to the proton beam. The voltage of the signal pulse to the backside contact of the sensor was altered in a range starting from 0 V up to 5 V in steps of 0.1 V. The uppermost panel shows the result for the "high gain" mode. The result of the same voltage sweep in "low gain" mode is given in the panel below[3]. As the charge generated by the backside injection has a linear dependence on the signal pulse voltage, the respective gain in ADU/V can be determined by a linear fit (red dashed lines) to the measurement points. By dividing the value for the "high gain" mode by the value for the "low gain" mode the so-called, dimension-less "cross-calibration" factor is calculated.

In the next step, the full non-linear system response (NLSR) of the DSSC prototype system was scanned by gradually increasing the intensity of an infrared laser irradiating the detector. In order to compensate any non-linearity introduced by the laser diode (e.g. due to temperature effects), the total laser output was measured with the reference diode sensor (fig. 6.5). It was assumed that the beam profile of the laser in the region of the irradiated DSSC detector pixels

---

[3]The step size of this voltage sweep is even fine enough to identify some of the ADC steps similar to a DAC sweep (sec. 3.1.4)
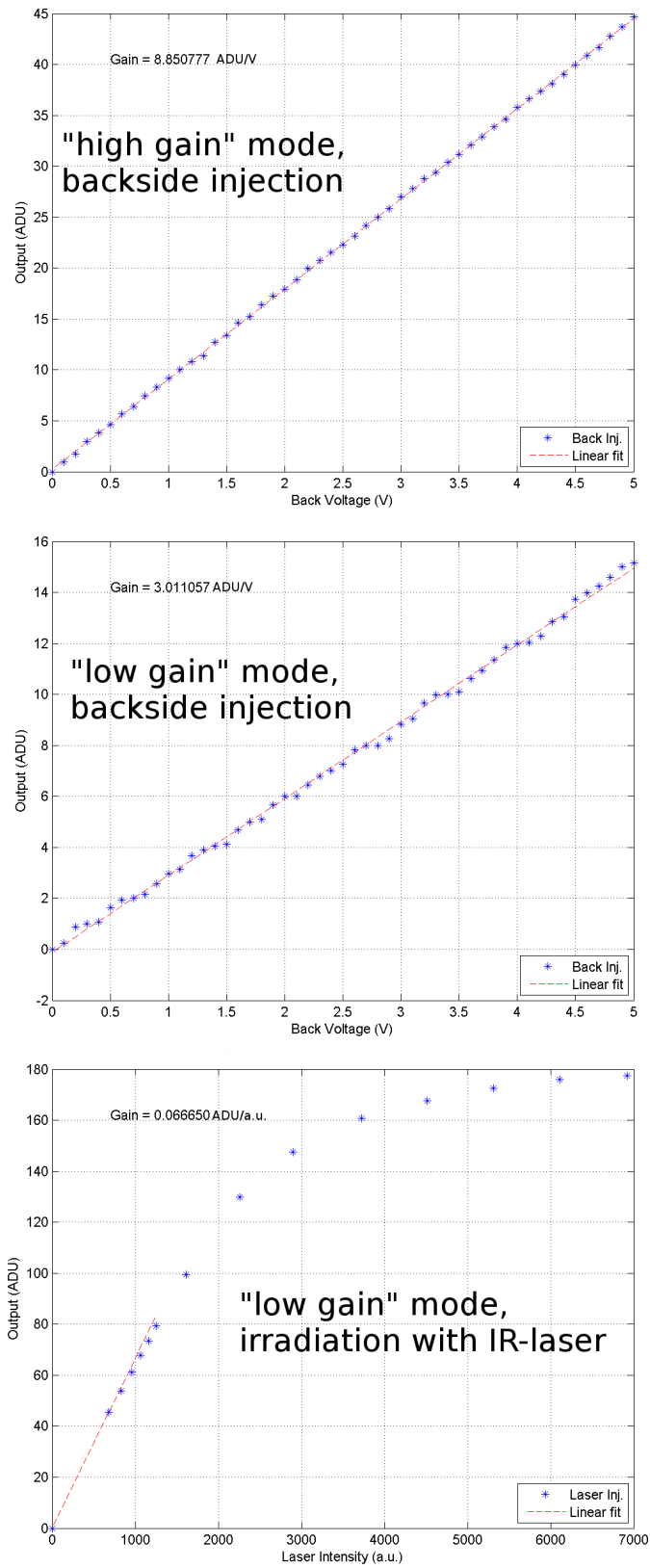
Figure 6.16: Determination of calibration factors. The output ADU values have been calculated as the mean of 11 read-out frames each. Graphic by S. Maffessanti, Politecnico di Milano.

does not depend on its intensity. If this is the case, the linearization given by the intensity measured with the reference diode is valid for the individual pixels.

The last panel of fig. 6.16 gives the output of the DSSC prototype setup (in ADU) depending on the measured laser intensity (in arbitrary units "a.u."). With a linear fit to the measurement points in the linear region of the NLSR (red dashed line), the "laser gain" factor can be calculated in units of "ADU/a.u.".

(a)

(b)

(c)

(d)
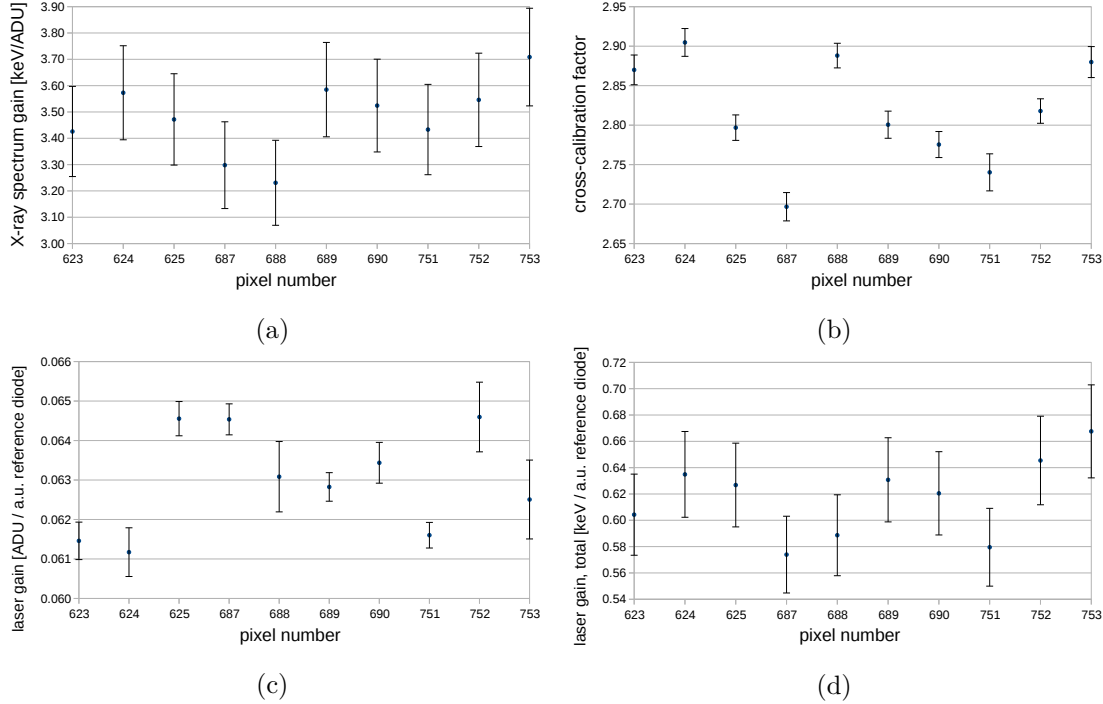
Figure 6.17: Overview of gain and cross-calibration factors for all 10 pixels.

Fig. 6.17 gives an overview over all measurements that in composition were used to determine non-linear system response in form of detector output (ADU) vs. signal energy (keV). The plots show the results of the 10 individual detector pixels analyzed in this study:

- In panel (a) the result of the gain calibration in the "high gain" mode based on the X-ray tube spectra (sec. 6.2.2) is plotted. The error bars correspond to the estimated error of the fit with the global fit function (sec. 6.2.2, about 5%).

- Panel (b) gives the cross-calibration factor determined by the backside-injection measurements in "high gain" and "low gain" mode. The error is calculated from the fit error of the two individual, linear fits.

- Panel (c) gives the "laser gain" factor for all pixels. It has been determined by fitting the first 6 laser intensity-settings. The error bar corresponds to the fit error.

- Panel (d) is the scalar product of panels (a) to (c). With the calculated factor, the energy calibration (units keV/ADU) from the detector "high gain" mode can be mapped to the

signal energy created by the IR laser that was linearized by the measurement of the reference diode (a.u.). With this combined gain factor, the energy calibration of the complete dynamic range of the NLSR can be assessed, similar to the proposed two-step approach (sec. 3.3.2).

6.2.4 Comparison of results and summary
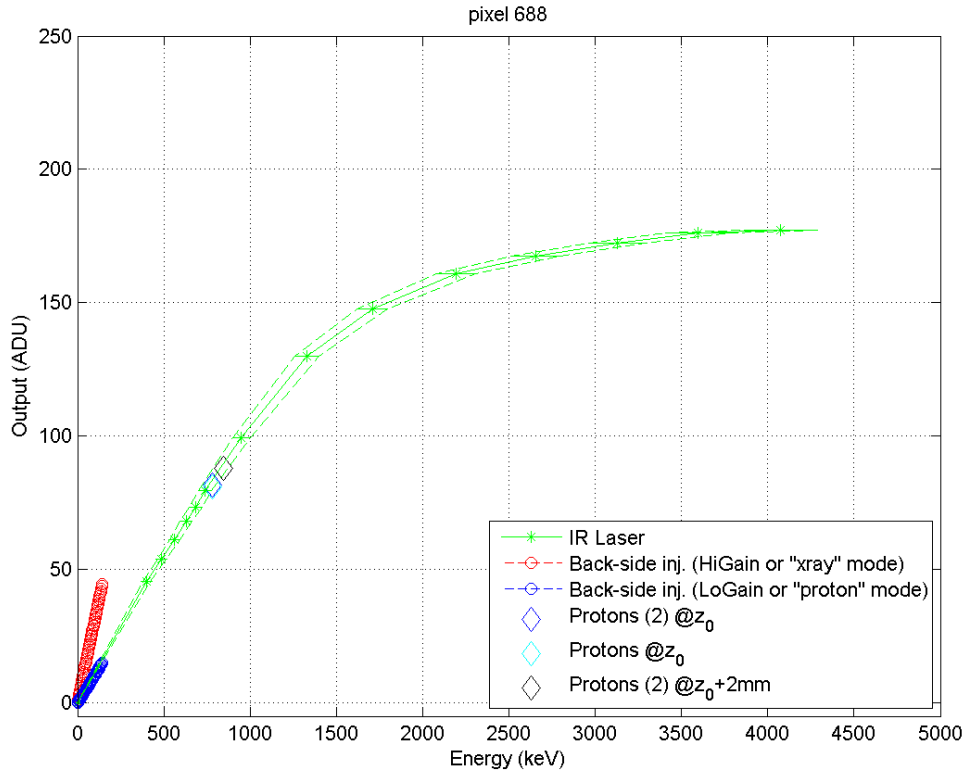
Figure 6.18: Example of calibration cross-check for an individual pixel. Graphic by S. Maffessanti, Politecnico di Milano.

Fig. 6.18 shows the energy-calibrated non-linear system response (NLSR) based on the gain determination with the X-ray tube (sec. 6.2.2) and the cross calibration with the backside-injection (sec. 6.2.3). The two sweeps with the backside-injection are given in small red and blue circles. The scan with the IR laser is given by the green stars and line. The two dashed green lines illustrate the accumulated error ($\pm 1\sigma$) from the individual steps of the calibration as detailed in the last section (panel (d) of fig. 6.17). The three individual proton measurements are visualized by the diamond shaped symbols. The energy level of these data points is obtained from the measurement with the reference diode, the ADU value is given by the fits to the proton spectra (sec. 6.2.1). A complete view on the results of the other 9 pixels analyzed in this study can be found in the appendix in fig. C.5.

Fig. 6.19 illustrates how the absolute energy deviation and the respective error can be
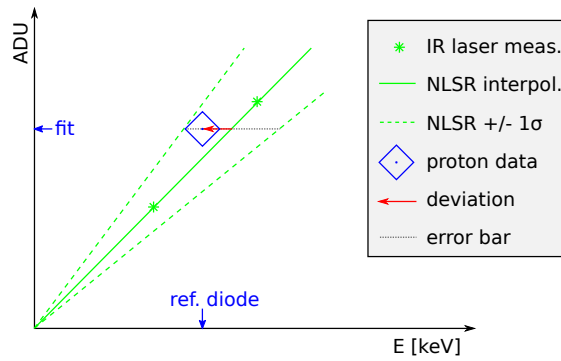
Figure 6.19: Schematic visualization of the determination of the deviation and the error in the amplitude and energy dimension.

determined from the data: The deviation is based on the linear interpolation between the laser measurement data points. It is calculated by subtracting the respective energy value given by detector output in ADU and the calibrated NLSR from the proton energy determined with the reference diode. The corresponding error is given by the $\pm 1\sigma$ envelope of the NLSR. Fig. 6.20 gives an overview over the energy deviation of the 10 pixels in the analysis.
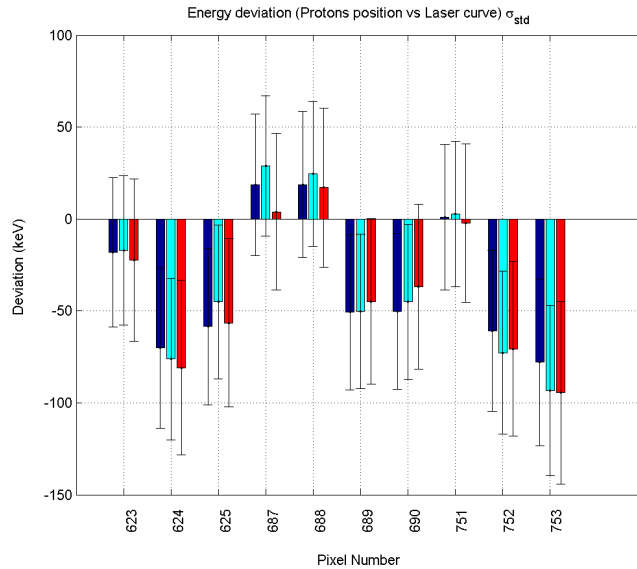
Figure 6.20: Overview of energy deviation. The three different colors visualize the three proton measurements:
Blue, cyan: Protons @ z_0 (distance 18 mm)
Red: Protons @ $z_0 + 2mm$ (distance 20 mm)
Graphic by S. Maffessanti, Politecnico di Milano.

The mean energy deviation of all 10 analyzed pixels is approximately -40 keV. That means that on average the proton energy determined by the measurement with the DSSC prototype setup is about 5% higher than the energy of the protons measured with the reference diode. Whereas the error of the latter measurement can be considered negligible due to the high precision

of the alignment of reference diode and DSSC prototype, the NLSR calibration shows a relatively high error that is dominated by the gain determination based on the X-ray tube measurements (sec. 6.2.2).

All pixels show deviations smaller than $\pm 2\sigma$ of the given error dimension, 30% of the individual pixel deviations are smaller than $\pm 1\sigma$. The study demonstrates that the proposed approach of the NLSR calibration based on X-ray fits and signal charge injection works in principle. As the DSSC prototype setup was operated at the LABEC beamline using settings (read-out sequencing, biasing) very similar to the operation modes that will be used at the European XFEL, the relevance of this result for the DSSC project cannot be underestimated.

7. Summary

The DSSC is a large-scale, ultra-fast, 2d megapixel imaging detector specifically designed for diffraction imaging in the low-energy regime (0.26 keV to 3 keV, corresponding to a wavelength of 4.7 nm to 0.4 nm) of the European XFEL light source that has started science operation in September 2017 in Hamburg and Schenefeld in Northern Germany. Unique scientific requirements of the foreseen experiments motivated its unique design that is based on the compression of the analog signal and will provide both single photon sensitivity and a high dynamic range of up to 10^4 photons at the same time. In order to fully exploit the high repetition rate of the X-ray flashes at the European XFEL, the DSSC can operate with a frame rate of up to 4.5 MHz. The combination of these features is achieved by equipping each individual sensor pixel with its own read-out chain providing analog filtering, signal compression, digitization and digital storage.

Due to unavoidable process inhomogeneities during the chip production process and the intrinsic low energy resolution (in ADC) of the DSSC, a pixel-by-pixel calibration of the more than one million individual pixels is required in order to provide the user of the instrument with the correct assignment of the digital output to the incident photon intensity. Because of the peculiar, non-linear system response of the DSSC a custom calibration approach had been proposed in [19] that is presented here in a form adapted to the latest experimental findings (sec. 3.3.2).

In the following list, the achievements and central aspects of this thesis are summarized:

- The central part of this work proposes and compares several methods for the offset and gain calibration of the DSSC and the characterization of the system noise. A custom, parametrized, analytical global fit function for the gain characterization in low-resolution single-pixel calibration spectra is proposed. This part of my work is published in [56] and [57].

- I have visualized the functional principle of so-called "split pixel events" and the forming of a low-energy "trough" between calibration lines and noise peak by implementing an illustrative, GUI-driven Monte-Carlo simulation approach (sec. 4.1). A comparison of simulated spectra with measured datasets shows good agreement in regions most critical for the gain characterization. The availability of this "toy-model" contributed to the development of the DSSC detector simulation software package [44].

- In the scope of this work, I developed and distributed an analysis and calibration software tool that makes use of modern multi-core computing systems, enabling the possibility to process large datasets. Its performance proofs the applicability of the presented methods to datasets comparable in size and complexity to the expected calibration data from the full megapixel detector. The presented methods for offset, gain and noise calibration of the DSSC proved to be robust even under adverse effects of erroneous or skewed ADC binning.

- I validated the proposed calibration methods by analyzing simulated datasets with my calibration software tool. Thereby, I could evaluate their performance by a comparison of the results to the settings of the simulation, i.e. the "simulation truth":

  - The most stable and accurate method to characterize the system noise is the so-called "error function method" (sec. 5.2.2). For the two different calibration goals (sensitivity to 1 keV respectively 0.5 keV photons) analyzed in the study, the standard deviation of the distribution of all results in all tested ADC binning environments is usually smaller than 2% of the peak width of the simulated data. For datasets simulating the conditions in the final DSSC detector system the noise can be characterized with a very high accuracy, usually deviating only a few percent from the simulated values. An assessment of different calibration strategies for individual combinations of achievable accuracy of the binning determination and expected DNL of the ADC is given in sec. 5.2.6.

  - The digital offset can best be calibrated by individual likelihood-fits to the respective data histograms (sec. 5.2.10). Even for the most adverse conditions tested in this study, approximately 99% of the results show a loss in accuracy not greater than 3‰, with none exceeding 25% of a bin-width – compared to the highest achievable offset calibration accuracy given by the simulation truth.

  - I could show that using the proposed global fit function and e.g. ^{109}Cd as a calibration source, the system gain can be determined with a systematic uncertainty lower than 0.5% (a deviation less than half of the setting granularity of 2%) in more than 99% of all cases. Similar to the noise characterization, an assessment of different ADC environments and ADC DNL properties is given in sec. 5.3.8.

- With the help of the developed tools, the proposed global fit function was applied to data I had measured with DSSC prototypes. In order to facilitate experimental studies, I developed a remote controlled, micro controller based manipulator[1] for radioactive pellet sources (sec. 3.4.2) and a setup temperature control system. In one example presented here (sec. 6.1), I was able to study gain and noise inhomogeneities on a 10 x 64 pixel matrix irradiated with a radioactive calibration source.

- The two-step approach of the calibration of the non-linear system response of the DSSC was verified in the scope of this work for 10 DSSC prototype pixels by a cross-check with accelerated protons serving as an energy reference (sec. 6.2). Using the proposed and tested methods for the DSSC gain determination, the achieved accuracy of this study is smaller than $\pm 2\sigma$ of the given error dimension, which is a good result for the DSSC prototypes available at the time of the measurement.

- During the preparation of the thesis I contributed to the development of the DSSC instrument by characterizing and confirming crucial operational properties of DSSC DEPFET prototype sensor pixels on a dedicated sensor test bench and DSSC system prototypes equipped with

---

[1] Great thanks to D. Pietschner (MPE) for the mechanical design.

DEPFET and MiniSDD test chips in experimental measurements. This part of my work is not documented in the thesis at hand.

As the DSSC project is currently progressing very fast towards the final detector systems, newer chip and setup generations are currently being operated. The commissioning of the full megapixel camera is planned for September 2018. Current efforts of the DSSC calibration workpackage are oriented at the application of the tested methods to DSSC detector systems with larger formats, such as the simultaneous illumination of 128 x 512 pixels with fluorescence photons[2] for the gain calibration. The calibration methods presented in this work will serve as a basis for the analysis of first full-format detector calibration data.

---

[2]Accepted proposal I-20170570 for the P64-beamline at the PETRA III facility, Hamburg. Allocated beam time: June 7-13, 2018.

A. Mathematical definitions

A.1 Arithmetic mean

The arithmetic mean of a dataset $X = \{x_1, x_2, \ldots, x_n\}$ is defined as:

$$\overline{m}_{arith.}(X) = \frac{1}{N} \sum_{n=1}^{N} x_n \tag{A.1}$$

with the standard deviation

$$\sigma_{\overline{m}_{arith.}} = \sqrt{\frac{1}{N} \sum_{n=1}^{N} \left(x_n - \overline{m}_{arith.}(X)\right)^2} \tag{A.2}$$

A.2 Weighted arithmetic mean

The robustness of the arithmetic mean against outliers can be improved using weights. Often, data outliers can be identified by certain criteria such as extremely high or low fit errors in comparison to other elements of the dataset. The fit error of `MINUIT's` [51] `MIGRAD` can be assumed to be a good estimator of the variance σ_n^2 of the respective fit parameter.

When the dimension of the individual weights is given by the standard deviation σ_n of the individual elements, the weighted arithmetic mean of a dataset $X = (x_1, x_2, \ldots, x_n)$ is defined as:

$$\overline{m}_{w.arith.}(X) = \frac{\sum_{n=1}^{N} \frac{x_n}{\sigma_n^2}}{\sum_{n=1}^{N} \sigma_n^{-2}} \tag{A.3}$$

The standard deviation of the weighted mean based on the variance of the individual data points is:

$$\sigma_{\overline{m}_{w.arith.}} = \sqrt{\frac{1}{\sum_{n=1}^{N} \sigma_n^{-2}}} \tag{A.4}$$

A.3 Median

The median is another so-called location parameter of a distribution of values. In comparison to the arithmetic mean, it is more robust against extremely low or high values, so-called outliers. It is defined as the value in the middle of an ordered dataset $X = \{x_1, x_2, \ldots, x_n\}$ with $x_1 \leq x_2 \leq \ldots \leq x_n$:

$$\text{median}(X) = \begin{cases} x_{\frac{n+1}{2}} & \text{if N is odd} \\ \frac{1}{2}\left(x_{\frac{n}{2}} + x_{\frac{n}{2}+1}\right) & \text{if N is even} \end{cases} \tag{A.5}$$

As a measure of deviation from the median of a distribution, the median absolute deviation (`MAD`) is often used. It is defined as follows:

$$\texttt{MAD} = \text{median}\left(|x_i - \text{median}(X)|\right) \tag{A.6}$$

According to [70], the `MAD` estimator can be made consistent with the "usual" σ measure of a standard Gaussian distribution by help of a conversion factor b:

$$\sigma = b \cdot \texttt{MAD} \tag{A.7}$$

with $b = 1.4826$.

A.4   Normalization of eq. 5.19

This section gives a short motivation for the normalization of the tail components of the proposed global fit function for single-pixel spectra.

The identity that needs to be proven is

$$\frac{1}{2} \int_{-\infty}^{\infty} e^{\frac{x}{b}} \, \text{erfc}\left(\frac{x}{c} + \frac{c}{2b}\right) \text{dx} = b \, e^{-\left(\frac{c}{2b}\right)^2} \tag{A.8}$$

Following the definitions

$$\text{erf}(x) = 1 - \text{erfc}(x) \tag{A.9}$$

$$\text{erfc}(x) = \frac{2}{\sqrt{\pi}} \int_{x}^{\infty} e^{-t^2} \text{dt} \tag{A.10}$$

and the fundamental theorem of calculus, it is clear that

$$\frac{\text{d}}{\text{dx}} \, \text{erfc}(x) = -\frac{2}{\sqrt{\pi}} e^{-x^2} \tag{A.11}$$

Using partial integration, the left side of eq. A.8 can be written as

$$\frac{1}{2} \left\{ \left[b \, e^{\frac{x}{b}} \, \text{erfc}\left(\frac{x}{c} + \frac{c}{2b}\right) \right]_{-\infty}^{\infty} - \int_{-\infty}^{\infty} b \, e^{\frac{x}{b}} \left(-\frac{2}{\sqrt{\pi} \, c} e^{-\left(\frac{x}{c} + \frac{c}{2b}\right)^2} \right) \text{dx} \right\} \tag{A.12}$$

The term in brackets is 0 according to the rules of l'Hospital. From the integral one gets

$$\frac{b}{\pi \, c} \int_{-\infty}^{\infty} e^{\frac{x}{b} - \left(\left(\frac{x}{c}\right)^2 + \frac{x}{b} + \left(\frac{c}{2b}\right)^2\right)} \text{dx} = b \, e^{-\left(\frac{c}{2b}\right)^2} \frac{1}{\sqrt{\pi} \, c} \int_{-\infty}^{\infty} e^{-\left(\frac{x}{c}\right)^2} \text{dx} \tag{A.13}$$

The integral and its prefactor calculate to exactly one, therefore eq. A.8 is correct.

B. Analyses of simulated datasets

B.1   Offset residual comparison
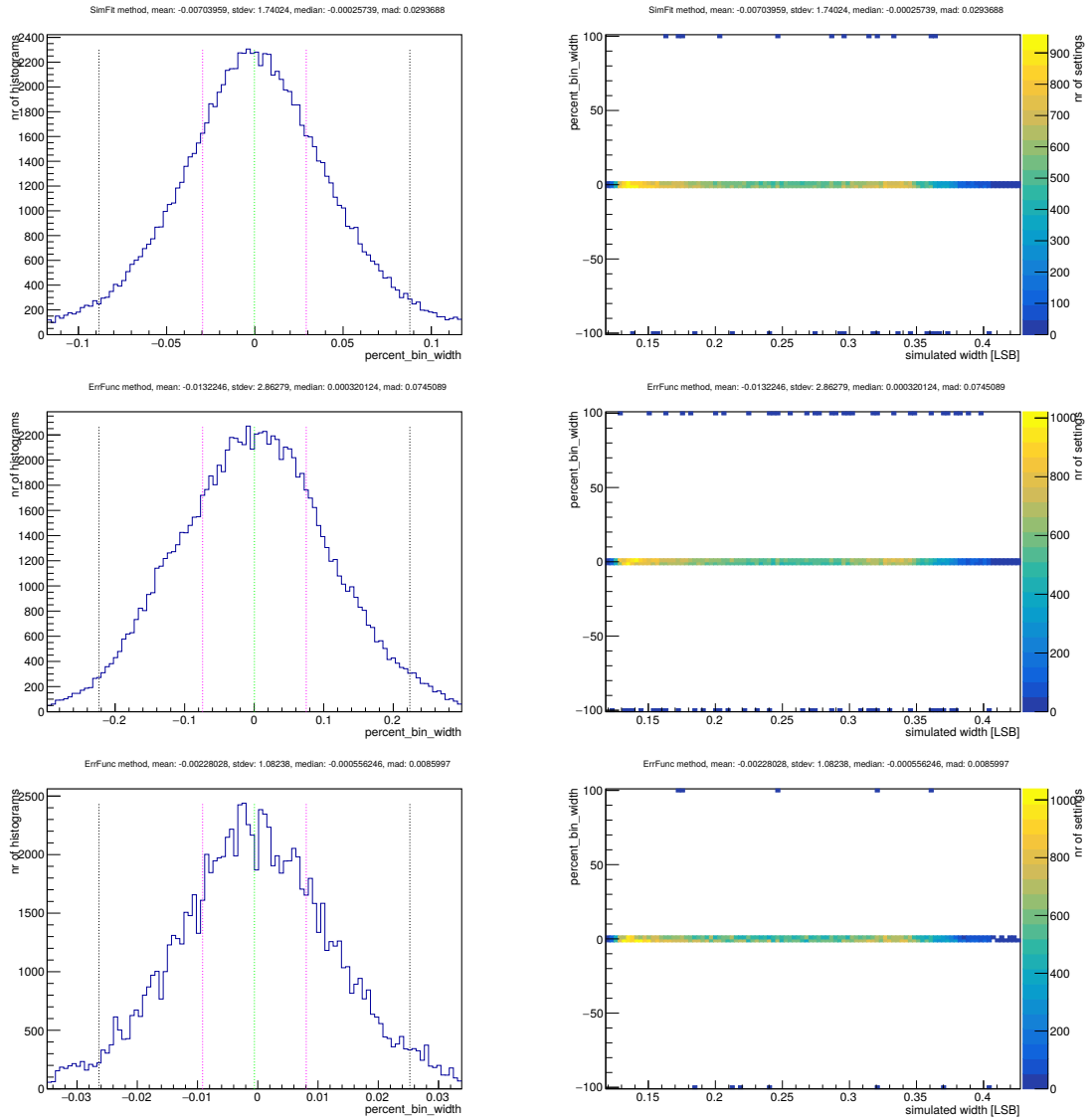
Figure B.1: Offset residual for simultaneous fit method (first row), error function method (second row) and error function method with ideally known pixel-delay step sizes (last row). Ideal binning.
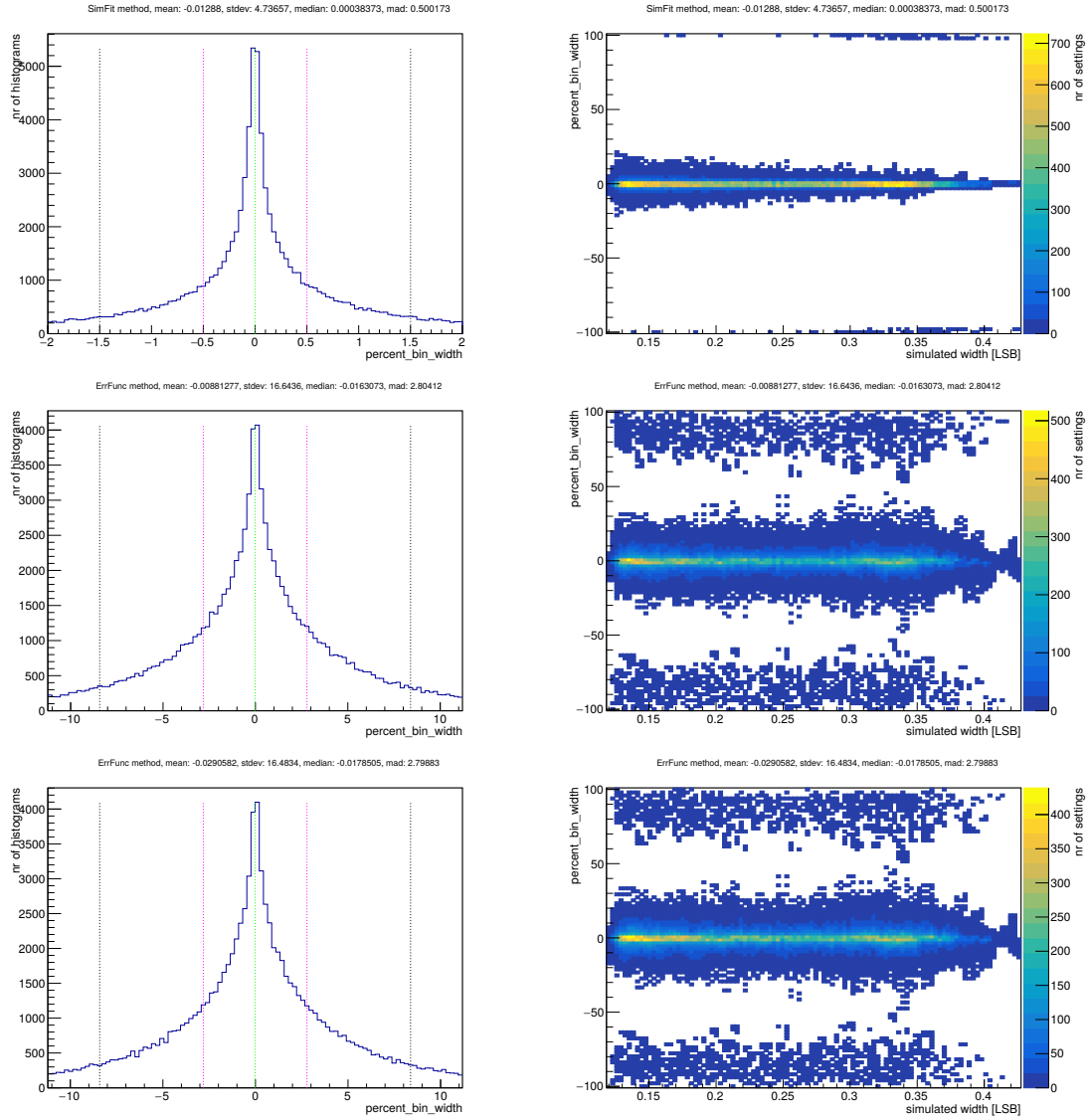
Figure B.2: Offset residual for simultaneous fit method (first row), error function method (second row) and error function method with ideally known pixel-delay step sizes (last row). Ideal binning, blurred with $\sigma_{\text{blur}} = 0.1$.
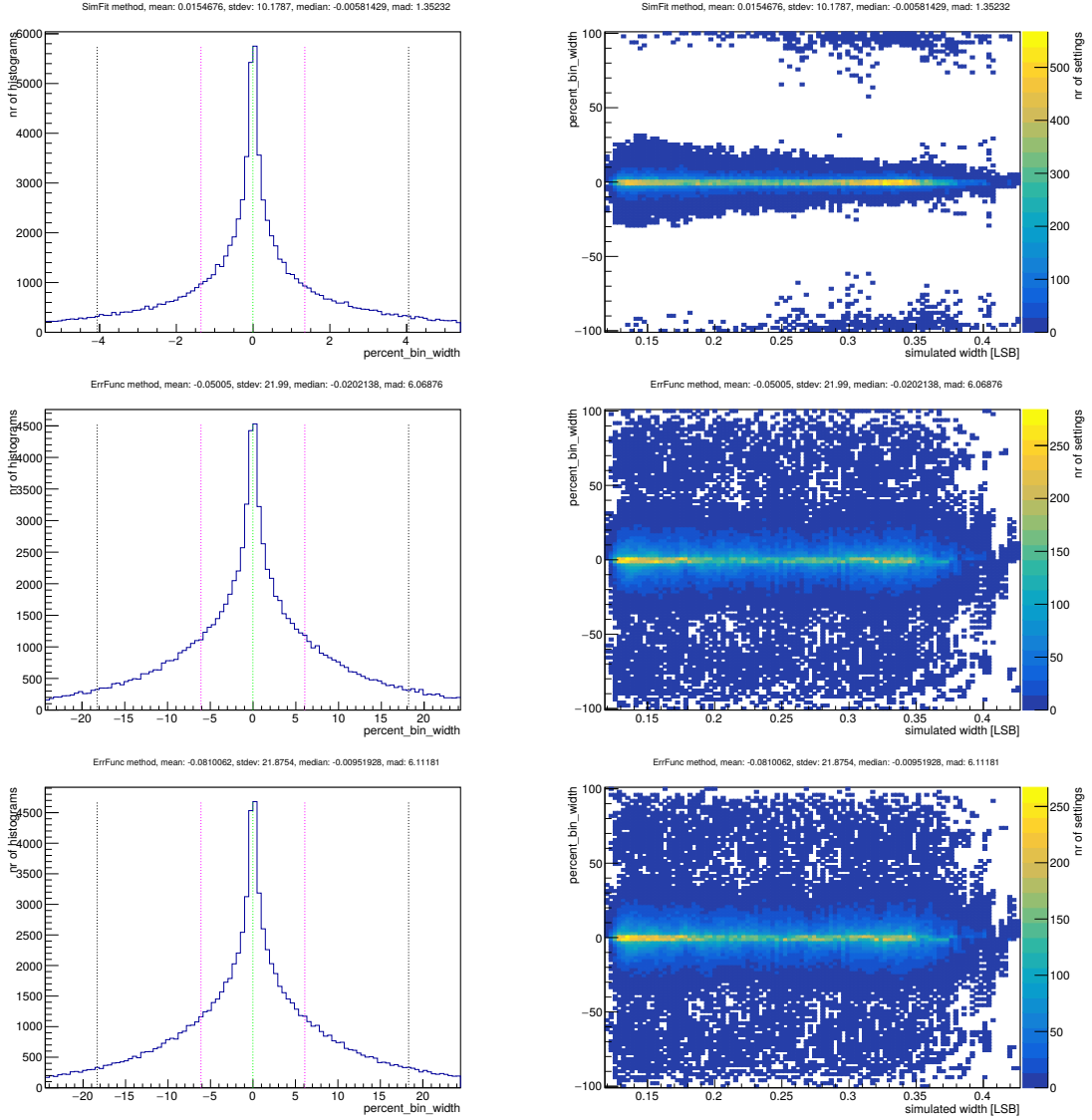
Figure B.3: Offset residual for simultaneous fit method (first row), error function method (second row) and error function method with ideally known pixel-delay step sizes (last row). Simulated GCC with $\sigma_{\mathrm{DNL}} = 0.3$, assumed to be ideal in the analysis.

B.2 Pixel delay step averaging
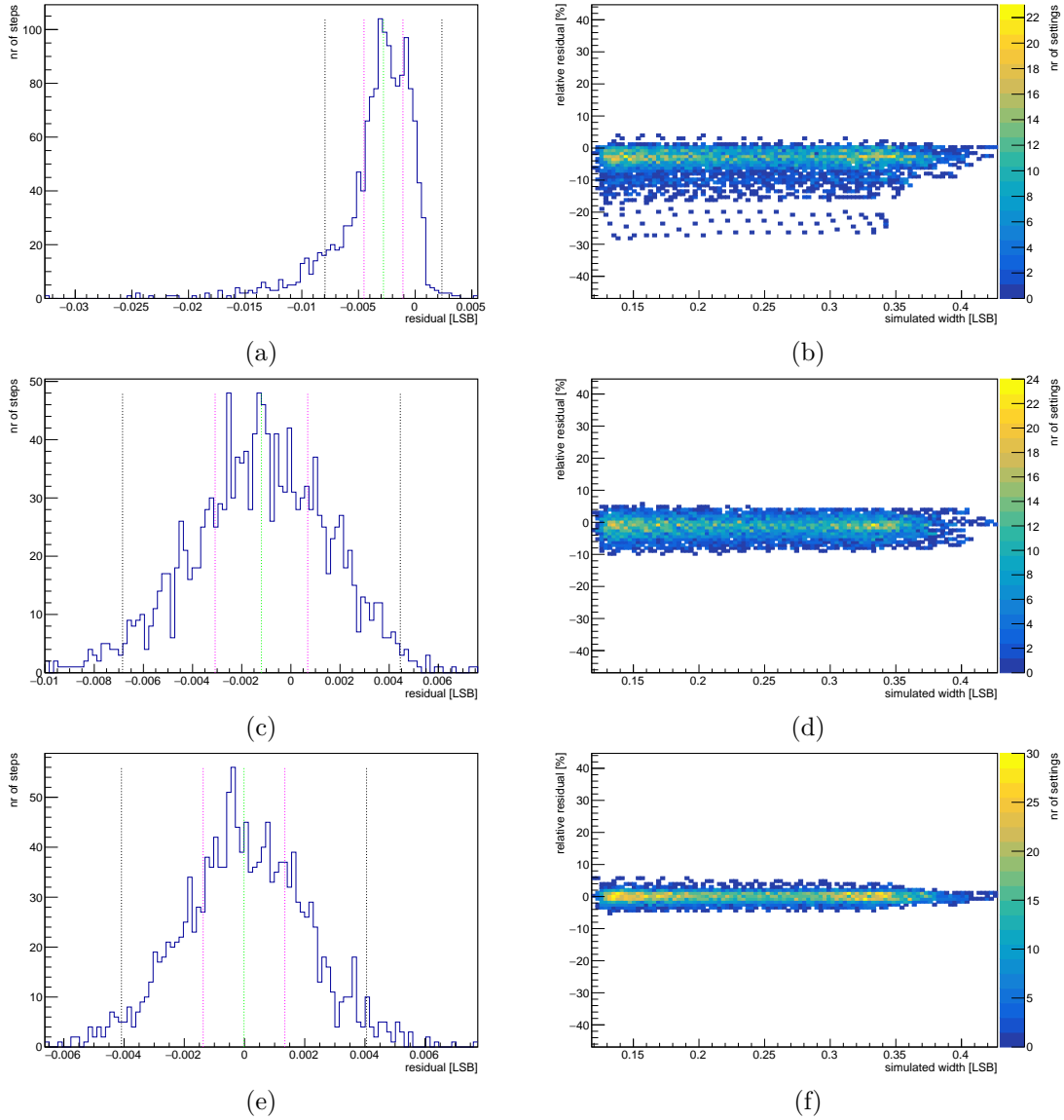
Figure B.4: Ideal binning, blurred with $\sigma_{\mathrm{blur}} = 0.1\,\mathrm{LSB}$. Full jk-grid of 100 pixels. Left column: Absolute residual of the determined to the simulated pixel delay steps. Right column: Relative residual of the noise determined with the error function method, plotted as a function of the simulated noise. Comparison of three different averaging methods for the pixel delay step determination:
(a) and (b) weighted arithmetic mean
(c) and (d) median method
(e) and (e) arithmetic mean
$\sigma(a) = 3.6 \cdot 10^{-3}\mathrm{LSB}$, $\sigma(b) = 3.9\%$
$\sigma(c) = 2.8 \cdot 10^{-3}\mathrm{LSB}$, $\sigma(d) = 2.7\%$
$\sigma(e) = 2.1 \cdot 10^{-3}\mathrm{LSB}$, $\sigma(f) = 1.4\%$

(a)

(b)

(c)

(d)

(e)

(f)
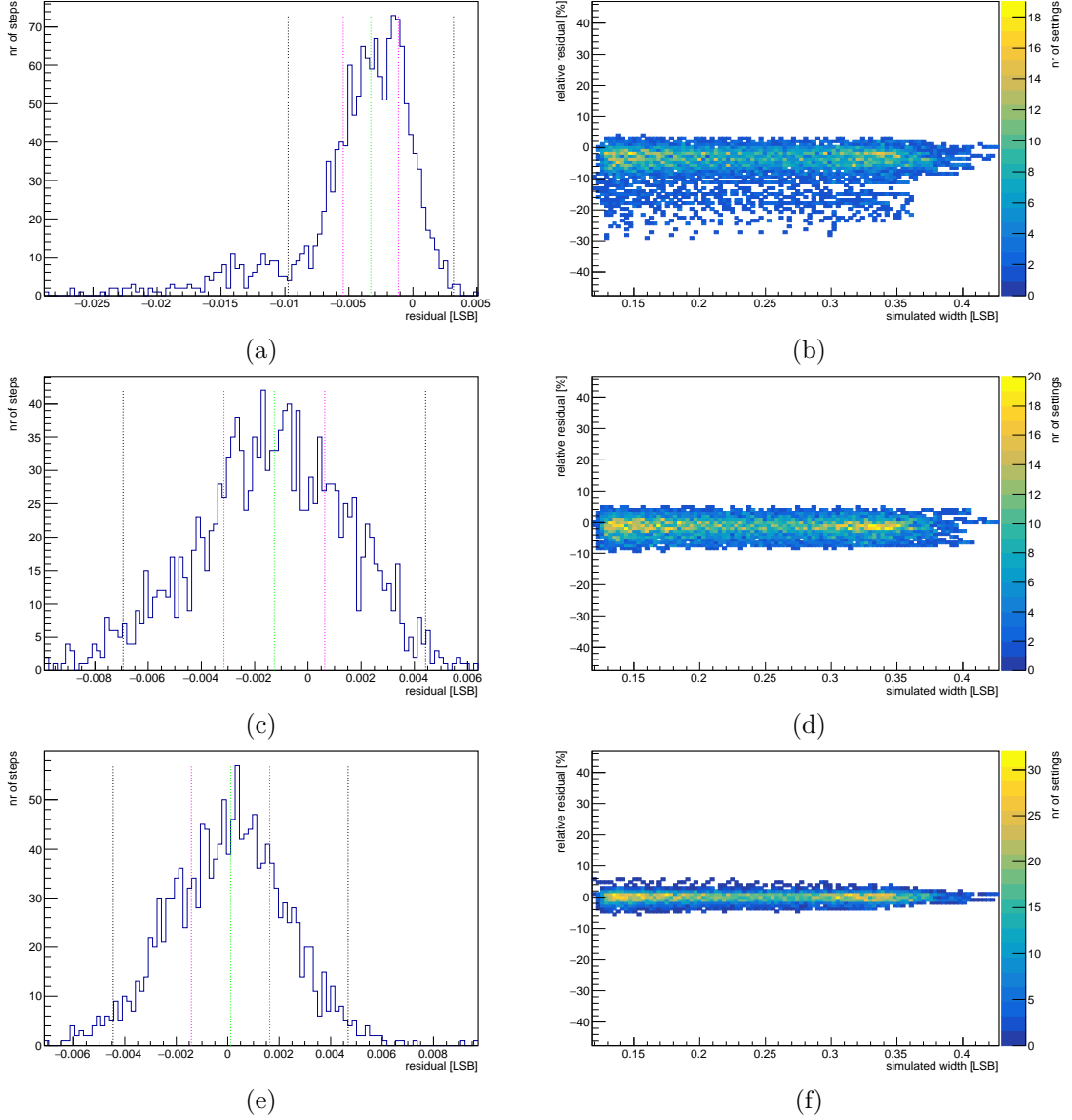
Figure B.5: As fig. B.4, but here the ADC was simulated with a cyclic DNL with $\sigma_{\mathrm{DNL}} = 0.1\,\mathrm{LSB}$ and additionally blurred with $\sigma_{\mathrm{blur}} = 0.1\,\mathrm{LSB}$ (as in fig. 5.7, (g)).
$\sigma(a) = 4.7 \cdot 10^{-3}\mathrm{LSB}$, $\sigma(b) = 5.2\%$
$\sigma(c) = 2.8 \cdot 10^{-3}\mathrm{LSB}$, $\sigma(d) = 2.7\%$
$\sigma(e) = 2.3 \cdot 10^{-3}\mathrm{LSB}$, $\sigma(f) = 1.4\%$

C. Analyses of the LABEC measurement campaign

C.1 Fits and Figures from the LABEC measurement

This section documents in detail the recorded data and the respective analysis of each of the 9 pixels additional to pixel 688 (fig. 6.7) that were selected during the LABEC measurement campaign (sec. 6.2). As described, this selection was based upon the amount of proton counts available in each spectrum.

Fig. C.1 to C.3 show the results of the fit to the proton spectra:

- Fig. C.1, first proton measurement, distance of 18 mm from detector to beam window.

- Fig. C.2, second proton measurement, distance of 20 mm from detector to beam window.

- Fig. C.3, third proton measurement, distance of 20 mm from detector to beam window.

As fig. 6.9, these plots show the fit boundaries of the automated fit algorithm with dashed, black lines and the fit result in red. In addition, the start values estimated by the start value algorithm (sec. 5.3.6) are given by a green line. It becomes obvious, that due to the very low signal in several of the spectra, the correct determination of the proton peak position becomes a challenging task. This is reflected in some of the fit results showing bad convergence (error range $\pm$nan).

Figs. C.4 to C.5 show the subsequent analysis of the pixel array with X-ray tube spectra fits and cross-calibration as described in sections 6.2.2 to 6.2.4.
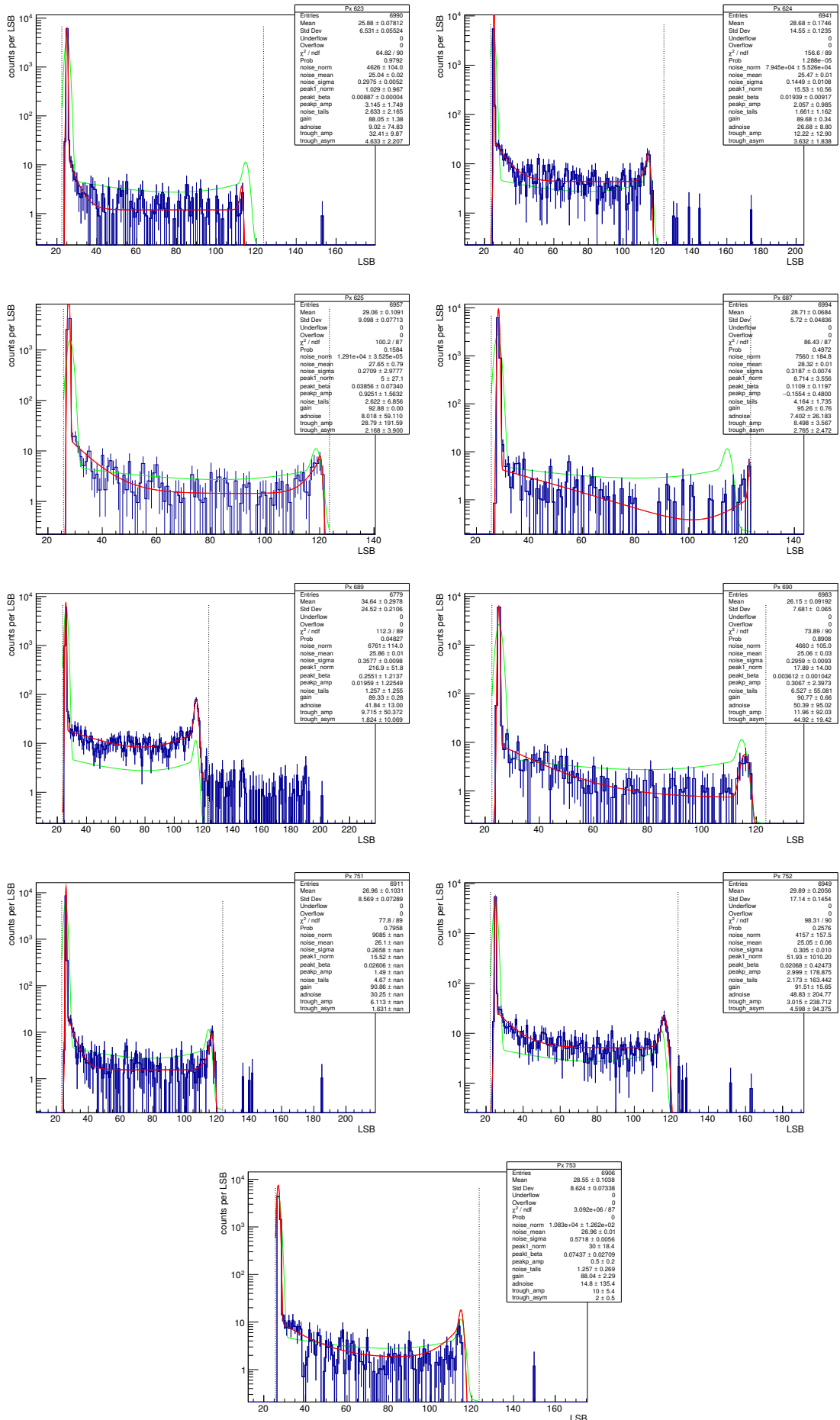
Figure C.1: LABEC - proton fits, distance 18 mm
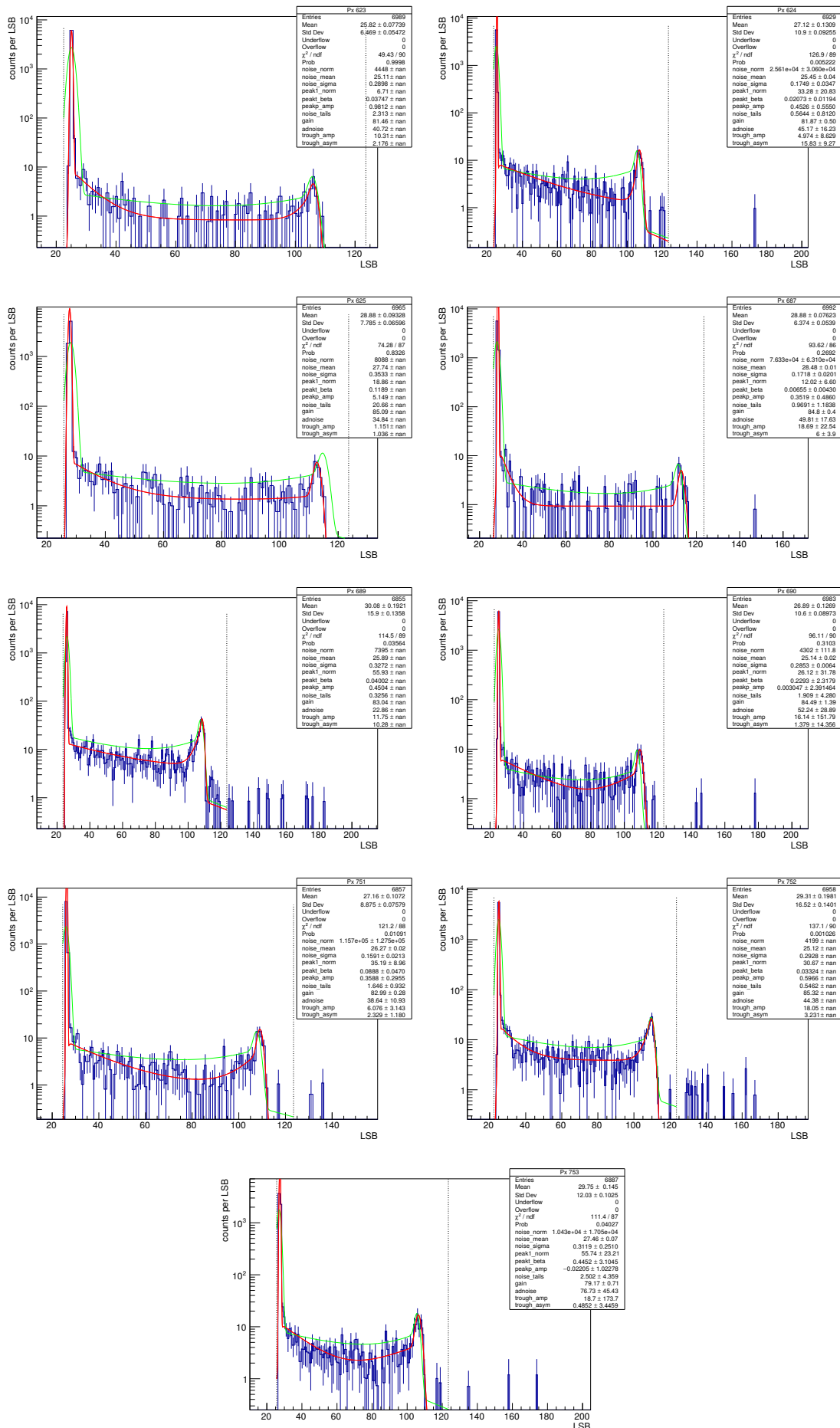
Figure C.2: LABEC - proton fits, distance 20 mm
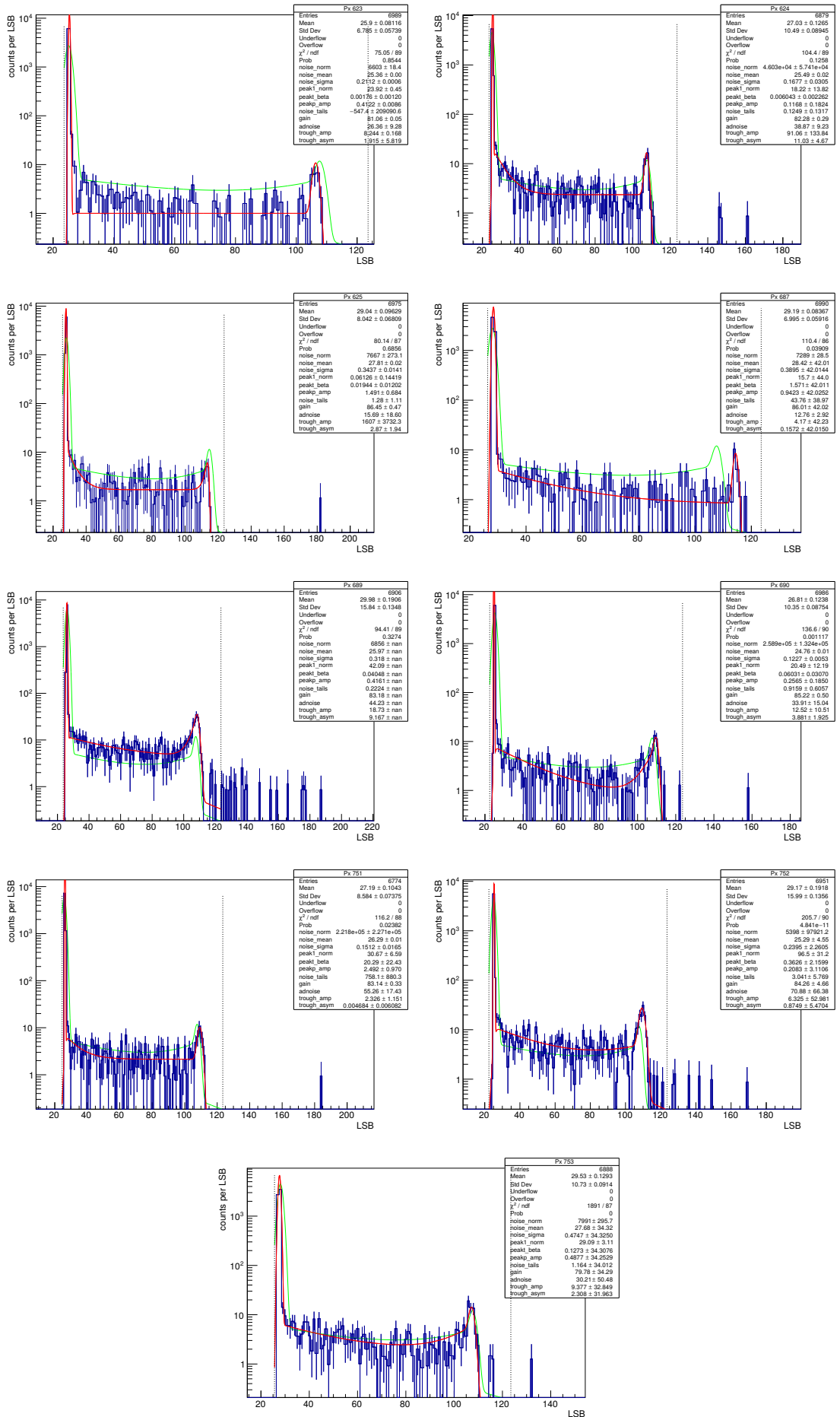
Figure C.3: LABEC - proton fits, distance 20 mm
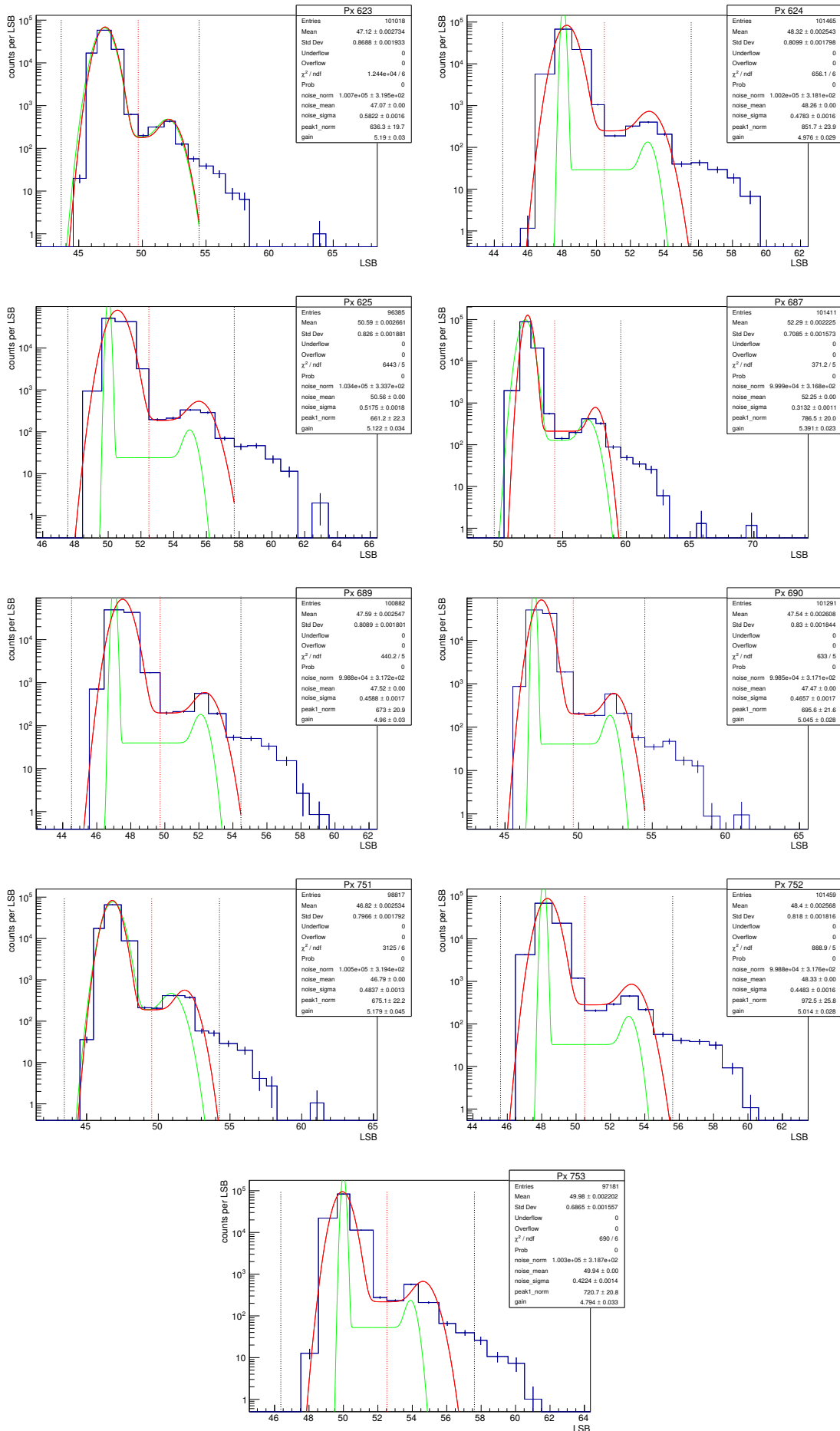
Figure C.4: LABEC - X-ray tube spectra fits
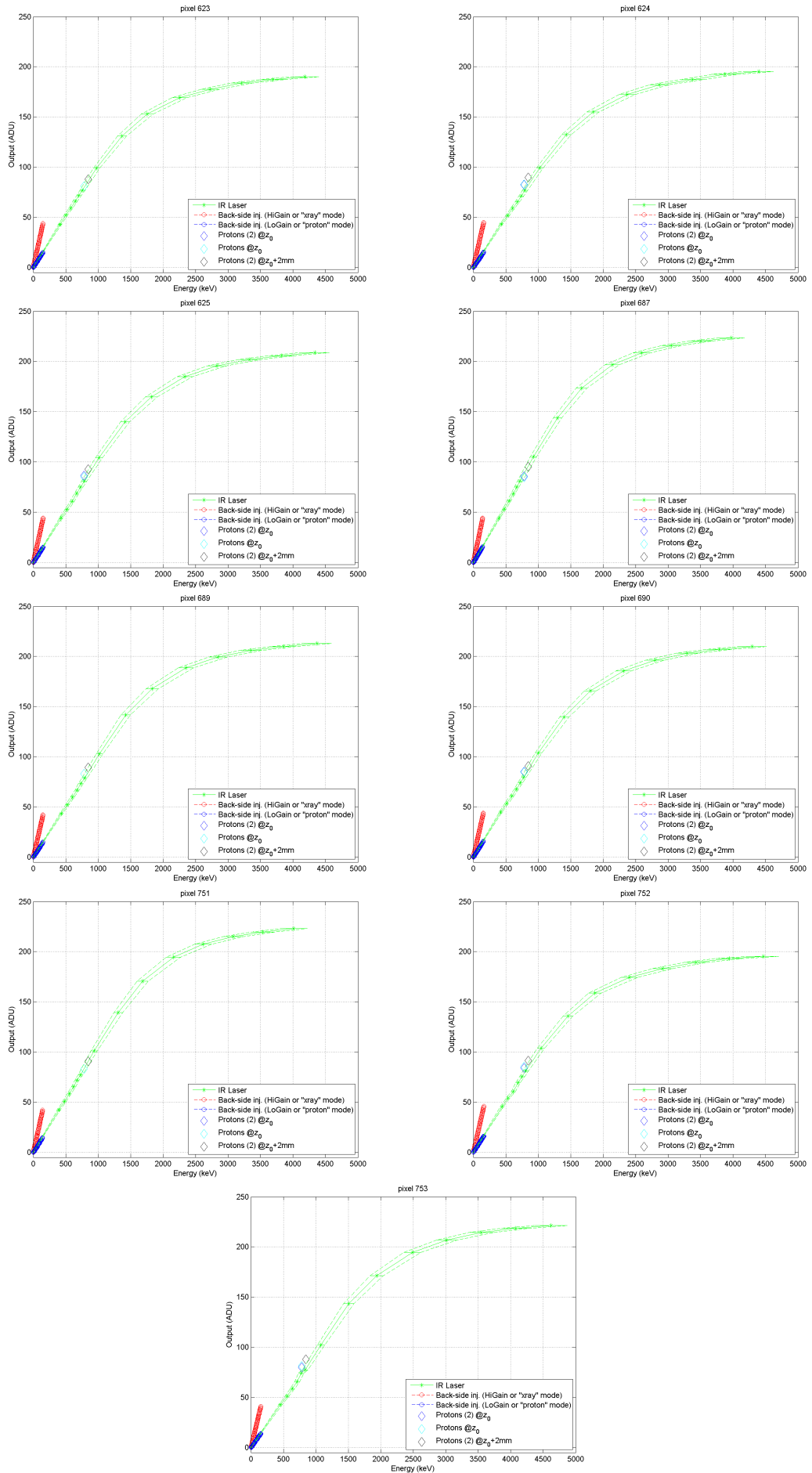
Figure C.5: LABEC - cross-check of calibration of the system response (NLSR)

List of Abbreviations

ADC   Analog-to-digital converter

ADU   Arbitrary digital unit

ASIC   Application-specific integrated circuit

CAD   Computer aided design

CPU   Central processing unit

DAC   Digital-to-Analog converter

DAQ   Data aquisition

DEPFET Depleted p-channel field effect transistor

DNL   Dynamic non-linearity

DSSC   DEPFET sensor with intrinsic signal compression

DUT   device under test

ENC   Equivalent noise charge

FEL   Free electron laser

FPGA   field-programmable gate array

INL   Integrated non-linearity

LPC   Linear pixel characteristic

LRCC   Linear read-out channel characteristic

LSB   Least significant bit

MiniSDD Miniature Silicon Drift Detector

NLPC   Non-linear pixel characteristic

NLRCC   Non-linear read-out channel characteristic

NLSR   Non-linear system response

PCB   printed circuit board

SASE   Self-amplified spontaneous emission

XFEL   X-ray free electron laser

List of Figures

Bibliography

[1] GS Hawkins. Stonehenge decoded. *Nature*, 200:306 EP –, 10 1963.

[2] XFEL GmbH. The European XFEL. http://www.xfel.eu/, August 2017.

[3] Massimo Altarelli et al. The European X-Ray Free-Electron Laser Technical design report. *DESY 2006-097*, 2007.

[4] Matthias Fuchs. *Laser-Driven Soft-X-Ray Undulator Source*. Phd thesis, Ludwig-Maximilians-Universität München, 2010.

[5] P. Schmüser, M. Dohlus, and J. Rossbach. *Ultraviolet and Soft X-Ray Free-Electron Lasers: Introduction to Physical Principles, Experimental Results, Technological Challenges*. Springer, 2008.

[6] C. Bostedt et al. Ultrafast x-ray scattering of xenon nanoparticles: Imaging transient states of matter. *Phys. Rev. Lett.*, 108:093401, Feb 2012.

[7] Yevheniy Ovcharenko, European XFEL GmbH Instrument SQS. Priv. communication. 2017.

[8] DESY. Snapshots of Firework in Nanoparticles at FLASH: Beyond Conventional Ultrafast Spectroscopy (Mar.2012). http://www.desy.de/, November 2017.

[9] W. Ackermann et al. Operation of a free-electron laser from the extreme ultraviolet to the water window. *Nature Photonics 1*, pages 336–342, 2007.

[10] K. Tiedtke et al. The soft x-ray free-electron laser flash at desy: beamlines, diagnostics and end-stations. *New Journal of Physics*, 11(2):023029, 2009.

[11] Glenn F. Knoll. *Radiation Detection and Measurement*. John Wiley & Sons, 3rd edition, January 2000.

[12] R. Neutze et al. Potential for biomolecular imaging with femtosecond X-ray pulses. *Nature*, 406, 2000.

[13] Stefan M. Aschauer. *There is never enough dynamic range – DEPFET active pixel sensors with analog signal compression*. Phd thesis, Technische Universität München, 2014.

[14] Heinz Graafsma. Requirements for and development of 2 dimensional X-ray detectors for the European X-ray Free Electron Laser in Hamburg. *Journal of Instrumentation*, 4(12), 2009.

[15] B. Henrich et al. The adaptive gain integrating pixel detector AGIPD a detector for the European XFEL. *Nuclear Instruments and Methods in Physics Research A*, 2011.

[16] G. Lutz, P. Lechner, M. Porro, L. Strüder, and G. de Vita. DEPFET sensor with intrinsic signal compression developed for use at the XFEL free electron laser radiation source. *Nuclear Instruments and Methods in Physics Research A*, 2010.

[17] M. Porro, G. Lutz, L. Strüder, G. Weidenspointner, et al. Expected performance of the DEPFET sensor with signal compression: A large format X-ray imager with mega-frame readout capability for the European XFEL. *Nuclear Instruments and Methods in Physics Research A*, March 2010.

[18] M. Porro et al. Development of the DEPFET Sensor with Signal Compression: a Large Format X-ray Imager with Mega-Frame Readout Capability for the European XFEL. *Transactions on Nuclear Sciences*, August 2012. Manuscript received June 15, 2012; revised August 11, 2012. In press.

[19] G. Weidenspointner et al. Strategy for calibrating the non-linear gain of the DSSC detector for the European XFEL. *Nuclear Science Symposium and Medical Imaging Conference (NSS/MIC), 2011 IEEE*, 2011.

[20] P. Fischer et al. Pixel Readout ASIC with per Pixel Digitization and Digital Storage for the DSSC Detector at XFEL. *Nuclear Science Symposium Conference Record (NSS/MIC), IEEE*, 2010.

[21] Gerhard Lutz. *Semiconductor Radiation Detectors.* Device Physics. Springer, 1st edition, 1999.

[22] Thomas Lauf. *Analysis and Operation of DePFET X-ray Imaging Detectors.* Dissertation, Technische Universität München, 2011.

[23] Lawrence Berkeley National Laboratory. The Center for X-Ray optics. http://www.cxro.lbl.gov/, 2012.

[24] M.J. Berger et al. NIST Standard Reference Database 8 (XGAM). http://www.nist.gov/, 2017.

[25] P. Rehak E. Gatti. Semiconductor drift chamber – An application of a novel charge transport scheme. *Nuclear Instruments and Methods in Physics Research*, 1984.

[26] Florian Erdinger. *Design of Front End Electronics and a Full Scale 4k Pixel Readout ASIC for the DSSC X-ray Detector at the European XFEL.* Phd thesis, Universität Heidelberg, 2016.

[27] C Fiorini et al. A Simple Technique for Signal Compression in High Dynamic Range, High Speed X-ray Pixel Detectors. 61:2595–2600, 10 2014.

[28] U. Tietze, C. Schenk, and E. Gamm. *Halbleiter-Schaltungstechnik.* Springer, 2002.

[29] S. Facchinetti et al. Characterization of the Flip Capacitor Filter for the XFEL-DSSC Project. 58:2032–2038, 8 2011.

[30] K. Hansen et al. Pixel-level 8-bit 5-MS/s Wilkinson-type digitizer for the DSSC X-ray imager: Concept study. *Nuclear Instruments and Methods in Physics Research Section A: Accelerators, Spectrometers, Detectors and Associated Equipment*, 629:269 – 276, 2011.

[31] Robert Beinert. *Entwicklung und Anwendung eines Verfahrens zur Kalibration von Flächendetektoren unter Berücksichtigung von Nichtlinearitäten.* Bachelorarbeit, Fachhochschule Flensburg, 2011.

[32] David Stefan Moch. *Calibration of the Non-Linear System Characteristic of the DSSC system.* Phd thesis, Universität Hamburg, in preperation.

[33] R. W. Hamming. Error detecting and error correcting codes. *Bell System Tech J.*, 1950.

[34] M. Manghiosi et al. High accuracy injection circuit for pixel-level calibration of readout electronics. *Nuclear Science Symposium Conference Record (NSS/MIC), 2010 IEEE*, 6 2010.

[35] Stephan Schlee. *Calibration of a novel, non-linear DePFET pixel in a prototype sensor setup for the European XFEL.* Diplomarbeit, Ludwig-Maximilians-Universität München, 2012.

[36] Jan Soldat. *Characterization, Operation and Wafer-level Testing of an ultra-fast 4k Pixel Readout ASIC for the DSSC X-ray Detector at the European XFEL.* Phd thesis, Universität Heidelberg, 2017.

[37] Manfred Kirchgessner. *Control, Readout and Commissioning of the Ultra-High Speed 1 Megapixel DSSC X-Ray Camera for the European XFEL.* Phd thesis, Universität Heidelberg, 2017.

[38] Alexander Bähr. *Experimenteller Betrieb neuartiger DEPFET-RNDR Detektoren und mathematische Beschreibung der Mehrfachauslese.* Diplomarbeit, Hochschule für angewandte Wissenschaften – FH München, 2010.

[39] IEEE. IEEE Standard for Verilog Hardware Description Language. *IEEE Std 1364-2005 (Revision of IEEE Std 1364-2001)*, 2006.

[40] L.W. Nagel and D.O. Pederson. SPICE (Simulation Program with Integrated Circuit Emphasis). Technical report, EECS Department, University of California, Berkeley, Apr 1973.

[41] Matsumoto and T. Nishimura. Mersenne Twister: A 623-diminsionally equidistributed uniform pseudorandom number generator. *ACM Transactions on Modeling and Computer Simulation*, Vol. 8, No. 1:3–30, 1998.

[42] The ROOT Team. Cern ROOT, A Data Analysis Framework, Version 5.30/03 on linuxx8664gcc. http://root.cern.ch, October 2011.

[43] PNSensor GmbH Stefan Aschauer. Priv. communication. 2017.

[44] G. Weidenspointner, S. Schlee, et al. The calibration and system simulation software package for the European XFEL DSSC detector. *Nuclear Science Symposium and Medical Imaging Conference (NSS/MIC), 2016 IEEE*, 2016.

[45] S. Agostinelli et al. Geant4-a simulation toolkit. *Nuclear Instruments and Methods in Physics Research Section A: Accelerators, Spectrometers, Detectors and Associated Equipment*, 506(3):250 – 303, 2003.

[46] J. Allison et al. Geant4 developments and applications. *IEEE Transactions on Nuclear Science*, 53(1):270–278, Feb 2006.

[47] J. Allison et al. Recent developments in geant4. *Nuclear Instruments and Methods in Physics Research Section A: Accelerators, Spectrometers, Detectors and Associated Equipment*, 835:186 – 225, 2016.

[48] A. Zoglauer, G. Weidenspointner, M. Galloway, S. E. Boggs, and C. B. Wunderer. Cosima, The cosmic simulator of MEGAlib. *2009 IEEE Nuclear Science Symposium Conference Record (NSS/MIC)*, pages 2053–2059, Oct 2009.

[49] Nils Kimmel. *Analysis of the charge collection process in solid state X–ray detectors*. Phd thesis, Universität Siegen, 2008.

[50] Trond Hjorteland. *The Action Variation Principle In Cosmology*. Phd thesis, University of Oslo - Institute of Theoretical Astrophysics, 1999.

[51] Fred James. *MINUIT - Function Minimization and Error Analysis (Reference Manual)*. CERN Geneva, Switzerland, 1994.

[52] James Theiler Mark Galassi, Jim Davies. *GNU Scientific Library (Reference Manual)*. The GSL Team, 2.3 edition, 2016.

[53] Norbert Meidinger. *Diffusion und Drift von Ladungen in Halbleiter-Detektoren*. Diplomarbeit, Technische Universität München, 1990.

[54] Martin Popp. *Untersuchung und analytische Modellierung der Systemantwort von pn-CCD Detektoren*. Phd thesis, Ludwig-Maximilians-Universität Münchenn, 2000.

[55] Robert Andritschke, Max-Planck Institute for extraterrestrial Physics. Priv. communication. 2017.

[56] S. Schlee et al. Methods for calibrating the gain and offset of the DSSC detector for the European XFEL. *Nuclear Science Symposium and Medical Imaging Conference (NSS/MIC), 2015 IEEE*, 2015.

[57] S. Schlee et al. Methods for calibrating the gain and offset of the DSSC detector for the European XFEL using X-ray line sources. *Journal of Instrumentation*, 11(01):C01001, 2016.

[58] G. Phillips and K. Marlow. Automatic Analysis of Gamma-Ray Spectra From Germanium Detectors. *Nuclear Instruments and Methods*, 1976.

[59] O. Forster. *Analysis 1 - Differential- und Integralrechnung einer Veränderlichen.* Vieweg+Teubner Verlag, 2006.

[60] Stefanie Granato. *The response of silicon PNCCD sensors with aluminum on-chip filter to visible light, UV- and X-ray radiation.* Phd thesis, Universität Siegen, 2012.

[61] L.P. Ekström S.Y.F. Chu and R.B. Firestone. WWW Table of Radioactive Isotopes. *database version 1999-02-28 from URL http://nucleardata.nuclear.lu.se/nucleardata/toi/.*

[62] Georg Weidenspointner, European XFEL GmbH. Priv. communication. 2017.

[63] B.C. Heisen et al. Karabo: an integrated software framework combining control, data management and scientific computing tasks. *14th International Conference on Accelerator and Large Experimental Physics Control Systems, ICALEPCS, San Francisco, U.S.A.*, 2013.

[64] Eckart u. Ziegler. Eckert u. Ziegler Reference and Calibration Sources. *URL https://www.jrias.or.jp/products/pdf/20090401-135217.pdf, 2018-05-27.*

[65] Eckart u. Ziegler. Recommended Nuclear Decay Data Cd-109. *URL https://www.ezag.com, 2018-05-27.*

[66] Florian Erdinger, University of Heidelberg. Priv. communication. 2017.

[67] A. Castoldi, C. Guazzoni, D. Mezza, G.V Montemurro, L. Carraresi, and F. Taccetti. Upgrade of the DEFEL proton beam line for detector response mapping. *IEEE Nuclear Science Symposium Conference Record*, 2013.

[68] A. Castoldi, C. Guazzoni, S. Maffessanti, M. Porro, S. Schlee, and G. Weidenspointner. Calibration sources and techniques for large format X-ray imagers at XFEL. *Nuclear Science Symposium Conference Record (NSS/MIC), 2016 IEEE*, 2016.

[69] A. Castoldi, C. Guazzoni, G. V. Montemurro, L. Carraresi, M. Porro, S. Schlee, and G. Weidenspointner. Validation of proton tests in air for detector calibration over a wide range of charge injection levels. *Nuclear Science Symposium Conference Record (NSS/MIC), 2015 IEEE*, 2015.

[70] P.J. Rousseeuw and C. Croux. Alternatives to the median absolute deviation. *Journal of the American Statistical Association*, 88(424):1273–1283, 1993.

Acknowledgement

Eidesstattliche Versicherung / Declaration on oath

Hiermit versichere ich an Eides statt, die vorliegende Dissertationsschrift selbst verfasst und keine anderen als die angegebenen Hilfsmittel und Quellen benutzt zu haben.

Die eingereichte schriftliche Fassung entspricht der auf dem elektronischen Speichermedium.

Die Dissertation wurde in der vorgelegten oder einer ähnlichen Form nicht schon einmal in einem früheren Promotionsverfahren angenommen oder als ungenügend beurteilt.

München, den 14. September 2018.

_____

Stephan Schlee